The Dissociation of Metalloporphyrin Anions

Guangliang Chen

Thesis submitted to the

Faculty of Graduate & Postdoctoral Studies

in partial fulfillment of the requirements for the

M.Sc. degree in Chemistry

Department of Chemistry and Biomolecular Sciences

Faculty of Science

University of Ottawa

Abstract

ESI-MS spectra of Ni^{II}, Co^{III}, Mg^{III}, and Fe^{II} porphyrin solutions in methanol show porphyrin monomer species with different charge states, such as $[Ni^{II}TPPS+H]^{3-}$, $[Co^{III}TPPS]^{3-}$, $[Mn^{III}TPPS]^{3-}$, $[Mn^{III}TPPS+H]^{2-}$, $[Fe^{II}TPPS+H]^{3-}$, and $[Fe^{II}TPPS+2H]^{2-}$ ions. Collision-induced dissociation (CID) of these monomer species produced primarily losses of neutral SO_3 and SO_2. The mechanisms, in which these dissociation pathways took place, were investigated by the means of DFT calculations of the corresponding dissociation of neutral and ionized benzenesulfonate (B3-LYP/6-31+G(2d, p) level) and porphyrin monomer (B3-LYP/6-31+G(2d, p)+LANL2DZ//PM7 level). RRKM fitting of the CID breakdown curves showed that the activation energies of the reactions that experience a loss of SO_2 from $[Co^{III}TPPS]^{3-}$ and $[Mn^{III}TPPS]^{3-}$ were similar, but of a lower magnitude than those for a loss of SO_3. On the other hand, for $[Ni^{II}TPPS+H]^{3-}$ and $[Fe^{II}TPPS+2H]^{2-}$, the activation energies of the reaction leading to a loss of SO_2 were also similar, but this time were larger than those leading to SO_3 loss. These results are consistent with a mechanism by which the SO_2 loss starts with $-C_6H_4SO_3^-$, while the SO_3 loss has to begin with $-C_6H_4SO_3H$. To lose this SO_3, extra energy is required for $[Co^{III}TPPS]^{3-}$ and $[Mn^{III}TPPS]^{3-}$ in order for them to overcome the barrier of H transfer from the porphyrin ring to $-SO_3^-$, but this is irrelevant when it comes to $[Ni^{II}TPPS+H]^{3-}$ and $[Fe^{II}TPPS+2H]^{2-}$ since the $C_6H_4SO_3H$ moiety already exists. In addition, the reaction of $[Fe^{II}TPPS+H]^{3-}$ losing H leads to a unique dissociation mechanism.

Acknowledgements

I would like to thank the John Holmes Mass Spectrometry Centre for giving me this memorable experience for the past two years.

Thank you Dr. Ameneh Gholami and Shaan Rashid for their valuable time in helping me with the experiment. I would not able to finish without them.

I would also like to thank Dr. Justin Renaud, and Dr. Barbara Francisco and Jenna Hamilton for always being there when I was in need. I am grateful to Eduardo Solano and Alicia Sit for helping me understand RRKM theory, and use RRKM and GaussView programs. In addition, I would like to acknowledge the other members of the Mayer research group: Dr. Brandi West, Huayu Xue, Jaleh Halvachizadeh, Jeffery Butson, Samata Mosammat Khan, Sabria Mohamed, Iden Djavani, Emily Gee, Naomi Mattli-Lewis, and Anaïs Ryc.

Thank you Dr. Sharon Curtis, Dr. Sander Mommers, and Sean Overton for their assistance in getting the instrument back to work when the instrument was down.

I am grateful towards Wanying Zhang, André Hughes, Matthew Schwarzkopf, Rochelle Mathew, Andrea Liu, Roch Boisvert, Liem Whelan, and Mary Morley for proofreading and editing my thesis.

Most of all, I would like to thank my supervisor Dr. Mayer for patiently guiding me throughout the entire project. As an international student, there is a culture difference and language barrier, and his understanding encouraged me a lot. In addition, I learned many things from him; not only knowledge, but also Canadian culture. His mentorship will benefit me for a lifetime.

Table of Contents

List of Figures

List of Tables

Abbreviations

BIRD	Blackbody infrared radiative dissociation
BEP	Bell-Evans-Polanyi
CID	Collision-induced dissociation
CRM	Charge residue model
DC	Direct current
DFT	Density functional theory
DOF	Degree of freedom
E_0	Activation energy
ECD	Electron-capture dissociation
ESI	Electrospray ionization
ETD	Electron-transfer dissociation
IEM	Ion evaporation model
IR	Infrared
IRMPD	Infrared multiphoton dissociation
KS	Kohn-Sham
MAD	Mean absolute deviation
MS/MS	Tandem mass spectrometry
NDDO	Neglect of diatomic differential overlap
NMR	Nuclear magnetic resonance
Q-TOF	Quadrupole-time-of-flight
RF	Radio frequency
RMS	Root mean square residuals
RRKM	Rice–Ramsperger–Kassel–Marcus
StdDec	Standard deviation
TOF	Time-of-flight
TPP	Tetraphenyl porphyrin
TPPS	Meso-tetra(4-sulfonatophenyl) porphine (acid form)
TW-IMS	Travelling-wave ion mobility spectrometry
$\Delta^{\ddagger}S$	Entropy of activation

Chapter 1. Introduction

1.1 Objective

The primary focus of this research is to investigate the mechanism by which the gas-phase ionized metalloporphyrins dissociate into fragment ions. In previous studies [1-5], mass spectrometry (MS) was proven to be efficient at structural analysis of porphyrins. Here, the properties of meso-tetra(4-sulfonatophenyl) porphine (acid form) (TPPS) solubilized in methanol were investigated when bound to various metals using several methods: namely, electrospray ionization mass spectrometry (ESI-MS), electrospray ionization tandem mass spectrometry (ESI-MS/MS), and the in-source-collision-induced-dissociation-MS/MS on a Waters Synapt G1 ion mobility/tandem mass spectrometer.

The dissociation of monomer MTPPS (M = Ni^{II}, Co^{III}, Mn^{III}, and Fe^{II}) ions were studied in detail in this research. The common charge states of these monomers are -2 and -3. However, only $[Ni^{II}TPPS+H]^{3-}$, $[Co^{III}TPPS]^{3-}$, $[Mn^{III}TPPS]^{3-}$, $[Mn^{III}TPPS+H]^{2-}$, $[Fe^{II}TPPS+H]^{3-}$, and $[Fe^{II}TPPS+2H]^{2-}$ were studied because there was insufficient signal for $[Ni^{II}TPPS+2H]^{2-}$ and $[Co^{III}TPPS+H]^{2-}$ (See Figure 1.1 for structures, and see Figure 4.1, A1.1, A2.1 and A4.1 for abundances). Those six ions are similar in structure, but are different in charge states (which influences the number of hydrogen atoms) and metal centers:

- Charge states: The charge state of metalloporphyin ions and the oxidation state of their metal centers can influence the number of H atoms. $[Co^{III}TPPS]^{3-}$ and $[Mn^{III}TPPS]^{3-}$ have no H^+ binding to $-SO_3^-$; $[Ni^{II}TPPS+H]^{3-}$, $[Mn^{III}TPPS+H]^{2-}$, and

$[Fe^{II}TPPS+H]^{3-}$ have one H^+ binding to $-SO_3^-$, while $[Fe^{II}TPPS+2H]^{2-}$ has two H^+ binding to two $-SO_3^-$ groups.

- Metal centers: manganese (Mn), iron (Fe), cobalt (Co), and nickel (Ni) (Table 1.1), all transition elements of the forth row, have atomic numbers of 25, 26, 27, and 28, respectively. Electron affinities and main oxidation states of these metals are different [6].

The dissociation process of these six ions were studied to explore the influence of H atoms and metal centers on dissociation pathways and activation energies of gas-phase metalloporphyrin ions.

Table 1.1 Property of Mn, Fe, Co and Ni

	Atomic Number	Electron Affinity	Main Oxidation States
Mn	25	< 0 eV	7, 4, 2
Fe	26	0.151 ± 0.003 eV	3, 2
Co	27	0.6633 ± 0.0006 eV	3, 2
Ni	28	1.15716 ± 0.00012 eV	2

For the analysis of $[Fe^{II}TPPS+2H]^{2-}$ and $[Mn^{III}TPPS+H]^{2-}$, the use of ion mobility separation (IMS) was required because there could be different species present, such as monomers, dimers and trimers. These different species could have the same mass to charge ratio which would make it challenging to distinguish one from another without IMS. $[Fe^{II}TPPS+H]^{3-}$, $[Mn^{III}TPPS]^{3-}$, $[Co^{II}TPPS]^{3-}$, and $[Ni^{II}TPPS+H]^{3-}$ only contain monomers in solution, thus the use of IMS was optional.

The main mathematical model in this study is RRKM theory. RRKM theory was used to model the MS/MS breakdown diagrams to obtain meaningful relative energies

for the dissociation of these ions. Molecular simulations were used to help interpret the RRKM results.

1.2 Metalloporphyrins

Porphyrins, especially iron derivatives of porphyrins, play a very important role in all living systems. The nucleus of a porphyrin molecule, which consists of a macrocyclic ring with two removable hydrogens (Figure 1.1), is able to coordinate with a metal that has a maximum diameter of approximately 3.7 Å [7]. Metals suitable for coordination include Fe, Mn, Co, Ni and Sn. There is an abundance of different kinds of porphyrin compounds, such as iron(III) tetraphenyl porphyrin chloride (Fe^{III}TPPCl), iron(II) meso-tetra(4-sulfonatophenyl) porphyrin (Fe^{II}TPPS), iron(lll) meso-tetra(methylpyridinium-4-yl) porphyrin (Fe^{III}TMPyP) etc.

TPPS (Meso-tetra(4-sulfonatophenyl) porphine) with different metal centers are of special interest in this study. The TPPS with an iron (II) center, [Fe^{II}TPPS] (Figure 1.1), is well-known as a catalyst for the transport and storage of oxygen in hemoglobin, cytochromes and myoglobin [8]. On the other hand, iron porphyrin has a stronger affinity for CO, NO, and NO_2 compared to O_2 [5]. As such, the binding of iron to gases other than oxygen is known to cause O_2 deprivation in animals, which can be fatal. Then there is also manganese(III) porphyrin, [Mn^{III}TPPS], which plays an essential role in the photosynthesis processes in chlorophyll [8], and cobalt(III) porphyrin, [Co^{III}TPPS], which acts as a catalyst for the oxidation of water in terrestrial life [9]. Finally, nickel(II) porphyrin, [Ni^{II}TPPS], is a highly sensitive probe for applications in bio-sensing via circular dichroism signal amplification [10].

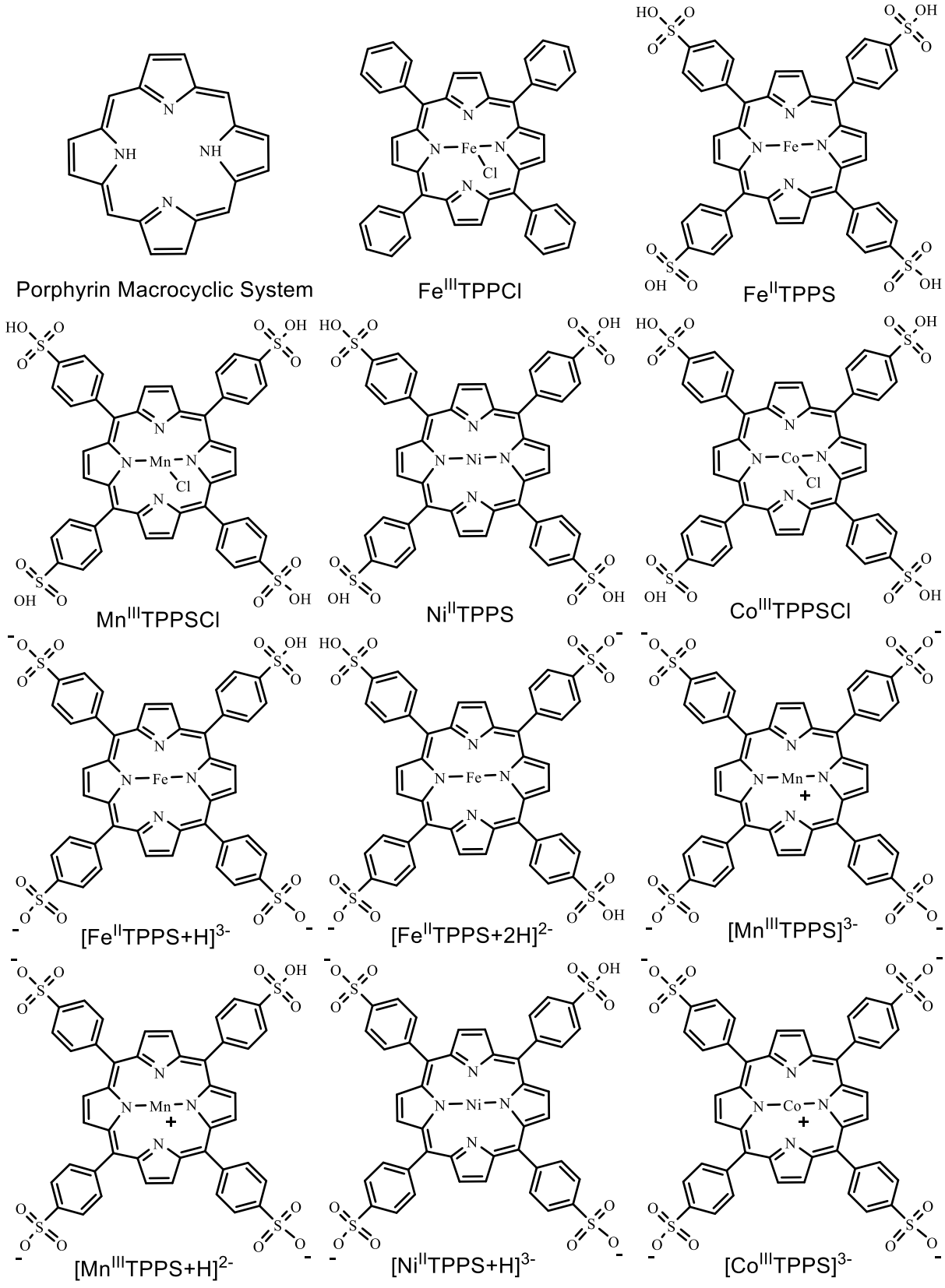

Figure 1.1 Structures of porphyrin anions

The chemical properties and reactions of metalloporphyrins have been extensively studied. Thousands of studies about TPPS were found by a quick look at SciFinder. A few examples to highlight the range of interest are: Gsponer et al. used $[TPPS]^{4-}$ to mediate Escherichia coli [11]. Fernandez et al. quantitatively investigated the reduction process of $(Fe^{III}TPPS)(H_2O)_2$ to $(Fe^{II}TPPS)(NO)$ in buffer solution [12]. Kadish et al. studied the effects of micelles on the aggregation of $[TPPS]^{4-}$ and $[MTPPS]^{4-}$ ($M = Zn^{II}$, Cu^{II}, VO^{2+}) [13]. Rahman et al. investigated the interaction of TPPS with trinitrotoluene (TNT) [14]. Zhang et al. conducted an electrochemical investigation of the interaction of TPPS with bovine serum albumin [15]. Aggarwal et al. studied the dynamics of the TPPS aggregation in aqueous solutions [16]. Karpuschkin et al. reported the binding of O_2 and CO to $Fe^{II}TPPS$ and $Mn^{II}TPPS$ [5].

There has also been research performed about the dissociation of gas-phase metalloporphyrins. The gas-phase was chosen because it allows the system to be studied in the absence of solvent effects to highlight the intrinsic properties of the metalloporphyrins. In order to learn about the binding of TPPS multimers in aggregates in the gas-phase, Schwarz et al. probed the dissociation of the metastable dimer species $(Mn^{III}TPPS)_2$ and $(Fe^{III}TPPS)_2$ with different charges by electrospray ionization tandem mass spectrometry in combination with ion mobility (ESI-MS/MS) (Figure 1.2) [1]. They found that the main dissociation channels for high charge state $(Fe^{III}TPPS)_2$ dimers ($z = 5, 6$) are: a) dimer to monomer, b) loss of SO_2 from the monomer, c) loss of SO_3 from the monomer. However, the dissociation of SO_2 and SO_3 were not studied in detail, and the dissociation energies were not determined.

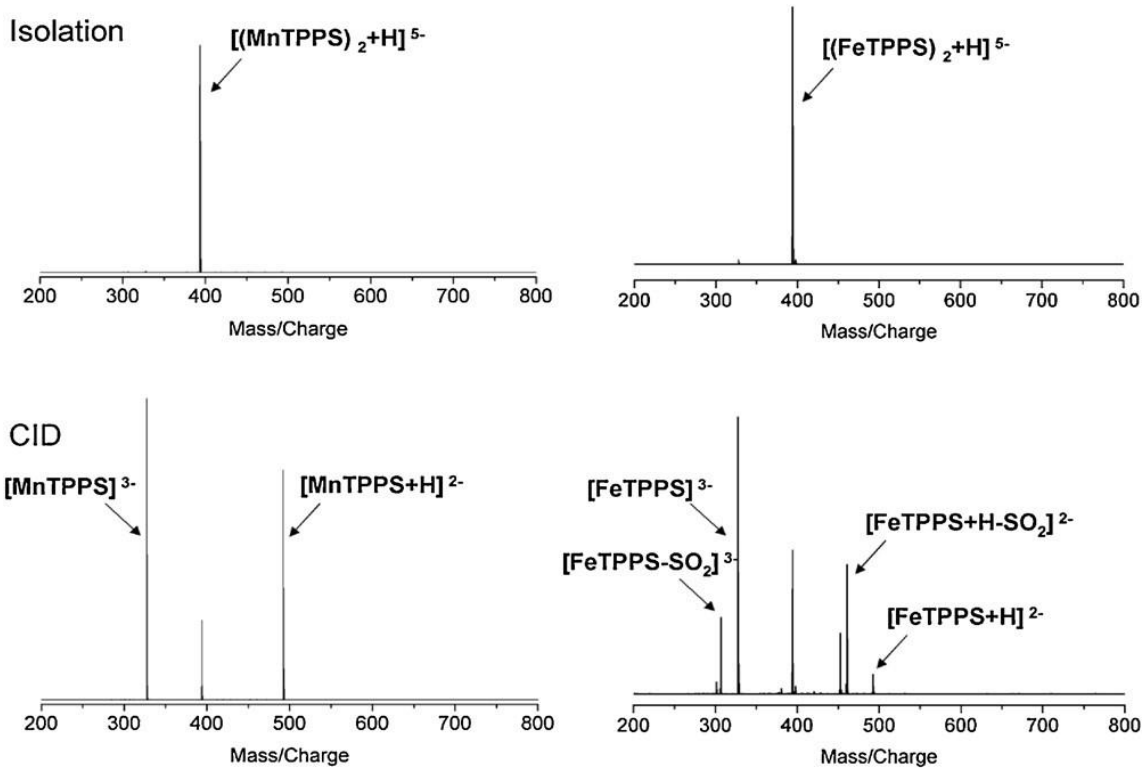

Figure 1.2 Collision-induced dissociation of $[(Mn^{III}TPPS)_2+H]^{5-}$ and $[(Fe^{III}TPPS)_2+H]^{5-}$ Schwarz et al. found that the main dissociation channels for both of these dimers are dimer to monomer; however, monomer fragment ions, $[Fe^{III}TPPS+H]^{2-}$ and $[Fe^{III}TPPS]^{3-}$, fragment further via SO_2 and SO_3 loss. (Reprinted from Schwarz et al., 2013 with permission) [1].

Secondly, Gozet et al. studied the dissociation of the related Fe(III) and Mn(III) tetraphenyl porphyrin chloride species ($Fe^{III}TPPCl$ and $Fe^{III}TPPCl$) by ESI-MS/MS. With enough collision energy applied in the collision cell of the triple quadrupole mass spectrometer, they found the loss of H_2 and C_6H_6 (Figure 1.3 and 1.4).

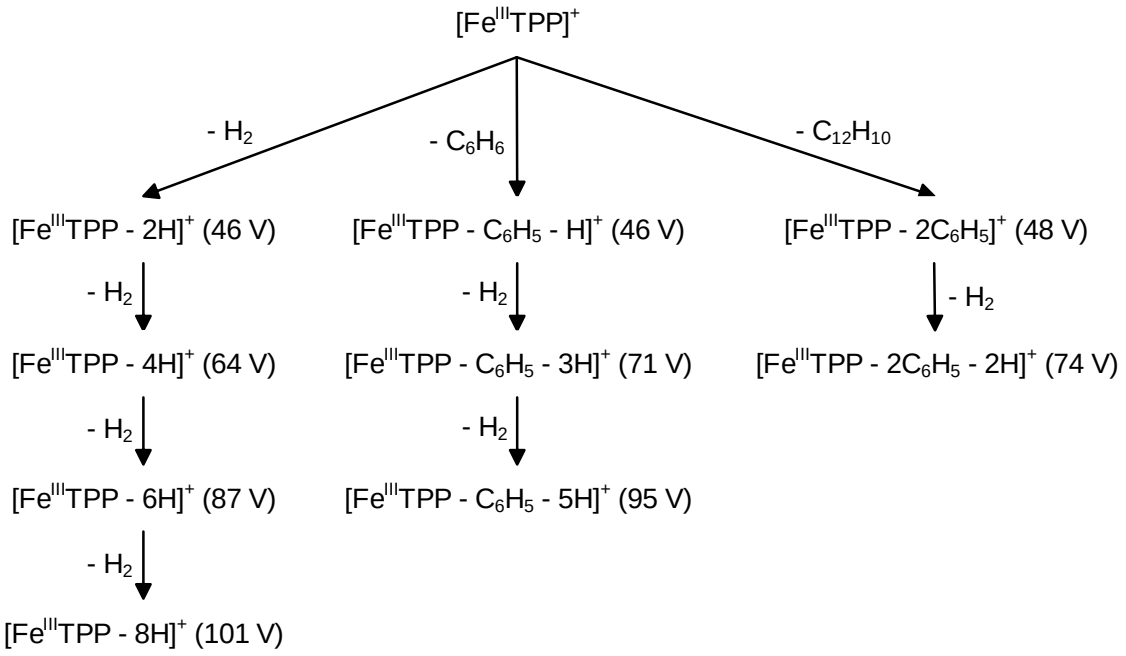

Figure 1.3 The proposed dissociation channels of $[Fe^{III}TPP]^+$. T. Gozet *et al.* determined the dissociation channels by the ESI-MS/MS [17].

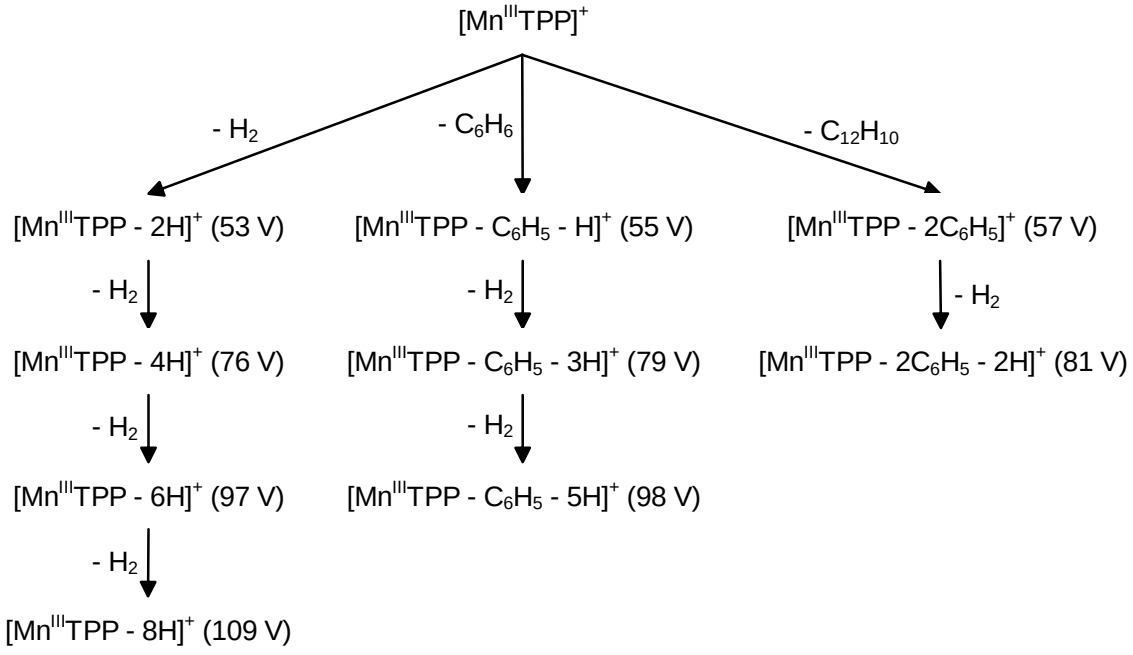

Figure 1.4 The proposed dissociation channels of $[Mn^{III}TPP]^+$. T. Gozet *et al.* determined the dissociation channels by the ESI-MS/MS [17].

The dissociation of monomers MTPPS (where M = Ni^{II}, Co^{III}, Mn^{III}, Fe^{II}, etc) has not yet been studied in detail. As mentioned above, metalloporphyrins perform important roles in all living systems. Thus, a thorough understanding of their dissociation properties can offer some useful information, especially as they are present in biological systems as charged species. In this research, the primary focus is to systematically study the dissociation processes of gas-phase $[Ni^{II}TPPS+H]^{3-}$, $[Co^{III}TPPS]^{3-}$, $[Mn^{III}TPPS]^{3-}$, $[Mn^{III}TPPS+H]^{2-}$, $[Fe^{II}TPPS+H]^{3-}$, and $[Fe^{II}TPPS+2H]^{2-}$ ions. Detailed dissociation pathways for each metalloporphyrin were estimated, and the activation energies for the main pathways were modeled by RRKM theory and molecular simulations.

1.3 References

[1] Schwarz U, Vonderach M, Kappes M, Kelting R, Brendle K, Weis P. Structural characterization of metalloporphyrin-oligomer multianions by mass spectrometry and ion mobility spectrometry-Observation of metastable species. International Journal of Mass Spectrometry. 2013;339:24-33.

[2] Schwarz U, Vonderach M, Armbruster MK, Fink K, Kappes MM, Weis P. Cu(II)- and Mn(III)-porphyrin-derived oligomeric multianions: Structures and photoelectron spectra. Journal of Physical Chemistry a. 2014;118(2):369-79.

[3] Silva EMP, Domingues MRM, Barros C, Faustino MAF, Tome JPC, Neves MGPMS, et al. Characterization of dinitroporphyrin zinc complexes by electrospray ionization tandem mass spectrometry. Unusual fragmentations of beta-(1,3-dinitroalkyl) porphyrins. Journal of Mass Spectrometry. 2005;40(1):117-22.

[4] Silva EMP, Domingues P, Tome JPC, Faustino MAF, Graca M, Neves PMS, et al. Electrospray tandem mass spectrometry of beta-nitroalkenyl meso-tetraphenylporphyrins. European Journal of Mass Spectrometry. 2008;14(1):49-59.

[5] Karpuschkin T, Kappes MM, Hampe O. Binding of O-2 and CO to metal porphyrin anions in the gas phase. Angewandte Chemie-International Edition. 2013;52(39):10374-7.
[6] KnowledgeDoor. Elements Handbook. 2014 [cited 2015 May 5th]; Available from: http://www.knowledgedoor.com/2/elements_handbook/electron_affinity.html
[7] Biesaga M, Pyrzynska K, Trojanowicz M. Porphyrins in analytical chemistry. A review. Talanta. 2000;51(2):209-24.
[8] Chai Z, Gao H, Ren J, An Y, Shi L. MgTPPS/block copolymers complexes for enhanced stability and photoactivity. Rsc Advances. 2013;3(40):18351-8.
[9] Nakazono T, Parent A, Sakai K. Cobalt porphyrins as homogeneous catalysts for water oxidation. Chemical Communications. 2013;49(56):6325-7.
[10] Choi JK, Sargsyan G, Shabbir-Hussain M, Holmes AE, Balaz M. Chiroptical detection of condensed nickel(II)-Z-DNA in the presence of the B-DNA via porphyrin exciton coupled circular dichroism. Journal of Physical Chemistry B. 2011;115(33):10182-8.
[11] Gsponer N, Spesia M, Durantini E. Effects of divalent cations, EDTA and chitosan on the uptake and photoinactivation of Escherichia coli mediated by cationic and anionic porphyrins. Photodiagnosis and Photodynamic Therapy. 2015;12(1):67-75.
[12] Fernandez B, Lorkovic I, Ford P. Nitrite catalyzes reductive nitrosylation of the water-soluble ferri-heme model Fe-III(TPPS) to Fe-II(TPPS)(NO). Inorganic Chemistry. 2003;42(1):2-4.
[13] Kadish KM, Maiya GB, Araullo C, Guilard R. Micellar effects on the aggregation of tetraanionic porphyrins-spectroscopic characterization of free-base meso-tetrakis(4-sulfonatophenyl) porphyrin, (TPPS)H-2, and (TPPS)Zn(II), (TPPS)Cu(II), (TPPS)VO2+ in aqueous micellar media. Inorganic Chemistry. 1989;28(14):2725-31.
[14] Rahman M, Harmon H. Absorbance change and static quenching of fluorescence of meso-tetra(4-sulfonatophenyl)porphyrin (TPPS) by trinitrotoluene (TNT). Spectrochimica Acta Part a-Molecular and Biomolecular Spectroscopy. 2006;65(3-4):901-6.

[15] Zhang H, Zhu Z, Li N. Electrochemical studies of the interaction of tetraphenylporphyrin tetrasulfonate (TPPS) with albumin. Fresenius Journal of Analytical Chemistry. 1999;363(4):408-12.
[16] Aggarwal LPF, Borissevitch IE. On the dynamics of the TPPS4 aggregation in aqueous solutions - Successive formation of H and J aggregates. Spectrochimica Acta Part a-Molecular and Biomolecular Spectroscopy. 2006;63(1):227-33.
[17] Gozet T, Huynh L, Bohme D. Collision-induced dissociation of tetraphenyl iron and manganese porphyrin ions by electrospray ionization mass spectrometry. International Journal of Mass Spectrometry. 2009;279(2-3):113-8.

Chapter 2. Methods of Study

2.1 Theory of MS and MS/MS

Mass spectrometry (MS) is an analytical tool that can analyze qualitatively and quantitatively chemicals present in a sample by measuring the mass-to-charge ratio (m/z) and abundance of gas-phase ions. MS differs from other common organic spectral analysis techniques, such as infrared (IR), or nuclear magnetic resonance (NMR) spectroscopy. While the sample used for IR and NMR can be reused, the sample for MS is depleted in the process of mass spectral analysis. However, MS is more sensitive than IR or NMR and thus it requires less sample [1].

Tandem mass spectrometry (MS/MS) is a technique that involves two stages of mass analysis: the first mass analysis selects the ion of interest with specific m/z, the second stage is to analyze all the fragment ions from the dissociation of the pre-selected ions. There are four steps in an MS/MS experiment: a) ion generation, b) ion selection, c) pre-selected ion dissociation, and d) fragment analysis [2, 3]. These four steps can be separated “in time”, such as using ion traps; or they can also be separated “in space”, such as using double focusing instruments, triple quadrupoles and ion mobility-tandem mass spectrometers.

The essential part of MS/MS is the fragmentation of gas-phase ions. There are many techniques which can be used to dissociate gas-phase ions, such as collision-induced dissociation (CID) [4], electron-transfer dissociation (ETD) [5], electron-capture dissociation (ECD) [6], infrared multiphoton dissociation (IRMPD) [7], and blackbody infrared radiative dissociation (BIRD) [8]. These methods use different types of

fragmentation which provide different information about the composition of parent ions and their fragment ions.

In this study, all the MS/MS experiments were run in a Waters Synapt G1 ion mobility/tandem mass spectrometer (Waters Corporation, USA). It is an updated version of a quadrupole-time-of-flight (Q-TOF) [9]. It is able to produce high resolution mass spectrometry and is able to separate different ions with the same m/z by their collision cross-section in the ion mobility spectrometer (IMS). Collision of the selected ions can be performed in the trap cell or transfer cell. Product ions are then analyzed in the time-of-flight mass spectrometer in either “W” or “V” mode.

2.2 Experiment techniques

The instrument used in this study is a Waters Synapt G1 ion mobility/tandem mass spectrometer (Waters Corporation, USA) (Figure 2.1). Ions travel through the Synapt in sequence through several main parts, namely electrospray ionization source, quadrupole, trap cell, ion mobility cell, transfer cell, and time of flight.

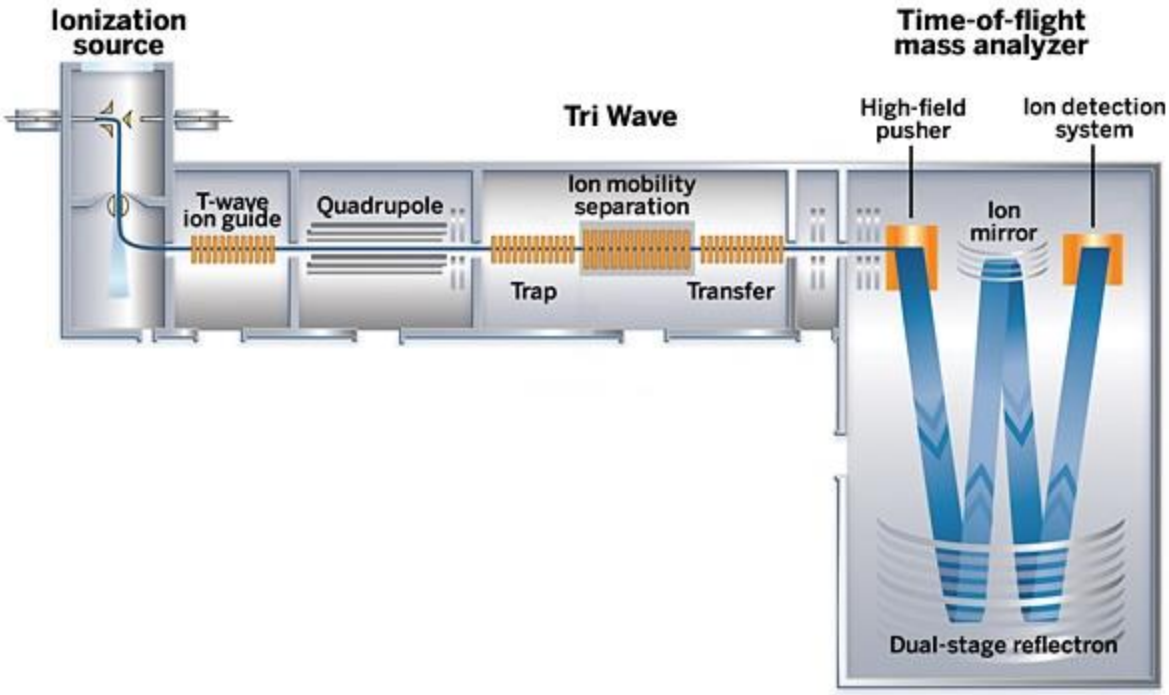

Figure 2.1 Schematic diagram of Waters Synapt G1 [9]

2.2.1 Electrospray ionization

In 2002, John B. Fenn was awarded a share of the Nobel Prize in Chemistry for his contribution in electrospray ionization (ESI) [10]. ESI is a technique for introducing an analyte in solution into the gas phase through a highly charged capillary (Figure 2.2). The ions are directed to a sampling cone where they are held at much lower voltages compared with the capillary voltage, and then directed into the vacuum system of the mass spectrometer.

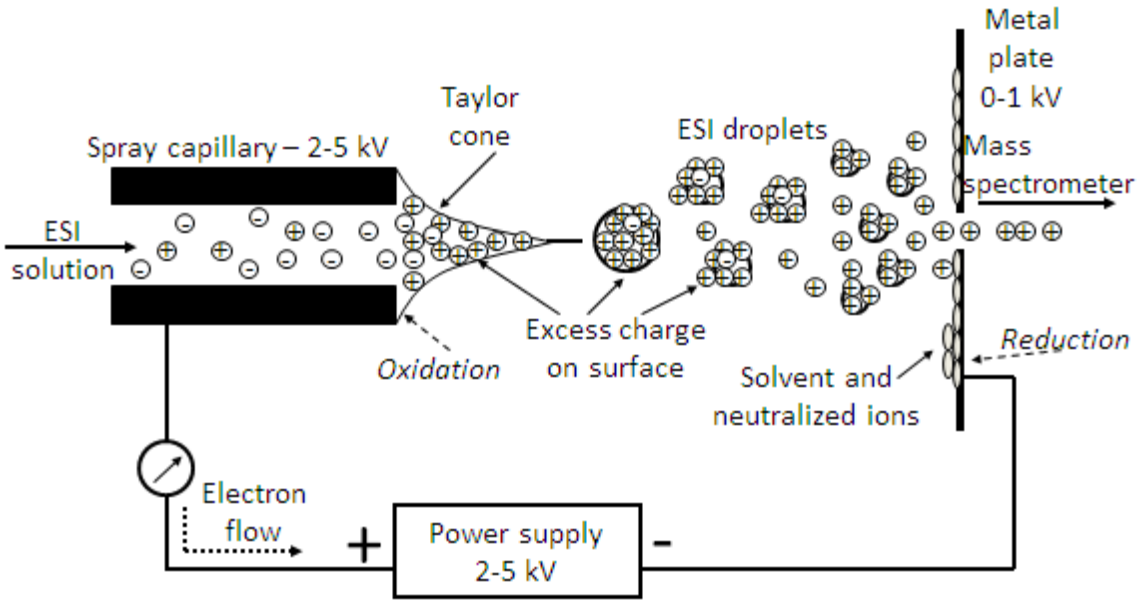

Figure 2.2 Diagram of positive mode ESI process [11]

The formation of gas-phase anions in a Taylor Cone is the beginning of the electrospraying process. The analyte and solvent droplets go through the loop of evaporation and subdivision in the ESI process undergoing uneven Rayleigh fission. This step is followed by the desolvation of the shrunken analyte and solvent droplets. However, there are two different ion desolvation theories: the Ion Evaporation Model (IEM) and the Charge Residue Model (CRM) (Figure 2.3). The IEM suggests that with the decreasing size of the highly charged droplet, the field strength at the surface of the droplet increases, and eventually results in the field desorption of solvated clusters [12, 13]. The CRM suggests that evaporation of solvent from the charged droplets increases surface charge density, resulting in subdivision into smaller charged droplets. The charged analyte and solvent droplets are in the loop of evaporation and fission, and eventually when all of the solvent is evaporated and the charged analyte becomes a gas-phase ion [14, 15].

During the ESI process, high energy ions collide with gas molecules at atmospheric pressure, which slows down the ions, so ESI can be coupled to other lower energy instruments, such as quadrupole mass spectrometers [16].

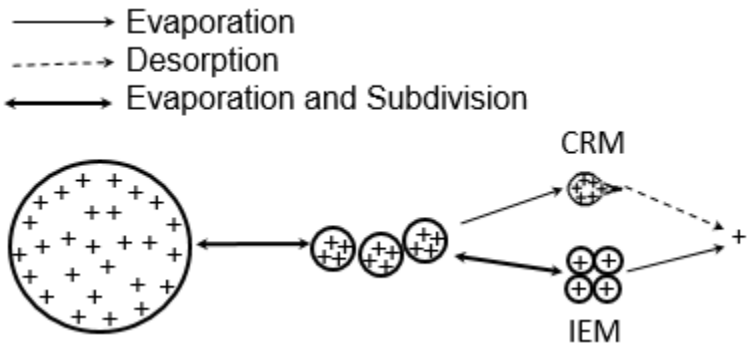

Figure 2.3 Schematic of the possible pathways for ion formation in a Taylor Cone. "+" represents a desolvated solution ion. The major difference between CRM and IEM: The final ion in CRM is produced by desorption, whereas the one for IEM is produced by evaporation of solvent [13].

2.2.2 Quadrupole mass spectrometer

Quadrupole mass spectrometry (Figure 2.4) can be used for scanning all the ions in the gas phase, and can also be used for selecting specific ions for MS/MS**.** Detailed theories and applications of quadrupoles are found in Raymond E. March's review about quadrupole ion trap mass spectrometry published in the Journal of Mass Spectrometry [17]. The quadrupole consists of four cylindrical parallel metal rods with a 90^{o} angle to each other. The two rods that are orthogonal to each other are paired with the same experiment conditions. A radio frequency (RF) voltage is applied on one pair of rods and 180^{o} out of phase on the other pair. A direct current (DC) voltage is then superimposed on the RF voltage. DC is positive on the x pair and negative on the y pair.

Rods opposite to each other have identical voltage, so a net zero potential is formed in x and y directions. In the process of filtering ions, ions are guided by altering radio frequencies (RF) and direct current (DC) voltages.

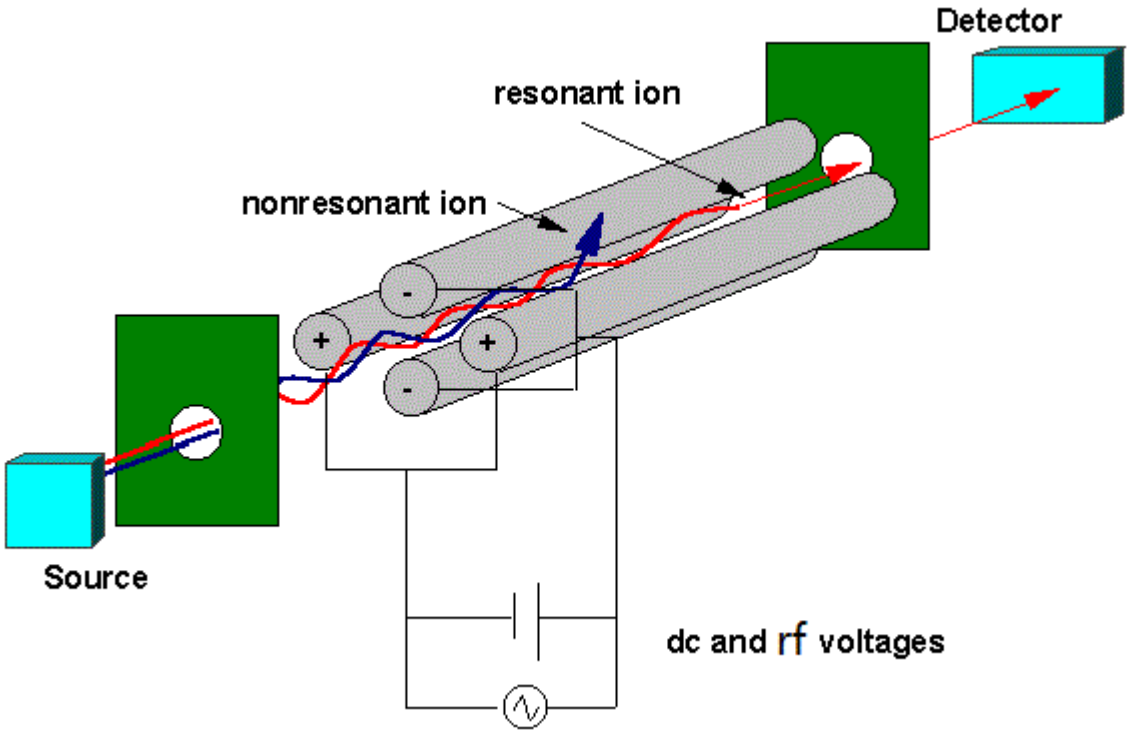

Figure 2.4 Schematic diagram of quadrupole [18]

The applied electric potential (Φ) of X and Y can be characterized by the following equitions:

X axis: $\Phi_x = U + V\cos\Omega t$ (Equation 2.1)

Y axis: $\Phi_y = -(U + V\cos\Omega t)$ (Equation 2.2)

where Ω is the angular frequency in rad/s of RF field; and V is the initial RF potential. The radio frequency allows a wide range of mass to go through the quadrupole, while a DC voltage allows none by discharging ions on the rods with opposite polarity.

Therefore, by altering the ratio of the DC/RF, one can selectively control a specific ion m/z to transmit through the quadrupole, and discharge all of the other ions.

2.2.3 Travelling-wave ion mobility spectrometry

Ion mobility spectrometry (IMS) is a method for separating and identifying ionized molecules in the gas phase based on their mobility in a carrier buffer gas (Figure 2.5). It was introduced in 1960s and was original known as Plasma Chromatography [19]. Recently, the travelling-wave IMS (TW-IMS) became available in a commercial instrument. In this TW-IMS, ions are injected in a radio-frequency (RF)-only stacked ring ion guide filled with a neutral buffer gas, and are separated by their ability to keep up with a traveling wave pulse through the buffer gas, which is so called ion mobility [20]. The ion mobility (K) is the ion's velocity divided by the electric field U (Equation 2.3) [21]. The ion's velocity can be experimentally determined by measuring drift time t_D, and the length L of the drift tube is known, so K can be calculated by:

$$K = \frac{L}{t_D \times U} \qquad \text{(Equation 2.3)}$$

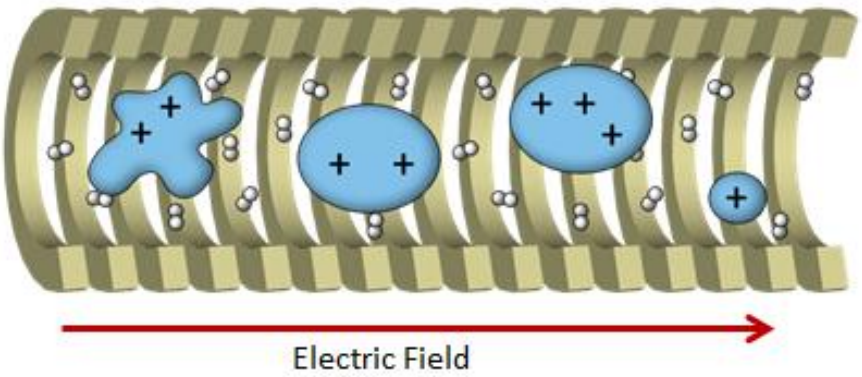

Figure 2.5 Schematic diagram of ion mobility spectrometry [22]

As ions travel through the drift tube, the drift gas moves in the opposite direction. Thus, the drift gas collides with the ions. An ion's collision cross-section is defined as the area where the drift gas strikes, so it is directly proportional to the size and shape of the ion. In other words, the larger the cross-section, the more drift gas colliding with the ion, and the longer the drift time for the ion travel through the tube. The collision cross-section Ω is calculated by:

$$\Omega = \frac{3ze}{16N}\sqrt{\frac{2\pi}{\mu k_B T}}\frac{1}{K} \qquad \text{(Equation 2.4)}$$

where z is the number of charges on the ion, e (C) is the elementary charge, N (m^{-3}) is the buffer gas number density, μ is the reduced mass of the ion-neutral pair, k_B is the Boltzmann's constant, T (K) is the draft gas temperature, and K ($m^2 \cdot V^{-1} \cdot s^{-1}$) is the reduced mobility (=measured mobility corrected to 760 Torr and 272.15 K) [23].

As can be seen in Equation 2.4, the mobility of the ion is inversely proportional to its cross-section, so ions with the same m/z can be separated based on their size and shape in IMS. However, the above equations are strictly true for a field-free drift tube ion mobility experiment. Due to the complexity of the ion motion in TW-IMS, it is not possible to directly relate drift time to cross section without calibration. In the current study, TW-IMS was only used to separate porphyrin anions with the same m/z ratio and not to determine their cross-section.

2.2.4 Collision-induced dissociation

Collision-induced dissociation (CID) is a method for inducing fragmentation of gas phase molecular ions in mass spectrometry. In August of 1968, both Jennings [24] and Haddon et al. [25] reported the first CID mass spectra. In 1973, MaLafferty et al. detailed valuable additional information of ion reaction mechanisms and structure determination by CID [4], which led to CID becoming an independent and essential technique in mass spectrometry. On a Waters Synapt G1 ion mobility/tandem mass spectrometer, CID can be done in a trap cell or transfer cell. In this study, CID experiments were done in the transfer cell, with and without IMS.

CID has four experimental conditions: high center-of-mass collision energies $\mathrm{E_{com}}$ (> 100 eV), intermediate $\mathrm{E_{com}}$ (1 – 100 eV), low $\mathrm{E_{com}}$ (multiple low-energy collisions such as MS/MS performed in ion traps) and surface-induced dissociation. Details are found in Mayer and Poon's review about the mechanism of collision activation of ions in mass spectrometry [26]. The collision regime in this study is intermediate $\mathrm{E_{com}}$.

Under the condition of intermediate $\mathrm{E_{com}}$, the general shape of the post-collision internal energy distributions for the dissociation ions, which can be derived from the relative abundance of the fragment ion peaks, resembles a Boltzmann or related distribution (Figure 2.6) [27-29]. In Figure 2.6 and 2.7, YGGFL 1 and 2 represent different experimental parameters.

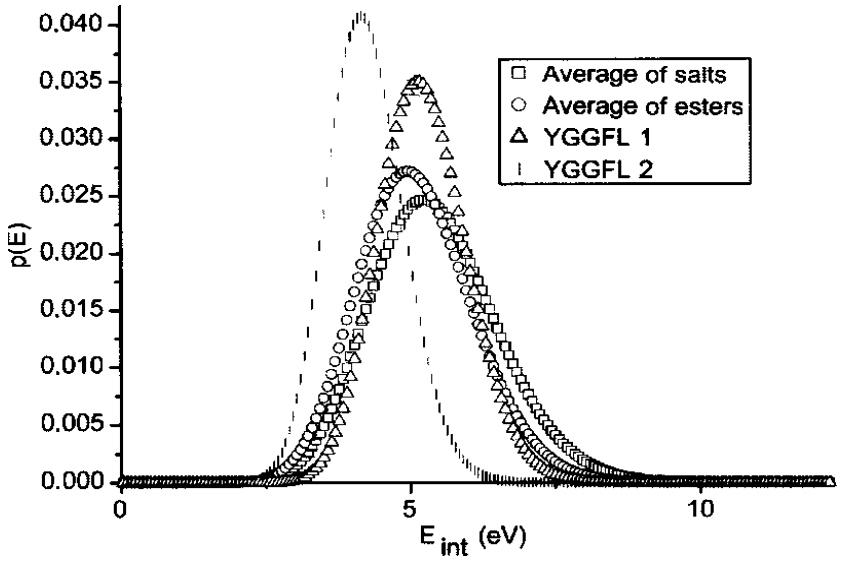

Figure 2.6 Internal energy distributions of benzylpyridinium ions, ester ions and protonated leucine encephalin (Reprinted from Naban-Maillet et al., 2005 with permission) [30]

In a CID process, the molecular ions with a charge z are accelerated by a designed potential V_{lab} to get a laboratory kinetic energy E_{lab} [31]:

$$E_{lab} = zV_{lab} \quad \text{(Equation 2.5)}$$

The ions are then allowed to collide with neutral molecules (argon in this research). The velocity of the target argon is considered to be zero because its velocity is much smaller than the velocity of the accelerated molecular ions. In the collision, the relative kinetic energy of the ion is transferred into internal energy. The center-of-mass collision energy, E_{com}, is the fraction of the laboratory kinetic energy E_{lab} that is available to be converted into internal energy [32]:

$$E_{com} = E_{lab} \cdot \frac{m_{Ar}}{m_{Ar}+m_{ion}} \quad \text{(Equation 2.6)}$$

where m_{ion} and m_{Ar} are the molecular weight of the ion and target neutral molecule argon respectively. Collisions will result in the breakdown of the molecular ion. The fragment ions can then be analyzed by time of flight.

Naban-Maillet et al. findings show that when the cone voltage ranges from 10-50 eV, the mean internal energies linearly increased with collision voltage (Figure 2.7) [30]. In addition, Mayer and Martineau [32] used Equation 2.7 to approximate the relationship between the effective temperature (T_{eff}) and the center-of-mass collision energy (E_{com}), based on the following three conditions: (a) $E_{com}$is in a small absolute range, (b) all of the species studied dissociates over the same range of E_{com}, and (c) all of the systems are of similar degrees of freedom.

$$T_{eff} = T_{ini} + \alpha E_{com} \quad \text{(Equation 2.7)}$$

where T_{ini} represents the pre-collision (initial) internal temperature of the ions, and α (unit: K eV^{-1}) is an adjustable parameter that represents the influence of E_{com} on the T_{eff}. The post-collision internal energy distribution can then be approximated by calculating the effective temperature (T_{eff}) in Equation 2.7.

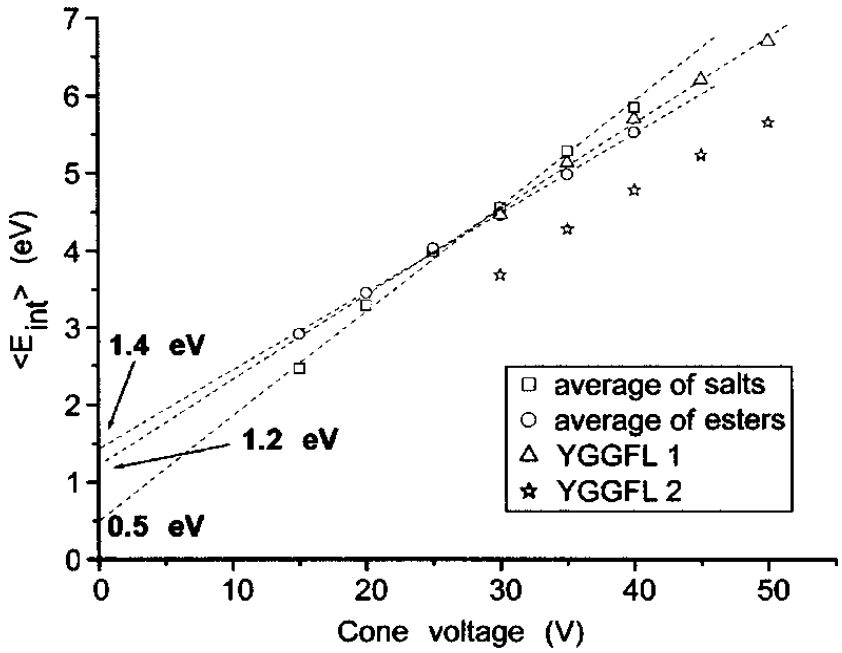

Figure 2.7 Average of mean internal energies of benzylpyridinium ions, ester ions and protonated leucine enkephalin as a function of the cone voltage in triple quadrupole mass spectrometer. YGGFL 1 and 2 represent different literature parameters. (Reprinted from Naban-Maillet et al., 2005 with permission) [30].

2.2.5 In-source-CID

In-source-CID is similar to CID except for the collision location. Molecular ions are accelerated by a high sample cone voltage in the ion source to gain enough kinetic energy and collide with neutral molecules in the source (nitrogen in this study). Certain fragment ions in the source can then be selected by the first quadrupole. In-source-CID is often used in addition to tandem mass spectrometry to allow for two steps of fragmentation in a pseudo MS/MS/MS-type of experiment [33].

2.2.6 Time of flight mass spectrometry

In this study, time of flight (TOF) mass spectrometry was used as a mass analyzer in the last part of the Waters Synapt G1 ion mobility/tandem mass spectrometer. A detailed theory of the TOF analyzer is found in Curt Brunnee's review about mass analyzer [34] and Chernushevich et al.'s publication about quadrupole TOF mass spectrometry [35]. The TOF analyzer separates ions by the time it takes for an ion to travel a fixed distance. An equation for an ion's TOF (t_{tof}) can be derived from the kinetic energy (E_k) of an ion in the drift tube:

$$E_k = \frac{1}{2} \cdot m_{ion} \cdot v^2 = zU \quad \text{(Equation 2.8)}$$

and the time it takes the ion to travel the effective length L_{eff} of the flight tube:

$$t_{tof} = \frac{L_{eff}}{v} \quad \text{(Equation 2.9)}$$

Substituting the equation into the kinetic energy equation, the ion's TOF is given by:

$$t_{tof} = \frac{L_{eff}}{\sqrt{2U}} \sqrt{\frac{m_{ion}}{z}} \quad \text{(Equation 2.10)}$$

During the analysis, the effective length of the drift tube L_{eff}, and the voltage from the ion source U are held constant. As a result, time of flight is directly proportional to the root of m_{ion}/z.

In the TOF mass analyzer, the resolution is the observed mass divided by the difference between two masses that can be separated, $m_{ion}/\Delta m_{ion}$. Resolution (R) is calculated by:

$$m_{ion} = \frac{2Ut_{tof}^2}{L_{eff}^2} \cdot z \qquad \text{(Equation 2.11)}$$

$$R = \frac{m_{ion}}{\Delta m_{ion}} = \frac{t_{tof}^2}{t_{tof}^2 - (t_{tof} - \Delta t_{tof})^2} \approx \frac{t_{tof}}{2 \cdot \Delta t_{tof}} = \frac{L_{eff}}{2(v \cdot \Delta t_{tof})} \qquad \text{(Equation 2.12)}$$

where m_{ion} and t_{tof} are mass (in Daltons) and flight time of the ion, Δm_{ion} and Δt_{tof} are the peak widths measured at the 50% level on the mass and time scales, respectively. $v \cdot \Delta t_{tof}$ is the thickness of an ion packet approaching the detector and L_{eff} is the effective length of the TOF tube (Figure 2.8).

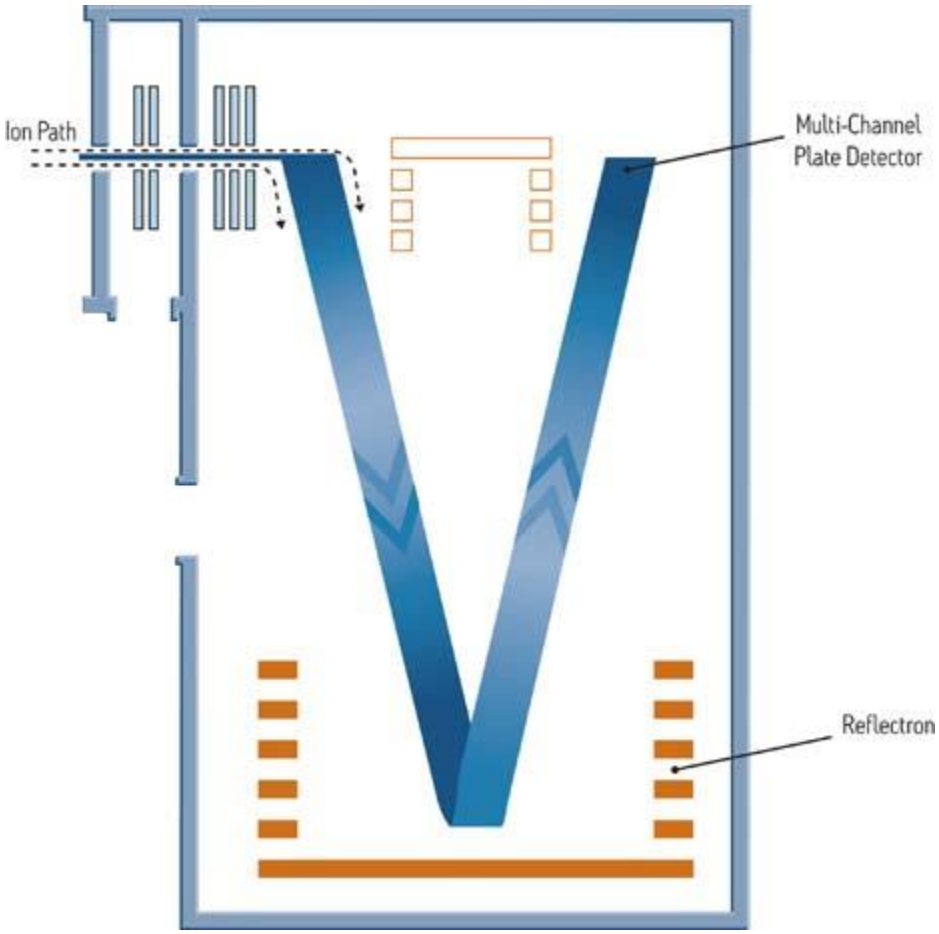

Figure 2.8 Schematic diagram of time of flight [36]

The TOF applied in this study is a reflecting TOF (V-geometry) (Figure 2.8). However, the Waters Synapt G1 contains a double-reflectron (W, or two Vs), which increases the resolving power by doubling the effective length (L_{eff}) of the TOF tube if needed (but not used in this study). The reflectron also provides kinetic energy focussing of the ion packet.

2.3 Understanding CID mass spectra

To understand CID mass spectra, the CID breakdown diagrams (plots of ion relative abundance vs centre-of-mass collision energy) are modeled by Rice–Ramsperger–Kassel–Marcus (RRKM) theory. RRKM theory [37] estimates the unimolecular dissociation rate constants from a few characteristics of the potential energy surface. In 1927, Rice and Ramsperger developed a collision theory, named Theory II, to model the unimolecular gas reaction rate at low pressures by treating a molecule as a collection of identical harmonic oscillators. Theory II suggests that one oscillator has only a single degree of freedom, DOF (DOF is the number of variables required to describe the motion of a particle completely), and the unimolecular dissociation requires two conditions: a) a minimum total energy E_0, and b) some single DOF to acquire energy of E_0 or greater. In 1928, Kassel developed Theory II into Theory III [38] by proving: it is some particular bond (two DOF), rather than some single DOF, that acquires energy of E_0 or greater for the unimolecular dissociation. To put it simply, Theory III suggests one oscillator has two DOF, rather than one DOF. Theory III was named the RRK theory later [37]. From 1951 to 1965, Marcus and others [39-42]

developed the RRK theory into the RRKM theory by taking the transition state theory developed by Eyring [43] into consideration.

There are a few concepts involved in modeling the experimental CID breakdown curves, including vibrational frequencies, the time-scale of dissociation, the microcanonical rate constant, k(E), the entropy of activation, the post-collision internal energy distribution, and the fraction of ions dissociating. Sections 2.3.1 to 2.3.6 introduce the concepts involved in modeling experimental CID data. Section 2.3.7 is the procedure for fitting breakdown diagrams by two RRKM programs. Details are found in a publication by Mayer and Martineau [32] and a publication by Baer and Mayer [44].

2.3.1 Obtaining vibrational frequencies of porphyrins.

To apply the RRKM theory, the harmonic vibrational frequencies of all the porphyrins were calculated by geometry optimizations followed by frequency calculations at the PM6 theory level using Gaussian 09. All frequencies are listed in Appendix 6 Table A6.1

The transition state vibrational frequencies were approximated by removing the last oscillator from the reactant ion in this study, and scaling the first 10 vibrational frequencies by a common factor. In addition, since the transition state vibrational frequencies are being adjusted to fit the experimental data, the actual choice of which oscillator to remove is irrelevant [32].

2.3.2 Time-scale of dissociation

In the Waters Synapt instrument, there are two collision cells: a) the trap cell before the IMS cell, b) the transfer cell after IMS cell. All the collision activities happened in the transfer cell in this research. The time scale (t) of events in the transfer cell is the time it takes for the ion to travel through the cell (10 cm) at a certain velocity (the travelling wave velocity) and arrive at the TOF mass spectrometer [21]:

$$t = \frac{l_{transfer}}{v_{wave}} \qquad \text{(Equation 2.13)}$$

2.3.3 Microcanonical rate constant

Rice-Ramsperger-Kassel-Marcus (RRKM) calculates rate constants in a unique way (Figure 2.9), which not only takes into account the number of degrees of freedom (DOF) but also their different vibrational frequencies

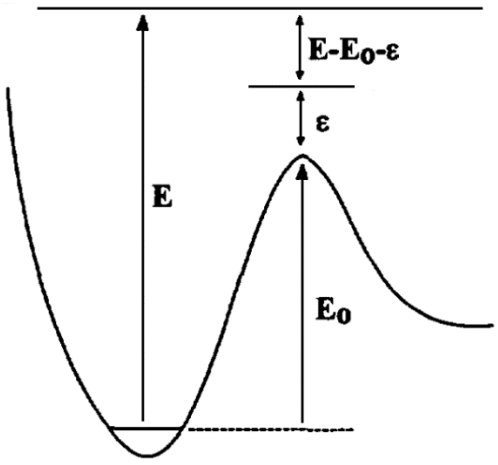

Figure 2.9 Reaction coordinate for a dissociation with a real barrier. E and E_0 are the total energy and activation energy. ε is the transitional energy in the reaction coordinate. $E – E_0 – ε$ is the energy available to be statistically distributed. (Reprinted from Baer and Mayer 1997 with permission) [44].

The rate constant is calculated using this equation:

$$k(E) = \frac{\sigma N^{\ddagger}(E-E_0)}{h\rho(E)} \quad \text{(Equation 2.14)}$$

where σ is the reaction degeneracy or the symmetry of the reactant structure, $N^{\ddagger}(E - E_0)$ is the sum-of-states for the transition states at an internal energy from 0 to $(E - E_0)$, h is Planck's constant, and $\rho(E)$ is the vibrational density of states of the parent ion at an internal energy E. The sum of states represents the number of ways to pass through the transition state that has a total energy of $(E - E_0)$. The density of states represents the number of ways to get lost in the molecular ion phase space at an internal energy E. The transition state sum-of-states and reactant densities of states are calculated from the vibrational frequencies of the parent ion and the transitional state structure obtained from section 2.3.1, by using the direct count algorithm of Beyer and Swinehart [45].

2.3.4 Entropy of activation $\Delta^{\ddagger}S$

In thermodynamics, entropy (S) is a measure of the disorder of a thermodynamic system. Thus, the entropy $\Delta^{\ddagger}S$ of activation has a negative value if the transition states are more ordered than the reactant ions, which usually means a rearrangement process. Conversely, $\Delta^{\ddagger}S$ has a positive value if the transition states are less ordered than the reactant ions. $\Delta^{\ddagger}S$ can be calculated with the vibrational frequencies and the transition state:

$$\Delta^{\ddagger}S = k_B \ln\frac{Q^{\ddagger}}{Q} + \frac{U^{\ddagger}-U}{T} = k_B \ln\frac{\prod q_i^{\ddagger}}{\prod q_i} + \frac{U^{\ddagger}-U}{T} \quad \text{(Equation 2.15)}$$

where the average internal energy U and $U^{\ddagger}$ can be calculated from the usual formulas by using the vibrational partition functions. Q is the total partition functions q_i (Equation 2.16). T is a specified absolute temperature (300 K in this study) for the report of $\Delta^{\ddagger}S$ values.

$$q_i = \frac{1}{1-e^{-h\cdot v_i/(k_B\cdot T)}} \quad \text{(Equation 2.16)}$$

where h is Planck's constant, v_i is the frequency of oscillator i, k_B is the Boltzmann constant.

2.3.5 The post-collision internal energy distribution

The post-collision internal energy distribution is a function of the center-of-mass collision energy, E_{com}. As mentioned in section 2.2.4, E_{com} can be converted from the laboratory kinetic energy E_{lab} by Equation 2.6. The post-collision internal energy distribution can be approximated by calculating the effective temperature (T_{eff}) by the Equation 2.7. The internal energy distribution after collision $P(E, E_{com})$ can then be calculated:

$$P(E, E_{com}) = \frac{\rho(E)e^{-E/(R\cdot T_{eff})}}{Q(E_{com})} \quad \text{(Equation 2.17)}$$

where $\rho(E)$ is density of states of the ion at a certain effective temperature T_{eff}, and $Q(E_{com})$ is the total vibrational partition function at the effective temperature.

2.3.6 The fraction of ions dissociating

The fraction of ions dissociating can be calculated as a function of internal energy by:

$$\mathrm{F(E)} = 1 - \mathrm{e}^{-\mathrm{k(E)t}} \qquad \text{(Equation 2.18)}$$

where t is the maximum time of the observation, i.e., the time required for the ion to move from the collision region to the analyzer region of the mass spectrometer. The total observation is then given by multiplying $\mathrm{F(E)}$ and $\mathrm{P(E, E_{com})}$, and integrating over the internal energy:

$$\mathrm{F_i(E)} = \int_0^\infty \mathrm{F(E)} \times \mathrm{P(E, E_{com})} \times \frac{\mathrm{k_i(E)}}{\mathrm{k(E)}} \times \mathrm{dE} \quad \text{(Equation 2.19)}$$

2.3.7 Theoretical breakdown diagram fitting

A complete theoretical breakdown diagram is obtained automatically by running two FORTRAN programs written by Dr. Paul Mayer, namely “dcms.exe” and “quattro.exe”. The theoretical breakdown diagram can be changed by altering the following four parameters: i) the activation energy $\mathrm{E_0}$, ii) the first ten vibrational frequencies of the transition state (which alters $\Delta^{\ddagger}\mathrm{S}$), iii) initial temperature $\mathrm{T_{ini}}$, iv) α. These four parameters are changed manually until the best-fitted theoretical breakdown diagram that matches the experimental breakdown diagram is found. The following two paragraphs explain how these two FORTRAN programs work:

a) “dcms.exe” is responsible for calculating: (a) microcanonical rate constant $\mathrm{k(E)}$, which can be adjusted by altering the activation energy $\mathrm{E_0}$ and the first ten

vibrational frequencies of the transition; (b) the entropy of activation $\Delta^{\ddagger}S$, which can be adjusted by altering the first ten vibrational frequencies of the transition.

b) "quattro.exe" is responsible for calculating: (a) the pre-collision reactant ion internal energy, which can be adjusted by altering the initial temperature T_{ini}; (b) the post-collision internal energy distribution, which can be adjusted by changing T_{ini} and α; and (c) the fraction of ions dissociating, which will be the theoretical breakdown diagram.

2.4 Molecular simulation

While RRKM modeling of the CID breakdown curves provides information on the activation energies and entropies of each process, this data must be interpreted with respect to the mechanism of the reactions, something that often requires computational chemistry to elucidate.

There are many reaction pathways from a reactant to a product. However, the most likely one is that which proceeds with the minimum energy via the saddle point (transition structure) (Figure 2.10).

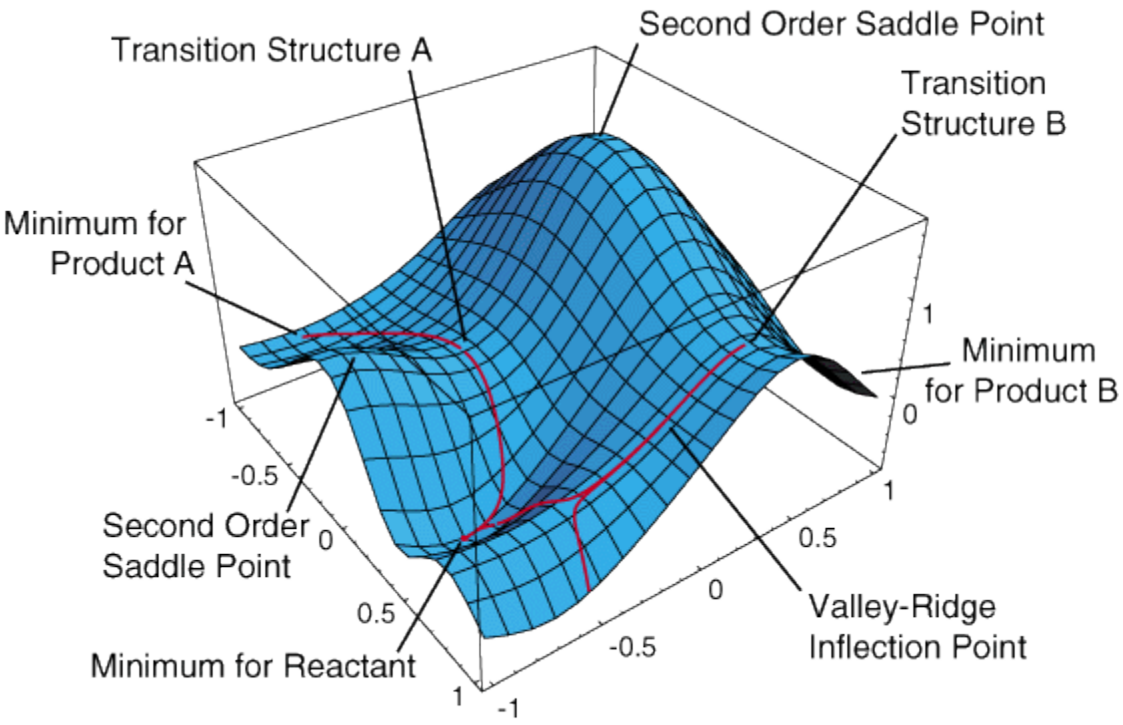

Figure 2.10 Key points on a reaction potential energy surface [46]

It is trivial to find the minimum point for small molecules as their potential energy surfaces are small, while it is difficult to find the minimum point for big molecules. For example, a big molecule such as porphyrin has a big and relatively flat potential surface, which results in many local minimum points, and thus the global minimum point is difficult to find. At low-levels of theory, such as PM6, the optimization of big molecule is easy to converge, but the optimization from different initial structures may result in a different local minima, and it must be noted that the energy cannot be trusted because low-levels of theory are not accurate. At high-levels theory, such as B3-LYP/6-31+G(2d, p), the optimization of big molecules may never converge, and it may take even a few weeks or months to optimize a transition state with the current limited available resources even if it does converge.

As a result, large molecules are often not feasible to calculate with high level quantum computational chemistry methods. A practical approach to rectify this problem is to perform a thorough molecular simulation of the active functional groups of the big molecule on a high-level theory, and then do the necessary calculation for the big molecule at a lower level theory.

2.4.1 Density functional theory

Density functional theory (DFT) is a popular widely used method in quantum chemistry for the calculation of molecular structures and energies. DFT is based on the Hoheberg-Kohn (KH) theorems, and became practical after Kohn and Sham devised the Kohn-Sham (KS) equation [47], for which Kohn won the Nobel Prize in Chemistry in 1998**.** The details about DFT are found in Gos's [48] and Yin's doctoral thesis [49]. The main idea of DFT is to describe energy of an atomic system based on the ground state electron density, instead of the electron wavefunction, through the use of functions of the electron density. The ground state electron density depends on only three spatial coordinates, while the electron wavefunction depends on 3N (N electrons) spatial coordinates. The 3N spatial coordinates are rapidly becoming more computationally demanding as the atomic system gets larger. However, the calculation of three spatial coordinates is much cheaper, which can even be handled by a personal laptop.

Figure 2.11 represents the iteration scheme of DFT. The DFT optimization of molecular structure starts with an initial electron density guess, followed by the calculation of the effective KS potential $v_{eff}(r)$. The next step is to solve the KS equation with single-particle eigenvalues ε_i and KS orbital ψ_i. Then a new electron density $\rho(r)$ is

calculated from the KS orbital ψ_i followed by checking the convergence criterion. If the criterion does not match, the calculated electron density will be mixed with the old one from the previous iterations to get a new electron density. Finally, a new iteration will then start with the new electron density. This process is repeated until the convergence criteria are matched (see Table 2.1).

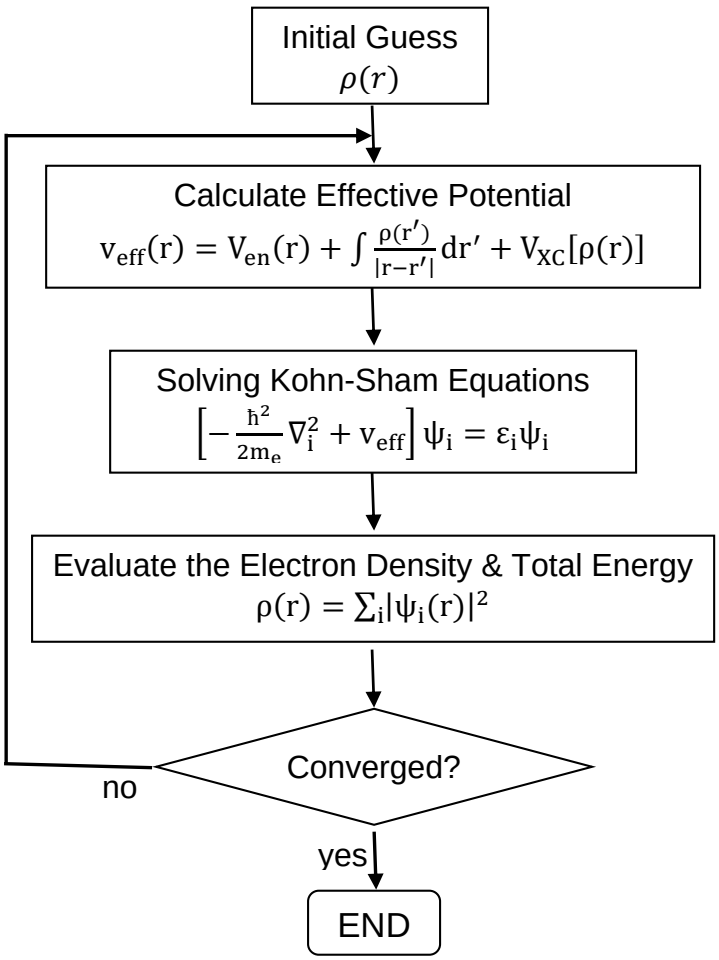

Figure 2.11 Flow chart of the iteration scheme of DFT [49]

Table 2.1 The general convergence criteria for structure optimization at Gaussian 09 ("RMS" and "Maximum" are Root Mean Square residuals and maximum residuals, respectively)

Item	Value	Threshold	Converged?
Maximum Force	0.000135	0.00045	YES
RMS Force	0.000016	0.0003	YES
Maximum Displacement	0.099278	0.0018	NO
RMS Displacement	0.014809	0.0012	NO

In this research, the dissociation process of negative and neutral benzenesulfonate was modeled based on Ben-Ari's experiment [50]. Since the electronic density is more spread out for molecules with excited states and anions, the normal basis functions B3-LYP/6-31G is not enough for modeling the dissociation process of negative benzenesulfonate ion. DFT calculations were performed at B3-LYP/6-31+G(2d, p) level, which designates the 6-31G basis set by adding one diffuse function "+" (a set of s and p orbitals) and two sets of d polarization functions to the heavy atoms (Li - Ca), and one set of p polarization functions on light atoms (H - He) [51-53].

2.4.2 B3-LYP/6-31+G(2d, p)+LANL2DZ//PM7

Semi-empirical quantum mechanical methods are based on Dewar and Thiel's "Neglect of Diatomic Differential Overlap" (NDDO) approximation [54, 55]. They are simplified versions of the Hartree-Fock theory by using parameters from empirical data in order to improve performance [56]**.** Semi-empirical quantum mechanical methods,

which draws a compromise between accuracy and economy, can be applied to systems with thousands of atoms [57]. The first generation semi-empirical method MNDO [58, 59], firstly appeared in 1977. It initially only had parameters available for C, H, N, and O. More parameters for other atoms and more semi-empirical methods were developed shortly after, including AM1 [60] in 1985, PM3 [61] in 1989, MNDO-d [62] in 1996, RM1 [63] in 2006, and PM6 [64] in 2007.

In 2012, a new semi-empirical method, PM7 [65], was released by Dr. Jimmy Stewart with his updated program “MOPAC2012” [66]. PM7 is an improved version of PM6. All parameters have been re-optimized. PM7 also removed a few errors in the NDDO theory that affected large systems. According to Stewart (the author of AM1, PM3, RM1, PM6 and PM7), PM7 reduces the average errors in organic compounds by around 10%. PM7 was proven to be the most robust tool among the semi-empirical methods.

However, semi-empirical is still a low level theory in quantum chemistry. It is fast but not as accurate when compared with higher level theories, such as DFT. In this research, there are plenty of calculations for metalloporphyrin, which is such a big system that it would take 7.5 days to run a single calculation at B3-LYP/6-31G(d, p) level if the starting structure is the optimal one by chance. A large number of calculations on metalloporphyrin are almost impossible with the current limited available resources at a DFT level of theory, especially when most starting structures never converge. Considering accuracy and economy of all the levels (see Figure 2.12), the structure optimization of all the porphyrins were done by PM7, followed by single point energy calculation with B3-LYP/6-31+G(2d, p)+LANL2DZ basis set. (There was no PM7

when Figure 2.12 was published in the book “Exploring chemistry with electronic structure methods” by Gaussian Inc. in 1996)

The B3-LYP/6-31+G(2d, p)+LANL2DZ basis set is a combination of the 6-31+G(2d, p) basis set and the LANL2DZ effective core basis set. Specifically the atoms H - Ar are described with the 6-31+G(2d, p) basis set, while heavier atoms are modeled using the LANL2DZ basis set [51, 67]. The 6-31+G(2d, p) basis set was chosen in order to keep the same level of theory with the calculation of benzenesulfonate.

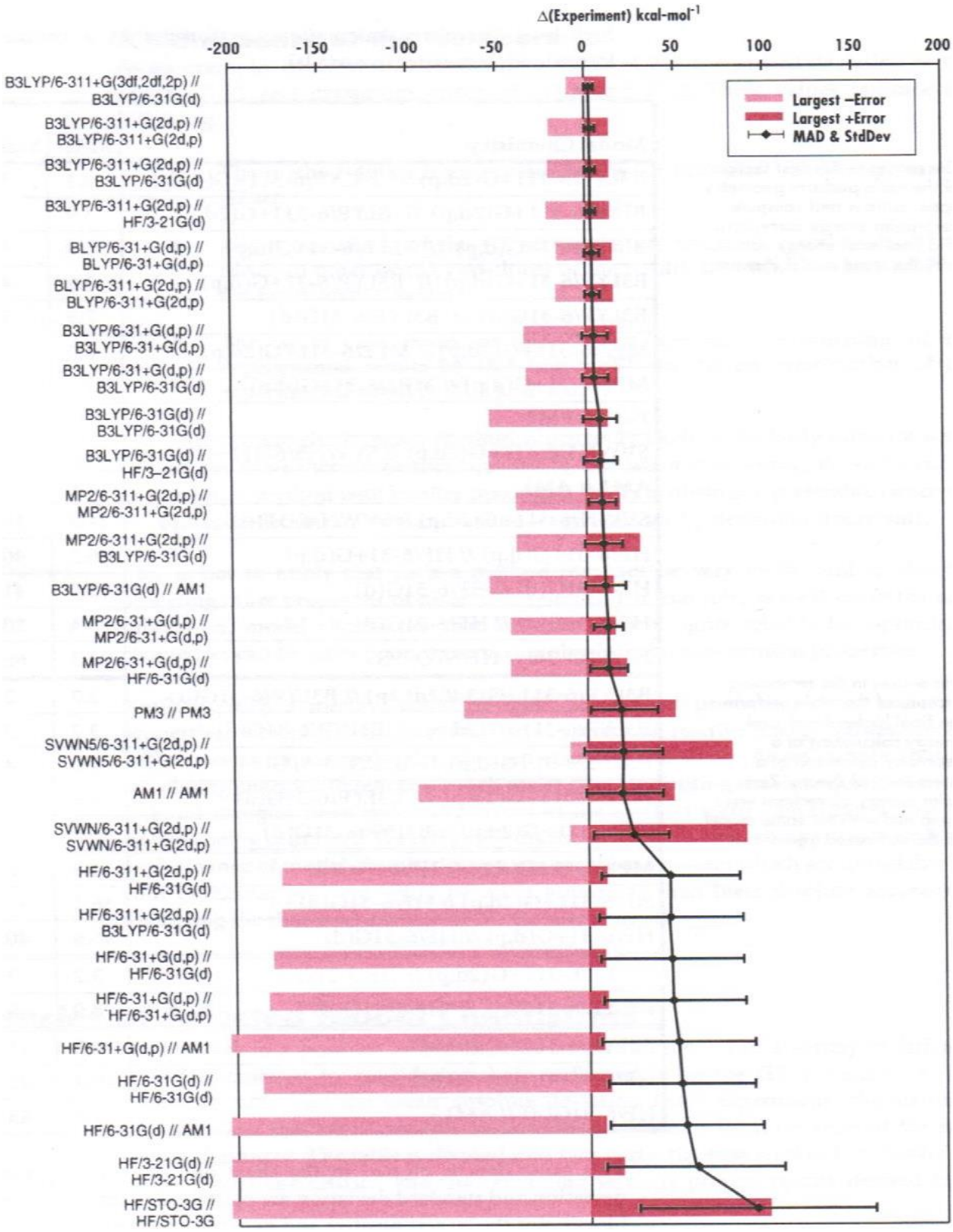

Figure 2.12 Relative accuracies of different level of theories (Reprinted from Foresman and Frisch, 1996 with permission from Gaussian Inc.) [68]. MAD is the mean absolute

deviation from experiments and StdDec is the standard deviation, and the largest positive and negative deviations from experiment for each chemistry model.

2.5 References

[1] Smith RM. Understanding mass spectra: a basic approach. 2nd ed. Hoboken, N.J.: Wiley Interscience; 2004.

[2] Lavagnini I. Quantitative applications of mass spectrometry. Chichester, West Sussex ; Hoboken, NJ: Wiley; 2006.

[3] Hoffmann Ed, Stroobant V. Mass spectrometry: principles and applications. 3rd ed. Chichester, West Sussex, England ; Hoboken, NJ: J. Wiley; 2007.

[4] McLafferty FW, Bente PF, Kornfeld R, Tsai SC, Howe I. Collisional activation spectra of organic ions. Journal of the American Chemical Society. 1973;95(7):2120-9.

[5] Syka JEP, Coon JJ, Schroeder MJ, Shabanowitz J, Hunt DF. Peptide and protein sequence analysis by electron transfer dissociation mass spectrometry. Proceedings of the National Academy of Sciences of the United States of America. 2004;101(26):9528-33.

[6] Zubarev RA, Kelleher NL, McLafferty FW. Electron capture dissociation of multiply charged protein cations. A nonergodic process. Journal of the American Chemical Society. 1998;120(13):3265-6.

[7] Little DP, Speir JP, Senko MW, O'Connor PB, McLafferty FW. Infrared multiphoton dissociation of large multiply charged ions for biomolecule sequencing. Analytical Chemistry. 1994;66(18):2809-15.

[8] Dunbar RC. BIRD (blackbody infrared radiative dissociation): Evolution, principles, and applications. Mass Spectrometry Reviews. 2004;23(2):127-58.

[9] Jacoby M. Doubling up on mass analysis. Chemical & Engineering News. 2010;88(13):35-7.

[10] Tabet JC, Rebuffat S. Nobel Prize 2002 for chemistry: mass spectrometry and nuclear magnetic resonance. M S-Medecine Sciences. 2003;19(8-9):865-72.

[11] Cech N, Enke C. Practical implications of some recent studies in electrospray ionization fundamentals. Mass Spectrometry Reviews. 2001;20(6):362-87.

[12] Iribarne JV, Thomson BA. Evaporation of small ions from charged droplets. Journal of Chemical Physics. 1976;64(6):2287-94.
[13] Nguyen S, Fenn J. Gas-phase ions of solute species from charged droplets of solutions. Proceedings of the National Academy of Sciences of the United States of America. 2007;104(4):1111-7.
[14] Dole M, Mack LL, Hines RL. Molecular beams of macroions. Journal of Chemical Physics. 1968;49(5):2240-9.
[15] Touboul D, Jecklin MC, Zenobi R. Ion internal energy distributions validate the charge residue model for small molecule ion formation by spray methods. Rapid Communications in Mass Spectrometry. 2008;22(7):1062-8.
[16] Fenn J. Electrospray wings for molecular elephants (Nobel lecture). Angewandte Chemie-International Edition. 2003;42(33):3871-94.
[17] March RE. An introduction to quadrupole ion trap mass spectrometry. Journal of Mass Spectrometry. 1997;32(4):351-69.
[18] Ramon F-R. The techniques of plasma-mass (ICP-MS). 2004 [cited 2015 April 16th]; Available from: https://www.uam.es/personal_pas/txrf/icpms.html
[19] Kanu AB, Dwivedi P, Tam M, Matz L, Hill HH. Ion mobility-mass spectrometry. Journal of Mass Spectrometry. 2008;43(1):1-22.
[20] Giles K, Pringle SD, Worthington KR, Little D, Wildgoose JL, Bateman RH. Applications of a travelling wave-based radio-frequencyonly stacked ring ion guide. Rapid Communications in Mass Spectrometry. 2004;18(20):2401-14.
[21] Renaud JB. Studying the dissociation behaviour of ionized non-covalent complexes with a cohesive energetic and structure approach. University of Ottawa, Doctoral thesis, 2014.
[22] Wysocki V. SID coupled with Ion Mobility. 2015 [cited 2015 April 16th]; Available from: https://research.cbc.osu.edu/wysocki.11/group-home/projects/sid/sid_im/
[23] Pringle SD, Giles K, Wildgoose JL, Williams JP, Slade SE, Thalassinos K, et al. An investigation of the mobility separation of some peptide and protein ions using a new hybrid quadrupole/travelling wave IMS/oa-ToF instrument. International Journal of Mass Spectrometry. 2007;261(1):1-12.

[24] Jennings KR. Collision-induced decompositions of aromatic molecular ions. International Journal of Mass Spectrometry and Ion Physics. 1968;1:227-35.
[25] Haddon WF, McLafferty FW. Metastable ion characteristics. VII. collision-induced metastables. Journal of the American Chemical Society. 1968;90(17):4745-6.
[26] Mayer PM, Poon C. The mechanisms of collisional activation of ions in mass spectrometry. Mass Spectrometry Reviews. 2009;28(4):608-39.
[27] Chen YL, Campbell JM, Collings BA, Konermann L, Douglas DJ. Stability of a highly charged noncovalent complex in the gas phase: Holomyoglobin. Rapid Communications in Mass Spectrometry. 1998;12(15):1003-10.
[28] Meroueh O, Hase WL. Collisional activation of small peptides. Journal of Physical Chemistry A. 1999;103(20):3981-90.
[29] Nesatyy VJ, Laskin J. Dissociation of noncovalent protein complexes by triple quadrupole tandem mass spectrometry: comparison of Monte Carlo simulation and experiment. International Journal of Mass Spectrometry. 2002;221(3):245-62.
[30] Naban-Maillet J, Lesage D, Bossee A, Gimbert Y, Sztaray J, Vekey K, et al. Internal energy distribution in electrospray ionization. Journal of Mass Spectrometry. 2005;40(1):1-8.
[31] Wells J, McLuckey S, Burlingame A. Collision-induced dissociation (CID) of peptides and proteins. Biological Mass Spectrometry. 2005;402:148-85.
[32] Mayer PM, Martineau E. Gas-phase binding energies for non-covalent A beta-40 peptide/small molecule complexes from CID mass spectrometry and RRKM theory. Physical Chemistry Chemical Physics. 2011;13(11):5178-86.
[33] Korner R, Wilm M, Morand K, Schubert M, Mann M. Nano electrospray combined with a quadrupole ion trap for the analysis of peptides and protein digests. Journal of the American Society For Mass Spectrometry. 1996;7(2):150-6.
[34] Brunnee C. The ideal mass analyzer - fact or fiction. International Journal of Mass Spectrometry and Ion Processes. 1987;76(2):125-237.
[35] Chernushevich IV, Loboda AV, Thomson BA. An introduction to quadrupole-time-of-flight mass spectrometry. Journal of Mass Spectrometry. 2001;36(8):849-65.

[36] Waters. What types of instruments are used? 2015 [cited 2015 April 19th]; Available from: http://www.waters.com/waters/en_US/What-Types-of-Instruments-Are-Used%3F/nav.htm?cid=10090937

[37] Green NJB. Unimolecular kinetics. Part 1, The reaction step. 1st ed. Amsterdam ; Boston: Elsevier; 2003.

[38] Kassel LS. Studies in homogeneous gas reactions I. Journal of Physical Chemistry. 1928;32(2):225-42.

[39] Marcus RA, Rice OK. The kinetics of the recombination of methyl radicals and iodine atoms. Journal of Physical and Colloid Chemistry. 1951;55(6):894-908.

[40] Marcus RA. Unimolecular dissociations and free radical recombination reactions. Journal of Chemical Physics. 1952;20(3):359-64.

[41] Wieder GM, Marcus RA. Dissociation and isomerization of vibrationally excited species. II. unimolecular reaction rate theory and its application. Journal of Chemical Physics. 1962;37(8):1835-52.

[42] Marcus RA. Dissociation and isomerization of vibrationally excited species. III. Journal of Chemical Physics. 1965;43(8):2658-61.

[43] Eyring H. The activated complex in chemical reactions. Journal of Chemical Physics. 1935;3(2):107-15.

[44] Baer T, Mayer PM. Statistical Rice-Ramsperger-Kassel-Marcus quasiequilibrium theory calculations in mass spectrometry. Journal of the American Society for Mass Spectrometry. 1997;8(2):103-15.

[45] Beyer T, Swinehart DF. Number of multiply-restricted partitions. Communications of the Acm. 1973;16(6):379.

[46] Schlegel HB. Potential energy surfaces. 2008 [cited 2015 May 24th]; Available from: http://www.chem.wayne.edu/~hbs/chm6440/PES.html

[47] Leeuwen RV. Kohn-Sham potentials in density functional theory; 1994.

[48] Gos W. Hole trapping and the negative bias temperature instability. Technical University of Vienna, Doctoral thesis, 2011.

[49] Yin Z. Microscopic mechanisms of magnetism and superconductivity studied from first principle calculations. University Of Califonia Davis, Doctoral dissertation, 2005.

[50] Ben-Ari J, Etinger A, Weisz A, Mandelbaum A. Hydrogen-shift isomerism: mass spectrometry of isomeric benzenesulfonate and 2-, 3- and 4-dehydrobenzenesulfonic acid anions in the gas phase. Journal of Mass Spectrometry. 2005;40(8):1064-71.
[51] Gaussian 09 user's reference: basis sets. 2014 [cited 2015 April 16th]; Available from: http://www.gaussian.com/g_tech/g_ur/m_basis_sets.htm
[52] Feller D. The role of databases in support of computational chemistry calculations. Journal of Computational Chemistry. 1996;17(13):1571-86.
[53] Schuchardt KL, Didier BT, Elsethagen T, Sun LS, Gurumoorthi V, Chase J, et al. Basis set exchange: A community database for computational sciences. Journal of Chemical Information and Modeling. 2007;47(3):1045-52.
[54] Pople JA, Santry DP, Segal GA. Approximate self-consistent molecular orbital theory. I. invariant procedures. Journal of Chemical Physics. 1965;43(10):S129-S35.
[55] Dewar MJS, Thiel W. Semiempirical model for 2-center repulsion integrals in NDDO approximation. Theoretica Chimica Acta. 1977;46(2):89-104.
[56] Semiempirical Methods. 2005 [cited 2015 May 17th]; Available from: http://www.cup.uni-muenchen.de/ch/compchem/energy/semi1.html
[57] Hostas J, Rezac J, Hobza P. On the performance of the semiempirical quantum mechanical PM6 and PM7 methods for noncovalent interactions. Chemical Physics Letters. 2013;568:161-6.
[58] Dewar MJS, Thiel W. Ground-states of molecules. 38. MNDO method - approximations and parameters. Journal of the American Chemical Society. 1977;99(15):4899-907.
[59] Dewar MJS, Thiel W. Ground-states of molecules. 39. MNDO results for molecules containing hydrogen, carbon, nitrogen, and oxygen. Journal of the American Chemical Society. 1977;99(15):4907-17.
[60] Dewar MJS, Zoebisch EG, Healy EF, Stewart JJP. The development and use of quantum mechanical molecular models. 76. AM1 - a new general purpose quantum-mechanical molecular mode. Journal of the American Chemical Society. 1985;107(13):3902-9.
[61] Stewart JJP. Optimization of parameters for semiempirical methods. 1. Method. Journal of Computational Chemistry. 1989;10(2):209-20.

[62] Thiel W, Voityuk AA. Extension of MNDO to d orbitals: Parameters and results for the second-row elements and for the zinc group. Journal of Physical Chemistry. 1996;100(2):616-26.
[63] Rocha GB, Freire RO, Simas AM, Stewart JJP. RM1: A reparameterization of AM1 for H, C, N, O, P, S, F, Cl, Br, and I. Journal of Computational Chemistry. 2006;27(10):1101-11.
[64] Stewart JJP. Optimization of parameters for semiempirical methods V: Modification of NDDO approximations and application to 70 elements. Journal of Molecular Modeling. 2007;13(12):1173-213.
[65] Stewart JJP. Optimization of parameters for semiempirical methods VI: more modifications to the NDDO approximations and re-optimization of parameters. Journal of Molecular Modeling. 2013;19(1):1-32.
[66] Stewart JJP. Stewart Computational Chemistry - MOPAC Home Page. 2015 [cited 2015 May 5th]; Available from: http://OpenMOPAC.net
[67] Klunzinger P. Basis Set FAQ. 2006 [cited 2015 May 7th]; Available from: https://www.wavefun.com/support/sp_compfaq/Basis_Set_FAQ.html
[68] Foresman JB, Frisch A, Gaussian Inc. Exploring chemistry with electronic structure methods. 2nd ed. Pittsburgh, PA: Gaussian, Inc.; 1996.

Chapter 3. Experimental Procedures

3.1 Materials

All the metalloporphyrins (Table 3.1) were purchased from Frontier Scientific, Inc. (Logan, UT 84321, USA). Methanol (A456-1) was purchased from Fisher Scientific (Fair Lawn, New Jersey, USA). All solutions of metalloporphyrins were prepared by diluting them with methanol with concentrations of 1×10^{-5} mol/L to 5×10^{-4} mol/L. A Diagger Vortex-Genie 2 shaker was used at a medium speed setting to shake each solution for approximately 5 minutes.

Table 3.1 Porphyrins studied in the research

	MW	Full Name
Fe^{III}TPPS	1024.27	Fe(III) meso-tetra(4-sulfonatophenyl) porphine chloride (acid form)
Mn^{III}TPPS	1023.36	Mn(III) meso-tetra(4-sulfonatophenyl) porphine chloride (acid form)
Co^{III}TPPS	1027.36	Co(III) meso-tetra(4-sulfonatophenyl) porphine chloride (acid form)
Ni^{II}TPPS	991.67	Ni(II) meso-tetra(4-sulfonatophenyl) porphine (acid form)

3.2 ESI-MS

The electrospray ionization mass spectrometry (ESI-MS) experiments of Fe^{III}TPPS, Mn^{III}TPPS, Co^{III}TPPS, and Ni^{II}TPPS were all run on a Waters Synapt G1 ion mobility/tandem mass spectrometer (Waters Corporation, USA) using the MassLynx V4.1 operating system under the same experiment condition. Before the experiment, the inlet was always first cleaned with a formic acid solution (5% formic acid, 47.5% distilled water, 47.5% methanol), and then cleaned with methanol. Sample solutions

were introduced via an automatic syringe pump at a flow rate of 20-40 $\mu L \cdot min^{-1}$ in negative ionization mode. The capillary, cone and extractor voltage were set at 2.50 kV, 34 V and 4 V, respectively. Source block temperature and desolvation temperature were set to 100 °C and 200 °C to control the desolvation of the porphryins. The desolvation gas flow was set at 176 L/Hr, and the cone gas flow was set at 40 L/Hr to help reduce adduct ions (dimers and trimers), and to keep the sample cone clean. The LM and HM resolution quadruple were both held constant at 10 in the MassLynx software (unit mass resolution) to resolve the different m/z values. The multiplier was held constant at 650. The mass-to-charge ratio range was set from 50 to 1000.

3.3 ESI-MS/MS

A Waters Synapt G1 ion mobility/tandem mass spectrometer (Waters Corporation, USA) was used to carry out the electrospray ionization tandem mass spectrometry (ESI-MS/MS) in negative ionization mode. The ion mobility spectrometry (IMS) was on or off. All the CID experiments were run in the transfer cell. There were seven MS/MS experiments in total for this study:

a) The iron porphyrin with a -2 charge, $[Fe^{II}TPPS+2H]^{2-}$, was selected at m/z 493.0, and the collision energies for CID ranged from 4 V to 62 V. The IMS was on because the ESI-MS experiment demonstrated that there were both monomer and dimer ions for the iron porphyrin at m/z 493.0. The **IMS was on** to separate monomers from dimers.

b) The iron porphyrin with a -3 charge, $[Fe^{II}TPPS+H]^{3-}$, was selected at m/z 328.3, with the IMS off, and the collision energies for CID ranged from 4 V to 23 V. The **IMS was off** because the ESI-MS experiment demonstrated that there were only monomer ions for the iron porphyrin at m/z 328.3. Prior to that, approximately 20% of $[Fe^{II}TPPS+H]^{3-}$ became fragment ions in the IMS when they collided with the helium buffer gas.

c) The manganese porphyrin with a -2 charge, $[Mn^{III}TPPS+H]^{2-}$, was selected at m/z 492.0, and the collision energies for CID ranged from 4 V to 50 V. The **IMS was on** to separate monomers from dimers.

d) The manganese porphyrin with a -3 charge, $[Mn^{III}TPPS]^{3-}$, was selected at m/z 327.6, with the IMS on, and the collision energies for CID ranged from 4 V to 42 V. The **IMS was on** to keep the experimental setting identical to $[Mn^{III}TPPS+H]^{2-}$, even though there were only monomers at m/z 327.6.

e) The cobalt porphyrin with a -3 charge, $[Co^{III}TPPS]^{3-}$, was selected at m/z 329.0. The collision energies for CID ranged from 4 V to 30 V when the **IMS was on**, and from 4 V to 20 V when the **IMS was off**. The ESI-MS experiment showed there were only monomers for the cobalt porphyrin ions at m/z 329.0. The IMS was on and off to determine the influence of IMS on the fragmentation process.

f) The nickel porphyrin with a -3 charge, $[Ni^{II}TPPS+H]^{3-}$, was selected at m/z 329.0. The collision energies for CID ranged from 4 V to 23 V. The **IMS was off** because ESI-MS experiments showed there were only monomers for nickel porphyrin ions at m/z 329.0.

Detail settings for each experiment are included in Table A6.2 in Appendix 6.

3.4 In-source-CID-MS/MS

A Waters Synapt G1 ion mobility/tandem mass spectrometer (Waters Corporation, USA) was used to carry out the in-source-CID-MS/MS experiments. The in-source-CID experiments were run on each molecular ion that were mentioned in section 3.3. The sample cone voltage was set to a high value to break the parent ion to its main fragment ions, among which two fragment ions (the loss of SO_2 and SO_3) were then selected for the MS/MS experiment. Experiment settings were re-optimized to maximize the abundance of these two fragment ions. The CID of these two fragment ions were then carried out in the transfer cell. Table 3.2 lists all the important parameters. It must be noted that the selected ions for $[Fe^{II}TPPS+2H]^{2-}$ were m/z 452.5 and 460.5 during this research, but theoretically they should be m/z 453.0 and 461.0. This should be for the reason of one hydrogen loss from $[Fe^{II}TPPS+2H]^{2-}$ caused by in-source-CID. See Appendix 5 for details about $[Fe^{II}TPPS+2H]^{2-}$.

Table 3.2 Settings for all the in-source-CID-MS/MS experiments

	Sample Cone Voltage (V)	Selected fragment ions from the in-source-CID (m/z)		Collision Voltage Range (V)
		SO_3 loss	SO_2 loss	
$[Fe^{II}TPPS+2H]^{2-}$	65	452.5	460.5	12-32
$[Fe^{II}TPPS+H]^{3-}$	52	301.6	306.7	4-23
$[Mn^{III}TPPS+H]^{2-}$	65	452.0	460.0	15-29
$[Mn^{III}TPPS]^{3-}$	65	301.0	306.3	4-20
$[Co^{III}TPPS]^{3-}$	52	302.3	307.7	4-20
$[Ni^{II}TPPS+H]^{3-}$	50	302.3	307.7	4-22

3.5 Obtaining experimental breakdown diagram

The fragmentation pathway map is the pathway of all the fragment ions from the dissociation of the parent ion. To know the pathway of each fragment ion, the first step is to perform the MS/MS of the parent ion under different collision energies, which is extracted to obtain the breakdown diagram. The main fragment ions are listed in the breakdown diagram. With the mass spectrum of each main fragment ion, the possible structure can be deduced. The possible structure of each fragment ion is then examined by comparing the theoretical isotope model with the experimental mass spectrum. Once the structures of all the fragment ions are clear, the assumption about main channels for those fragment ions is made. In the end, in-source-CID-MS/MS is performed to verify the assumption, and divide all the channels to the main fragment ions. A breakdown diagram of the main channels and the parent ion are plotted as a function of the center-of-mass collision energy, $\mathrm{E_{com}}$. (See Chapter 4)

Chapter 4. RRKM modeling for the dissociation of $[Ni^{II}TPPS+H]^{3-}$

4.1 ESI-MS of $Ni^{II}TPPS$

The mass spectrum of $Ni^{II}TPPS$ (Figure 4.1) shows that there are different charge states of $Ni^{II}TPPS$ in methanol solution, including $[Ni^{II}TPPS]^{4-}$, $[Ni^{II}TPPS+H]^{3-}$, and $[Ni^{II}TPPS+2H]^{2-}$. The one of interest is $[Ni^{II}TPPS+H]^{3-}$, which is only monomer instead of a mix of monomer $[Ni^{II}TPPS+H]^{3-}$ and dimer $[(Ni^{II}TPPS)_2+2H]^{6-}$. This was verified by turning on the ion mobility spectrometry (IMS), which showed that no extra ions could be separated.

The mass spectrum of $[Ni^{II}TPPS+H]^{3-}$ (Figure 4.2) matches its theoretical isotope model, so it proves to be a good reactant for the ESI-MS/MS experiment.

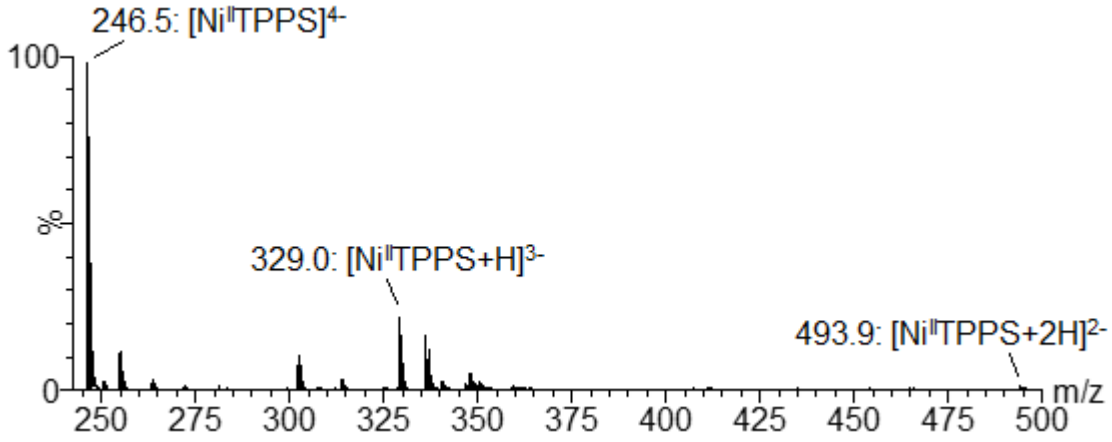

Figure 4.1 Mass spectrum of $Ni^{II}TPPS$

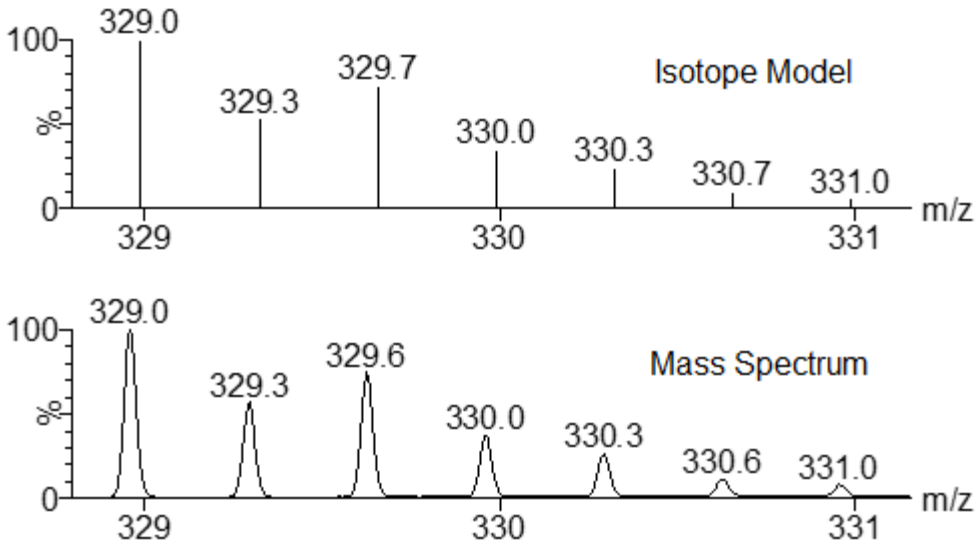

Figure 4.2 Mass spectrum of $[Ni^{II}TPPS+H]^{3-}$ and its isotope model

4.2 ESI-MS/MS of $[Ni^{II}TPPS+H]^{3-}$

The CID of $[Ni^{II}TPPS+H]^{3-}$ was selected at m/z 329.0 with the collision voltage ranging from 4 V to 23 V. Increasing the collision voltage decreases the abundance of the parent ion $[Ni^{II}TPPS+H]^{3-}$ to the point at which it disappears entirely and only fragment ions are observed (Figure 4.3). At low collision energy, fragment ions are m/z 302.3 and 307.7, but at higher collision energies, more fragment ions are formed. The lower half of Figure 4.3 contains all the main fragment ions resulting from the dissociation of $[Ni^{II}TPPS+H]^{3-}$. The m/z of those fragment ions are 281.0, 286.3, 298.3, 302.3, 307.7, 381.5, 389.5, 407.5, 413.5, 421.5, 429.5 and 453.5.

Figure 4.4 is the breakdown diagram of $[Ni^{II}TPPS+H]^{3-}$ with all the main fragment ions. They are plotted as a function of center-of-mass collision energy (E_{com}), which is a

fraction of the laboratory kinetic energy (E_{lab}) (Equation 2.6). E_{lab} equals the collision voltage V_{lab} multiplied by the charge state of $[Ni^{II}TPPS+H]^{3-}$ (Equation 2.5).

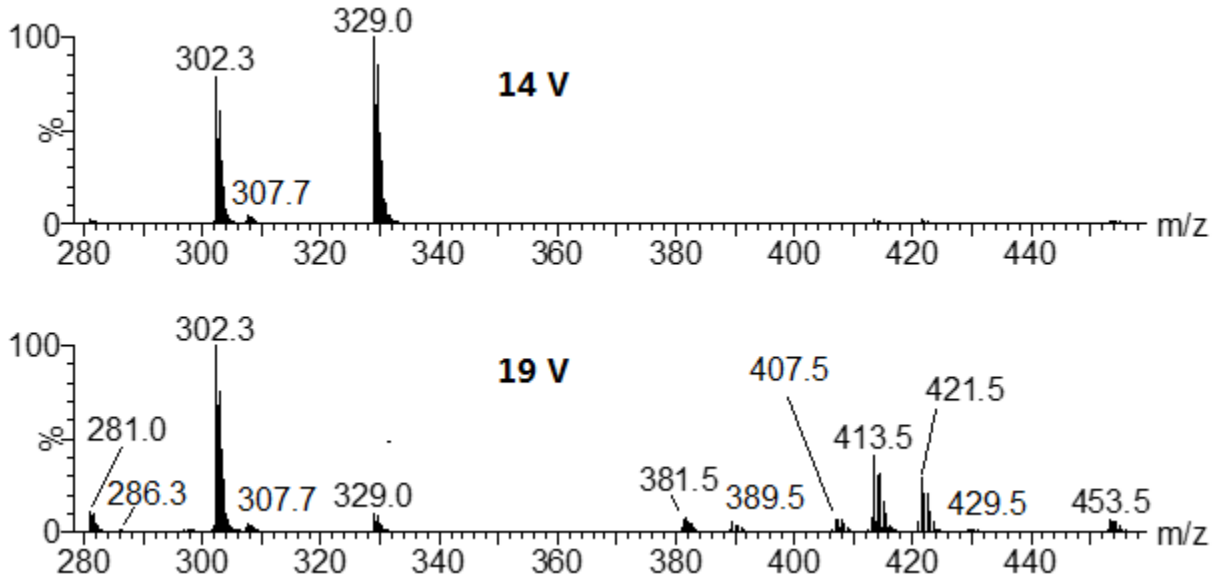

Figure 4.3 CID mass spectra of $[Ni^{II}TPPS+H]^{3-}$ at different collision voltages

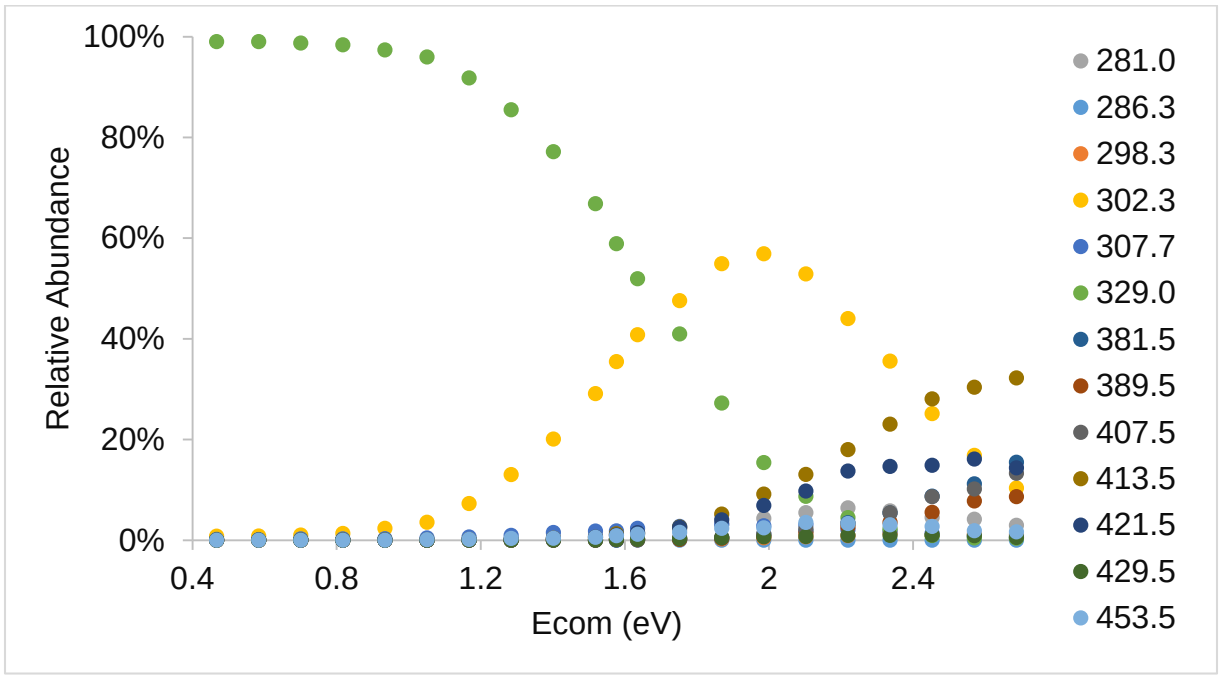

Figure 4.4 Breakdown diagram of $[Ni^{II}TPPS+H]^{3-}$ with all the fragment ions

4.3 Structure of all the fragment ions

The fragment ions mentioned in the section 4.2 can be calculated mathematically. For example, the mass spectrum shows that the fragment ion with m/z 302.3 has a -3 charge (Δm/z of adjacent peaks at m/z 302.3 is 0.33), so mass difference between this fragment ion and the parent ion is 3 × (329.0 – 302.3) = 80.1. Considering the big porphyrin ring has four benzenesulfonate functional groups that may lose SO_3 [1], the difference of m/z 80.1 should be a neutral SO_3, and the fragment ion with m/z 302.3 should be $[Ni^{II}TPPS+H-SO_3]^{3-}$. This result agrees with the mass spectrum isotope model of $[Ni^{II}TPPS+H-SO_3]^{3-}$ from MassLynx (Figure 4.5). In the same manner, structures of all the fragment ions from the $[Ni^{II}TPPS+H]^{3-}$ dissociation were estimated. Figure 4.6 lists all of them.

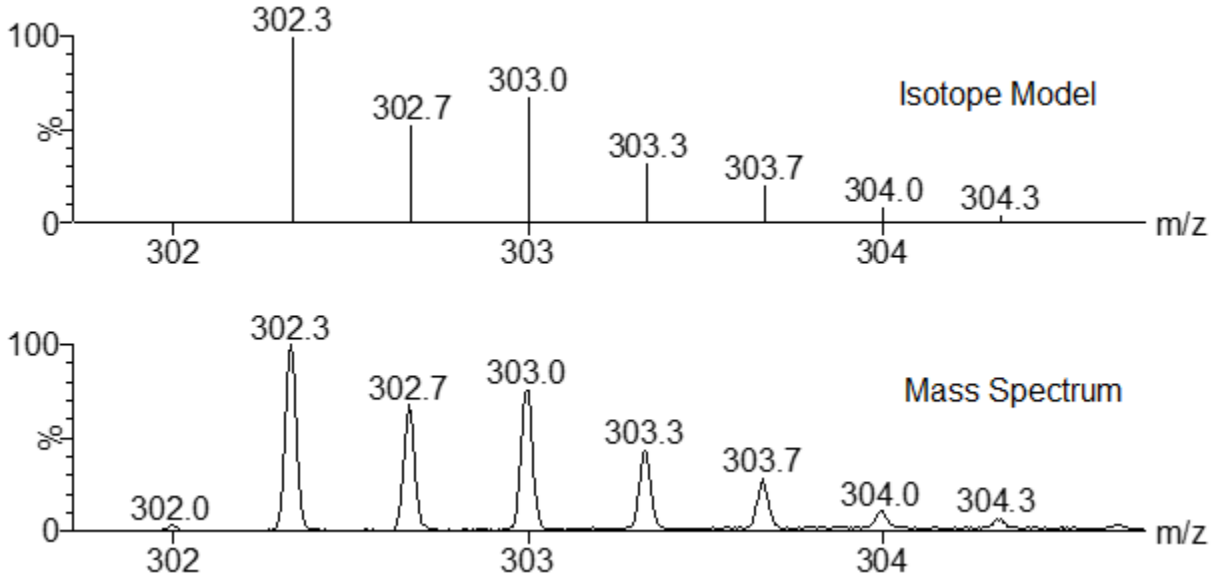

Figure 4.5 Mass spectrum of $[Ni^{II}TPPS+H-SO_3]^{3-}$ and its isotope model

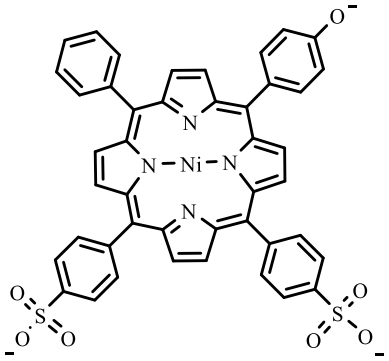

281.0: $[Ni^{II}TPPS+H-SO_3-SO_2]^{3-}$

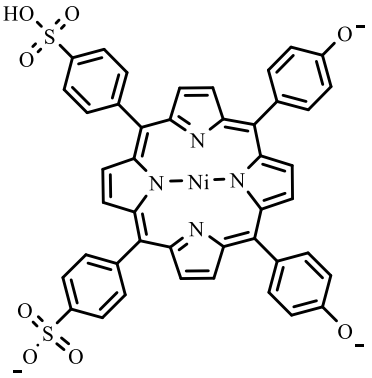

286.3: $[Ni^{II}TPPS+H-2SO_2]^{3-}$

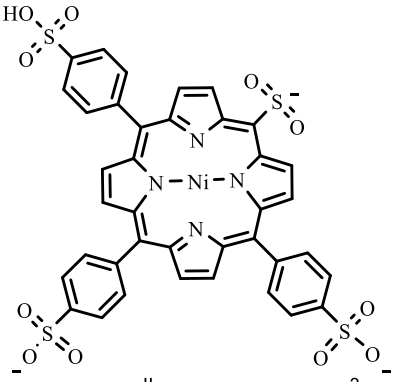

298.3: $[Ni^{II}TPPS+H-C_6H_4O]^{3-}$

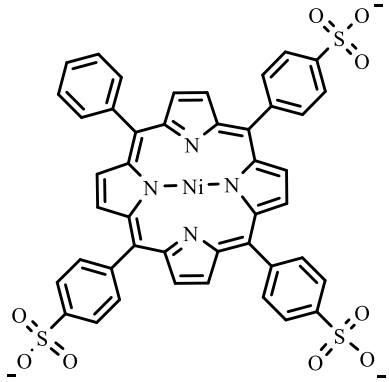

302.3: $[Ni^{II}TPPS+H-SO_3]^{3-}$

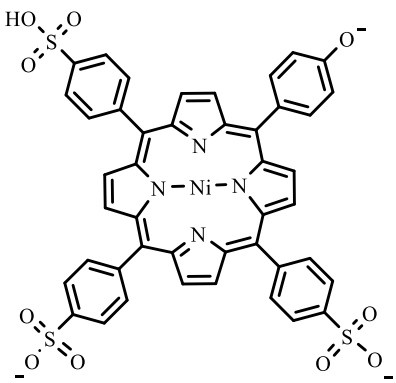

307.7: $[Ni^{II}TPPS+H-SO_2]^{3-}$

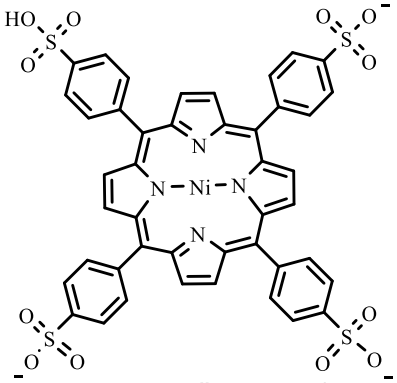

329.0: $[Ni^{II}TPPS+H]^{3-}$

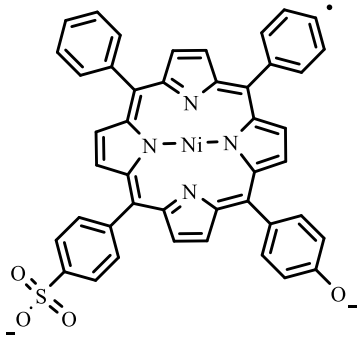

381.5: $[Ni^{II}TPPS+H-2SO_3-SO_2]^{2-}$

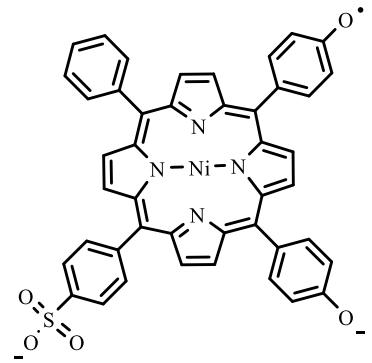

389.5: $[Ni^{II}TPPS+H-SO_3-2SO_2]^{2-}$

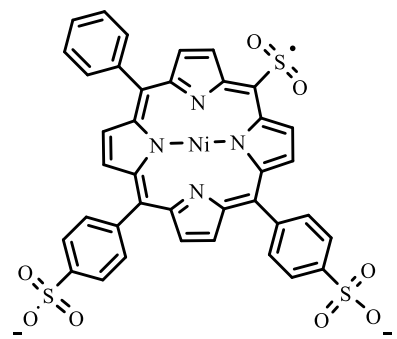

407.5: $[Ni^{II}TPPS+H-SO_3-C_6H_4O]^{2-}$

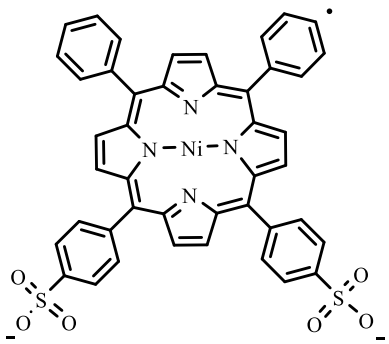

413.5: $[Ni^{II}TPPS+H-2SO_3]^{2-}$

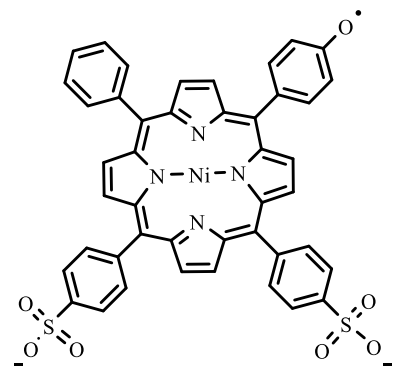

421.5: $[Ni^{II}TPPS+H-SO_3-SO_2]^{2-}$

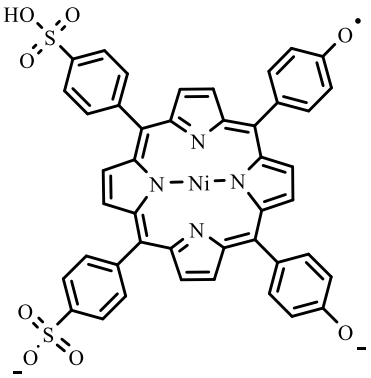

429.5: $[Ni^{II}TPPS+H-2SO_2]^{2-}$

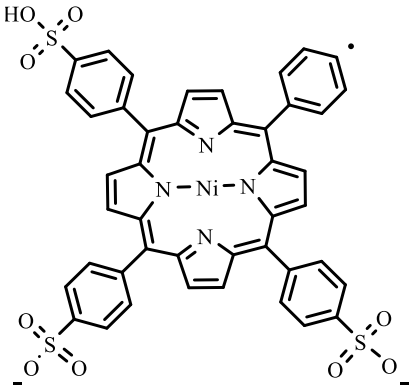

453.5: $[Ni^{II}TPPS+H-SO_3]^{2-}$

Figure 4.6 Possible structures of fragment ions from the dissociation of $[Ni^{II}TPPS+H]^{3-}$

4.4 In-source-CID-MS/MS and the map of the fragmentation pathways

There are 12 main fragment ions from the dissociation of $[Ni^{II}TPPS+H]^{3-}$ as mentioned in section 4.3. However, the pathways that these fragment ions take are still not clear. Structures of these fragment ions show that all the fragment ions result from the loss of one or several neutral/negative SO_2, SO_3, and C_6H_4O. When the collision voltage is low, only fragment ions with m/z 302.3 and m/z 307.7 appear. They are $[Ni^{II}TPPS+H-SO_3]^{3-}$ and $[Ni^{II}TPPS+H-SO_2]^{3-}$, respectively. This is reasonable considering that $[Ni^{II}TPPS+H]^{3-}$ has four benzenesulfonate groups, where it can lose SO_2/SO_3 with enough energy [1]. Also, it seems that the other fragment ions, which appear at a higher collision voltage, may all come from the breakup of the two main fragment ions $[Ni^{II}TPPS+H-SO_3]^{3-}$ and $[Ni^{II}TPPS+H-SO_2]^{3-}$.

To verify this assumption, the in-source-CID-MS/MS of $[Ni^{II}TPPS+H-SO_3]^{3-}$ and $[Ni^{II}TPPS+H-SO_2]^{3-}$ was carried out. The in-source-CID used a high sampling cone energy of 50 V to break up the parent ion in the source. Then all the negatively charged

fragment ions continued to the quadrupole, where ions with m/z 302.3 or 307.7 were selected and their CID mass spectra obtained.

Figure 4.7 and 4.8 represent the breakdown diagrams of m/z 302.3 and m/z 307.7 from collision voltage 4 V to 22 V, in which the center-of mass $\mathrm{E_{com}}$ is established on the x axis (Equation 2.5 and 2.6). There are four overlapped fragment ions present in both the in-source-CID-MS/MS of m/z 302.3 and m/z 307.7. They are $[Ni^{II}TPPS+H-2SO_3-SO_2]^{2-}$, $[Ni^{II}TPPS+H-SO_3-2SO_2]^{2-}$, $[Ni^{II}TPPS+H-SO_3-C_6H_4O]^{2-}$, and $[Ni^{II}TPPS+H-SO_3-SO_2]^{2-}$. All of the other fragment ions, with exception of m/z 453.5, are only present in the breakdown of either m/z 302.3 or m/z 307.7. See Figure 4.9 for the dissociation pathways of $[Ni^{II}TPPS+H]^{3-}$.

The fragment ion with m/z 453.5 is an independent channel: $[SO_3]^-$ loss from $Ni^{II}TPPS+H]^{3-}$ directly. However, this channel is ignored because it has a pretty low relative abundance (maximum 1.68%) compared with the other two channels, and it only appears at a high collision energy. Ignoring this channel will not influence the activation energy calculations of the other two channels.

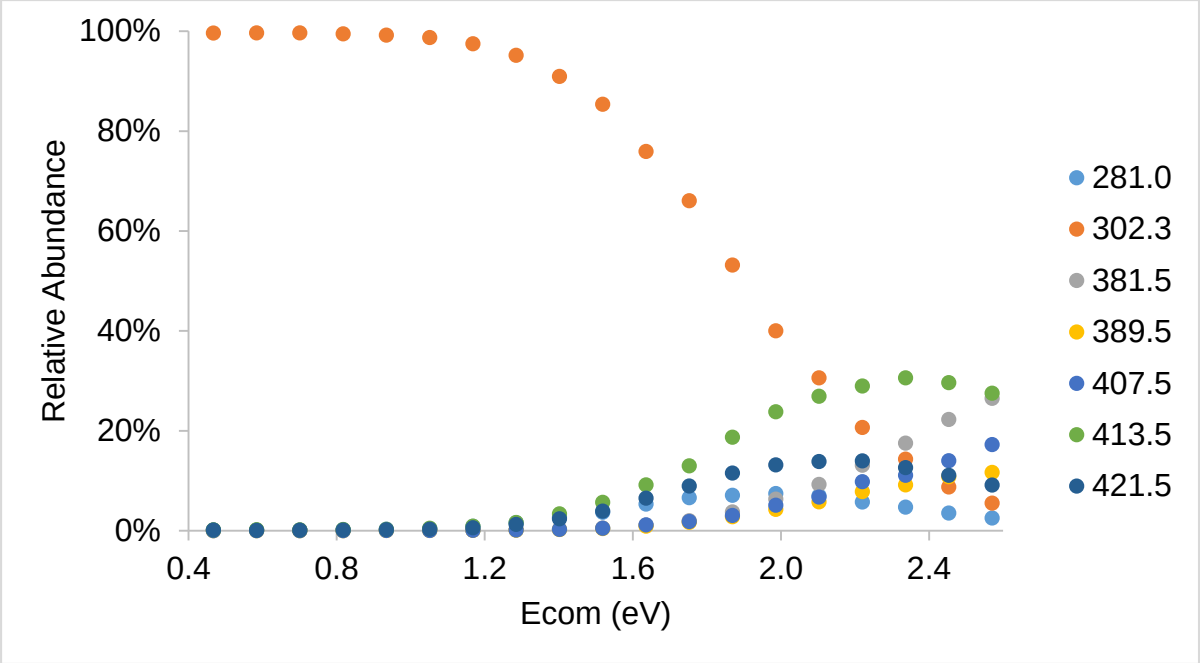

Figure 4.7 In-source-CID-MS/MS of $[Ni^{II}TPPS+H-SO_3]^{3-}$

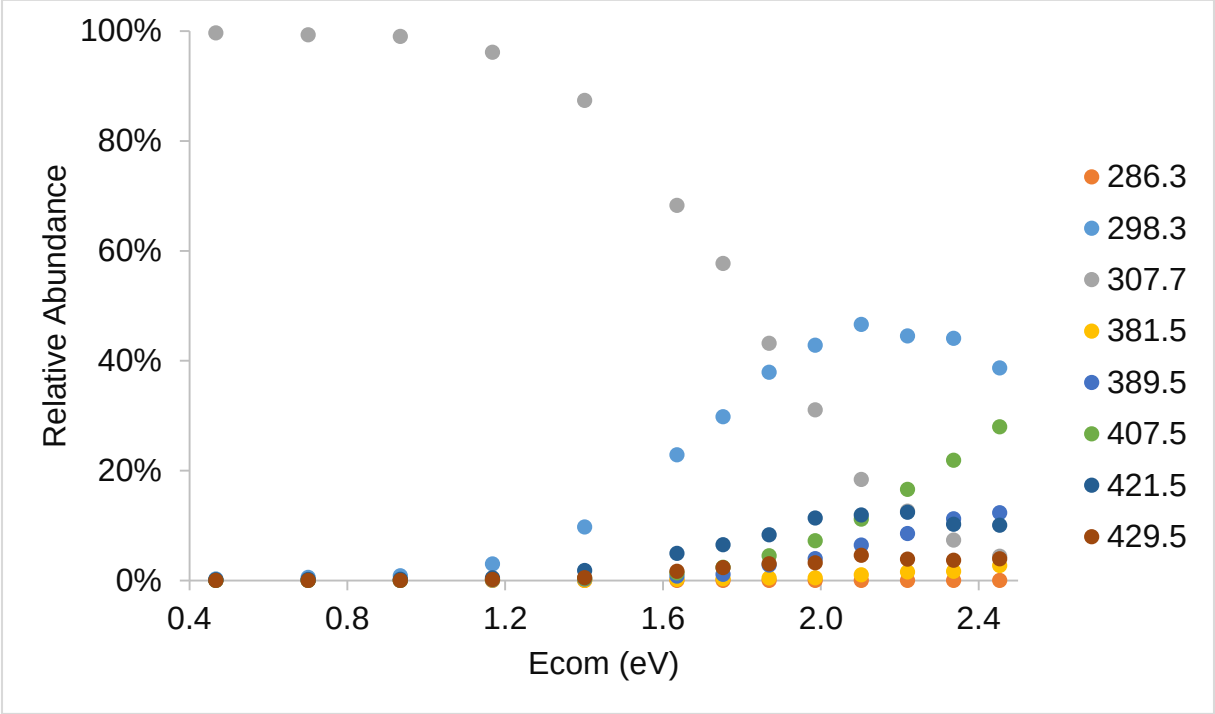

Figure 4.8 In-source-CID-MS/MS of $[Ni^{II}TPPS+H-SO_2]^{3-}$

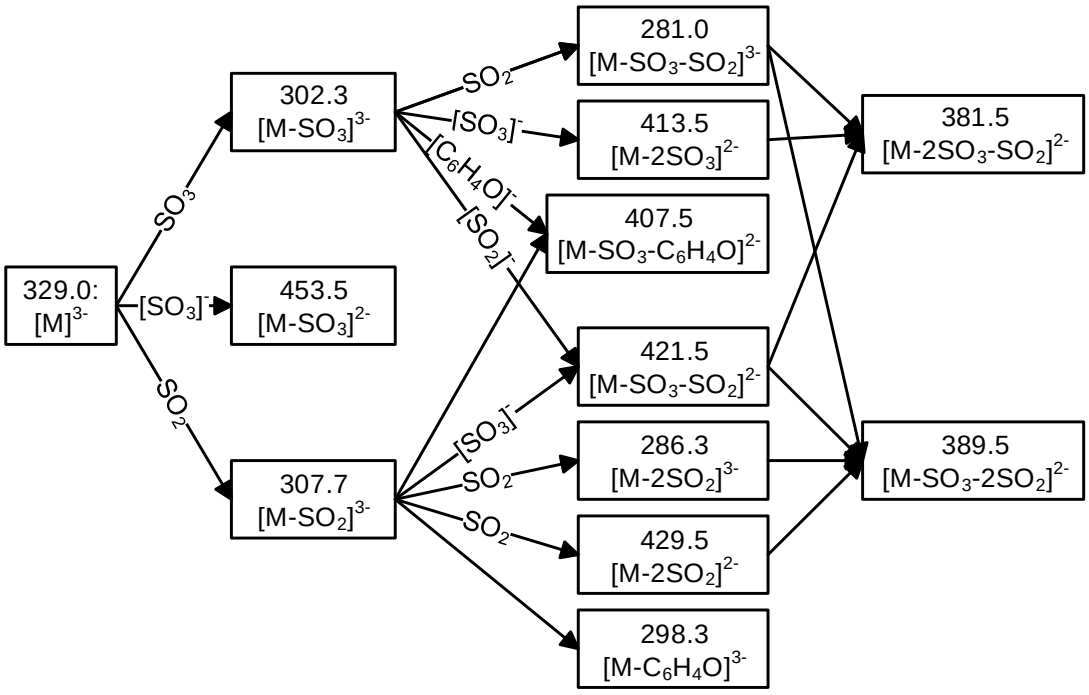

Figure 4.9 Possible dissociation pathways of $[M]^{3-}$ (where M = Ni^{II}TPPS+H)

4.5 Breakdown Diagram

The dissociation pathways of $[Ni^{II}TPPS+H]^{3-}$ have been evaluated in section 4.4. All the fragment ions, except for $[Ni^{II}TPPS+H-SO_3]^{2-}$, are created by these two channels: the breakdown of $[Ni^{II}TPPS+H-SO_3]^{3-}$ and $[Ni^{II}TPPS+H-SO_2]^{3-}$. However, the division of those four overlapped fragment ions into these two channels still remains unclear. The total relative abundance percent of all the overlapped fragment ions increase from 0 to 36.3% when increasing the collision energy (Figure 4.10), which is too significant to ignore. The contribution of $[Ni^{II}TPPS+H-SO_3]^{3-}$ to these four overlapped fragment ions are calculated by Equation 4.1. Figure 4.11 shows the % contribution of $[Ni^{II}TPPS+H-SO_3]^{3-}$ to those four overlapped fragment ions, which seems to be consistent when increasing the collision voltage.

$$\% = \frac{A_{SO_3 \text{ loss channel}}}{A_{SO_3 \text{ loss channel}} + A_{SO_2 \text{ loss channel}}} \qquad \text{(Equation 4.1)}$$

As a result, the average percentage value of each overlapped fragment ion was used to divide the overlapped fragment ions to the channels $[Ni^{II}TPPS+H\text{-}SO_3]^{3-}$ and $[Ni^{II}TPPS+H\text{-}SO_2]^{3-}$ for the breakdown diagram of the parent ion $[Ni^{II}TPPS+H]^{3-}$.

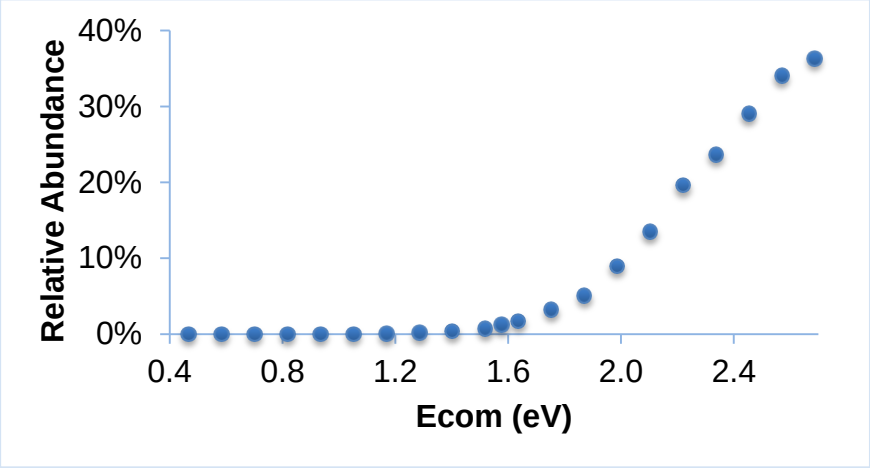

Figure 4.10 Total relative abundance of the overlapped fragment ions from both $[Ni^{II}TPPS+H\text{-}SO_3]^{3-}$ and $[Ni^{II}TPPS+H\text{-}SO_2]^{3-}$

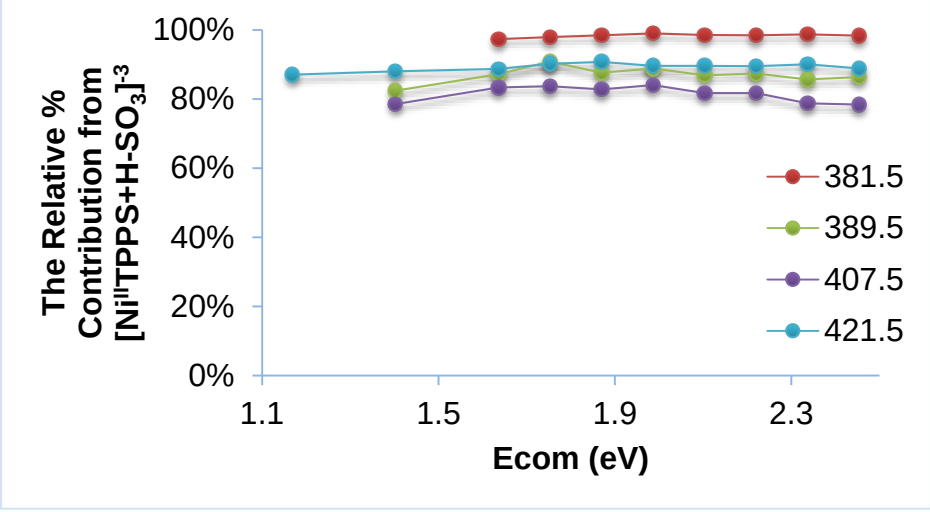

Figure 4.11 Relative abundance % contribution from $[Ni^{II}TPPS+H\text{-}SO_3]^{3-}$ to the overlapped fragment ions

Thus, equation 4.1 was used to assign the appropriate percentage of the four overlapping channels to the two main fragment ions to produce the breakdown diagram in Figure 4.12

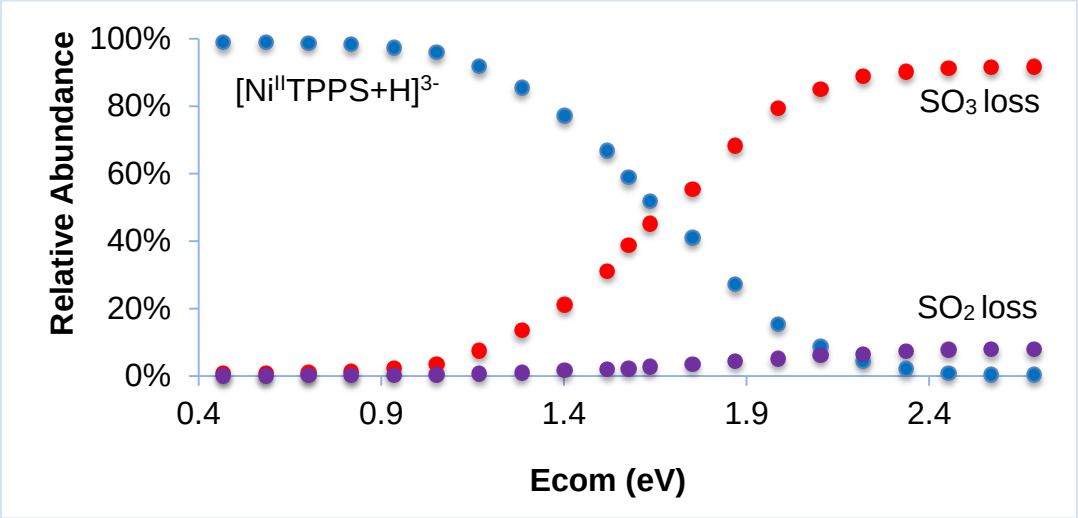

Figure 4.12 Final breakdown diagram for the dissociation of $[Ni^{II}TPPS+H]^{3-}$

4.6 RRKM modeling the dissociation of $[Ni^{II}TPPS+H]^{3-}$ and other metalloporphyrins

To understand CID mass spectra, the breakdown diagram was modeled by RRKM theory by using the harmonic vibrational frequencies of $[Ni^{II}TPPS+H]^{3-}$ (see Table A6.1 in Appendix 6). RRKM theory estimates the theoretical breakdown diagram by altering the following four parameters: i) the activation energy E_0, ii) the first ten vibrational frequencies of the transition state, iii) the pre-collision internal temperature of the ions T_{ini}, and iv) α (Equation 2.7). These four parameters were changed manually until the best-fitted theoretical breakdown diagram that matches the experimental breakdown diagram was found (Figure 4.13).

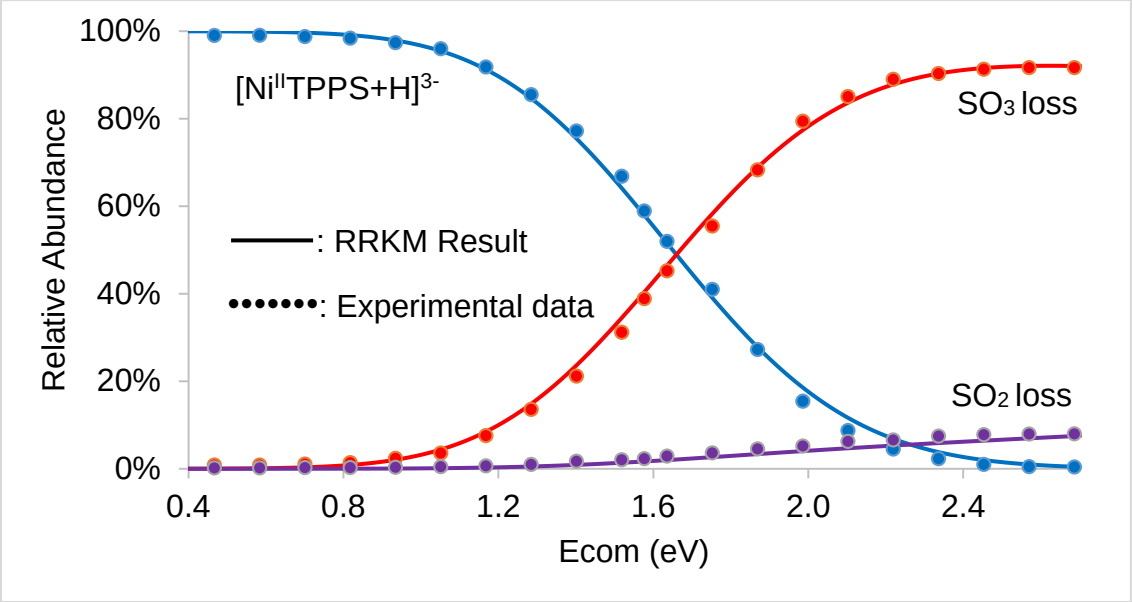

Figure 4.13 RRKM modeling results for the dissociation of $[Ni^{II}TPPS+H]^{3-}$

See Appendices 1 - 5 for the derivation of the breakdown diagrams and RRKM modeling for $[Co^{III}TPPS]^{3-}$, $[Mn^{III}TPPS]^{3-}$, $[Mn^{III}TPPS+H]^{2-}$, $[Fe^{II}TPPS+H]^{3-}$, and $[Fe^{II}TPPS+2H]^{2-}$. Table 4.1 lists all the activation energies and entropies modeled by RRKM for the dissociation of molecular ions. T_{ini} and α for all the six ions studied in this research were assumed to be 400 and 150, respectively. See Chapter 6 for the discussion of the meaning of these activation energies.

Table 4.1 RKKM modeling results for the dissociation of $[Ni^{II}TPPS+H]^{3-}$, $[Co^{III}TPPS]^{3-}$, $[Mn^{III}TPPS]^{3-}$, $[Mn^{III}TPPS+H]^{2-}$, $[Fe^{II}TPPS+H]^{3-}$, and $[Fe^{II}TPPS+2H]^{2-}$

Parent Ion	**IMS**	**RRKM Parameters**		**Channel**	**E_0** (eV)	**$\Delta^{\ddagger}S$** at 300 K ($J.mol^{-1}\cdot K^{-1}$)
		T_{ini} (K)	α ($K\cdot eV^{-1}$)			
$[Ni^{II}TPPS+H]^{3-}$	Off	400	150	SO_3 loss	1.30 ± 0.03	6 ± 5
				SO_2 loss	1.48 ± 0.03	9 ± 5
$[Co^{III}TPPS]^{3-}$	On	400	150	SO_3 loss	1.40 ± 0.02	2 ± 5
				SO_2 loss	1.33 ± 0.02	-3 ± 5
$[Fe^{II}TPPS+H]^{3-}$	Off	400	150	SO_3 loss	0.80 ± 0.10	-81 ± 15
				SO_2 loss	0.55 ± 0.10	-132 ± 15
$[Fe^{II}TPPS+2H]^{2-}$	On	400	150	SO_3 loss	1.47 ± 0.01	-48 ± 5
				SO_2 loss	1.49 ± 0.01	-57 ± 5
$[Mn^{III}TPPS]^{3-}$	On	400	150	SO_3 loss	1.60 ± 0.03	-50 ± 5
				SO_2 loss	1.33 ± 0.03	-73 ± 5
$[Mn^{III}TPPS+H]^{2-}$	On	400	150	SO_3 loss	2.56 ± 0.10	106 ± 15
				SO_2 loss	2.23 ± 0.10	63 ± 15

It has to be noted that due to the inherent limitations in the theory employed for modeling the breakdown curves, the values listed in Table 4.1 cannot be taken as absolute values, but rather their relative magnitudes should be reasonable. This is because the activation energy and entropy of a reaction change with T_{ini} and α, which are unknown in this research. T_{ini} and α are similar for the dissociation of ions with similar structures under similar experiments conditions, but they might be quite different under different experimental conditions, such as IMS on and off (see Appendix 1). However, the focus of this study is to compare the activation energies of the two dissociation channels of a same parent ion, and see which one is higher and how close

they are. RRKM modeling is good at this even when T_{ini} and α are unknown (see Appendix 1).

4.7 References

[1] Ben-Ari J, Etinger A, Weisz A, Mandelbaum A. Hydrogen-shift isomerism: mass spectrometry of isomeric benzenesulfonate and 2-, 3- and 4-dehydrobenzenesulfonic acid anions in the gas phase. Journal of Mass Spectrometry. 2005;40(8):1064-71.

Chapter 5. Molecular Simulation

As discussed in section 2.4, calculations on the metalloporphyrins are often not feasible with high level quantum computational chemistry methods. A practical approach to rectify this problem is to perform a thorough molecular simulation of the benzenesulfonate functional groups of metalloporphyrins on a high-level theory, and then perform the necessary calculations for the metalloporphyrins at a lower level theory.

5.1 Molecular simulation on the dissociation of negative and neutral benzenesulfonate at B3-LYP/6-31+G(2d, p) level

In this research, the dissociation processes of negative and neutral benzene-sulfonate (Figure 5.1) were modeled based on Ben-Ari's experiment [1]. Molecular simulations, including minimum energy state optimization, transition state optimization and intrinsic reaction coordinate calculations, were performed at B3-LYP/6-31+G(2d, p) level. The energy of each molecular was calculated by adding together values of "HF" and "zero-point correction" extracted from the Gaussian output file (unit: Hartree/Particle). The energies demonstrated in Hartree's were then subsequently converted to eV by multiplying them by 27.2114.

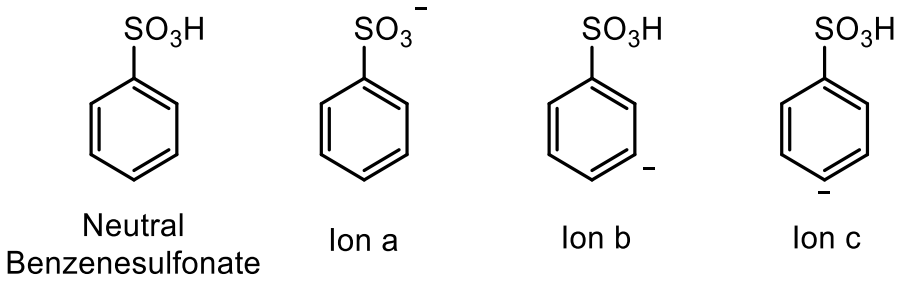

Figure 5.1 Structures of neutral and negative benzenesulfonate

Figure 5.2 shows the molecular simulation results obtained, in which neutral benzenesulfonate directly loses neutral SO_3 and SO_2. Activation energies needed for these losses (SO_3 and SO_2) were of the magnitude of 2.62 eV and 2.27 eV, respectively. By observation of this figure, it is easily identifiable that less energy is required to lose SO_3 compared to SO_2.

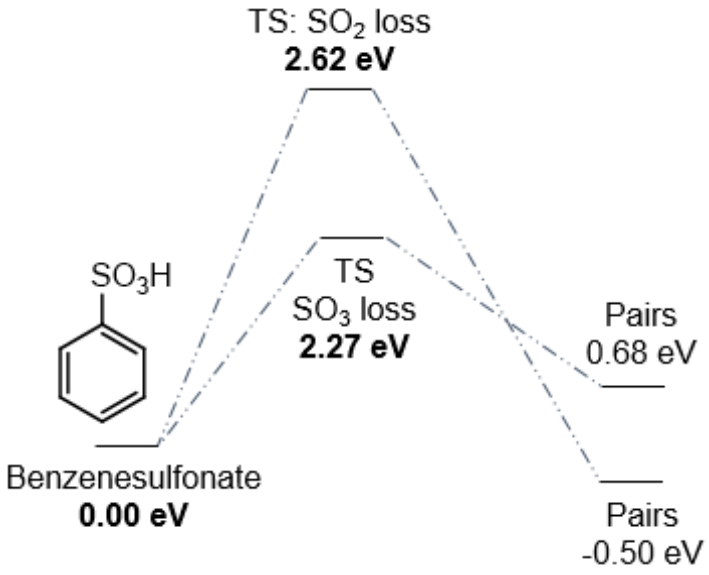

Figure 5.2 Mechanism of losing neutral SO_2 and SO_3 from neutral benzenesulfonate

Figure 5.3 shows the molecular simulation result of losing a neutral SO_2 from a negative benzenesulfonate ion. Negative benzenesulfonate ion can directly lose SO_2, but an activation energy of 2.32 eV is required.

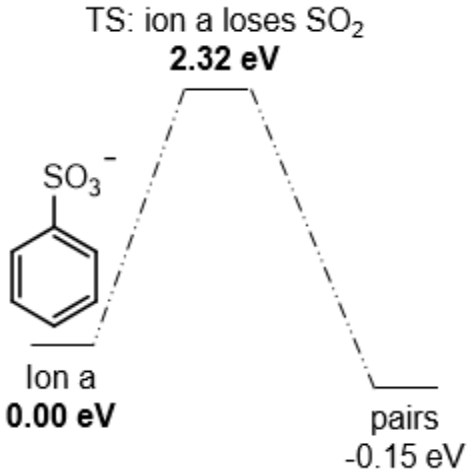

Figure 5.3 Mechanism of losing neutral SO_2 from negative benzenesulfonate ion (ion a)

Figure 5.4 illustrates the molecular simulation results for losing $[SO_3]^-$ from the negative benzenesulfonate ion. Negative benzenesulfonate ion (ion a) (Figure 5.1) cannot lose $[SO_3]^-$ directly. Instead, one H is donated from the benzene ring to the sulfonate functional group, forming $–SO_3H$ (ion b). Ion b can lose $[SO_3]^-$ if an activation energy greater than or equal to 4.33 eV is present. This ion (ion b) may also become ion c (Figure 5.4) if the H is moved from the para position to the meta position. However, ion b prefers to lose $[SO_3]^-$ instead of becoming ion c, since the loss has a much lower energy barrier than the conversion from ion b to c (4.33 eV vs 5.56 eV, respectively). The same pathway will hold for the loss of neutral SO_3, the fragment pair $[C_6H_5]^- + SO_3$ being 0.80 eV above those for the loss of $[SO_3]^-$ (The electron affinity of the phenyl

radical is 0.80 eV lower than that of SO_3). While higher in energy, the dissociation limit still lies below the 4.33 eV barrier in Figure 5.4.

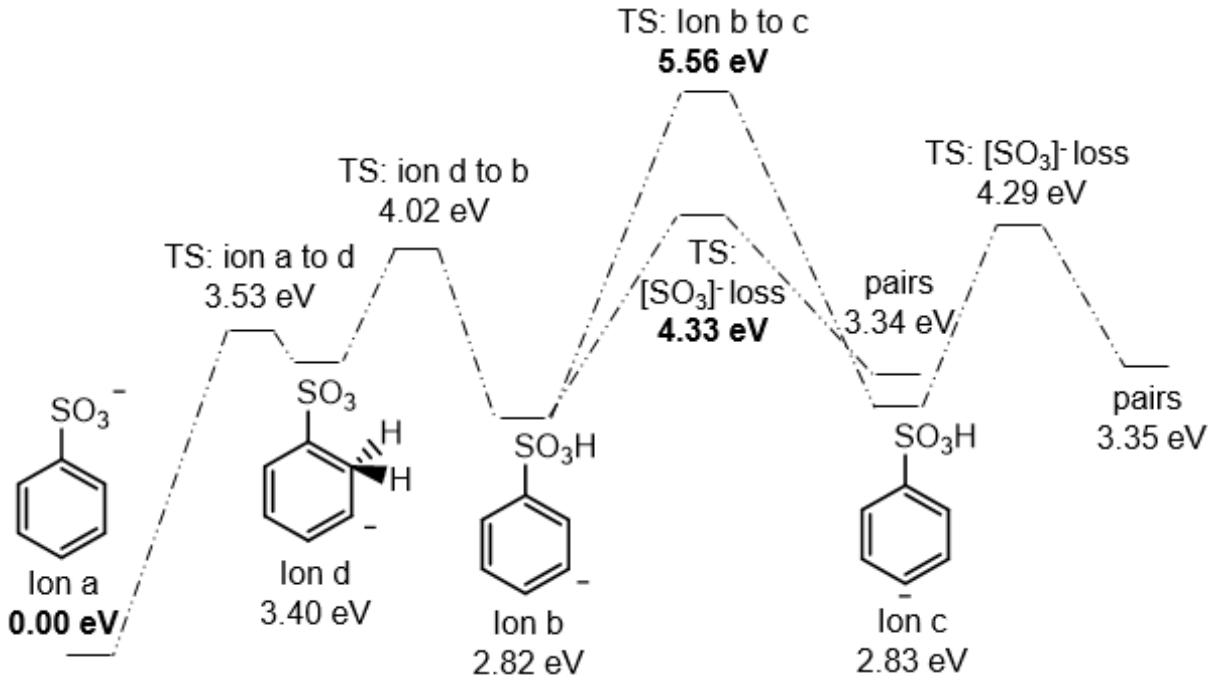

Figure 5.4 Mechanism of losing $[SO_3]^-$ from negative benzenesulfonate ion (ion a).

Table 5.1 The relative activation energies for SO_2/SO_3 loss from neutral and ionized benzenesulfonate investigated by molecular simulations at B3-LYP/6-31+G(2d, p) level

	E_0 of SO_3 loss (eV)	E_0 of SO_2 loss (eV)
$C_6H_5SO_3H$	2.27	2.62
$[C_6H_5SO_3]^-$ (Ion a)	4.33 ($[SO_3]^-$)	2.32

In summary, neutral benzenesulfonate can directly lose SO_2 and SO_3, but the loss of SO_3 is preferred. Negative benzenesulfonate ion can directly lose SO_2, while there must be one H transferred to the $–SO_3$ functional group before the negative

benzenesulfonate ion can lose $[SO_3]^-$, and in this case the barrier is huge for H movement on negative benzenesulfonate ion.

5.2 Molecular simulation on the energy changes for transferring H on $[Co^{III}TPPS]^{3-}$ and $[Mn^{III}TPPS]^{3-}$ at B3-LYP/6-31+G(2d, p)+LANL2DZ//PM7 level

$[Ni^{II}TPPS+H]^{3-}$, $[Mn^{III}TPPS+H]^{2-}$, $[Fe^{II}TPPS+H]^{3-}$, and $[Fe^{II}TPPS+2H]^{2-}$ have benzenesulfonate functional groups with and without H attached to $–SO_3$, while $[Co^{III}TPPS]^{3-}$ and $[Mn^{III}TPPS]^{3-}$ only have benzenesulfonate without H attached to $–SO_3$. The benzenesulfonate functional group without H attached to $–SO_3$ can be considered to be a negative benzenesulfonate (ion a), and the benzenesulfonate with H attached to $–SO_3$ is can be considered to be a neutral benzenesulfonate.

According to the summary in section 5.1, neutral benzenesulfonate can directly lose SO_2 and SO_3, and negative benzenesulfonate ion can directly lose SO_2. Therefore, $[Ni^{II}TPPS+H]^{3-}$, $[Mn^{III}TPPS+H]^{2-}$, $[Fe^{II}TPPS+H]^{3-}$, and $[Fe^{II}TPPS+2H]^{2-}$ can also directly lose those molecules. However, $[Co^{III}TPPS]^{3-}$ and $[Mn^{III}TPPS]^{3-}$ only have a negative benzenesulfonate functional group. As a result, negative benzenesulfonate functional group can directly lose SO_2, but there must be one H transferred to $–SO_3$ functional group before the negative benzenesulfonate group loses SO_3. However, H movement on $[Co^{III}TPPS]^{3-}$ and $[Mn^{III}TPPS]^{3-}$ may not need a huge barrier. As mentioned in section 1.2, T. Gozet et al. observed that H loss was one of the main dissociation channels for $[Fe^{III}TPP]^+$ and $[Mn^{III}TPP]^+$ [2].

Therefore, it is necessary to know the activation energies for transferring H from the porphyrin ring to the negative benzenesulfonate functional groups. If it is facile, it would be highly possible SO_3 and SO_2 loss will have similar activation energies.

The mechanism of H movement on porphyrin monomer was investigated by calculations at B3-LYP/6-31+G(2d, p)+LANL2DZ//PM7 level, which is a combination of the 6-31+G(2d, p) basis set and the LANL2DZ effective core basis set. The energy of each molecule was calculated by using “HF” value extracted from the Gaussian output file (unit: Hartree/Particle). It must be noted that there is no “zero-point correction” for single point energy calculation, because molecules are not optimized and frequencies are not calculated [3]. This correction differs from the calculations in section 5.1.

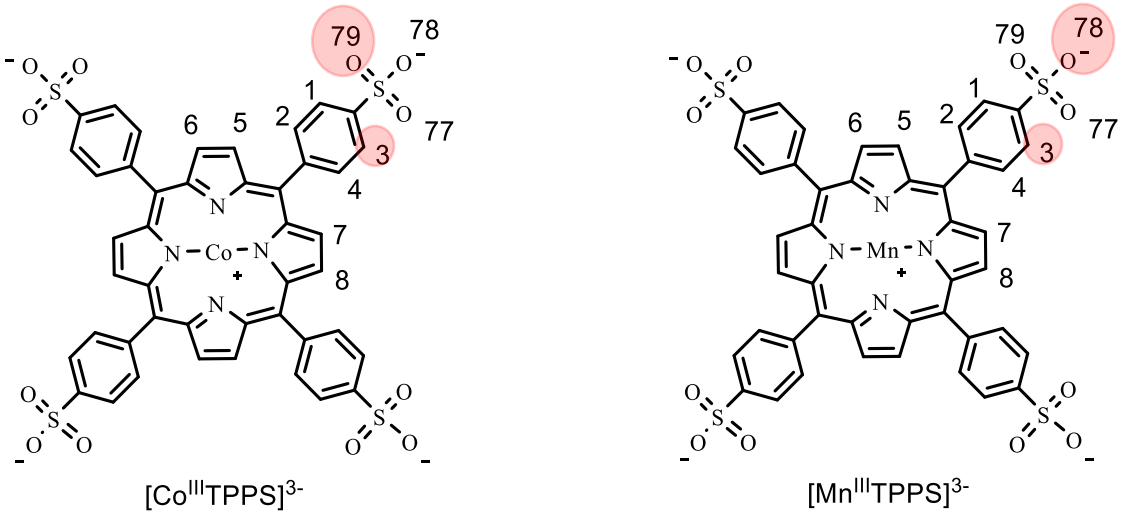

$[Co^{III}TPPS]^{3-}$ $[Mn^{III}TPPS]^{3-}$

Figure 5.5 H movement on cobalt porphyrin and manganese porphyrin investigated by molecular simulation at B3-LYP/6-31+G(2d, p)+LANL2DZ//PM7 level. 1 to 8 are the positions that might offer H. 77 to 79 are the positions that might accept the H. The numbers highlighted in circles are the ones that have the lowest energy change when the H moves from the H donor to the H acceptor.

Figure 5.5 shows the structure of $[Co^{III}TPPS]^{3-}$. Positions 1 to 8 are possible H donors, whereas 77 to 79 are possible H acceptors. Out of the 24 possible structures, the structure with the lowest energy is highlighted in circle, where the H moves from position 3 to 79 in $[Co^{III}TPPS]^{3-}$, with an energy change of + 2.11 eV. In addition, the structure with the lowest energy for $[Mn^{III}TPPS]^{3-}$ is the one where the H moves from position 3 to 78, with an energy change of + 2.25 eV. See Table 5.2 and 5.3 for all the energy changes after moving one H from the porphyrin ring to the negative benzene-sulfonate functional groups on $[Co^{III}TPPS]^{3-}$ and $[Mn^{III}TPPS]^{3-}$.

Table 5.2 Energy differences between the product and reactant when H moves from the porphyrin ring to the negative benzenesulfonate functional group on $[Co^{III}TPPS]^{3-}$

H Position	**Energy at B3-LYP/6-31+G(2d, p)+LANL2DZ //PM7 level (eV)**		
	O position 77	O position 78	O position 79
1	2.1132	2.6163	2.1173
2	2.6728	2.7117	2.6563
3	2.6083	2.1081	**2.1079**
4	2.7026	2.6958	2.6473
5	2.8326	2.5281	2.8485
6	2.7556	2.7633	2.7872
7	2.6974	2.7047	2.7062
8	2.9214	2.9173	2.9496

Table 5.3 Energy differences between the product and reactant when H moves from the porphyrin ring to the negative benzenesulfonate functional group on $[Mn^{III}TPPS]^{3-}$

H Position	**Energy at B3-LYP/6-31+G(2d, p)+LANL2DZ //PM7 level (eV)**		
	O position 77	O position 78	O position 79
1	2.2551	2.8286	2.2556
2	2.8828	2.8959	2.9177
3	2.8392	**2.2511**	2.2512
4	2.9288	2.9188	2.8825
5	2.5025	2.5114	2.5122
6	2.7515	2.7534	2.7670
7	2.5143	2.5144	2.5114
8	2.7680	2.7638	2.7498

The energy changes of H movement on $[Co^{III}TPPS]^{3-}$ (2.11 eV) and $[Mn^{III}TPPS]^{3-}$ (2.25 eV) are smaller than those of H movement on negative benzenesulfonate ion (2.82 eV: ion a to ion b). In addition, energies of $[Co^{III}TPPS]^{3-}$ and $[Mn^{III}TPPS]^{3-}$ were calculated at B3-LYP/6-31+G(2d, p)+LANL2DZ//PM7 level, and PM7 is a lower level of theory compared with the B3-LYP/6-31+G(2d, p)+LANL2DZ, so it is not as accurate as at B3-LYP/6-31+G(2d, p)+LANL2DZ. The energies of the products after H movement will be lower if using the B3-LYP/6-31+G(2d, p)+LANL2DZ basis set, and the energy changes might also be lower than 2.11 eV and 2.25 eV for $[Co^{III}TPPS]^{3-}$ and $[Mn^{III}TPPS]^{3-}$.

According to Bell-Evans-Polanyi (BEP) principle [4, 5], Hammond postulate [6] and Marcus theory [7, 8], for similar reactions, the more exothermic (endothermic) reaction will have the lower (higher) activation energy (See Figure 5.6).

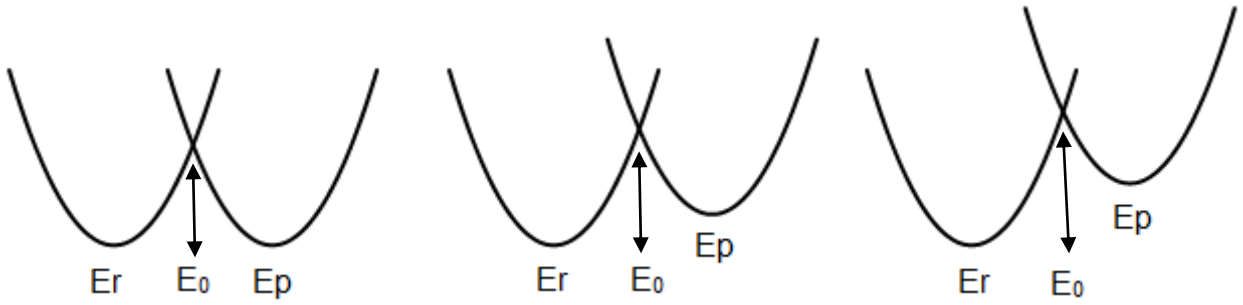

Figure 5.6 Curve-crossing model for a reaction. Er, E_0, and Ep represent reactant, activation, and product energy, respectively.

The H movement reactions in $[Co^{III}TPPS]^{3-}$ and $[Mn^{III}TPPS]^{3-}$ are both endothermic reactions, and H movement reactions with the smallest energy change both occurred in the benzenesulfonate functional groups (see Figure 5.5), which means the H movement reactions in $[Co^{III}TPPS]^{3-}$ and $[Mn^{III}TPPS]^{3-}$ should be similar with the reactions in the negative benzenesulfonate ion (ion a) (see Figure 5.4). As mentioned above, the H movement in $[Co^{III}TPPS]^{3-}$ and $[Mn^{III}TPPS]^{3-}$ is more facile compared with the H movement in the benzenesulfonate system, so it should occur with a smaller barrier.

5.3 References

[1] Ben-Ari J, Etinger A, Weisz A, Mandelbaum A. Hydrogen-shift isomerism: mass spectrometry of isomeric benzenesulfonate and 2-, 3- and 4-dehydrobenzenesulfonic acid anions in the gas phase. Journal of Mass Spectrometry. 2005;40(8):1064-71.

[2] Gozet T, Huynh L, Bohme D. Collision-induced dissociation of tetraphenyl iron and manganese porphyrin ions by electrospray ionization mass spectrometry. International Journal of Mass Spectrometry. 2009;279(2-3):113-8.

[3] Foresman JB, Frisch A. Exploring chemistry with electronic structure methods. 2nd ed. Pittsburgh, PA: Gaussian, Inc.; 1996.

[4] Bell RP. The Theory of Reactions Involving Proton Transfers. Proceedings of the Royal Society of London A. 1936;154:414-29.

[5] Evans MG, Polanyi M. Further considerations on the thermodynamics of chemical equilibria and reaction rates. Transactions of the Faraday Society. 1936;32(2):1333-59.

[6] Hammond GS. A correlation of reaction rates. Journal of the American Chemical Society. 1955;77(2):334-8.

[7] Jensen F. Introduction to computational chemistry. 2nd ed. Chichester, England ; Hoboken, NJ: John Wiley & Sons; 2007.

[8] Marcus RA. Theoretical relations among rate constants, barriers, and Broensted slopes of chemical reactions. Journal of Physical Chemistry. 1968;72(3):891-9.

Chapter 6. Conclusion

6.1 Common fragmentation pathways

The map of fragmentation pathways of metalloporphyrins with a -3 charge, namely $[Ni^{II}TPPS+H]^{3-}$, $[Co^{III}TPPS]^{3-}$ and $[Mn^{III}TPPS]^{3-}$, $[Fe^{II}TPPS+H]^{3-}$, are relatively similar. Figure 6.1 is common among all of them (see Figure 4.9, A1.10, A2.9, and A4.9). Metalloporphyrins with a -2 charge, namely $[Mn^{III}TPPS+H]^{2-}$ and $[Fe^{II}TPPS+2H]^{2-}$, have a common part shown in Figure 6.2 (see Figure A3.9, and A5.11).

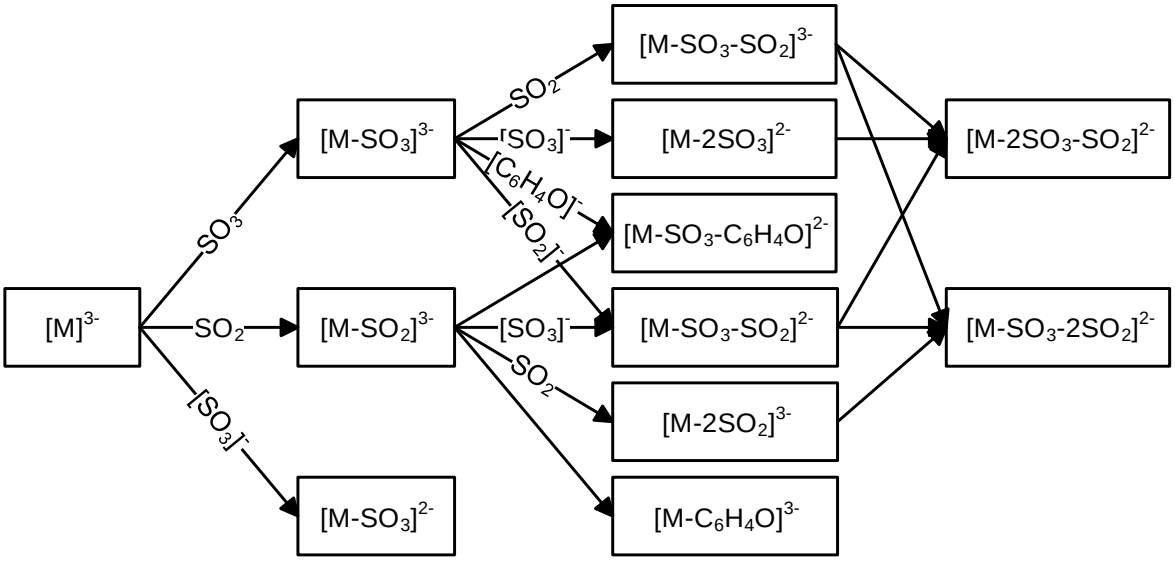

Figure 6.1 Common fragmentation pathways of $[Ni^{II}TPPS+H]^{3-}$, $[Co^{III}TPPS]^{3-}$ and $[Mn^{III}TPPS]^{3-}$, $[Fe^{II}TPPS+H]^{3-}$. (M represents these monomers with a -3 charge)

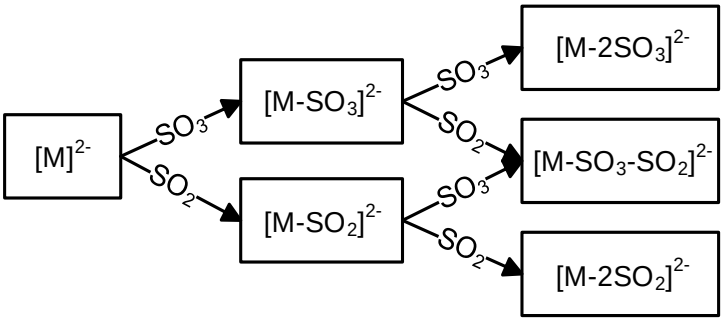

Figure 6.2 Common fragmentation pathways of $[Mn^{III}TPPS+H]^{2-}$ and $[Fe^{II}TPPS+2H]^{2-}$. (M represents these monomers with a -2 charge)

6.2 The dissociation of $[Co^{III}TPPS]^{3-}$ and $[Mn^{III}TPPS]^{3-}$

As summarized in section 5.2, H movement on $[Co^{III}TPPS]^{3-}$ and $[Mn^{III}TPPS]^{3-}$ are easy to occur with low energy barrier. As a result, the reaction that loses SO_3 from $[Co^{III}TPPS]^{3-}$ or $[Mn^{III}TPPS]^{3-}$ will have a lower activation energy, which might be similar to the activation energy for the reaction that loses SO_2. RRKM modeling shows that the loss of SO_3 and SO_2 from $[Co^{III}TPPS]^{3-}$ are 1.40 eV and 1.33 eV, respectively; and the loss of SO_3 and SO_2 from $[Mn^{III}TPPS]^{3-}$ are 1.60 eV and 1.33 eV, respectively (Table 4.1). The difference between the activation energies required for SO_3 and SO_2 loss are smaller for both $[Co^{III}TPPS]^{3-}$ (0.07 eV) and $[Mn^{III}TPPS]^{3-}$ (0.27 eV), compared with that of negative benzenesulfonate ion (ion a) (2.01 eV). Therefore results from RRKM modeling match the molecular simulation.

On the other hand, RRKM modeling shows that the loss of SO_3 requires a little bit higher activation energy compared with the loss of SO_2 from both $[Co^{III}TPPS]^{3-}$ and $[Mn^{III}TPPS]^{3-}$. This is reasonable because the activation energy for moving H from the porphyrin ring to the negative benzenesulfonate functional groups in $[Co^{III}TPPS]^{3-}$ and

$[Mn^{III}TPPS]^{3-}$ might be still higher than the activation energy of the loss of SO_2 and SO_3 from $[Co^{III}TPPS]^{3-}$ and $[Mn^{III}TPPS]^{3-}$, even though they are more facile than in the benzenesulfonate system (Figure 5.4). Therefore, the activation energies for the reactions of $[Co^{III}TPPS]^{3-}$ and $[Mn^{III}TPPS]^{3-}$ that lose SO_3 should actually be the activation energies for moving H from the porphyrin ring to the negative benzenesulfonate functional groups in $[Co^{III}TPPS]^{3-}$ and $[Mn^{III}TPPS]^{3-}$.

6.3 The dissociation of $[Ni^{II}TPPS+H]^{3-}$, $[Fe^{II}TPPS+2H]^{2-}$, $[Fe^{II}TPPS+H]^{3-}$ and $[Mn^{III}TPPS+H]^{2-}$

As mentioned in section 5.2, $[Ni^{II}TPPS+H]^{3-}$, $[Mn^{III}TPPS+H]^{2-}$, $[Fe^{II}TPPS+H]^{3-}$, and $[Fe^{II}TPPS+2H]^{2-}$ can directly lose SO_2 and SO_3 because they have both neutral and negative benzenesulfonate functional groups. Neutral benzenesulfonate can directly lose SO_2 and SO_3 with activation energies of 2.62 eV and 2.27 eV, respectively; and negative benzenesulfonate ion (ion a) can directly lose SO_2 with an activation energy of 2.32 eV (Table 5.1). As a result, when both $-C_6H_4SO_3^-$ and $-C_6H_4SO_3H$ are present in metalloporphyrins, the following reactions should occur: a) SO_3 loss (2.27 eV) directly from $-C_6H_4SO_3H$; b) SO_2 loss (2.32 eV) will prefer to directly occur on $-C_6H_4SO_3^-$, rather than on $-C_6H_4SO_3H$. Since 2.27 and 2.32 eV are similar, the activation energies for reactions that lose SO_2 and SO_3 from $[Ni^{II}TPPS+H]^{3-}$, $[Mn^{III}TPPS+H]^{2-}$, $[Fe^{II}TPPS+H]^{3-}$, and $[Fe^{II}TPPS+2H]^{2-}$ should be very similar, and SO_3 loss would requires a little bit lower activation energy (2.27 eV < 2.32 eV).

When it comes to **$[Ni^{II}TPPS+H]^{3-}$ and $[Fe^{II}TPPS+2H]^{2-}$**, the molecular simulations above match the RRKM modeling perfectly (see Table 4.1 for activation energies).

$[Ni^{II}TPPS+H]^{3-}$ needs 1.30 eV to lose SO_3, and 1.48 eV to lose SO_2. The activation energies are relatively close and 1.30 eV is a little bit lower than 1.48 eV. $[Fe^{II}TPPS+2H]^{2-}$ needs 1.47 eV for SO_3 and 1.49 eV for SO_2 loss, which is almost the same activation energy.

However, the RRKM modeling for $[Fe^{II}TPPS+H]^{3-}$ and $[Mn^{III}TPPS+H]^{2-}$ do not agree with the molecular simulations performed in Chapter 5. **$[Fe^{II}TPPS+H]^{3-}$** requires 0.80 and 0.55 eV to lose SO_3 and SO_2, respectively (see Table 4.1). This case is easy to understand, because the H loss from almost all of its fragments and the parent ion $[Fe^{II}TPPS+H]^{3-}$ disrupt the dissociation process (see Figure 6.3 and Figure A4.9). Considering there are almost 100% $[Fe^{II}TPPS\text{-}SO_2]^{3-}$ (m/z: 306.7), it might only come from the fragmentation of $[Fe^{II}TPPS]^{3-}$, instead of $[Fe^{II}TPPS+H\text{-}SO_2]^{3-}$. The real dissociation channels might be a mix of the following processes: a) $[Fe^{II}TPPS+H]^{3-}$ to $[Fe^{II}TPPS]^{3-}$, b) SO_3 loss from both $[Fe^{II}TPPS+H]^{3-}$, and c) SO_3 and SO_2 loss from $[Fe^{II}TPPS]^{3-}$.

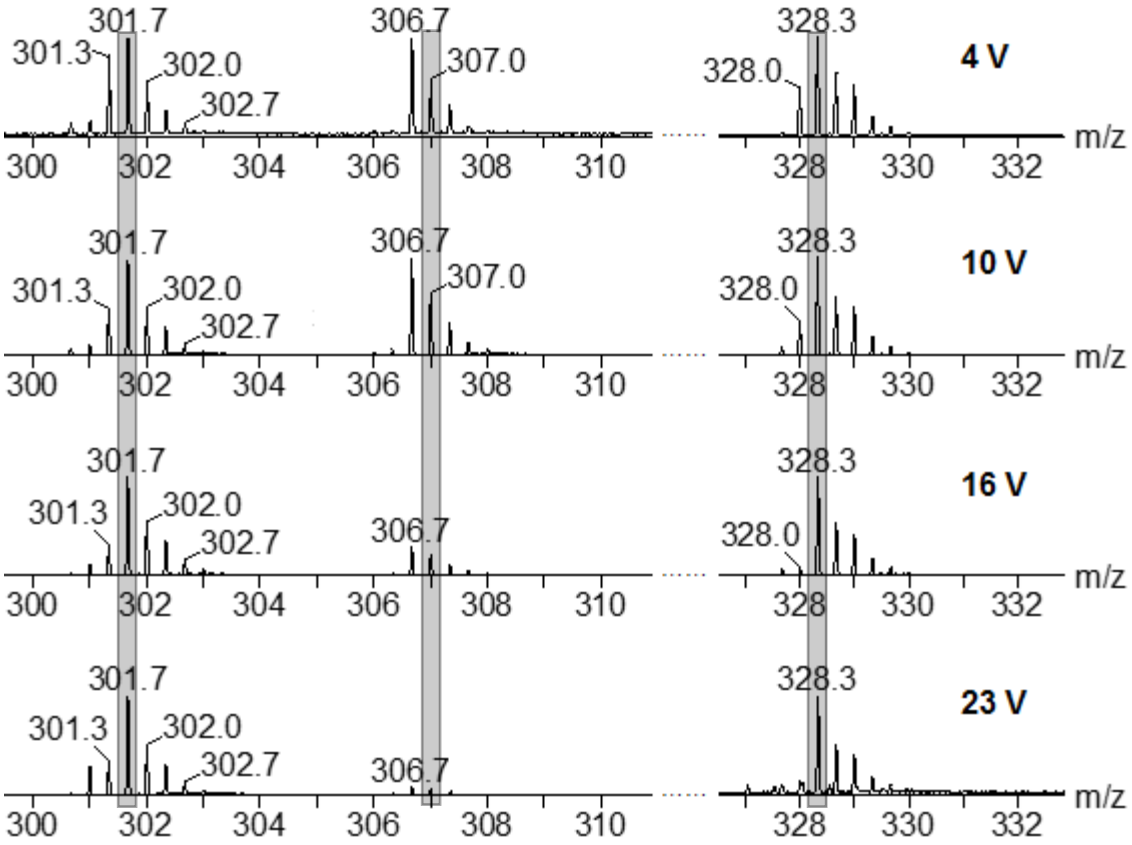

Figure 6.3 CID Mass spectra of $[Fe^{II}TPPS+H]^{3-}$ at different collision voltages (MS/MS experiments in Appendix 4). The y-axis of m/z 306.7 and 328.3 are not in the same scale. Peaks with a dark background have not lost H.

$[Mn^{III}TPPS+H]^{2-}$ requires higher activation energy for SO_3 loss (2.56 eV) compared with SO_2 loss (2.23 eV). This phenomenon might be caused by the metal center Mn. Table1.1 (see Chapter 1) shows Mn has the lowest electronic affinity (< 0 eV) compared with Fe (0.15 eV), Co (0.66 eV) and Ni (1.16 eV).

With the development of super computer technology, a thorough molecular simulation, including minimum energy state optimization, transition state optimization,

and intrinsic reaction coordinate calculation on the dissociation of metalloporphyrins, should be able to be performed to verify the conclusion of this research in a few years.

Statement of Original Research

- Activation energies for the dissociation of $[Ni^{II}TPPS+H]^{3-}$, $[Co^{III}TPPS]^{3-}$, $[Mn^{III}TPPS]^{3-}$, $[Mn^{III}TPPS+H]^{2-}$, $[Fe^{II}TPPS+H]^{3-}$, and $[Fe^{II}TPPS+2H]^{2-}$ were obtained by modeling their breakdown diagrams by using RRKM theory.
- In-source-CID-MS/MS experiments were performed to verify fragmentation pathways of $[Ni^{II}TPPS+H]^{3-}$, $[Co^{III}TPPS]^{3-}$, $[Mn^{III}TPPS]^{3-}$, $[Mn^{III}TPPS+H]^{2-}$, $[Fe^{II}TPPS+H]^{3-}$, and $[Fe^{II}TPPS+2H]^{2-}$.
- Molecular simulations were applied to investigate the energy changes for transferring H on $[Co^{III}TPPS]^{3-}$ and $[Mn^{III}TPPS]^{3-}$ at B3-LYP/6-31+G(2d, p)+LANL2DZ//PM7 level of theory
- Molecular simulation at B3-LYP/6-31+G(2d, p) level: a) SO_2 and SO_3 loss from neutral benzenesulfonate; b) H transferring process from ion a to b

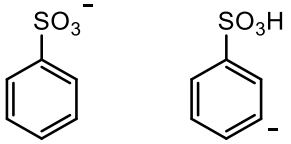

Ion a Ion b

Appendix 1. RRKM modeling for the dissociation of $[Co^{III}TPPS]^{3-}$

A1.1 ESI-MS of $Co^{III}TPPS$

The mass spectrum of $Co^{III}TPPS$ (Figure A1.1) shows there are different charge states of $Co^{III}TPPS$ in methanol solution, including $[Co^{III}TPPS]^{3-}$ and negligible $[Co^{III}TPPS+H]^{2-}$. The one of interest is $[Co^{III}TPPS]^{3-}$, which is only monomer, instead of a mix of monomer $[Co^{III}TPPS]^{3-}$ and dimer $[(Co^{III}TPPS)_2]^{6-}$. This was verified by turning on the ion mobility spectrometry (IMS), which showed no extra ions can be separated.

The mass spectrum of $[Co^{III}TPPS]^{3-}$ (Figure A1.2) totally agrees with its theoretical isotope model, so it proves to be a good reactant for the ESI-MS/MS experiment.

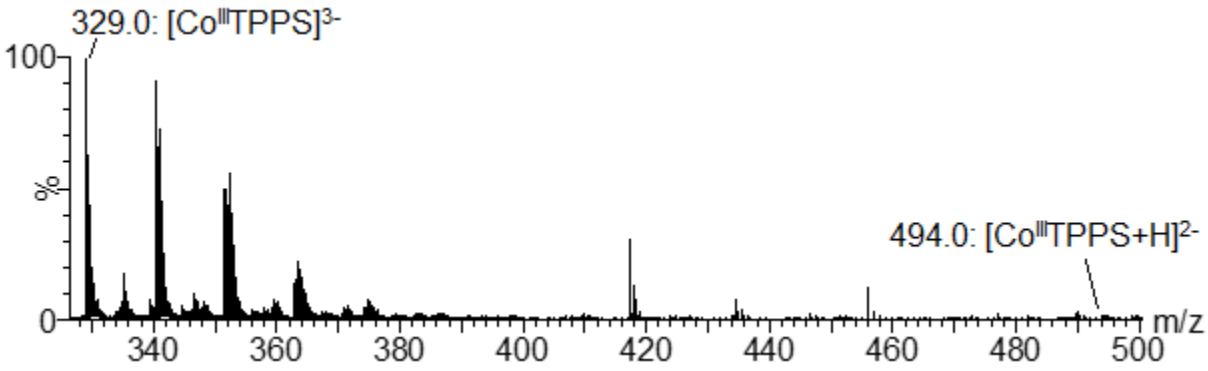

Figure A1.1 Mass spectrum of $Co^{III}TPPS$

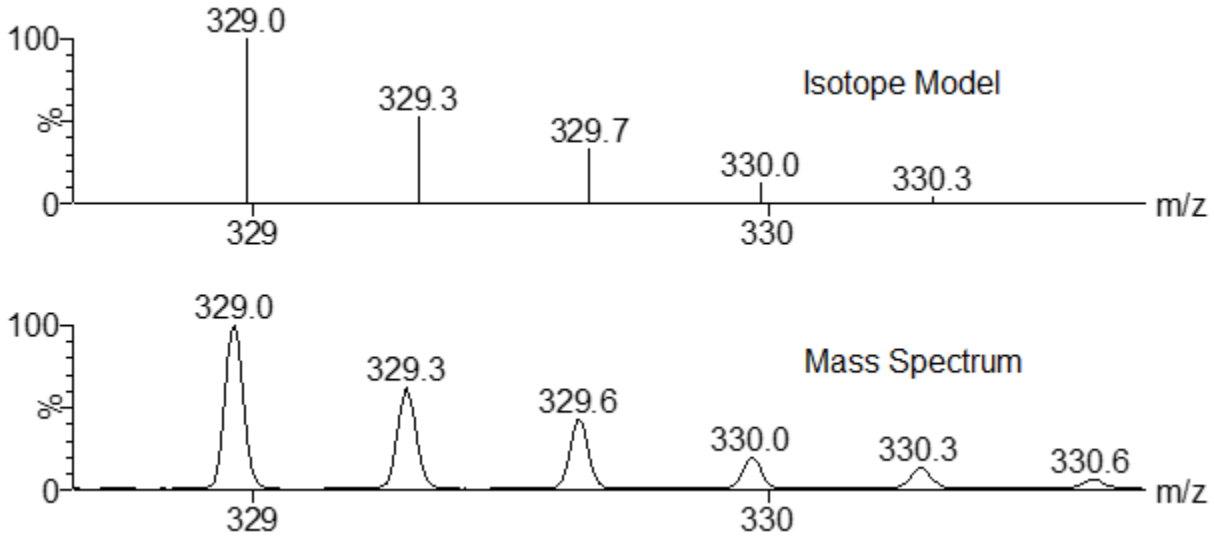

Figure A1.2 Mass spectrum of $[Co^{III}TPPS]^{3-}$ and its isotope model

A1.2 ESI-MS/MS of $[Co^{III}TPPS]^{3-}$

The CID of $[Co^{IIII}TPPS]^{3-}$ was selected at m/z 329.0 with the collision voltage ranging from 4 V to 30 V when the ion mobility separation (IMS) was on, and with the collision voltage ranging from 4 V to 20 V when the IMS was off. Increases of the collision voltage have the effect of decreasing the abundance of the parent ion $[Co^{III}TPPS]^{3-}$ to the point at which it disappears entirely and only fragment ions are observed (Figure A1.3). At low collision energy, fragment ions are m/z 302.3 and 307.7, but at higher collision energies, more fragment ions are formed. The lower half of Figure A1.3 contains all the main fragment ions resulting from the dissociation of $[Co^{III}TPPS]^{3-}$. The m/z of those fragment ions are 277.0, 281.0, 286.3, 289.7, 298.3, 302.3, 307.7, 369.5, 375.5, 381.5, 383.5, 389.5, 397.5, 407.5, 413.5, 421.5, 429.5 and 453.5.

Figure A1.4 and A1.5 are the breakdown diagram of $[Co^{III}TPPS]^{3-}$ with all the main fragment ions. They are plotted as a function of center-of-mass collision energy

(E_{com}), which is a fraction of the laboratory kinetic energy (E_{lab}) (Equation 2.6). E_{lab} equals the collision voltage V_{lab} multiplied by the charge state of $[Co^{III}TPPS]^{3-}$ (Equation 2.5).

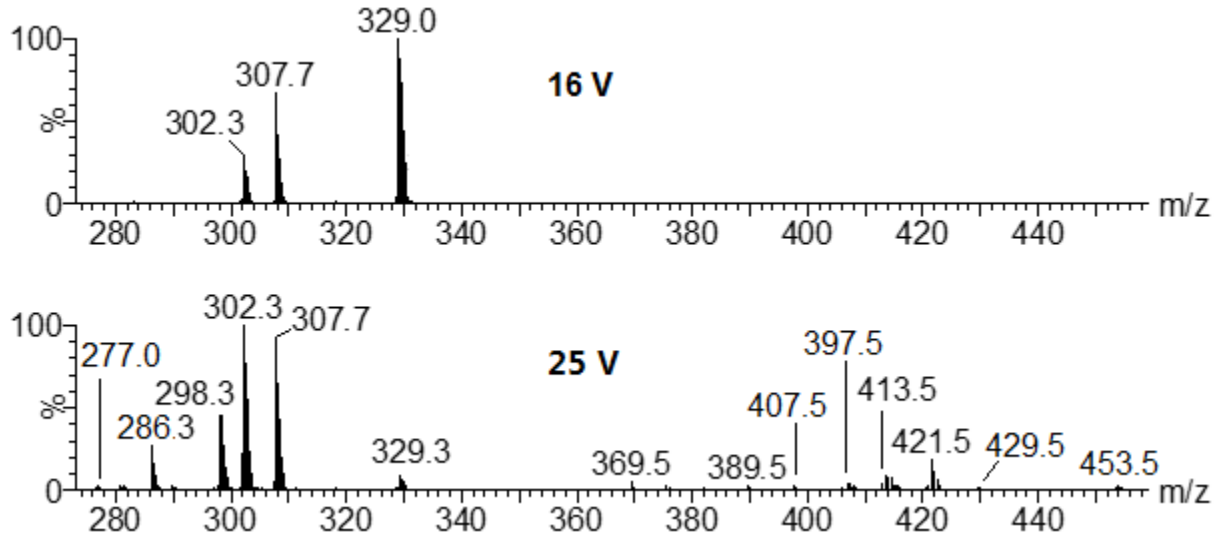

Figure A1.3 CID mass spectra of $[Co^{III}TPPS]^{3-}$ at different collision voltages (IMS on)

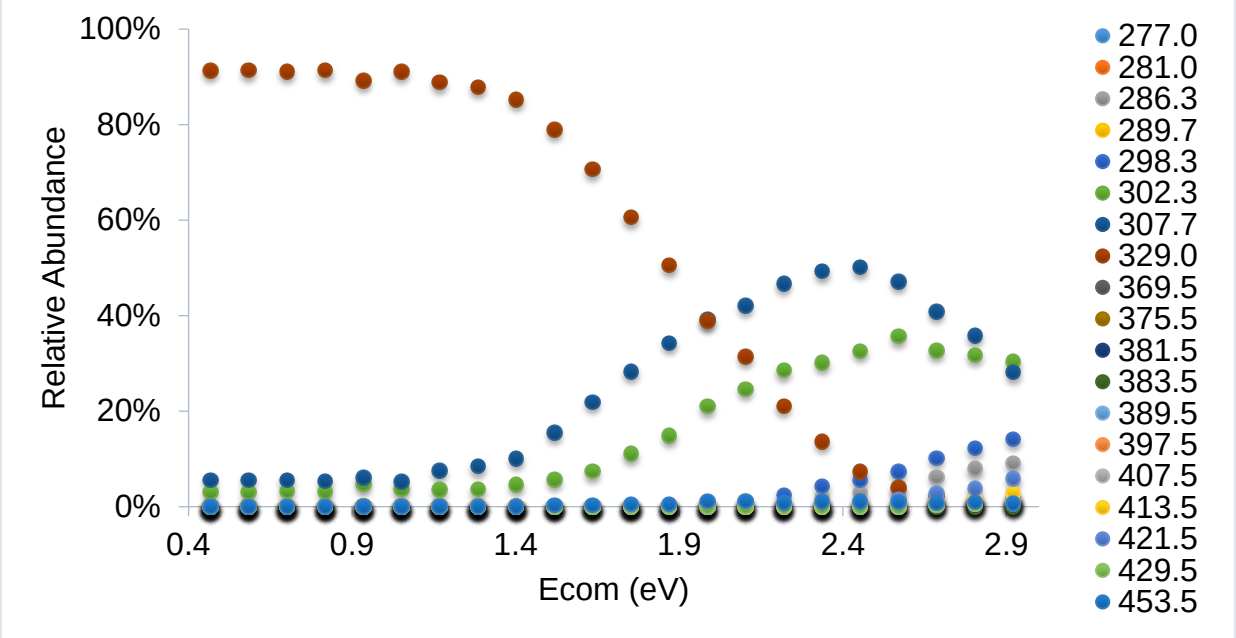

Figure A1.4 Breakdown diagram of $[Co^{III}TPPS]^{3-}$ with all the fragment ions (IMS on)

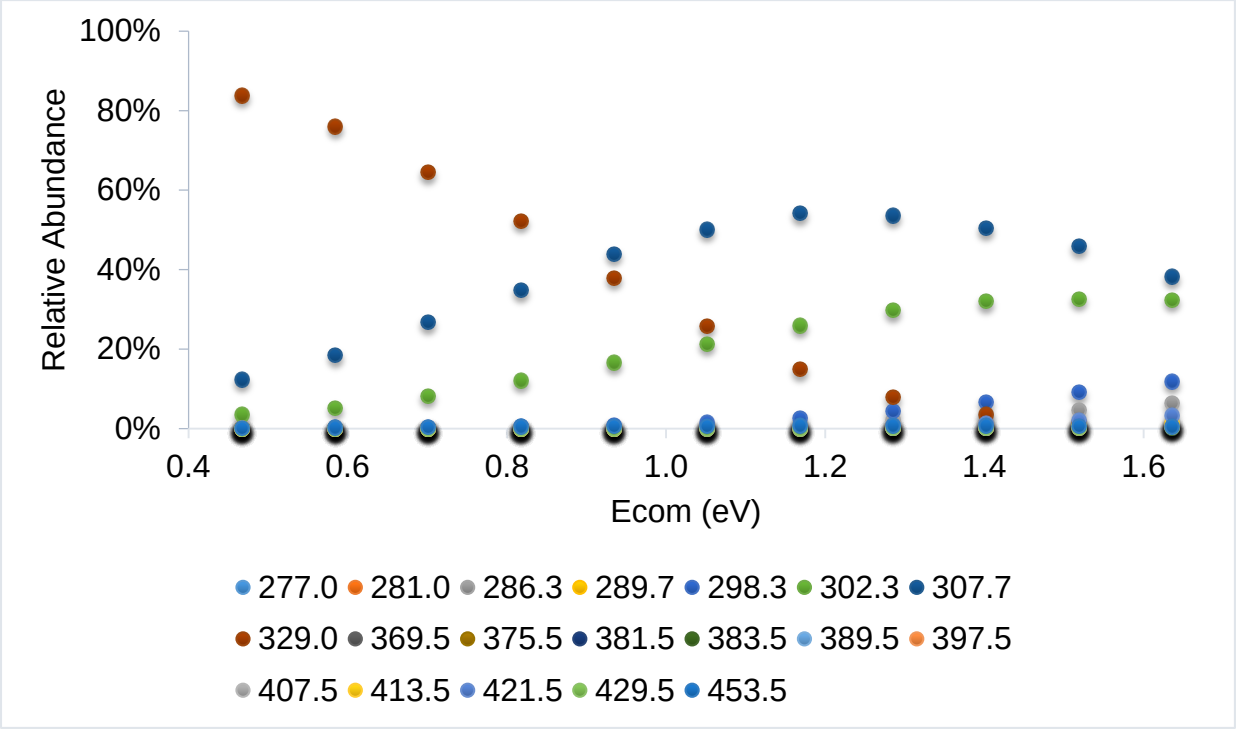

Figure A1.5 Breakdown diagram of $[Co^{III}TPPS]^{3-}$ with all the fragment ions (IMS off)

A1.3 Structure of all the fragment ions

The fragment ions mentioned in the section A1.2 can be calculated mathematically. For example, the mass spectrum shows that the fragment ion with m/z 302.3 has a -3 charge (Δm/z of adjacent peaks at m/z 302.3 is 0.33), so the mass difference between this fragment ion and the parent ion is 3 × (329.0 – 302.3) = 80.1. Considering the big porphyrin ring has four benzenesulfonate functional groups that might lose SO_3, the difference of m/z 80.1 should be a neutral SO_3, and the fragment ion m/z 302.3 should be $[Co^{III}TPPS\text{-}SO_3]^{3-}$. This result agrees with the mass spectrum isotope model of $[Co^{III}TPPS\text{-}SO_3]^{3-}$ from MassLynx (Figure A1.6). In the same manner,

structures of all the fragment ions from the $[Co^{III}TPPS]^{3-}$ dissociation were estimated. Figure A1.7 lists all of them.

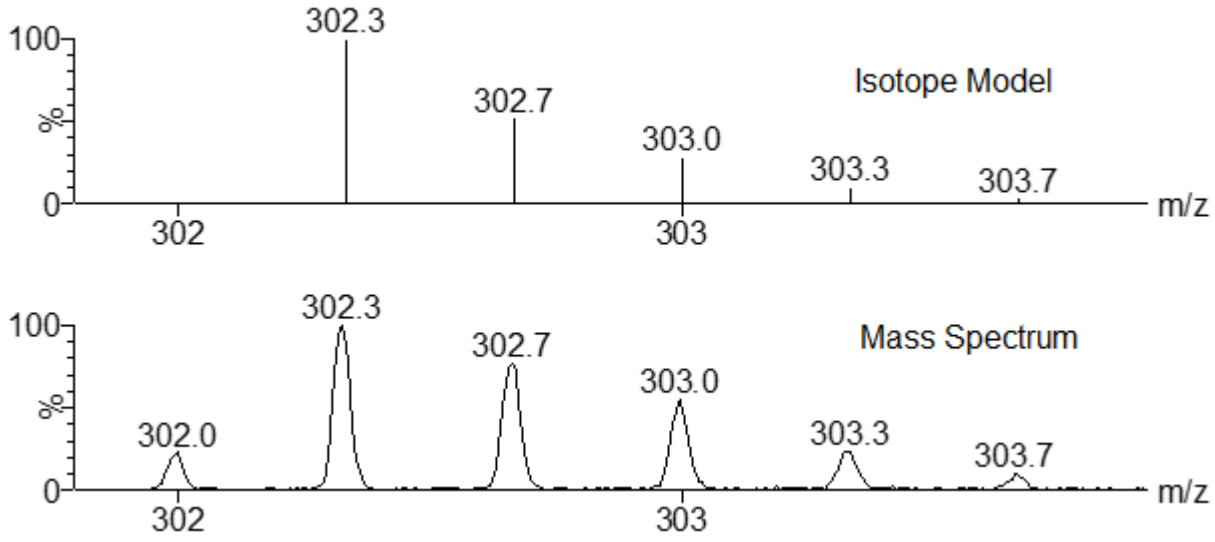

Figure A1.6 Mass spectrum of $[Co^{III}TPPS\text{-}SO_3]^{3-}$ and its isotope model

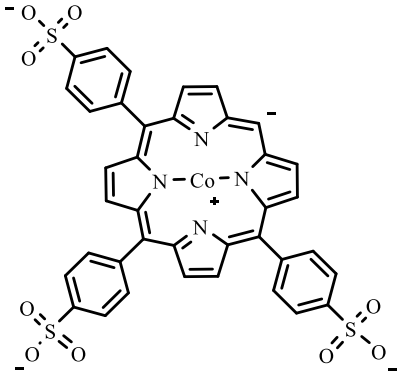

277.0: $[Co^{III}TPPS\text{-}C_6H_4SO_3]^{3-}$

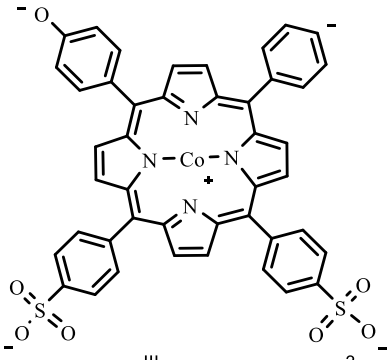

281.0: $[Co^{III}TPPS\text{-}SO_3\text{-}SO_2]^{3-}$

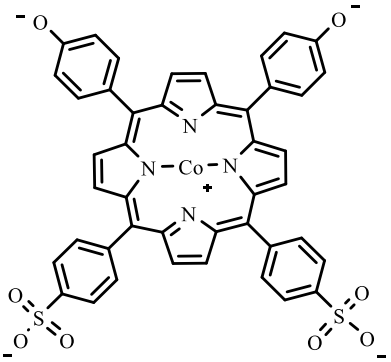

286.3: $[Co^{III}TPPS\text{-}2SO_2]^{3-}$

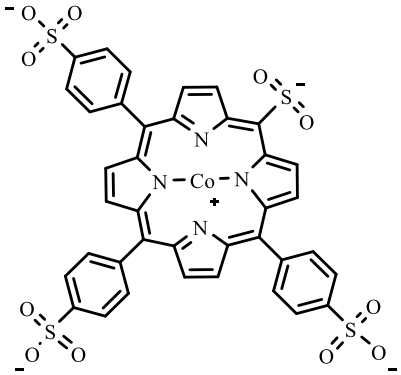

298.3: $[Co^{III}TPPS\text{-}C_6H_4O]^{3-}$

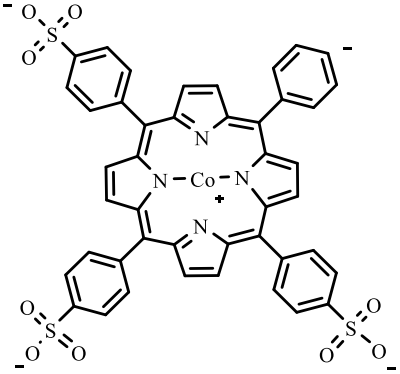

302.3: $[Co^{III}TPPS\text{-}SO_3]^{3-}$

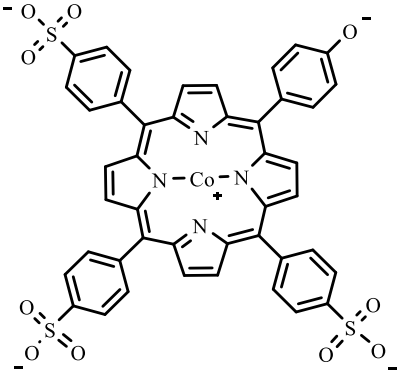

307.7: $[Co^{III}TPPS\text{-}SO_2]^{3-}$

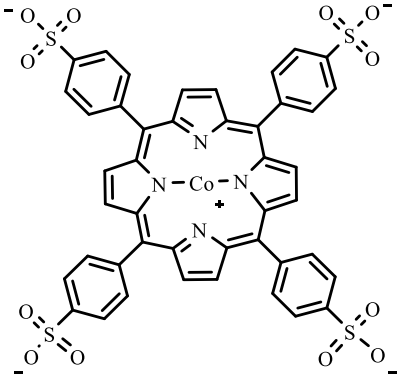

329.0: $[Co^{III}TPPS]^{3-}$

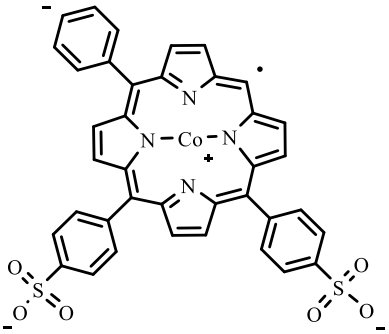

375.5: $[Co^{III}TPPS\text{-}C_6H_4SO_3\text{-}SO_3]^{2-}$

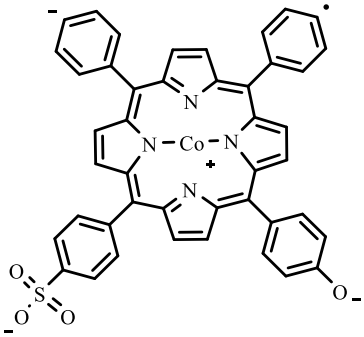

381.5: $[Co^{III}TPPS\text{-}2SO_3\text{-}SO_2]^{2-}$

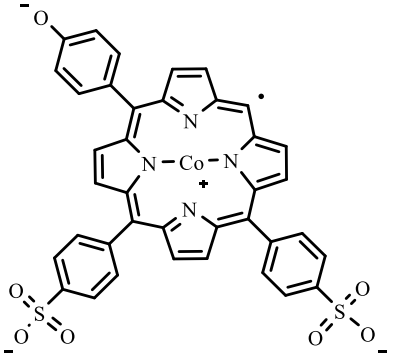

383.5: $[Co^{III}TPPS\text{-}C_6H_4SO_3\text{-}SO_2]^{2-}$

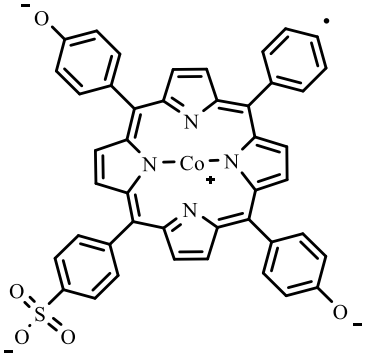

389.5: $[Co^{III}TPPS\text{-}SO_3\text{-}2SO_2]^{2-}$

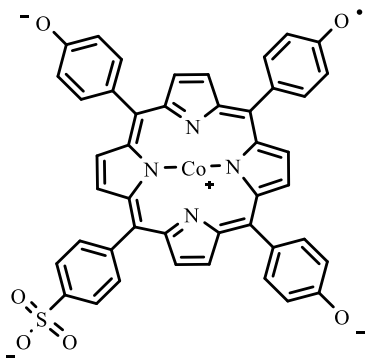

397.5: $[Co^{III}TPPS\text{-}3SO_2]^{2-}$

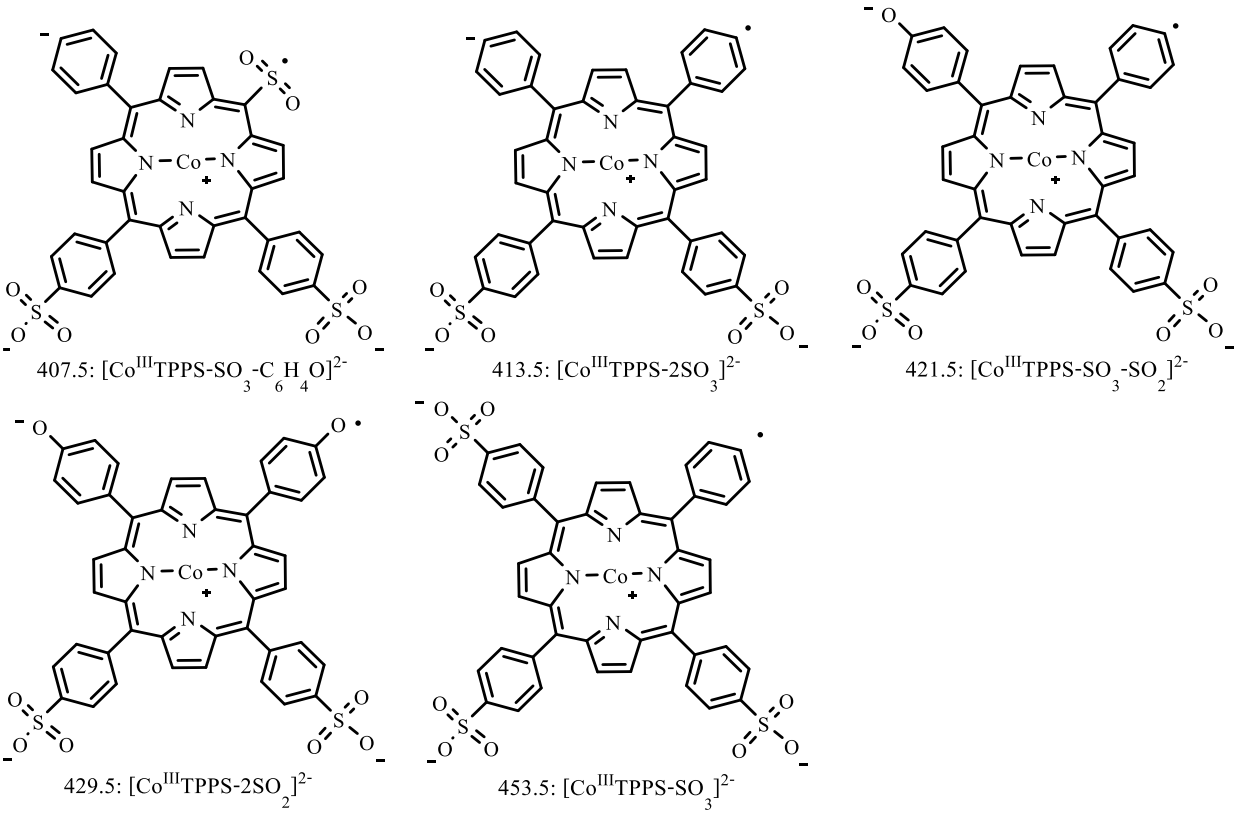

Figure A1.7 Possible structures of fragment ions from the dissociation of $[Co^{III}TPPS]^{3-}$

A1.4 In-source-CID-MS/MS and the map of the fragmentation pathways

There are 18 main fragment ions from the dissociation of $[Co^{III}TPPS]^{3-}$ as mentioned in section A1.3. However, the pathways that those fragment ions take are still not clear. Structures of these fragment ions show that all the fragment ions result from the loss of one or several neutral/negative SO_2, SO_3, and C_6H_4O. When the collision voltage is low, only fragment ions with m/z 302.3 and 307.7 appear. They are $[Co^{III}TPPS\text{-}SO_3]^{3-}$ and $[Co^{III}TPPS\text{-}SO_2]^{3-}$, respectively. This is reasonable considering that $[Co^{III}TPPS]^{3-}$ has four benzenesulfonate groups, where it can lose SO_2/SO_3 with enough energy. Also, it seems that the other fragment ions, which appear at a higher

collision voltage, may all come from the breakup of the two main fragment ions $[Co^{III}TPPS\text{-}SO_3]^{3-}$ and $[Co^{III}TPPS\text{-}SO_2]^{3-}$.

To verify this assumption, the in-source-CID-MS/MS of $[Co^{III}TPPS\text{-}SO_3]^{3-}$ and $[Co^{III}TPPS\text{-}SO_2]^{3-}$ was carried out. The in-source-CID used a high sampling cone energy of 52 V to break up the parent ion in the source. Then all the negatively charged fragment ions continued to the quadrupole, where ions with m/z 302.3 or 307.7 were selected and their CID mass spectra obtained.

Figure A1.8 and A1.9 represent the breakdown diagrams of m/z 302.3 and m/z 307.7 from collision voltage 4 V to 20 V, in which the center-of mass E_{com} is established on the x-axis (Equation 2.5 and 2.6). There are six overlapped fragment ions present in both the in-source-CID-MS/MS of m/z 302.3 and m/z 307.7. They are $[Co^{III}TPPS\text{-}C_6H_4SO_3\text{-}\ SO_3]^{2-}$, $[Co^{III}TPPS\text{-}2SO_3\text{-}SO_2]^{2-}$, $[Co^{III}TPPS\text{-}C_6H_4SO_3\text{-}\ SO_2]^{2-}$, $[Co^{III}TPPS\text{-}SO_3\text{-}2SO_2]^{2-}$, $[Co^{III}TPPS\text{-}C_6H_4O\text{-}\ SO_3]^{2-}$, and $[Co^{III}TPPS\text{-}SO_3\text{-}SO_2]^{2-}$. All of the other fragment ions, with exception of m/z 453.5, are only present in the breakdown of either m/z 302.3 or m/z 307.7. See Figure A1.10 for the dissociation pathways of $[Co^{III}TPPS]^{3-}$.

The fragment ion with m/z 453.5 is an independent channel: $[SO_3]^-$ loss from $Co^{III}TPPS]^{3-}$ directly. However, this channel is ignored because it has a pretty low relative abundance (maximum: 0.68%) compared with the other two channels, and it only appear at a high collision energy. Ignoring this channel will not influence the activation energy calculations of the other two channels.

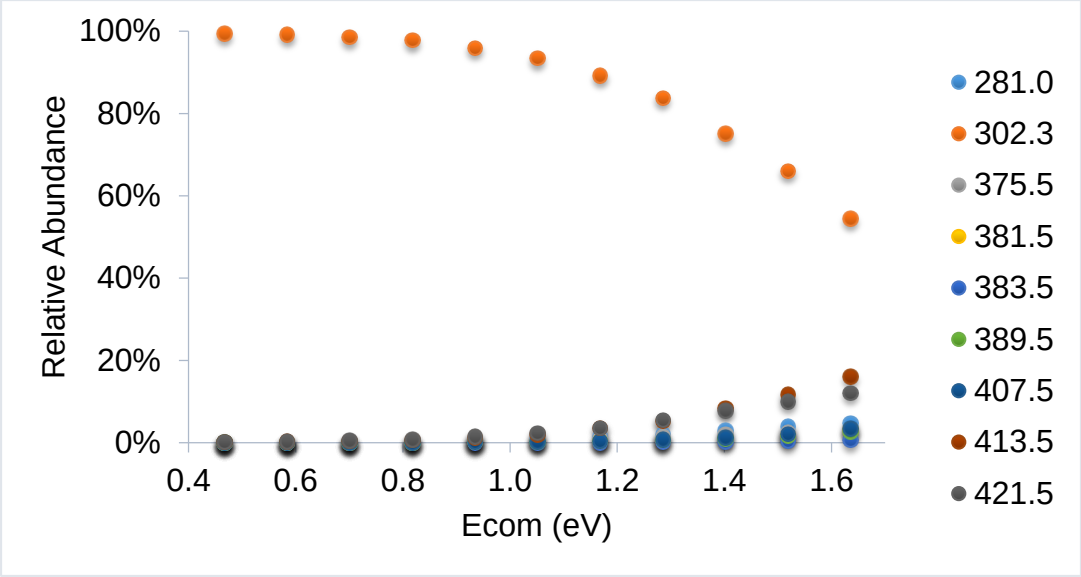

Figure A1.8 In-source-CID-MS/MS of $[Co^{III}TPPS\text{-}SO_3]^{3-}$

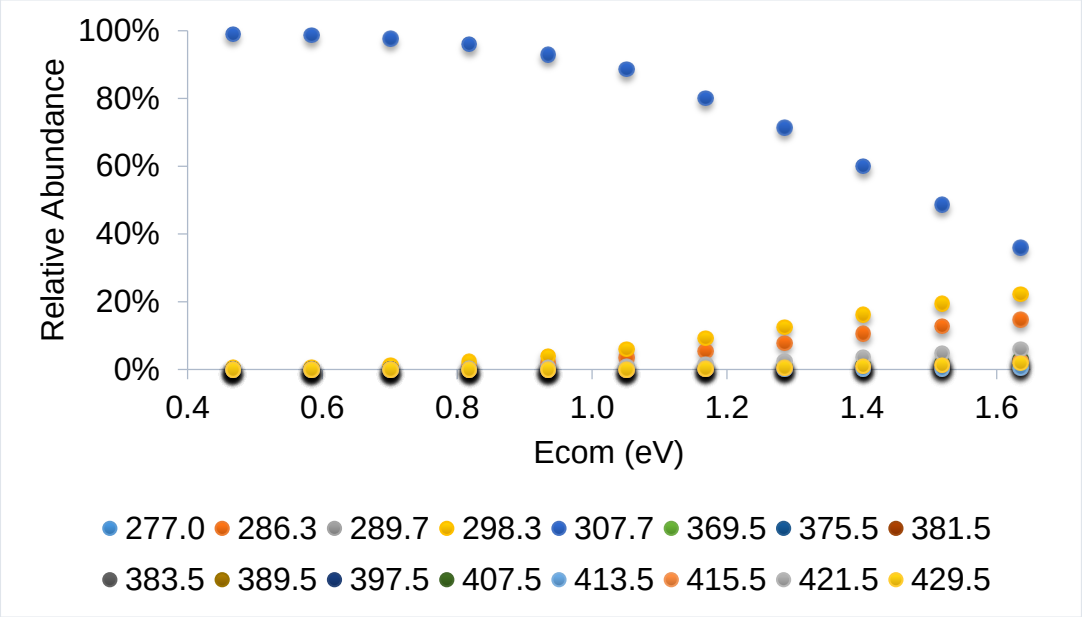

Figure A1.9 In-source-CID-MS/MS of $[Co^{III}TPPS\text{-}SO_2]^{3-c}$

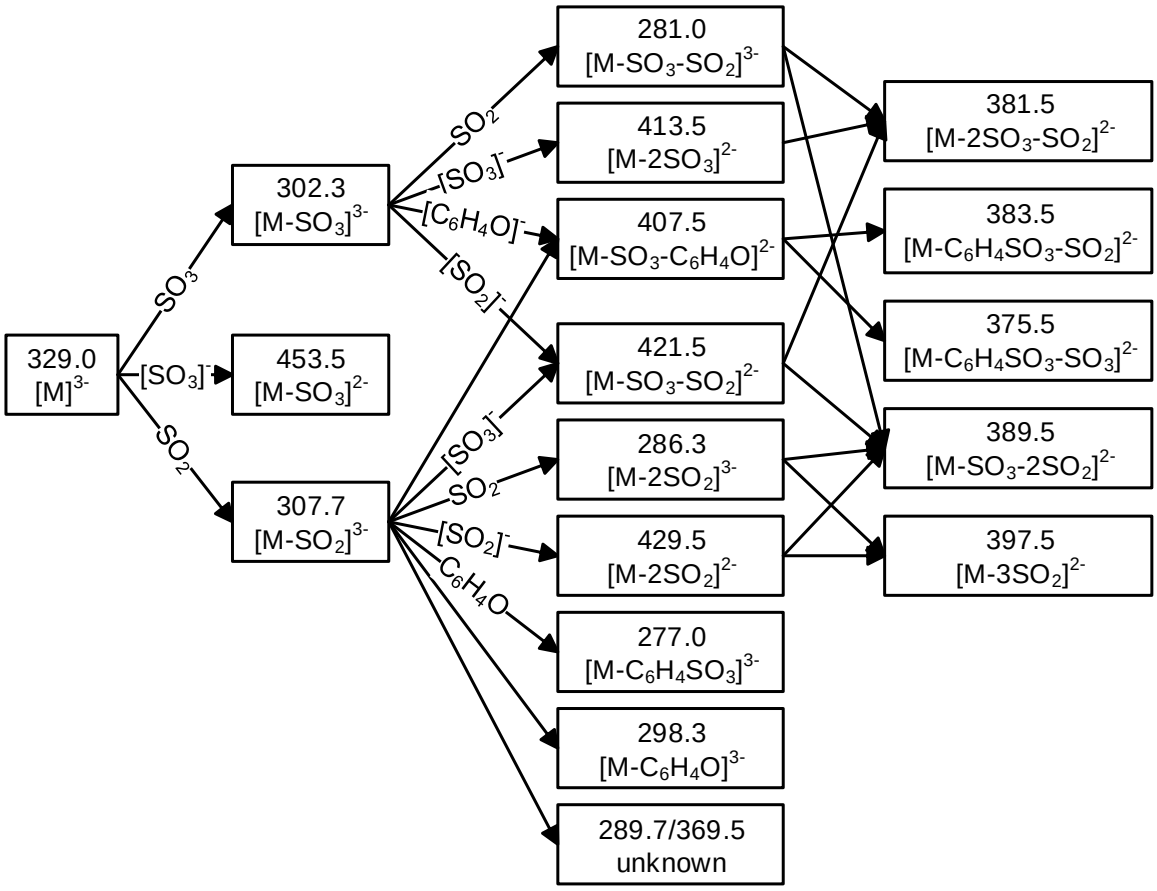

Figure A1.10 Possible dissociation pathways of $[M]^{3-}$ (where M = $Co^{III}TPPS$)

A1.5 Breakdown Diagram

The dissociation pathways of $[Co^{III}TPPS]^{3-}$ have been evaluated in section A1.4. All the fragment ions, except for $[Co^{III}TPPS\text{-}SO_3]^{2-}$, are created by these two channels: the breakdown of $[Co^{III}TPPS\text{-}SO_3]^{3-}$ and $[Co^{III}TPPS\text{-}SO_2]^{3-}$. However, the division of those six overlapped fragment ions into these two channels still remains unclear. The total relative abundance percent of all the overlapped fragment ions increase from 0 to 9.4% when increasing the collision energy with IMS on, while it is from 0 to 5.4% when the IMS is off (Figure A1.11). It might influence the RRKM calculation if those six overlapped fragment ions are just ignored. The % contributions of $[Co^{III}TPPS\text{-}SO_3]^{3-}$ to

these six overlapped fragment ions are calculated by Equation 4.1. Figure A1.12 shows the % contribution of $[Co^{III}TPPS\text{-}SO_3]^{3-}$ to those six overlapped fragment ions. The % contribution values seem to be consistent when increasing the collision voltage.

As a result, the average percentage value of each overlapped fragment ion was used to divide the overlapped fragment ions to the channels $[Co^{III}TPPS\text{-}SO_3]^{3-}$ and $[Co^{III}TPPS\text{-}SO_2]^{3-}$ for the breakdown diagram of the parent ion $[Co^{III}TPPS]^{3-}$.

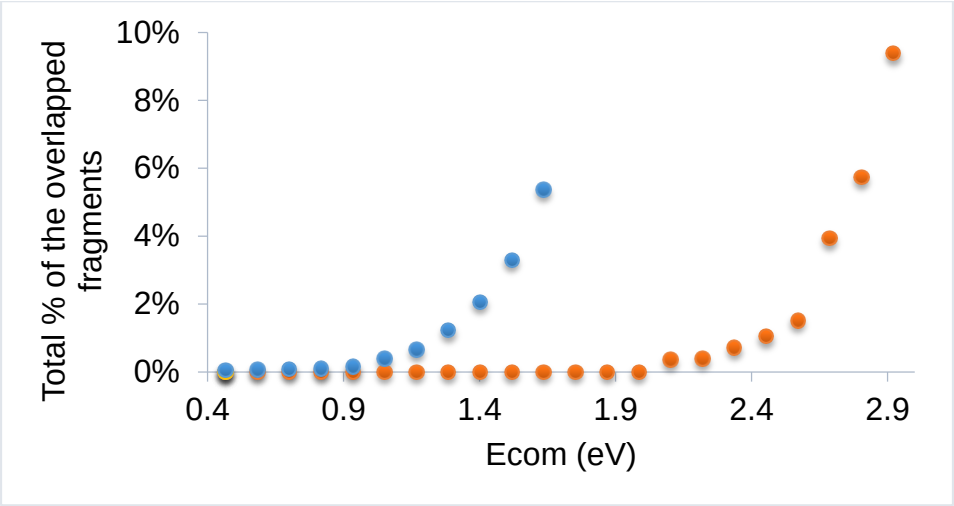

Figure A1.11 Total relative abundance of the overlapped Fragment ions from $[Co^{III}TPPS\text{-}SO_3]^{3-}$ and $[Co^{III}TPPS\text{-}SO_2]^{3-}$

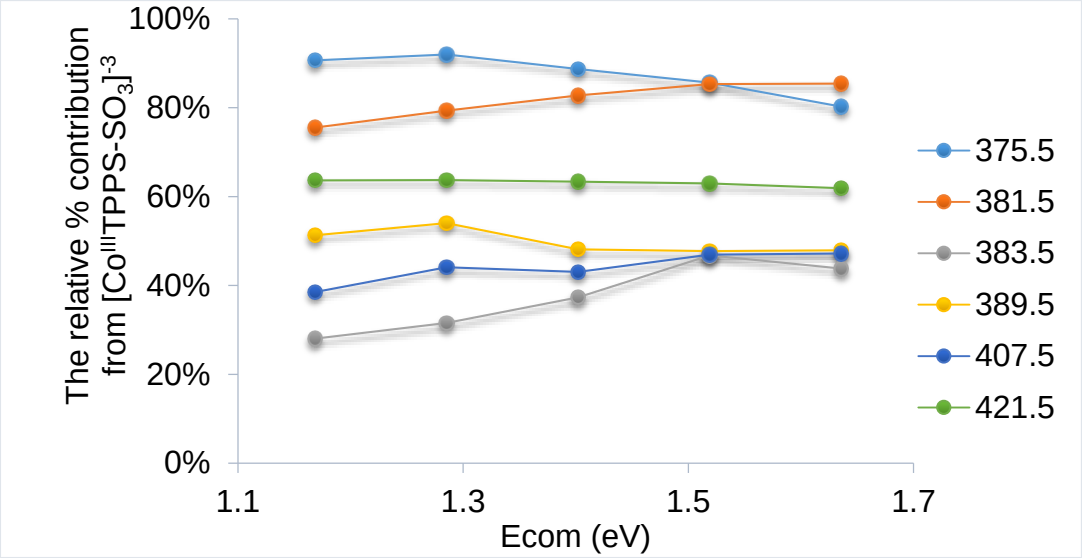

Figure A1.12 Relative abundance % contribution from $[Co^{III}TPPS\text{-}SO_3]^{3-}$ to the overlapped fragment ions

Thus, equation 4.1 was used to assign the appropriate percentage of the six overlapping channels to the two main fragment ions to produce the breakdown diagram in Figure A1.13.

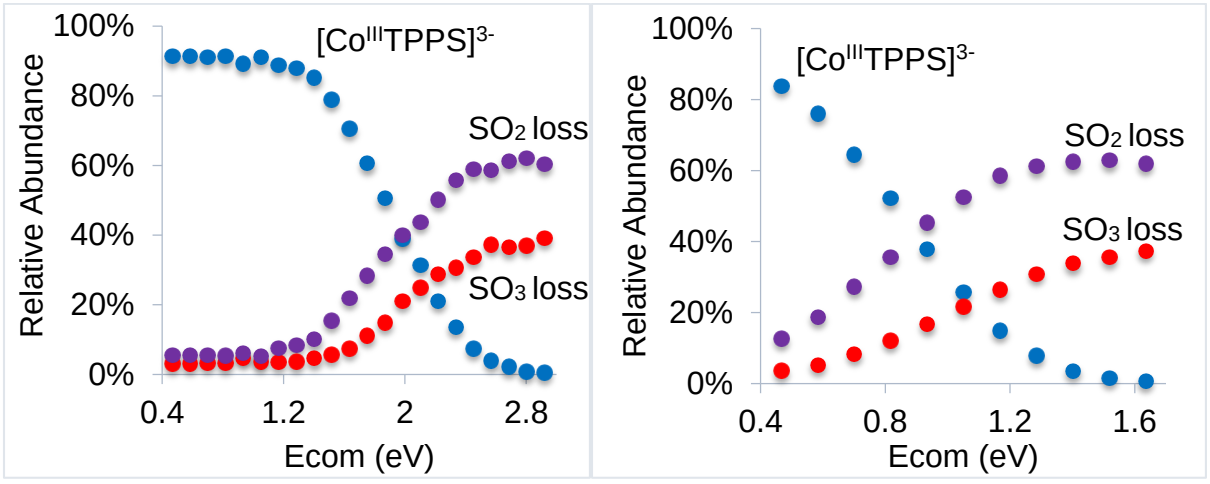

Figure A1.13 Final breakdown diagram for the dissociation of $[Co^{III}TPPS]^{3-}$. (Left: IMS on; right: IMS off)

A1.6 RRKM modeling

To understand CID mass spectra, the breakdown diagrams were modeled by RRKM theory by using the harmonic vibrational frequencies of $[Ni^{II}TPPS+H]^{3-}$ (see Table A6.1 in Appendix 6). RRKM theory estimates the theoretical breakdown diagram by altering the following four parameters: i) the activation energy E_0, ii) the first ten vibrational frequencies of the transition state, iii) the pre-collision internal temperature of the ions T_{ini}, iv) α (Equation 2.7). These four parameters were changed manually until the best-fitted theoretical breakdown diagram that matches the experimental breakdown diagram was found (See Figure A1.14, A1.15 and A1.16). Table A1.1 contains all the parameters and results of the RRKM modeling.

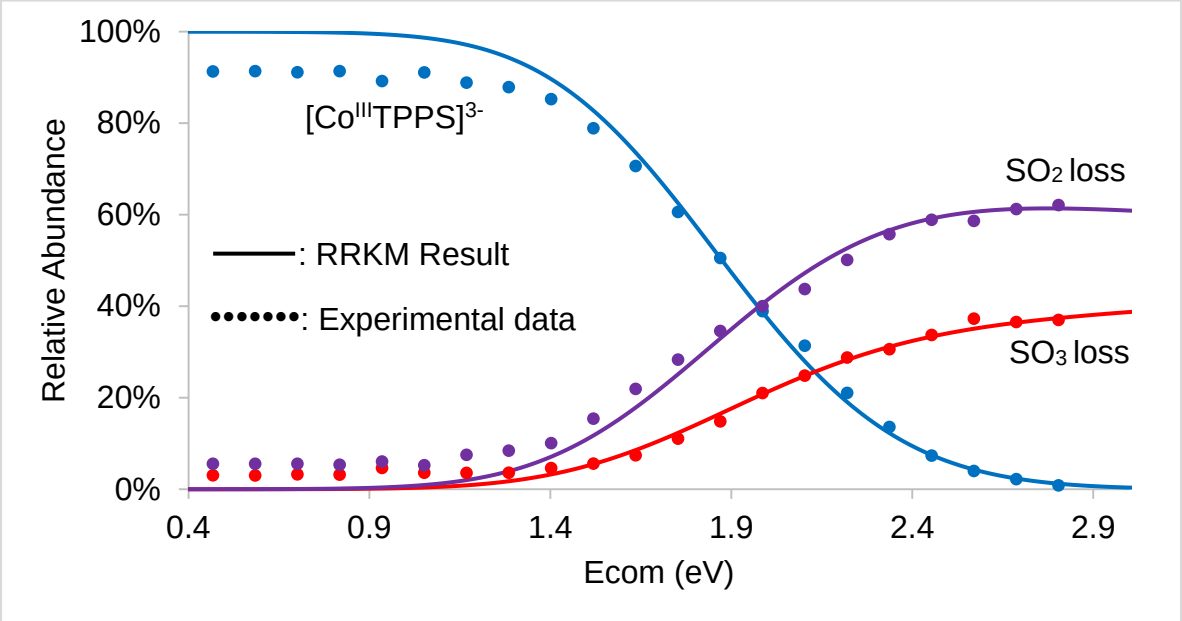

Figure A1.14 RRKM modeling results for the dissociation of $[Co^{III}TPPS]^{3-}$ with IMS on

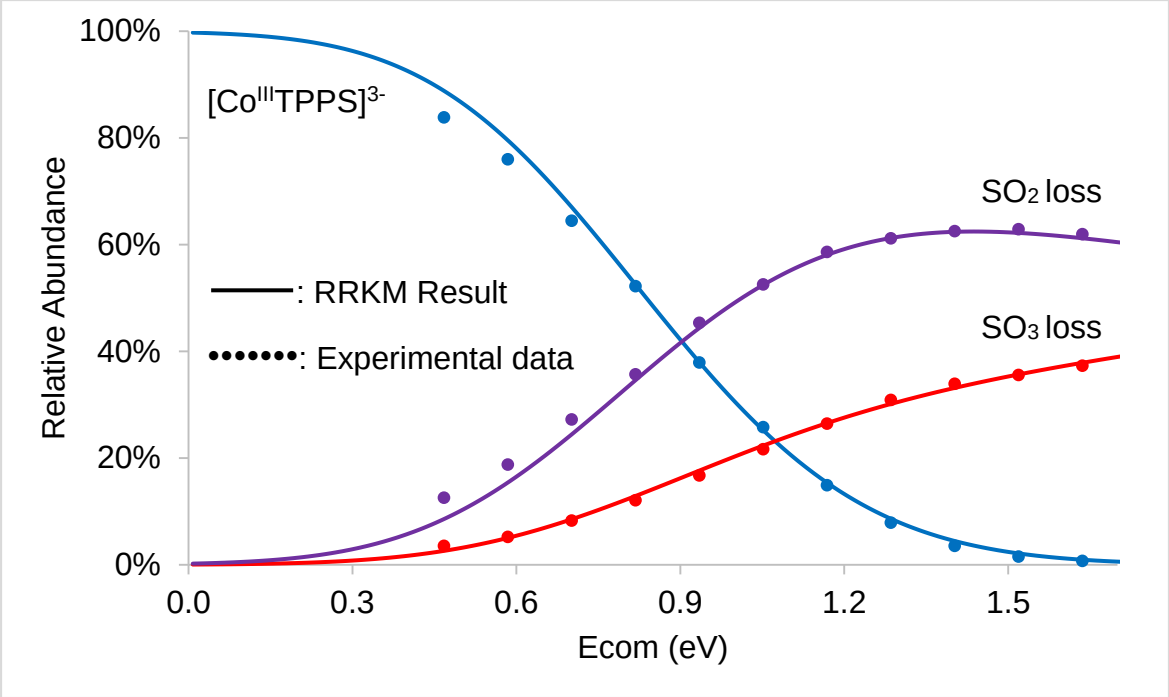

Figure A1.15 RRKM modeling results for the dissociation of $[Co^{III}TPPS]^{3-}$ with IMS off when keeping T_{ini} and α the same with Figure A1.14

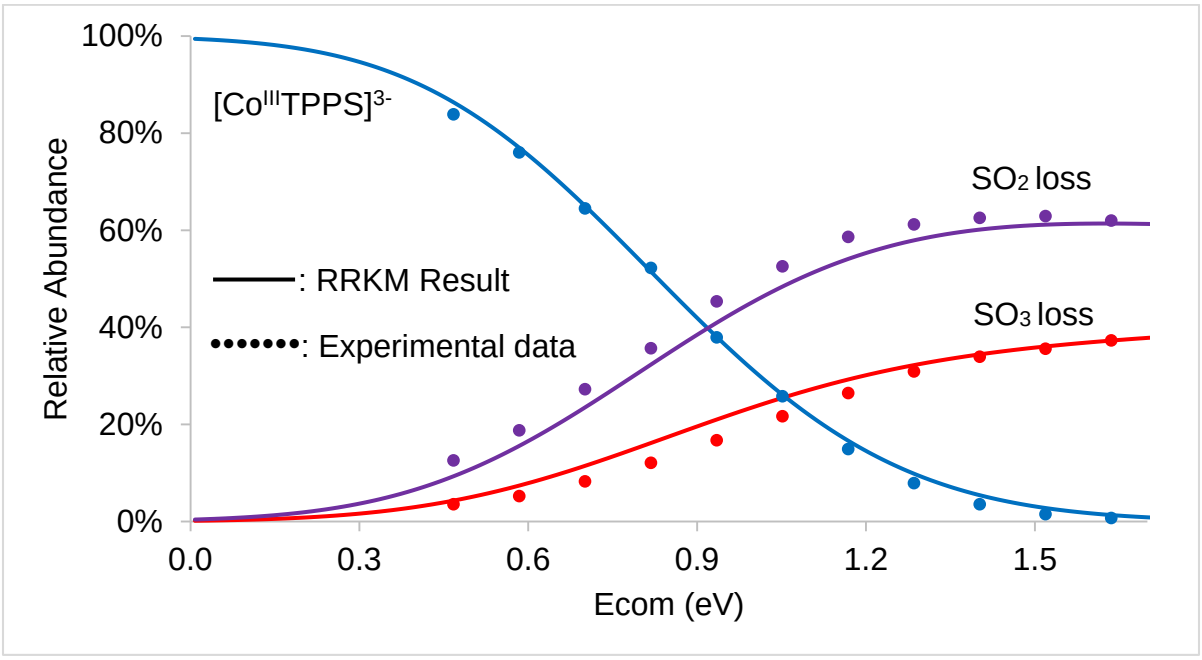

Figure A1.16 RRKM modeling results for the dissociation of $[Co^{III}TPPS]^{3-}$ with IMS off when keeping E_0 and $\Delta^{\ddagger}S$ the same with Figure A1.14

If the same RRKM parameters T_{ini} and α are used for modeling the breakdown diagrams of $[Co^{III}TPPS]^{3-}$ under different experimental conditions (IMS on and off), activation energy (E_0) and entropy of activation ($\Delta^{\ddagger}S$) will both be different (Table A1.1). However, E_0 and $\Delta^{\ddagger}S$ should be constants for a reaction. Therefore, T_{ini} and α should be changed in order to model a reaction under different experimental conditions. Theoretically, RRKM theory can model a breakdown diagram with any T_{ini} and α in a certain range, but results in different activation energies and entropies. The problem is that T_{ini} and α are unknown.

However, the focus of this study is on the relative activation energies between the reactions that lose SO_3 and lose SO_2 from the parent ion $[Co^{III}TPPS]^{3-}$. As shown in Table A1.1, SO_3 loss always requires a higher activation energy than SO_2 loss. This is also verified by fitting the breakdown diagram with many random T_{ini} and α. As a result, the relative energy of a reaction modeled by RRKM is still trustful even T_{ini} and α are unknown. See Chapter 6 for the discussion of the meaning of these activation energies.

Table A1.1 RKKM modeling results for the dissociation of $[Co^{III}TPPS]^{3-}$

Parent Ion	**IMS**	**RRKM Parameters**		**Channel**	**E_0** (eV)	**$\Delta^{\ddagger}S$** ($J.mol^{-1}\cdot K^{-1}$)
		T_{ini} (K)	α ($K\cdot eV^{-1}$)			
$[Co^{III}TPPS]^{3-}$	On	400	150	SO_3 loss	1.40 ± 0.02	2 ± 5
				SO_2 loss	1.33 ± 0.02	-3 ± 5
$[Co^{III}TPPS]^{3-}$	Off	540	170	SO_3 loss	1.40 ± 0.02	2 ± 5
				SO_2 loss	1.33 ± 0.02	-3 ± 5
$[Co^{III}TPPS]^{3-}$	Off	400	150	SO_3 loss	1.10 ± 0.02	9 ± 5
				SO_2 loss	0.98 ± 0.02	-7 ± 5

Appendix 2. RRKM modeling for the dissociation of $[Mn^{III}TPPS]^{3-}$

A2.1 ESI-MS of $Mn^{III}TPPS$

The mass spectrum of $Mn^{III}TPPS$ (Figure A2.1) shows there are different charge states of $Mn^{III}TPPS$ in methanol solution, including $[Mn^{III}TPPS]^{3-}$ and $[Mn^{III}TPPS+H]^{2-}$. In this chapter, the primary focus is to study $[Mn^{III}TPPS]^{3-}$. The peak m/z 327.7 is only monomer instead of a mix of monomer $[Mn^{III}TPPS]^{3-}$ and dimer $[(Mn^{III}TPPS)_2]^{6-}$. This was verified by turning on the ion mobility spectrometry (IMS), which shows no extra ions could be separated.

The mass spectrum of $[Mn^{III}TPPS]^{3-}$ (Figure A2.2) matches its theoretical isotope model, so it proves to be a good reactant for ESI-MS/MS experiment.

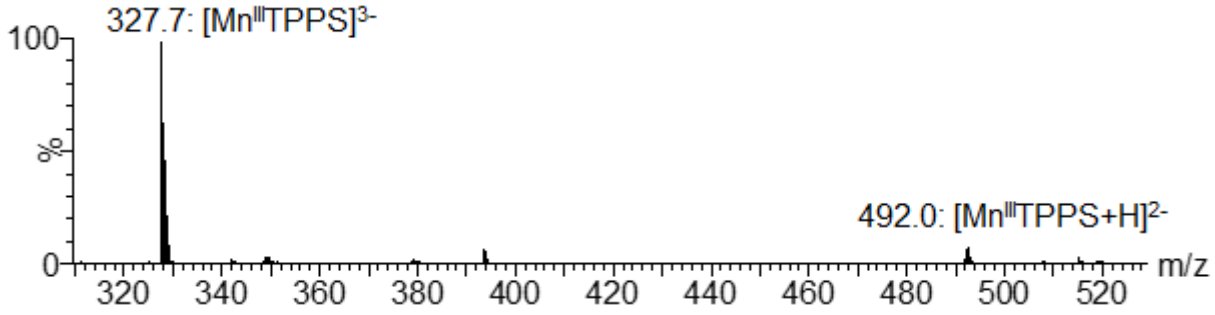

Figure A2.1 Mass spectrum of $Mn^{III}TPPS$

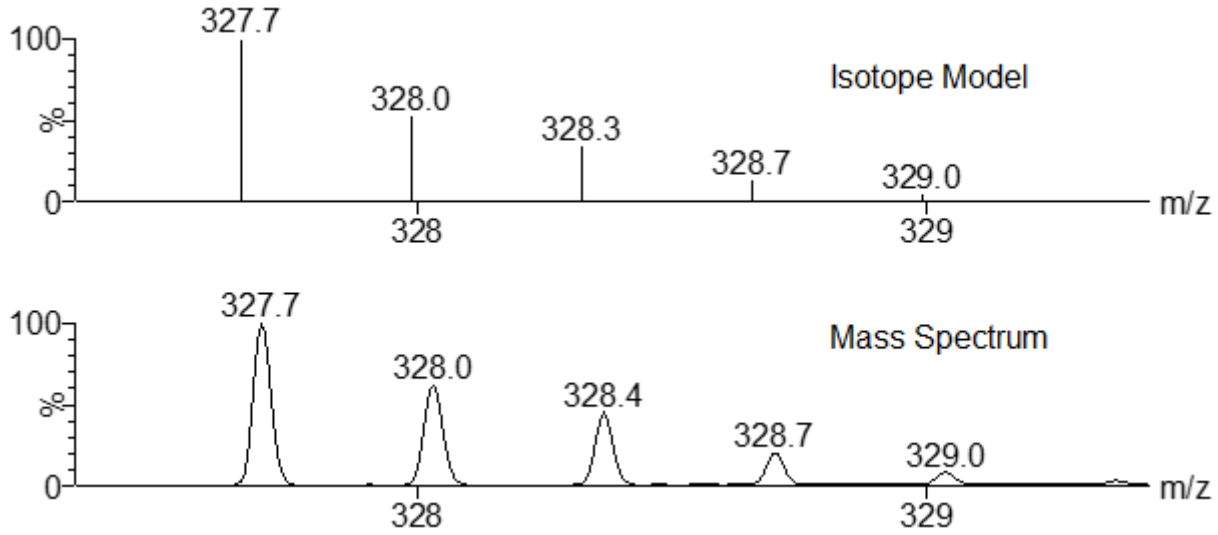

Figure A2.2 Mass spectrum of $[Mn^{III}TPPS]^{3-}$ and its isotope model

A2.2 ESI-MSMS of $[Mn^{III}TPPS]^{3-}$

The CID of $[Mn^{III}TPPS]^{3-}$ was selected at m/z 327.7 with the collision voltage ranging from 4 V to 42 V. Increasing the collision voltage decreases the abundance of the parent ion $[Mn^{III}TPPS]^{3-}$ to the point at which it disappears entirely and only fragment ions are observed (Figure A2.3). At low collision energy, fragment ions are only m/z 301.0 and 306.3, but at higher energies, more fragment ions are formed. The lower half of Figure A2.3 contains all the main fragment ions resulting from the dissociation of $[Mn^{III}TPPS]^{3-}$. The m/z of those fragment ions are 275.6, 279.3, 285.0, 288.3, 297.0, 301.0, 306.3, 355.5, 363.5, 367.5, 373.5, 379.0, 381.5, 387.5, 395.5, 405.5, 411.5, 419.5, 427.5, and 451.5.

Figure A2.4 is the breakdown diagram of $[Mn^{III}TPPS]^{3-}$ with all the main fragment ions. They are plotted as a function of center-of-mass collision energy (E_{com}), which is a

fraction of the laboratory kinetic energy (E_{lab}) (Equation 2.6). E_{lab} equals the collision voltage V_{lab} multiplied by the charge state of $[Mn^{III}TPPS]^{3-}$ (Equation 2.5).

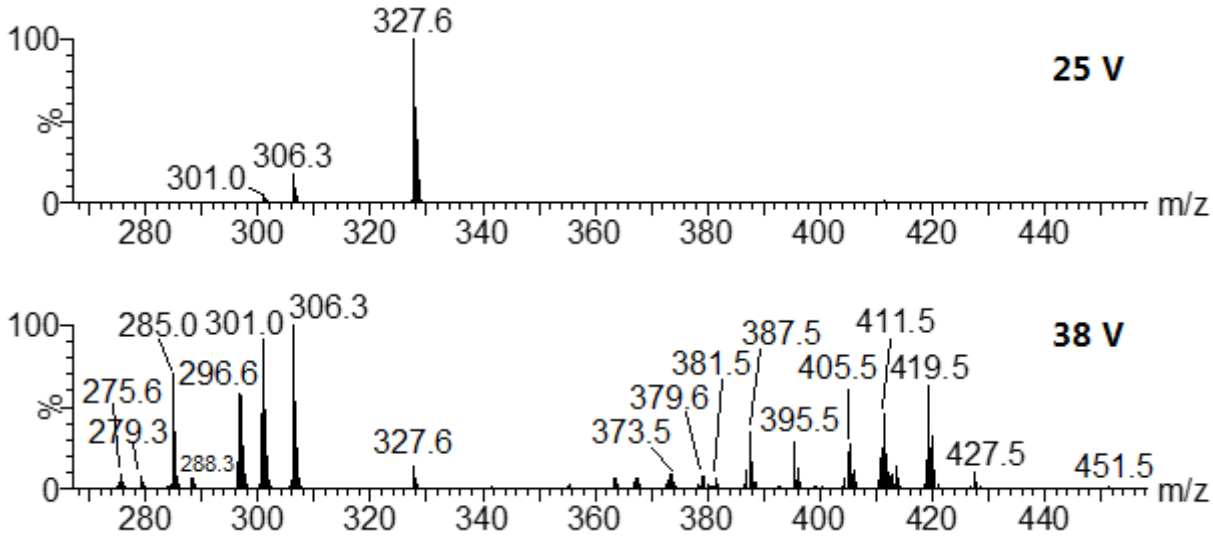

Figure A2.3 CID mass spectra of $[Mn^{III}TPPS]^{3-}$ at different collision voltages

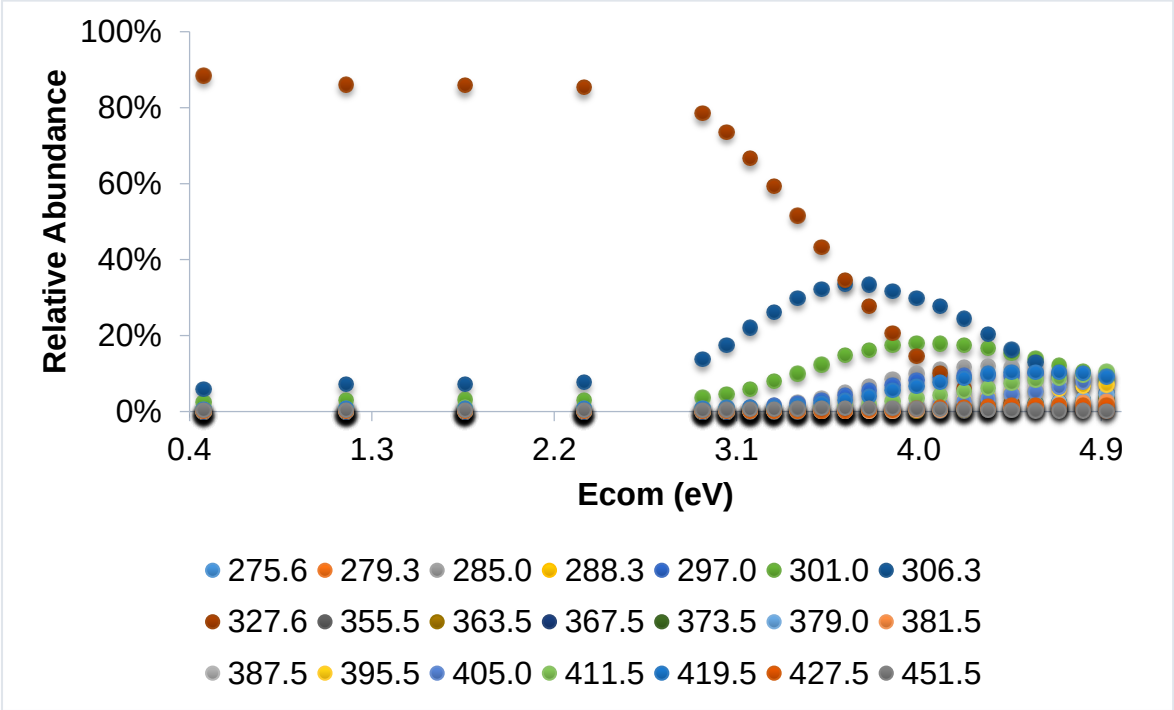

Figure A2.4 Breakdown diagram of $[Mn^{III}TPPS]^{3-}$ with all the fragment ions

A2.3 Structure of all the fragment ions

The fragment ions mentioned in the section A2.2 can be calculated mathematically. For example, the mass spectrum shows that the fragment ion with m/z 301.0 has a -3 charge (Δm/z of adjacent peaks at m/z 301.0 is 0.33), so the mass difference of this fragment ion and the parent ion is 3 × (327.6 – 301.0) = 79.8. Considering the big porphyrin ring has four benzenesulfonate functional groups that might lose SO_3, the difference of m/z 80.1 should be a neutral SO_3, and the fragment ion m/z 301.0 should be $[Mn^{III}TPPS\text{-}SO_3]^{3-}$. This result agrees with the mass spectrum isotope model of $[Mn^{III}TPPS\text{-}SO_3]^{3-}$ from MassLynx (Figure A2.5). In the same manner, structures of all the fragment ions from the $[Mn^{III}TPPS]^{3-}$ dissociation were estimated. Figure A2.6 lists all of them.

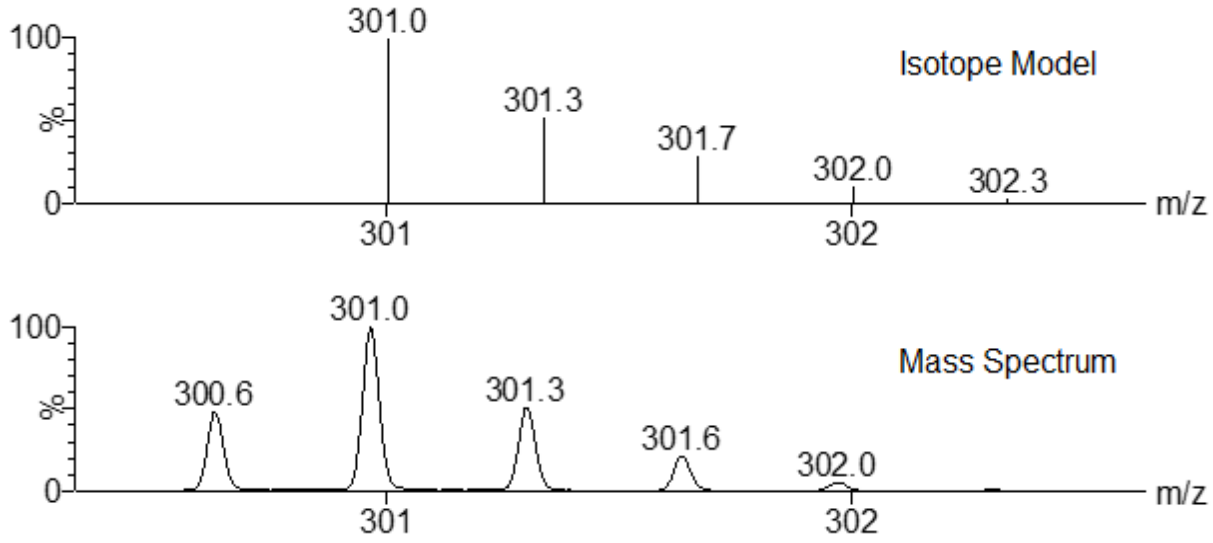

Figure A2.5 Mass spectrum of $[Mn^{III}TPPS\text{-}SO_3]^{3-}$ and its isotope model

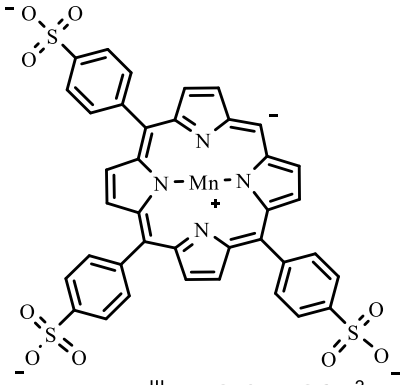

275.7: $[Mn^{III}TPPS\text{-}C_6H_4SO_3]^{3-}$

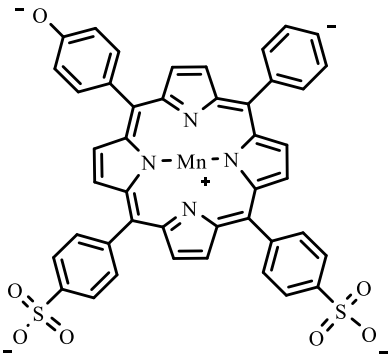

279.7: $[Mn^{III}TPPS\text{-}SO_3\text{-}SO_2]^{3-}$

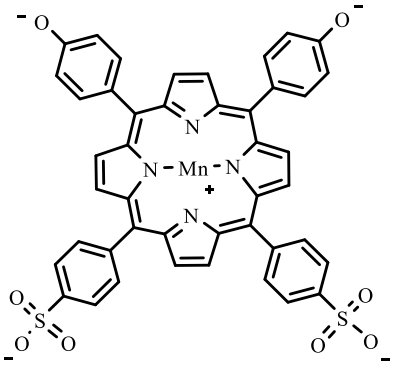

285.0: $[Mn^{III}TPPS\text{-}2SO_2]^{3-}$

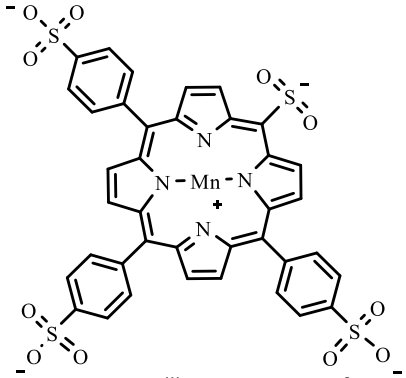

297.0: $[Mn^{III}TPPS\text{-}C_6H_4O]^{3-}$

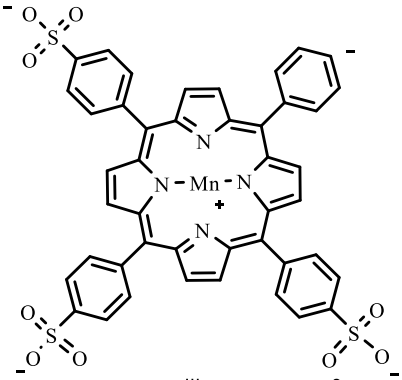

301.0: $[Mn^{III}TPPS\text{-}SO_3]^{3-}$

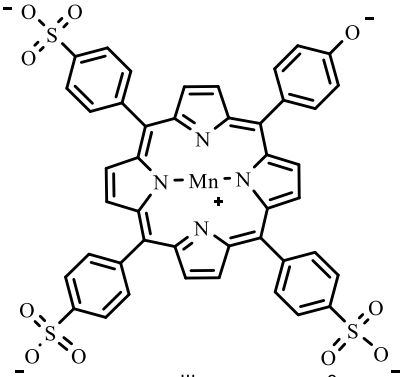

306.3: $[Mn^{III}TPPS\text{-}SO_2]^{3-}$

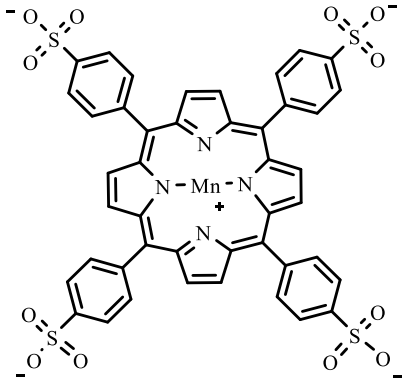

327.7: $[Mn^{III}TPPS]^{3-}$

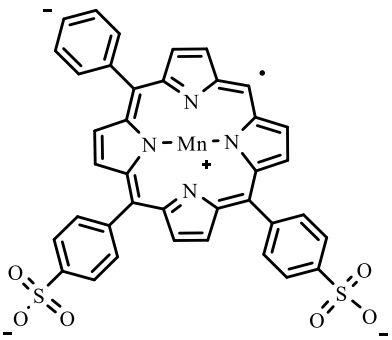

373.5: $[Mn^{III}TPPS\text{-}C_6H_4SO_3\text{-}SO_3]^{2-}$

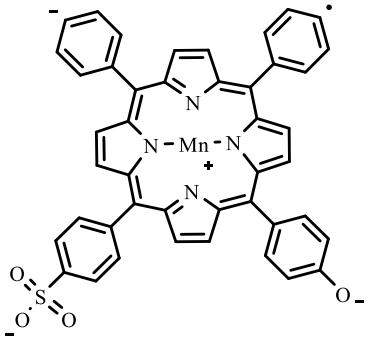

379.6: $[Mn^{III}TPPS\text{-}2SO_3\text{-}SO_2]^{2-}$

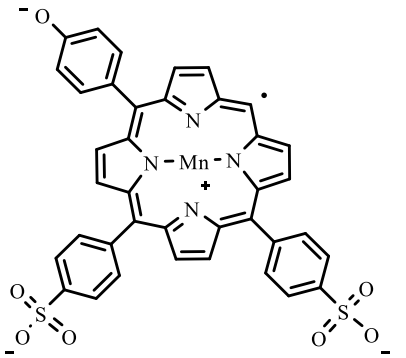

381.5: $[Mn^{III}TPPS\text{-}C_6H_4SO_3\text{-}SO_2]^{2-}$

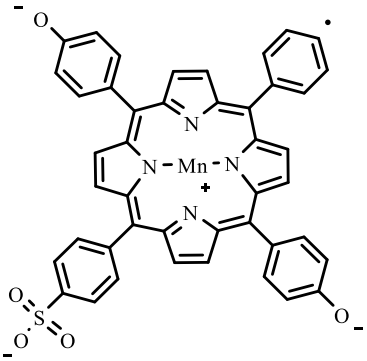

387.5: $[Mn^{III}TPPS\text{-}SO_3\text{-}2SO_2]^{2-}$

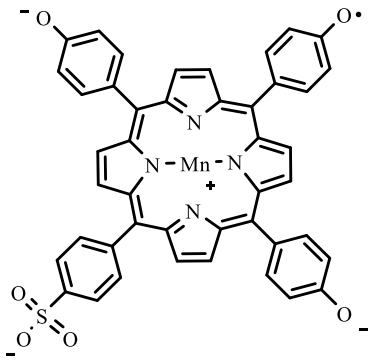

395.5: $[Mn^{III}TPPS\text{-}3SO_2]^{2-}$

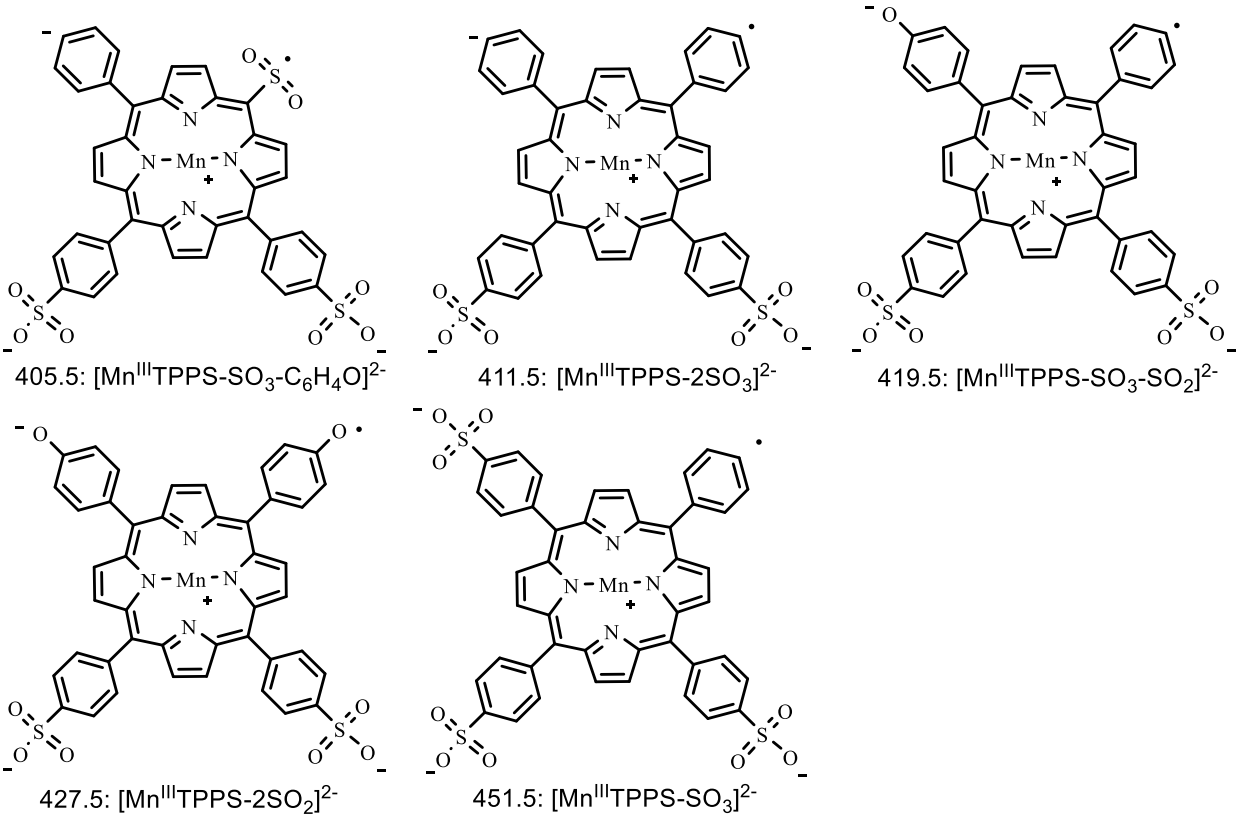

Figure A2.6 Possible structures of fragment ions from the dissociation of [Mn^{III}TPPS]$^{3-}$

A2.4 In-source-CID-MS/MS and the map of the fragmentation pathways

There are 20 main fragment ions from the dissociation of [Mn^{III}TPPS]$^{3-}$ as mentioned in section A2.3. However, the pathways that those fragment ions take are still not clear. Structures of these fragment ions show that all the fragment ions result from the loss of one or several neutral/negative SO_2, SO_3, and C_6H_4O. When the collision voltage is low, only fragment ions with m/z 301.0 and m/z 306.3 appear. They are [Mn^{III}TPPS-SO$_3$]$^{3-}$ and [Mn^{III}TPPS-SO$_2$]$^{3-}$, respectively. This is reasonable considering that [Mn^{III}TPPS]$^{3-}$ has four benzenesulfonate groups, where it can lose SO_2/SO_3 with enough energy. Also, it seems that the other fragment ions, which appear

at a higher collision voltage, may all come from the breakup of the two main fragment ions $[Mn^{III}TPPS\text{-}SO_3]^{3-}$ and $[Mn^{III}TPPS\text{-}SO_2]^{3-}$.

To verify this assumption, the in-source-CID-MS/MS of $[Mn^{III}TPPS\text{-}SO_3]^{3-}$ and $[Mn^{III}TPPS\text{-}SO_2]^{3-}$ was carried out. The in-source-CID used a high sampling cone energy of 65 V to break up the parent ion in the source. Then all the negatively charged fragment ions continued to the quadrupole, where m/z 301.0 or 306.3 was selected and their CID mass spectra obtained.

Figure A2.7 and A2.8 represent the breakdown diagrams of m/z 301.0 and 306.3 from collision voltage 4 V to 20 V, in which the center-of mass $\mathrm{E_{com}}$ is established on the x-axis (Equation 2.5 and 2.6). There are five overlapped fragment ions present in both the in-source-CID-MS/MS of m/z 301.0 and m/z 306.3. They are m/z 355.5 (unknown), $[Mn^{III}TPPS\text{-}C_6H_4SO_3\text{-}SO_3]^{2-}$, $[Mn^{III}TPPS\text{-}SO_3\text{-}2SO_2]^{2-}$, $[Mn^{III}TPPS\text{-}C_6H_4O\text{-}SO_3]^{2-}$, and $[Mn^{III}TPPS\text{-}SO_3\text{-}SO_2]^{2-}$. All of the other fragment ions, with exception of m/z 451.5, are only present in the breakdown of either m/z 301.0 or m/z 306.3. See Figure A2.9 for the dissociation pathways of $[Mn^{III}TPPS]^{3-}$.

The fragment ion with m/z 451.5 is an independent channel: $[SO_3]^-$ loss from $[Mn^{III}TPPS]^{3-}$ directly. However, this channel is ignored because it has a pretty low relative abundance (maximum 0.9%) compared with the other two channels, and it only appears at a high collision energy. Ignoring this channel will not influence the activation energy calculations of the other two channels.

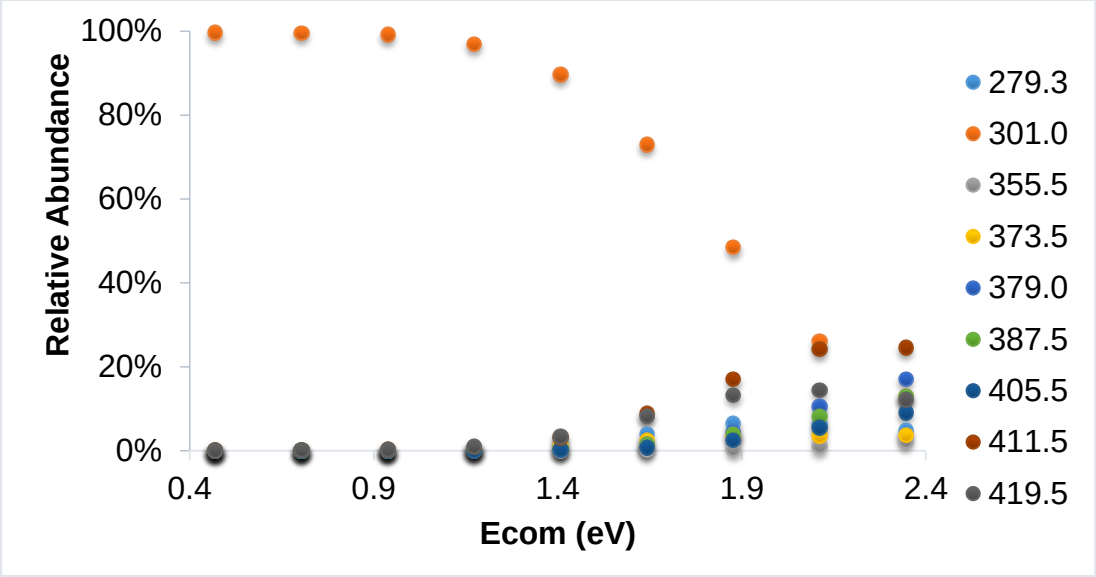

Figure A2.7 In-source-CID-MS/MS of $[Mn^{III}TPPS\text{-}SO_3]^{3-}$

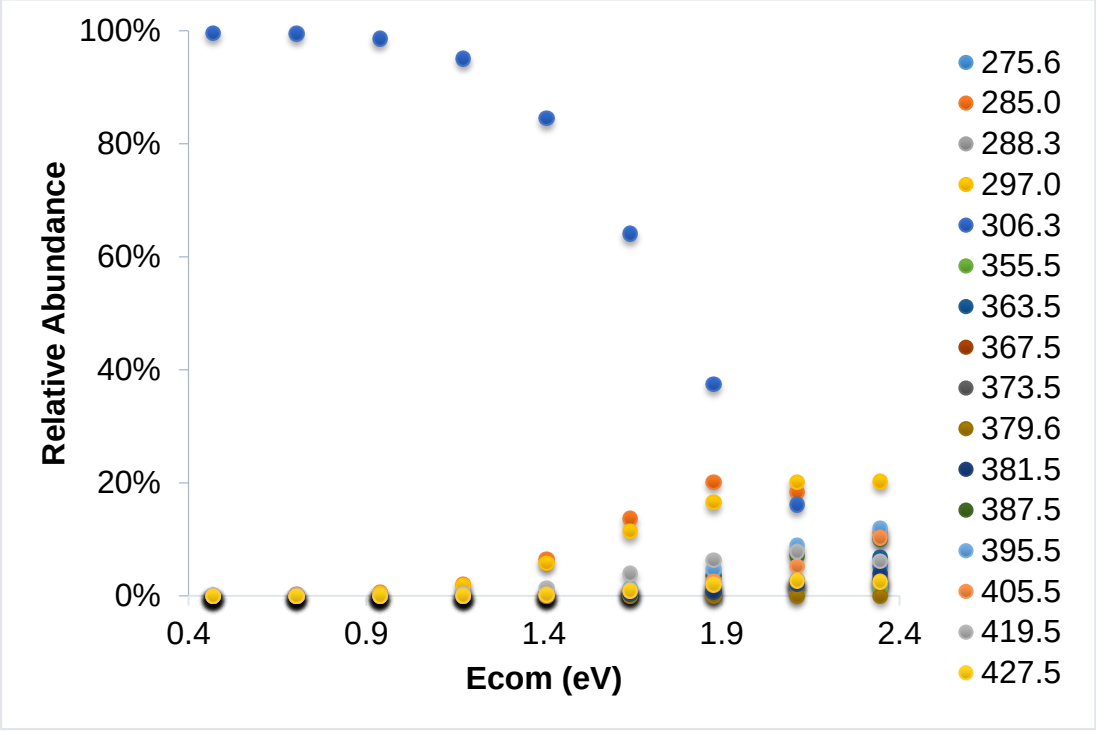

Figure A2.8 In-source-CID-MS/MS of $[Mn^{III}TPPS\text{-}SO_2]^{3-}$.

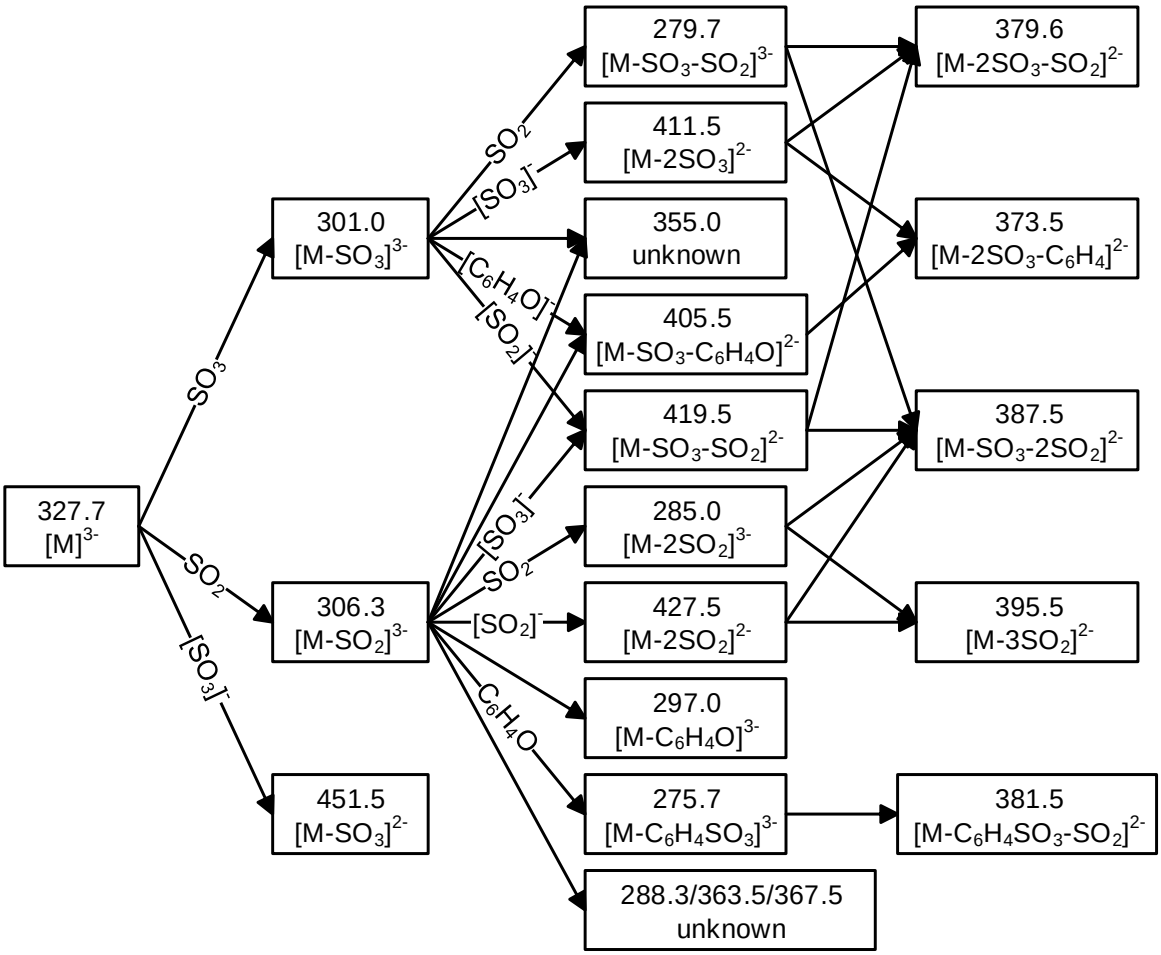

Figure A2.9 Possible dissociation pathways of $[M]^{3-}$ (where M = $Mn^{III}TPPS$). All the m/z of ions are using theoretical values from Figure A2.6, so some of them are a little different from the experimental m/z.

A2.5 Breakdown Diagram

The dissociation pathways of $[Mn^{III}TPPS]^{3-}$ have been evaluated in section A2.4. All the fragment ions, except for $[Mn^{III}TPPS\text{-}SO_3]^{2-}$, are created by these two channels: the breakdown of $[Mn^{III}TPPS\text{-}SO_3]^{3-}$ and $[Mn^{III}TPPS\text{-}SO_2]^{3-}$. However, except that m/z 379.6 was almost 100% from $[Mn^{III}TPPS\text{-}SO_3]^{3-}$, the division of other five overlapped fragment ions into these two channels still remains unclear. The total relative

abundance percent of all the overlapped fragment ions increase from 0 to 33.1% when increasing the collision energy (Figure A2.10), which is too significant to ignore. The contribution of $[Mn^{III}TPPS\text{-}SO_3]^{3-}$ to those five overlapped fragment ions are calculated by Equation 4.1. Figure A2.11 shows the results of the % contribution of $[Mn^{III}TPPS\text{-}SO_3]^{3-}$ to those five overlapped fragment ions, which seem to be consistent when increasing the collision voltage, with exception of m/z 373.5. The fragment ion m/z 373.5 can be ignored because it has a maximum relative abundance of 3.5%.

As a result, the average percentage value of each overlapped fragment ion was used to divide the overlapped fragment ions to the channels $[Mn^{III}TPPS\text{-}SO_3]^{3-}$ and $[Mn^{III}TPPS\text{-}SO_2]^{3-}$ for the breakdown diagram of the parent ion $[Mn^{III}TPPS]^{3-}$.

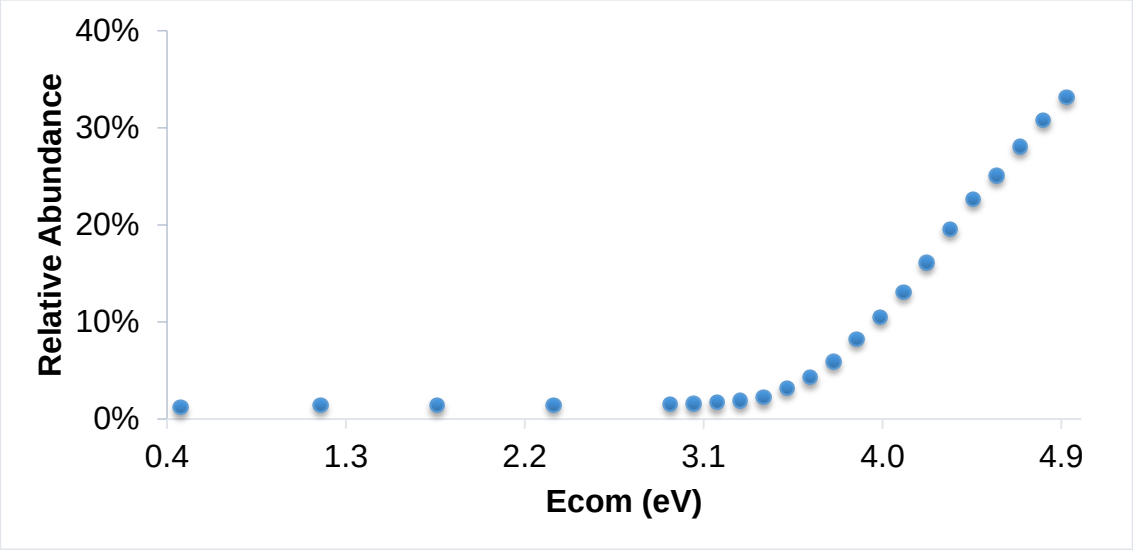

Figure A2.10 Total relative abundance of the overlapped fragment ions from $[Mn^{III}TPPS\text{-}SO_3]^{3-}$ and $[Mn^{III}TPPS\text{-}SO_2]^{3-}$

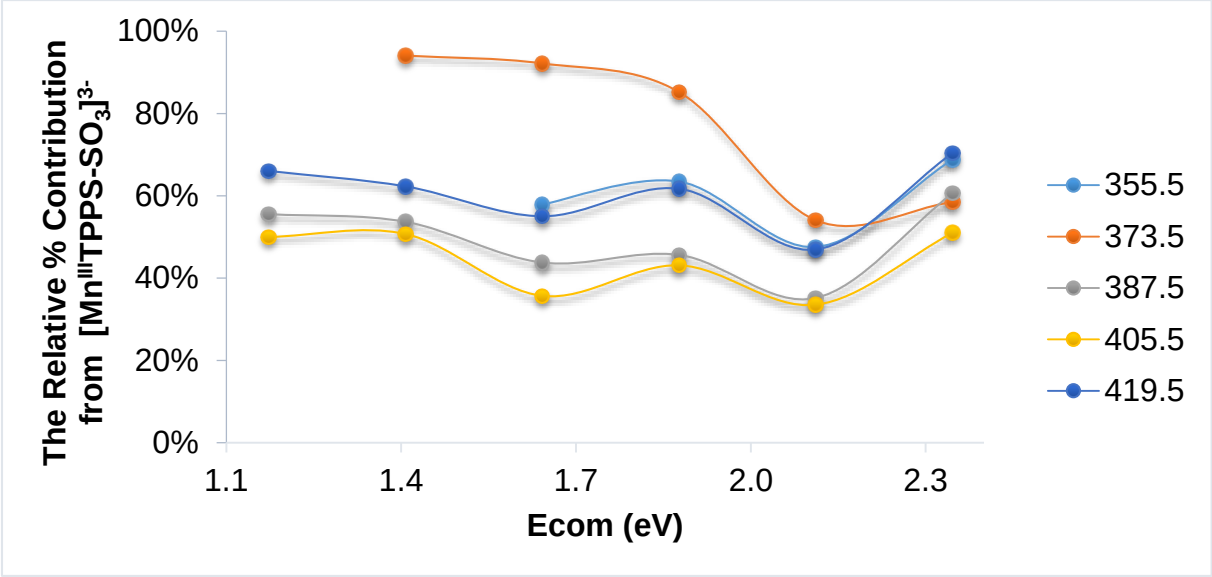

Figure A2.11 Relative abundance % contribution from $[Mn^{III}TPPS\text{-}SO_3]^{3-}$ to the overlapped fragment ions.

Thus, equation 4.1 was used to assign the appropriate percentage of the five overlapping channels to the two main fragment ions to produce the breakdown diagram in Figure A2.12.

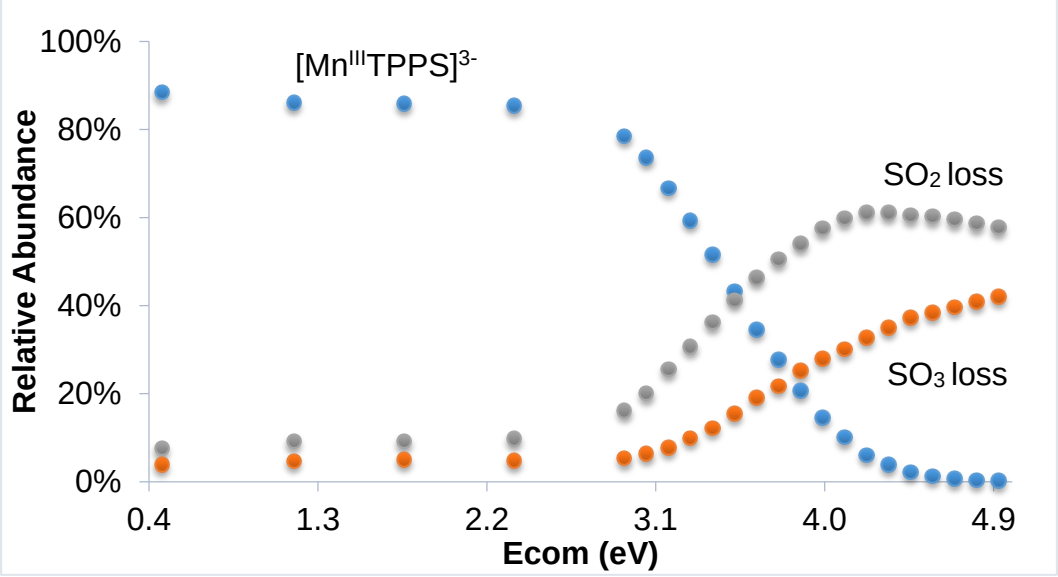

Figure A2.12 Final breakdown diagram for the dissociation of $[Mn^{III}TPPS]^{3-}$

A2.6 RRKM modeling

To understand CID mass spectra, the breakdown diagram was modeled by RRKM theory by using the harmonic vibrational frequencies of $[Mn^{III}TPPS]^{3-}$ (see Table A6.1 in Appendix 6). RRKM theory estimates the theoretical breakdown diagram by altering the following four parameters: i) the activation energy E_0, ii) the first ten vibrational frequencies of the transition state, iii) the pre-collision internal temperature of the ions T_{ini}, iv) α (Equation 2.7). These four parameters were changed manually until the best-fitted theoretical breakdown diagram that matches the experimental breakdown diagram was found (Figure A2.13).

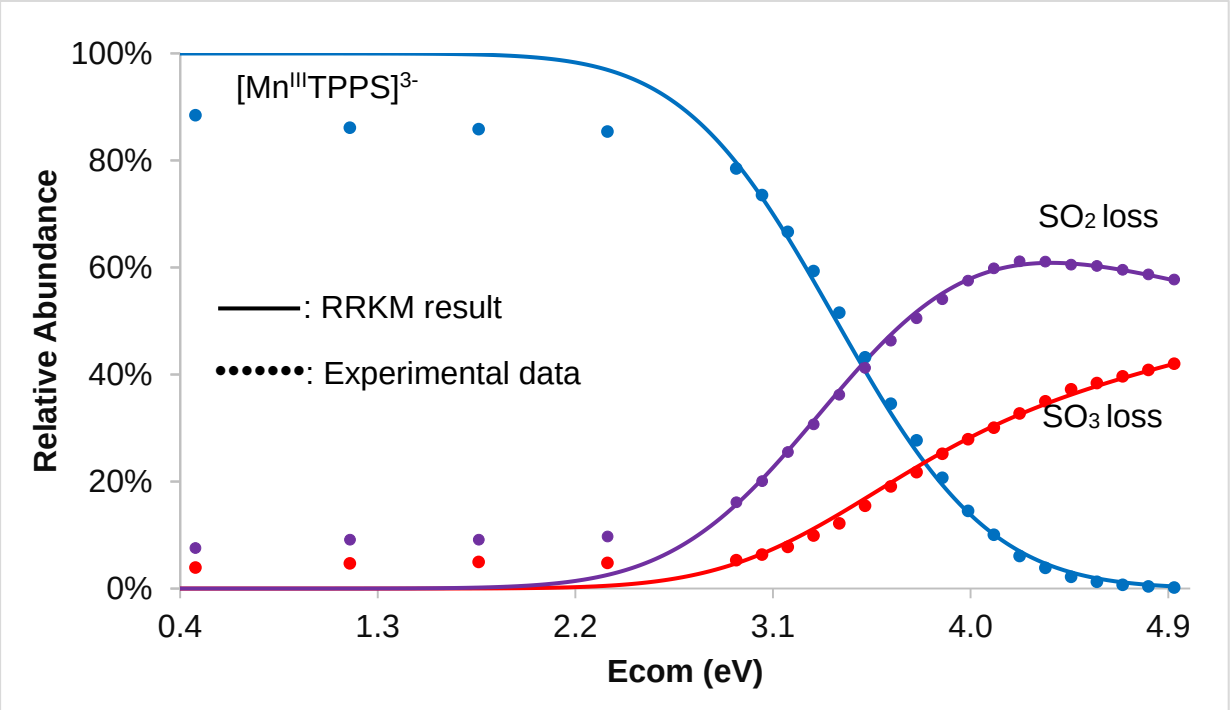

Figure A2.13 RRKM modeling results for the dissociation of $[Mn^{III}TPPS]^{3-}$

Table A2.1 contains results of the RRKM modeling for the $[Mn^{III}TPPS]^{3-}$ dissociation. See Chapter 6 for the discussion of the meaning of these relative activation energies.

Table A2.1 RKKM modeling results for the dissociation of $[Mn^{III}TPPS]^{3-}$

Parent Ion	**IMS**	**RRKM Parameters**		**Channel**	**E_0** (eV)	**$\Delta^{\ddagger}S$** ($J.mol^{-1}\cdot K^{-1}$)
		T_{ini} (K)	α ($K\cdot eV^{-1}$)			
$[Mn^{III}TPPS]^{3-}$	On	400	150	SO_3 loss	1.60 ± 0.03	-50 ± 5
				SO_2 loss	1.33 ± 0.03	-73 ± 5

Appendix 3. RRKM modeling for the dissociation of $[Mn^{III}TPPS+H]^{2-}$

A3.1 ESI-MS of $Mn^{III}TPPS$

As discussed in section A2.1 of Appendix 2, the mass spectrum of $Mn^{III}TPPS$ (Figure A2.1) shows there are different charge states of $Mn^{III}TPPS$ in methanol solution, including $[Mn^{III}TPPS+H]^{2-}$ and $[Mn^{III}TPPS+H]^{2-}$. At a high concentration (2.5×10^{-4} mol/L), mass spectrum (MS) shows that m/z 492.0 contains minor monomer $[Mn^{III}TPPS+H]^{2-}$ and major dimer $[(Mn^{III}TPPS+H)_2]^{4-}$ (Figure A3.1). At a low concentration (1.0×10^{-5} mol/L), ion mobility spectrometer shows that m/z 492.0 composed of minor monomer $[Mn^{III}TPPS]^{2-}$ and major monomer $[Mn^{III}TPPS+H]^{2-}$ (Figure A3.2). The primary focus in this chapter is to study monomer $[Mn^{III}TPPS+H]^{2-}$. Therefore, a low concentrated $Mn^{III}TPPS$ solution was used for the following ESI-MS/MS experiment. Since peak m/z 492.0 is a mixture, ion mobility separation (IMS) has to be turned on to obtain pure $[Mn^{III}TPPS+H]^{2-}$.

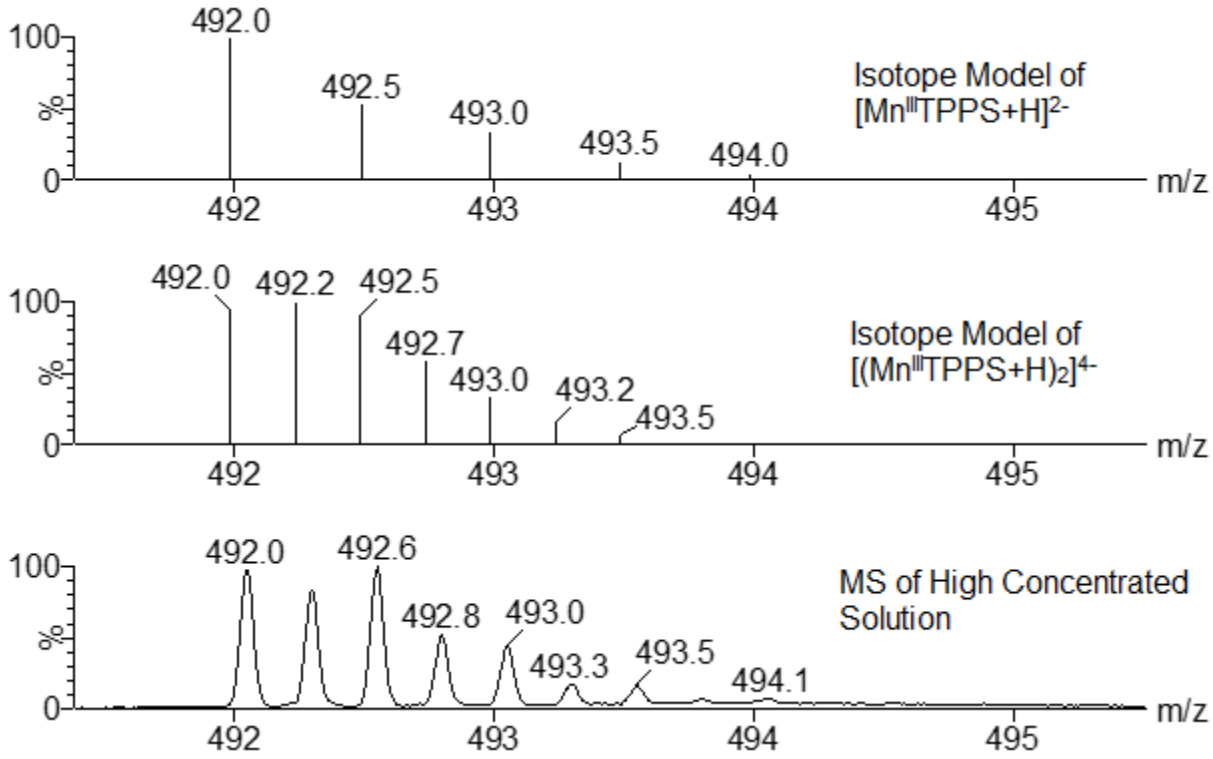

Figure A3.1 Mass spectrum at m/z 492.0 of high concentrated $Mn^{III}TPPS$ (2.5×10^{-4} mol/L). The majority of the solution at m/z 492.0 is made out of dimer $[(Mn^{III}TPPS+H)_2]^{4-}$.

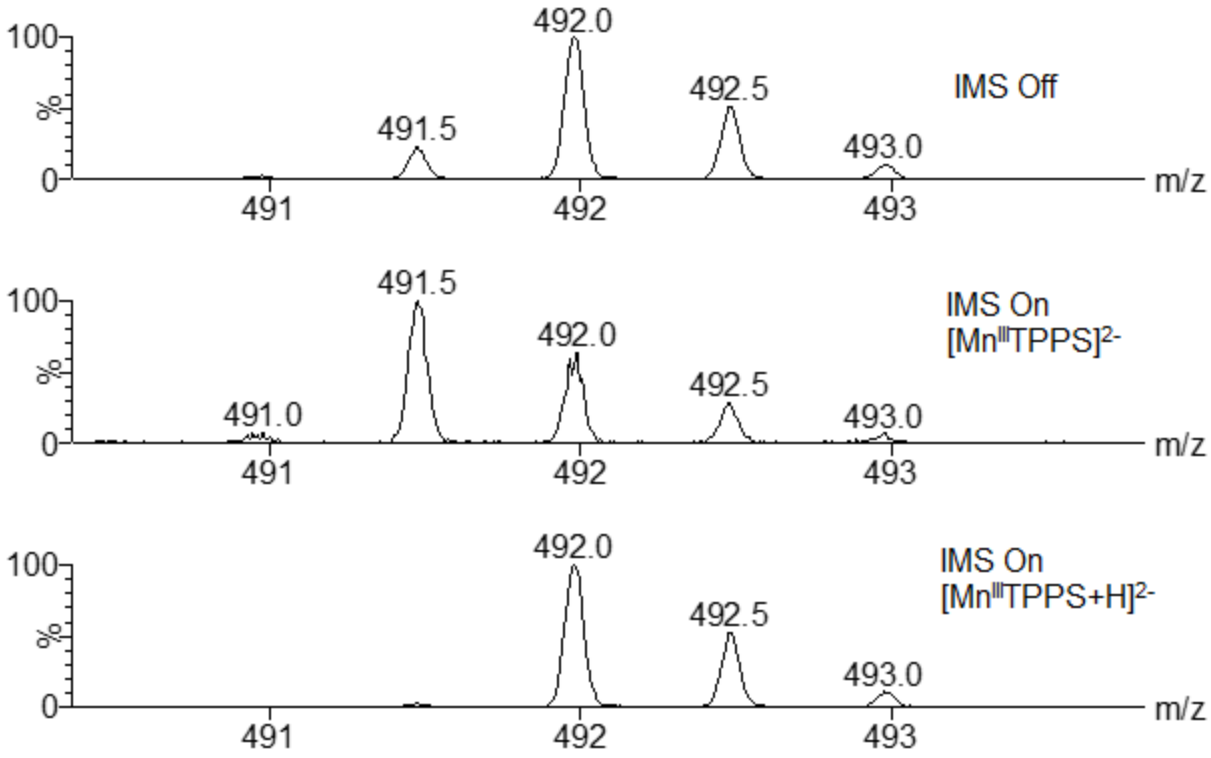

Figure A3.2 Mass spectrum at m/z 492.0 of low concentrated $Mn^{III}TPPS$ (1×10^{-5} mol/L). The majority of the solution at m/z 492.0 is made out of monomer $[Mn^{III}TPPS+H]^{2-}$.

A3.2 ESI-MSMS of $[Mn^{III}TPPS+H]^{2-}$

The CID of $[Mn^{III}TPPS+H]^{2-}$ was selected at m/z 492.0 with the collision voltage ranging from 4 V to 50 V. Increasing the collision voltage have the effect of decreasing the abundance of the parent ion $[Mn^{III}TPPS+H]^{2-}$ to the point at which it disappears entirely and only fragment ions are observed (Figure A3.3). At low collision energy, fragment ions are m/z 452.0 and 460.0, but at higher energies, more fragment ions are formed. The lower half of Figure A3.3 contains all the main fragment ions resulting from the dissociation of $[Mn^{III}TPPS+H]^{2-}$. The m/z of those fragment ions are 412.0, 420.0, 428.0, 446.0, 452.0 and 460.0.

Figure A3.4 is the breakdown diagram of $[Mn^{III}TPPS+H]^{2-}$ with all the main fragment ions. They are plotted as a function of center-of-mass collision energy (E_{com}), which is a fraction of the laboratory kinetic energy (E_{lab}) (Equation 2.6). E_{lab} equals the collision voltage V_{lab} multiplied by the charge state of $[Mn^{III}TPPS+H]^{2-}$ (Equation 2.5).

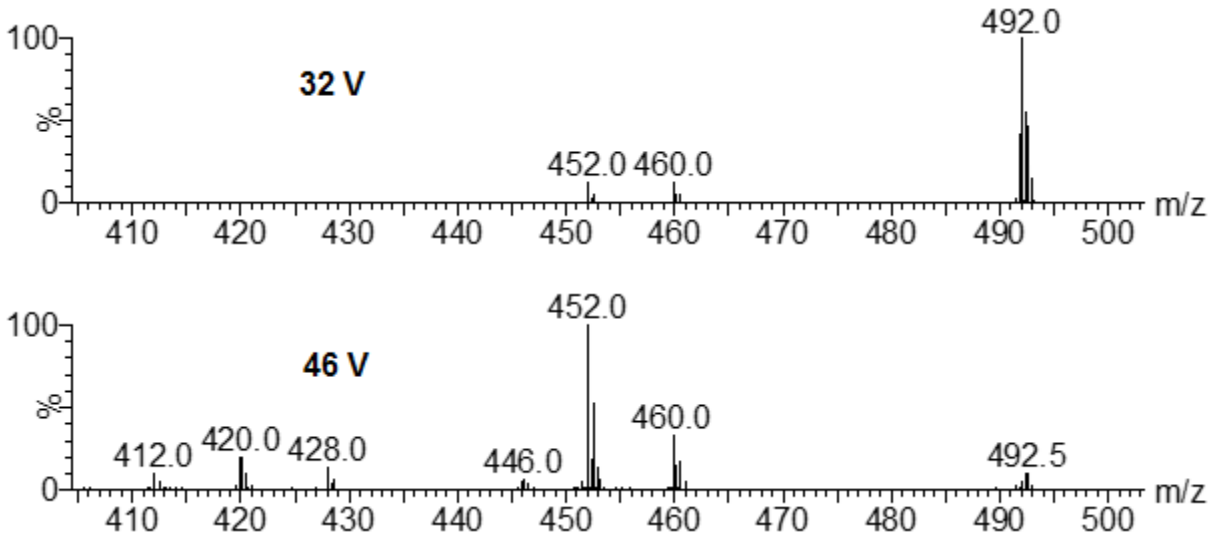

Figure A3.3 CID mass spectra of $[Mn^{III}TPPS+H]^{2-}$ at different collision voltages

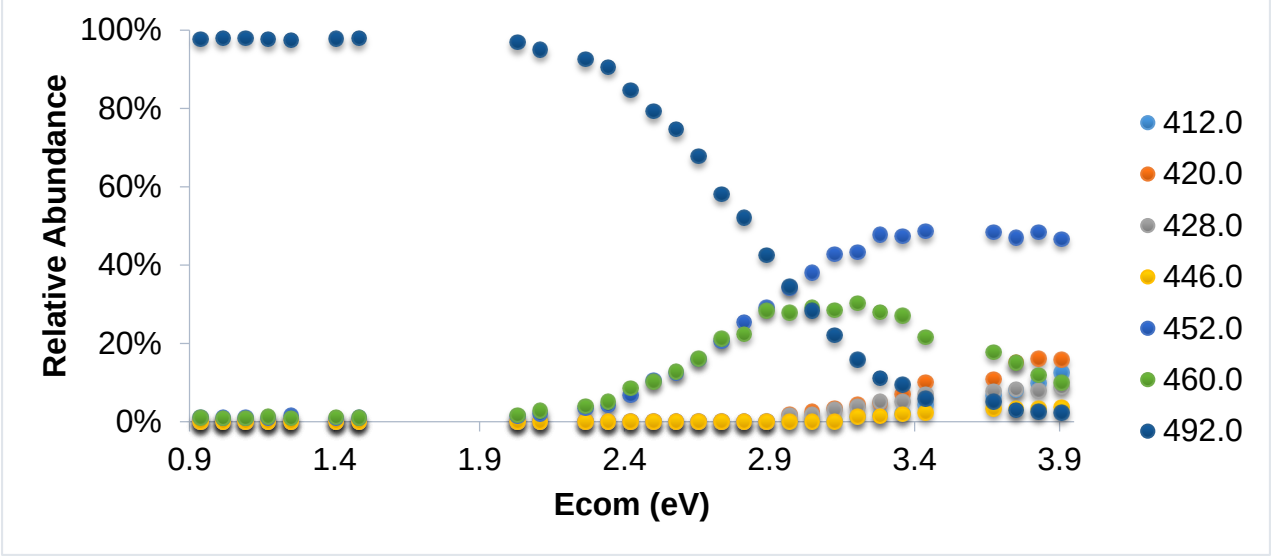

Figure A3.4 Breakdown diagram of $[Mn^{III}TPPS+H]^{2-}$ with all the fragment ions

A3.3 Structure of all the fragment ions

The fragment ions mentioned in the section A3.2 can be calculated mathematically. For example, the mass spectrum shows that the fragment ion with m/z 452.0 has a -2 charge (Δm/z of adjacent peaks at m/z 452.0 is 0.5), so the mass difference of this fragment ion and the parent ion is 2 × (492.0 – 452.0) = 80.0. Considering the big porphyrin ring has four benzenesulfonate functional groups that might lose SO_3, the difference of m/z 80.0 should be a neutral SO_3, and the fragment ion m/z 452.0 should be $[Mn^{III}TPPS+H-SO_3]^{2-}$. This result agrees with the mass spectrum isotope model of $[Mn^{III}TPPS+H-SO_3]^{2-}$ from MassLynx (Figure A3.5). In the same manner, structures of all the fragment ions from the $[Mn^{III}TPPS+H]^{2-}$ dissociation were estimated. Figure A3.6 lists all of their structures.

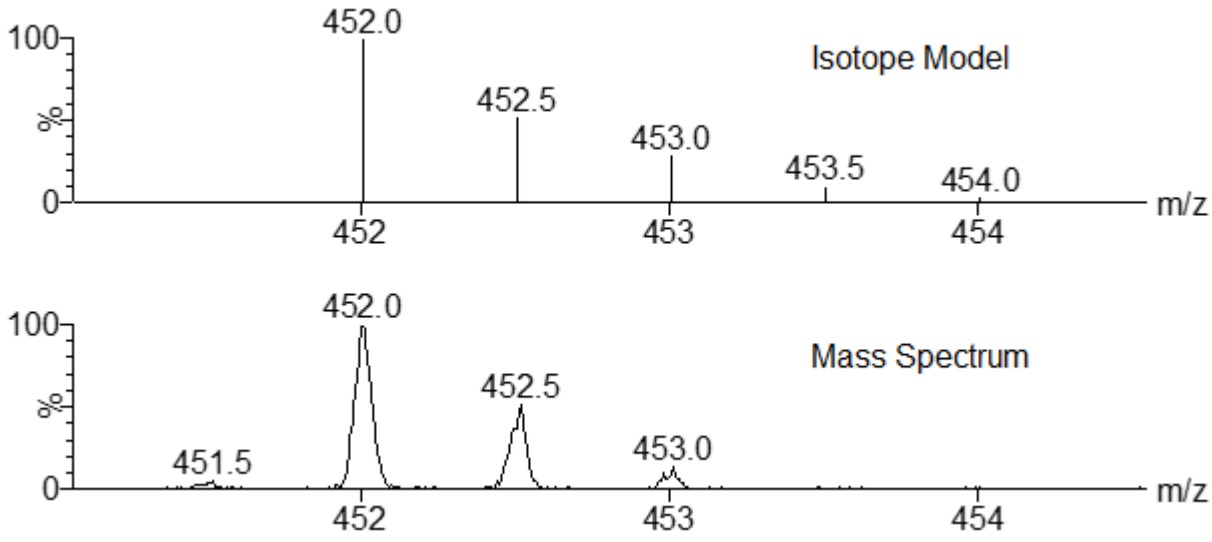

Figure A3.5 Mass spectrum of $[Mn^{III}TPPS+H-SO_3]^{2-}$ and its isotope model

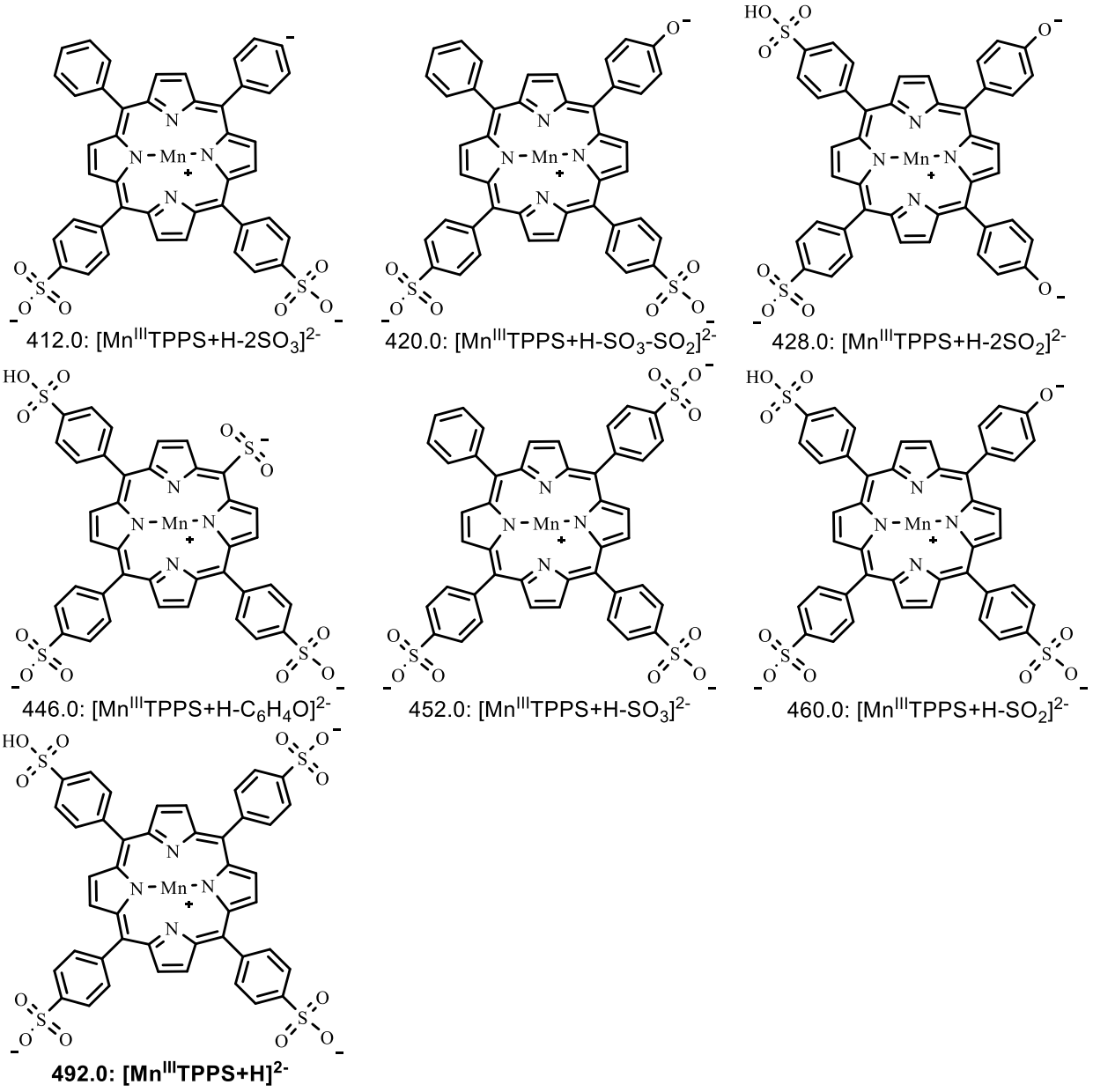

Figure A3.6 Possible structures of fragment ions from the $[Mn^{III}TPPS+H]^{2-}$ dissociation

A3.4 In-source-CID-MS/MS and the map of the fragmentation pathways

There are six main fragment ions from the dissociation of $[Mn^{III}TPPS+H]^{2-}$ as mentioned in section A3.3. However, the pathways that those fragment ions take are still not clear. Structures of these fragment ions show that all the fragment ions result from the loss of one or several neutral SO_2, SO_3, and C_6H_4O. When the collision voltage is low, only fragment ions with m/z 452.0 and m/z 460.0 appear. They are $[Mn^{III}TPPS+H\text{-}SO_3]^{2-}$ and $[Mn^{III}TPPS+H\text{-}SO_2]^{2-}$, respectively This is reasonable considering that $[Mn^{III}TPPS+H]^{2-}$ has four benzenesulfonate groups, which can lose SO_2/SO_3. Also, it seems that the other fragment ions, which appear at a higher collision voltage, may all come from the breakup of the two main fragment ions $[Mn^{III}TPPS+H\text{-}SO_3]^{2-}$ and $[Mn^{III}TPPS+H\text{-}SO_2]^{2-}$.

To verify this assumption, the in-source-CID-MS/MS of $[Mn^{III}TPPS+H\text{-}SO_3]^{2-}$ and $[Mn^{III}TPPS+H\text{-}SO_2]^{2-}$ was carried out. The in-source-CID used a high sampling cone energy of 65 V to break up the parent ion in the source. Then all the negatively charged fragment ions continued to the quadrupole, where m/z 452.0 or 460.0 were selected and their CID mass spectra obtained.

Figure A3.7 and A3.8 represent the breakdown diagrams of m/z 452.0 and m/z 460.0 from collision voltage 15 V to 29 V, in which the center-of mass $\mathrm{E_{com}}$ is established on the x-axis (Equation A3.1). There is only one overlapped fragment ion present in both the in-source-CID-MS/MS of m/z 452.0 and 460.0. It is $[Mn^{III}TPPS+H\text{-}SO_3\text{-}SO_2]^{2-}$. All of the other fragment ions only present in the breakdown of either m/z 452.0 or 460.0. See Figure A3.9 for the dissociation pathways of $[Mn^{III}TPPS+H]^{2-}$.

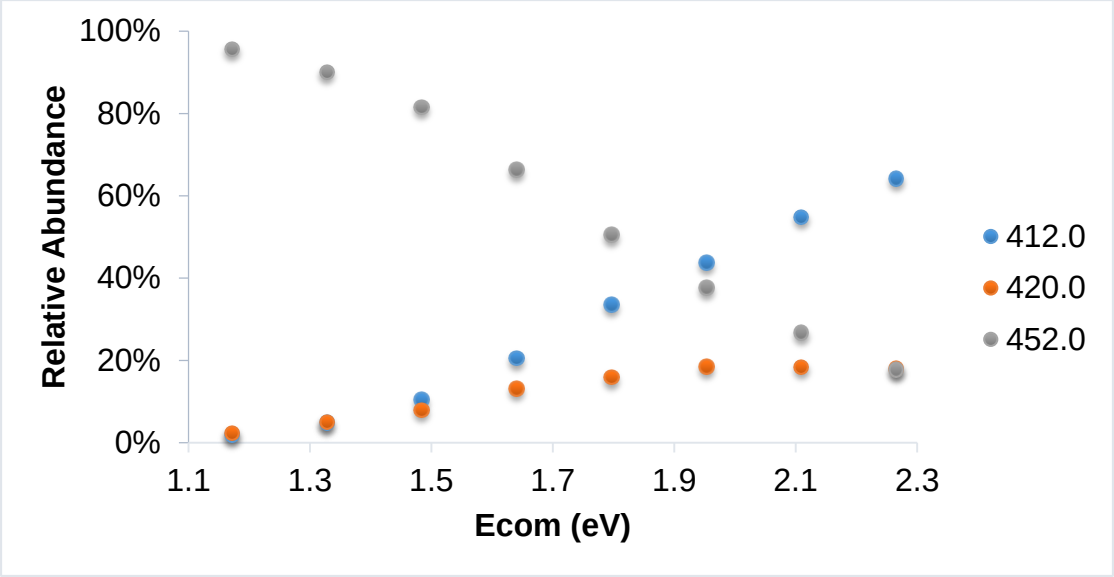

Figure A3.7 In-source-CID-MS/MS of $[Mn^{III}TPPS+H-SO_3]^{2-}$

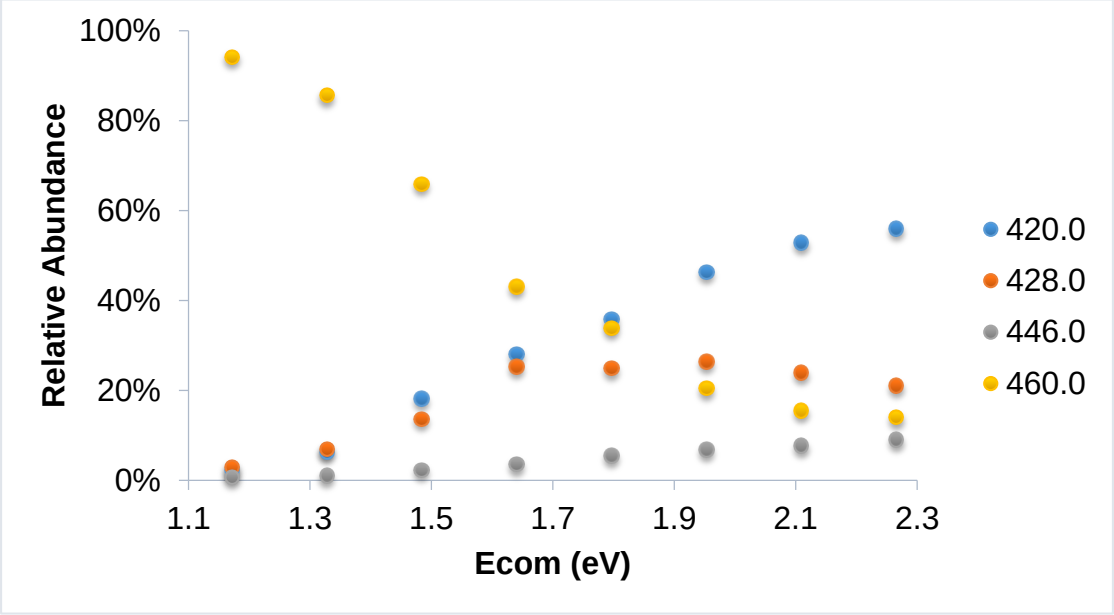

Figure A3.8 In-source-CID-MS/MS of $[Mn^{III}TPPS+H-SO_2]^{2-}$

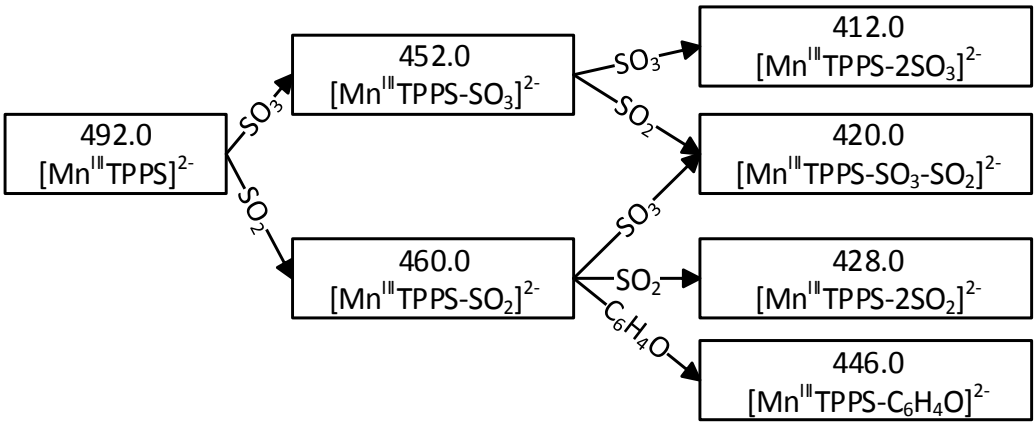

Figure A3.9 Possible dissociation pathways of $[Mn^{III}TPPS+H]^{2-}$

A3.5 Breakdown Diagram

The dissociation pathways of $[Mn^{III}TPPS+H]^{2-}$ have been evaluated in section A3.4. All the fragment ions, except for $[Mn^{III}TPPS+H-SO_3-SO_2]^{2-}$, come from these two channels: $[Mn^{III}TPPS+H-SO_3]^{2-}$ and $[Mn^{III}TPPS+H-SO_2]^{2-}$. The contribution of these two channels to the overlapped fragment ion $[Mn^{III}TPPS+H-SO_3-SO_2]^{2-}$ are pretty similar, so half of it was divided to each channel. Figure A3.10 the final breakdown diagram.

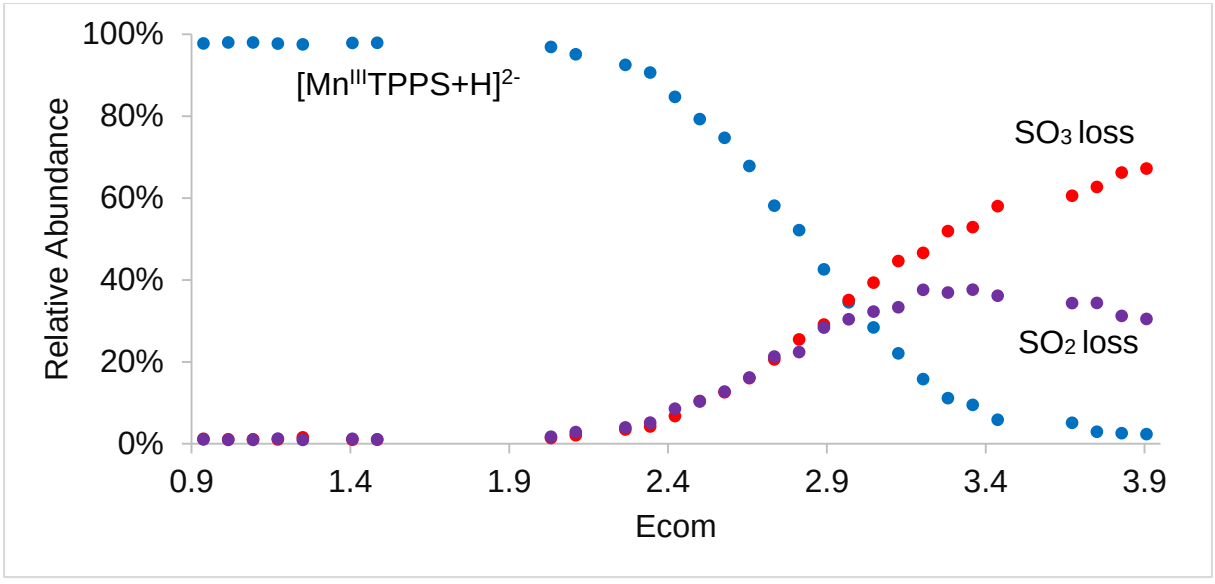

Figure A3.10 Final breakdown diagram for the dissociation of $[Mn^{III}TPPS+H]^{2-}$

A3.6 RRKM modeling

To understand CID mass spectra, the breakdown diagram was modeled by RRKM theory by using the harmonic vibrational frequencies of $[Mn^{III}TPPS+H]^{2-}$ (see Table A6.1 in Appendix 6). RRKM theory estimates the theoretical breakdown diagram by altering the following four parameters: i) the activation energy E_0, ii) the first ten vibrational frequencies of the transition state, iii) the pre-collision internal temperature of the ions T_{ini}, and iv) α (Equation 2.7). These four parameters were changed manually until the best-fitted theoretical breakdown diagram that matches the experimental breakdown diagram was found (Figure A3.11).

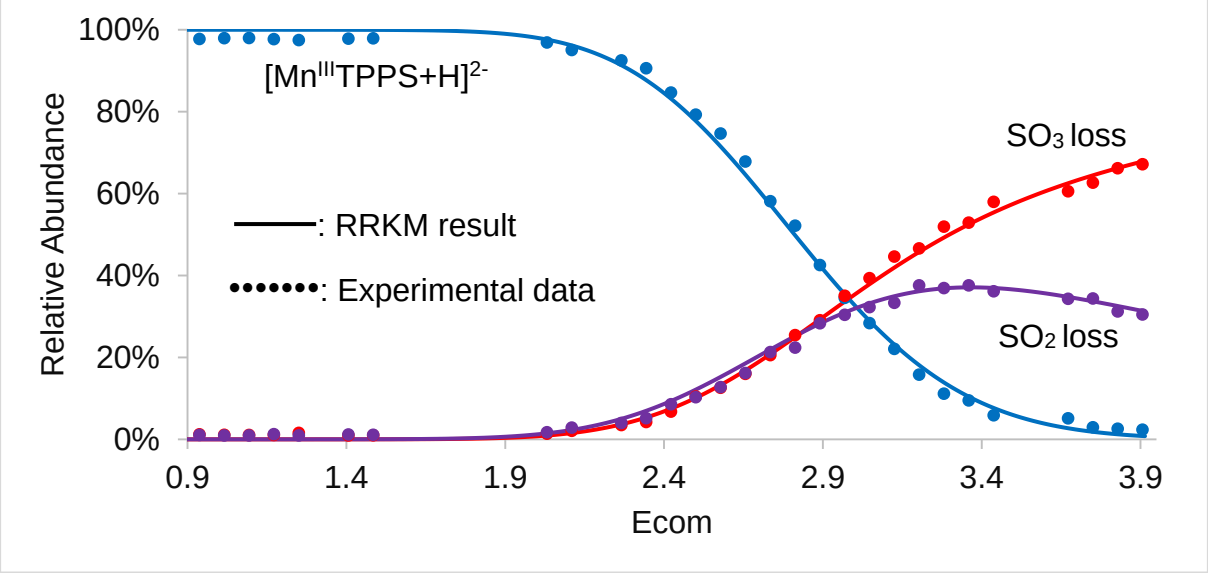

Figure A3.11 RRKM modeling results for the dissociation of $[Mn^{III}TPPS+H]^{2-}$

Table A3.1 contains results of the RRKM modeling for the $[Mn^{III}TPPS+H]^{2-}$ dissociation. See Chapter 6 for the discussion of the meaning of these activation energies.

Table A3.1 RKKM modeling results for the dissociation of $[Mn^{III}TPPS+H]^{2-}$

Parent Ion	**IMS**	**RRKM Parameters**		**Channel**	**E_0** (eV)	**Entropy** ($J.mol^{-1}\cdot K^{-1}$)
		T_{ini} (K)	α ($K\cdot eV^{-1}$)			
$[Mn^{III}TPPS+H]^{2-}$	On	400	150	SO_3 loss	2.56 ± 0.10	106 ± 15
				SO_2 loss	2.23 ± 0.10	63 ± 15

Appendix 4. RRKM modeling for the dissociation of $[Fe^{II}TPPS+H]^{3-}$

A4.1 ESI-MS of $Fe^{II}TPPS$

The mass spectrum of $Fe^{II}TPPS$ (Figure A4.1) shows there are different charge states of $Fe^{II}TPPS$ in methanol solution, including $[Fe^{II}TPPS]^{4-}$, $[Fe^{II}TPPS+H]^{3-}$, and $[Fe^{II}TPPS+2H]^{2-}$. The one of interest is $[Fe^{II}TPPS+H]^{3-}$, which is only monomer, instead of a mix of monomer $[Fe^{II}TPPS+H]^{3-}$ and dimer $[(Fe^{II}TPPS)_2+2H]^{6-}$. This was verified by turning on the ion mobility spectrometry (IMS), which showed no extra ions could be separated.

The mass spectrum of $[Fe^{II}TPPS+H]^{3-}$ (Figure A4.2) doesn't totally agree with its theoretical isotope model, because some $[Fe^{II}TPPS+H]^{3-}$ ions lose one proton, and some even lose 2 protons. That's why the peak m/z 328.4 shift to 328.0 (1 H loss) and 327.7 (2 H loss). In addition, H loss was also found in the ESI-MS/MS experiment. See Figure A4.9 for details.

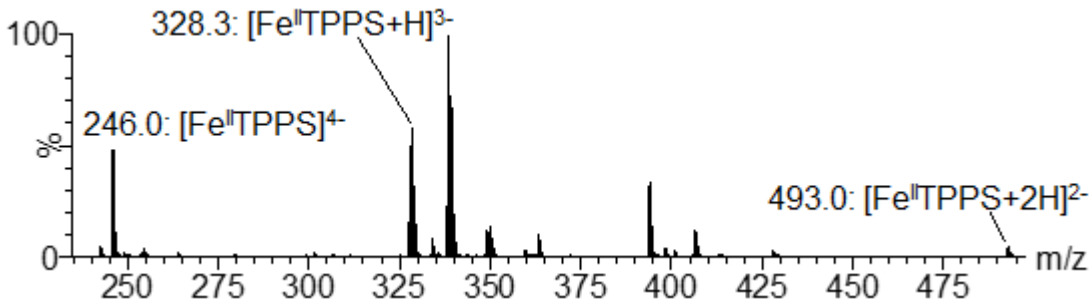

Figure A4.1 Mass spectrum of $Fe^{II}TPPS$

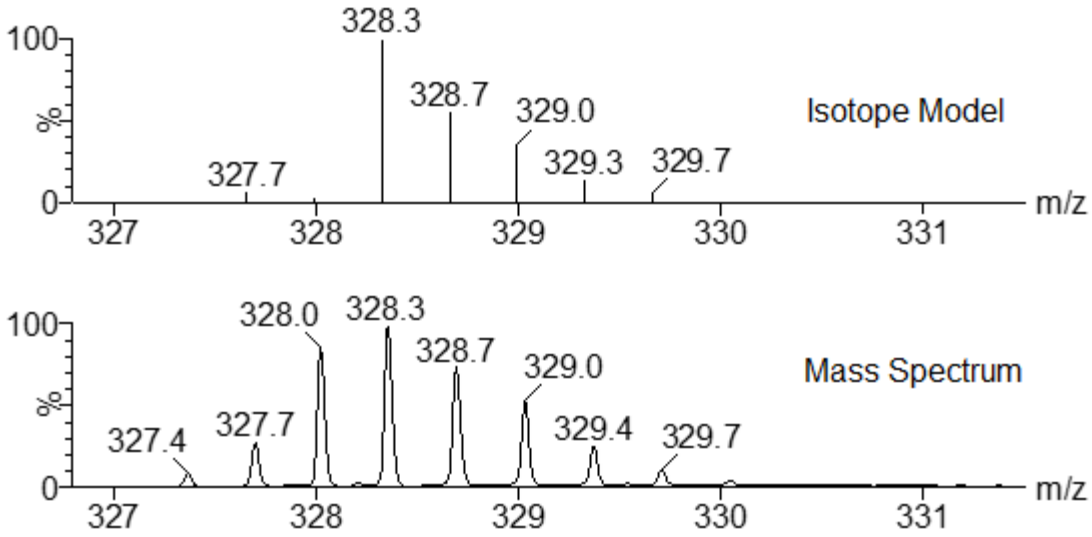

Figure A4.2 Mass spectrum of $[Fe^{II}TPPS+H]^{3-}$ and its isotope model

A4.2 ESI-MSMS of $[Fe^{II}TPPS+H]^{3-}$

The CID of $[Fe^{II}TPPS+H]^{3-}$ was selected at m/z 328.3 with the collision voltage ranging from 4 V to 23 V. Increasing the collision voltage decreases the abundance of the parent ion $[Fe^{II}TPPS+H]^{3-}$ to the point at which it disappears entirely and only fragment ions are observed (Figure A4.3). At low collision energy, fragment ions are m/z 301.7 and 306.7, but at higher collision energies, more fragment ions are formed. The lower half of Figure A4.3 contains all the main fragment ions resulting from the dissociation of $[Fe^{II}TPPS+H]^{3-}$. The m/z of those fragment ions are 280.4, 285.4, 288.7, 297.3, 301.6, 306.7, 374.0, 380.5, 388.5, 406.0, 412.5, 420.5, and 452.5.

Figure A4.4 represents the breakdown diagram of $[Fe^{II}TPPS+H]^{3-}$ with all the main fragment ions. They are plotted as a function of center-of-mass collision energy (E_{com}), which is a fraction of the laboratory kinetic energy (E_{lab}) (Equation 2.6). E_{lab}

equals the collision voltage V_{lab} multiplied by the charge state of $[Fe^{II}TPPS+H]^{3-}$ (Equation 2.5).

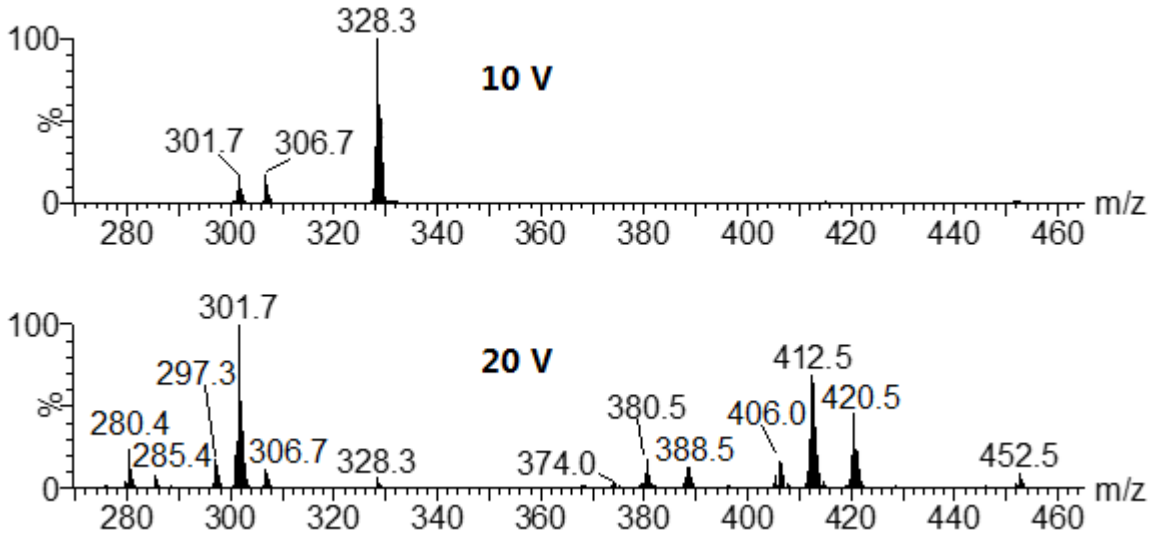

Figure A4.3 CID mass spectra of $[Fe^{II}TPPS+H]^{3-}$ at different collision voltages

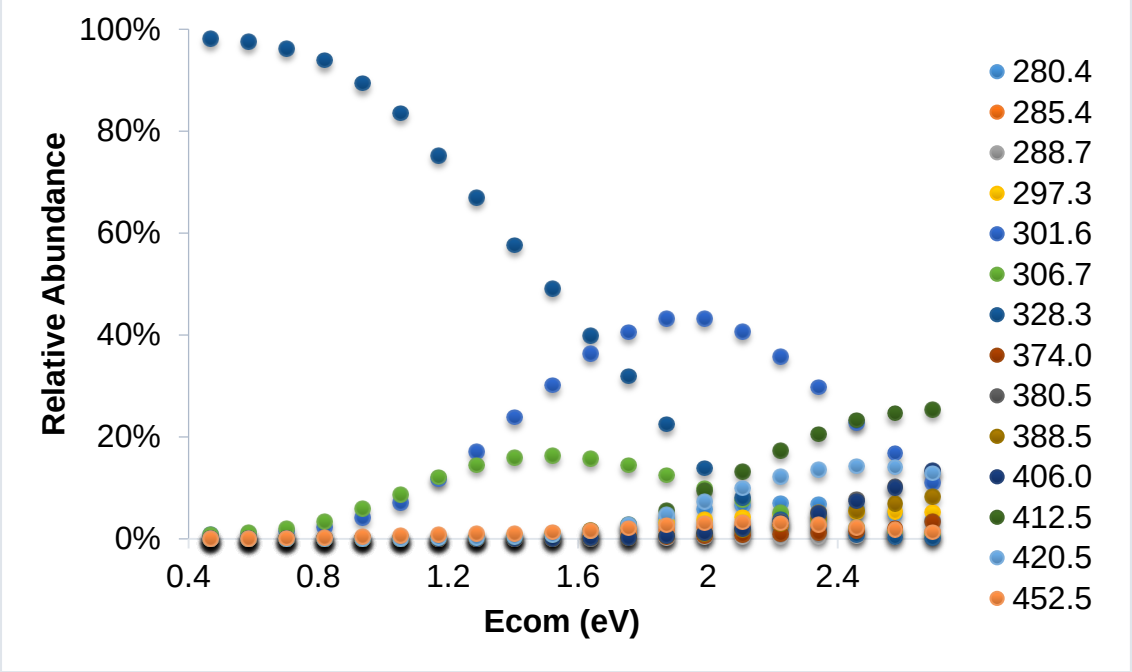

Figure A4.4 Breakdown diagram of $[Fe^{II}TPPS+H]^{3-}$ with all the fragment ions

A4.3 Structure of all the fragment ions

The fragment ions mentioned in the section A4.2 can be calculated mathematically. For example, the mass spectrum shows that the fragment ion with m/z 301.7 has a -3 charge (Δm/z of adjacent peaks at m/z 301.7 is 0.33), so the mass difference of this fragment ion and the parent ion is 3 × (328.3 – 301.7) = 79.8. Considering the big porphyrin ring has four benzenesulfonate functional groups that might lose SO_3, the difference of m/z 80.1 should be a neutral SO_3, and the fragment ion m/z 301.7 should be $[Fe^{II}TPPS+H-SO_3]^{3-}$. This result agrees with the mass spectrum isotope model of $[Fe^{II}TPPS+H-SO_3]^{3-}$ from MassLynx (Figure A4.5).

In the same manner, structures of all the fragment ions from the $[Fe^{II}TPPS+H]^{3-}$ dissociation were estimated. The fragment ions (see Figure A4.6) with theoretical m/z 285.7, 297.7, 307.0, 374.5, and 406.5 were observed to be 285.4, 297.3, 306.7, 374.0, and 406.0, respectively. This is because of one H loss from these fragment ions.

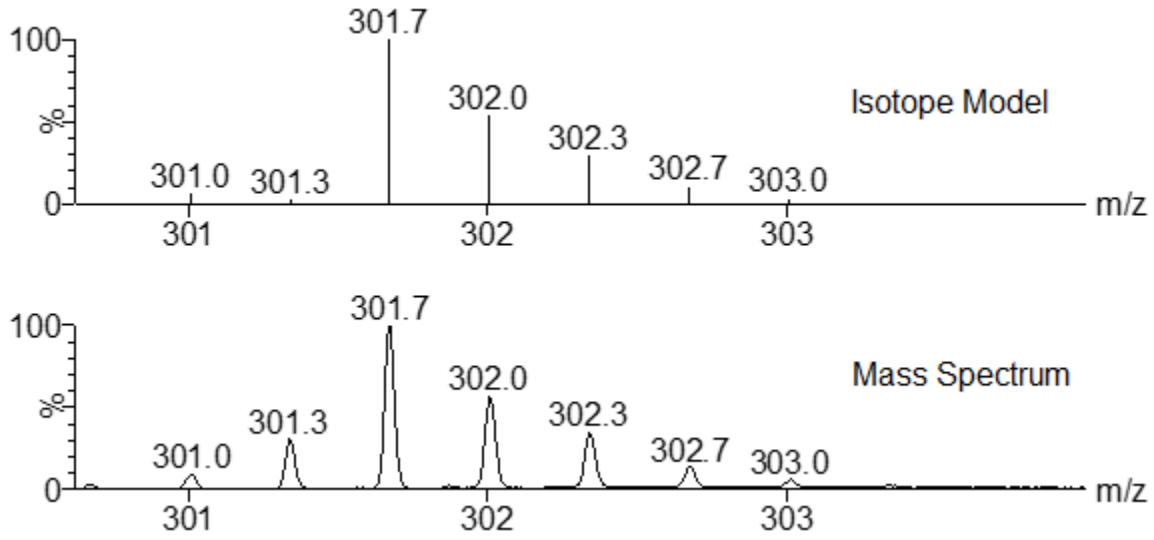

Figure A4.5 Mass spectrum of $[Fe^{II}TPPS+H-SO_3]^{3-}$ and its isotope model

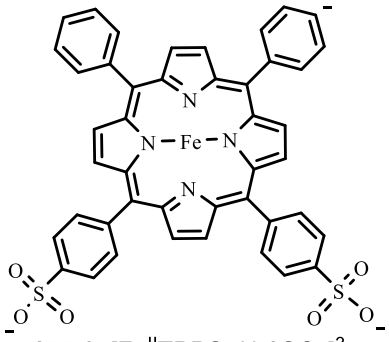

275.0: $[Fe^{II}TPPS+H-2SO_3]^{3-}$

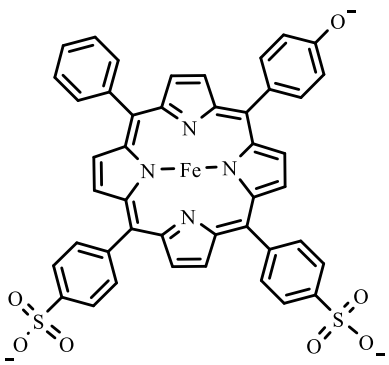

280.4: $[Fe^{II}TPPS+H-SO_3-SO_2]^{3-}$

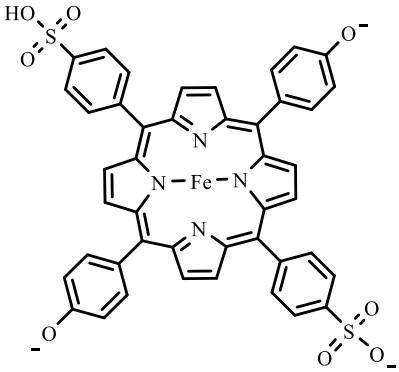

285.7: $[Fe^{II}TPPS+H-2SO_2]^{3-}$

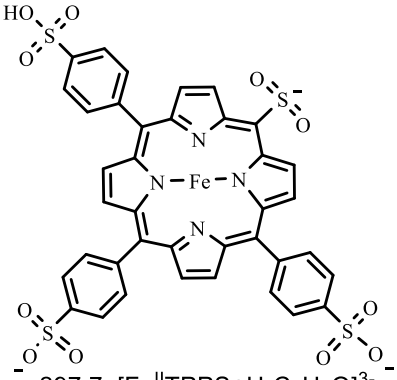

297.7: $[Fe^{II}TPPS+H-C_6H_4O]^{3-}$

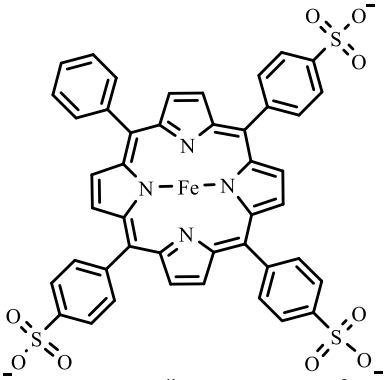

301.7: $[Fe^{II}TPPS+H-SO_3]^{3-}$

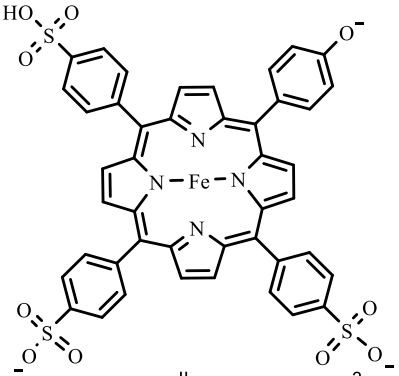

307.0: $[Fe^{II}TPPS+H-SO_2]^{3-}$

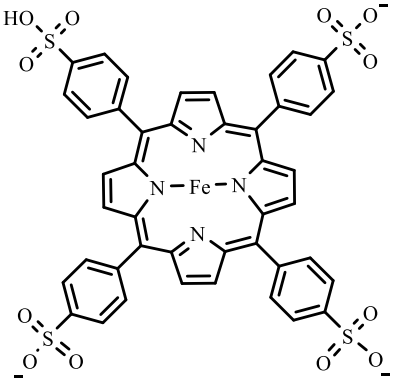

328.3: $[Fe^{II}TPPS+H]^{3-}$

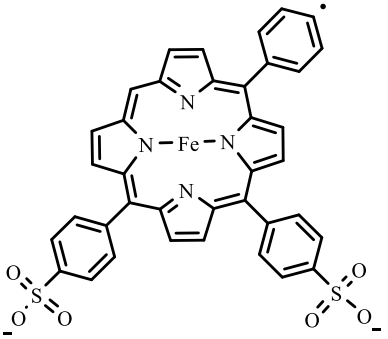

374.5: $[Fe^{II}TPPS+H-2SO_3-C_6H_4]^{2-}$

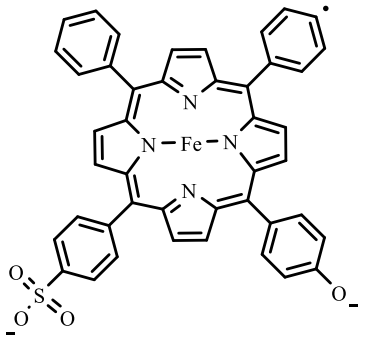

380.6: $[Fe^{II}TPPS+H-2SO_3-SO_2]^{2-}$

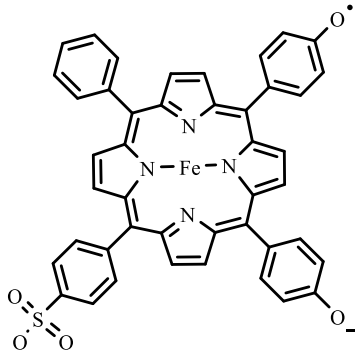

388.6: $[Fe^{II}TPPS+H-SO_3-2SO_2]^{2-}$

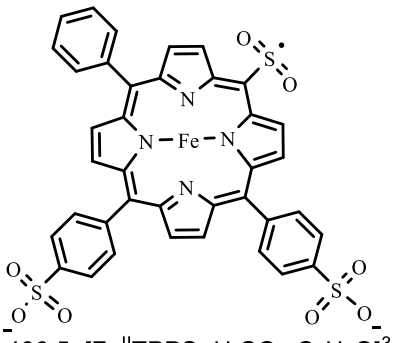

406.5: $[Fe^{II}TPPS+H-SO_3-C_6H_4O]^{3-}$

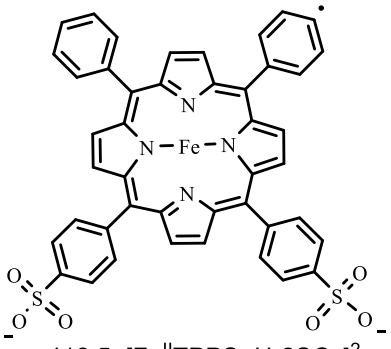

412.5: $[Fe^{II}TPPS+H-2SO_3]^{2-}$

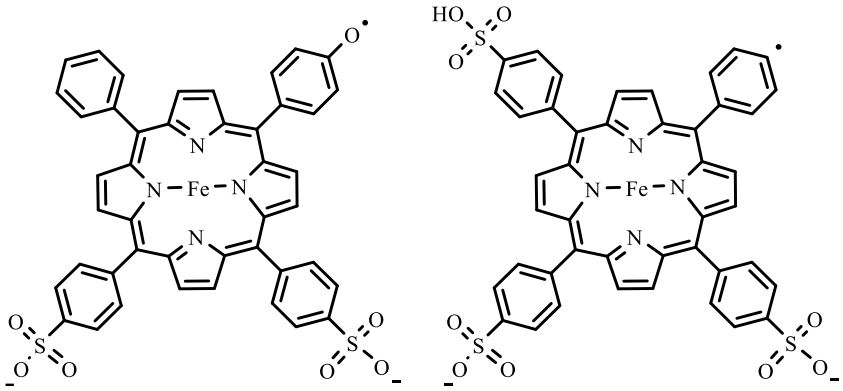

Figure A4.6 Possible structures of fragment ions from the [Fe^{II}TPPS+H]$^{3-}$ dissociation

A4.4 In-source-CID-MS/MS and the map of the fragmentation pathways

There are 13 main fragment ions from the dissociation of [Fe^{II}TPPS+H]$^{3-}$ as mentioned in section A4.3. However, the pathways that those fragment ions take are still not clear. Structures of these fragment ions show that all the fragment ions result from the loss of one or several neutral/negative SO_2, SO_3, and C_6H_4O. When the collision voltage is low, only fragment ions m/z 301.7 and m/z 306.7. They are [Fe^{II}TPPS+H-SO$_3$]$^{3-}$ and [Fe^{II}TPPS+H-SO$_2$]$^{3-}$, respectively. Also, it seems that the other fragment ions, which appear at a higher collision voltage, may all come from the breakup of the two main fragment ions [Fe^{II}TPPS+H-SO$_3$]$^{3-}$ and [Fe^{II}TPPS+H-SO$_2$]$^{3-}$.

To verify this assumption, the in-source-CID-MS/MS of [Fe^{II}TPPS+H-SO$_3$]$^{3-}$ and [Fe^{II}TPPS+H-SO$_2$]$^{3-}$ was carried out. The in-source-CID used a high sampling cone energy of 52 V to break up the parent ion in the source. Then all the negatively charged

fragment ions continued to the quadrupole, where m/z 301.7 or 306.7 were selected and their CID mass spectra were obtained.

Figure A4.7 and A4.8 represents the breakdown diagrams of m/z 301.7 and m/z 306.7 from collision voltage 4 V to 22 V, in which the center-of mass $\mathrm{E_{com}}$ is established on the x-axis (see Equation 2.5 and 2.6). There are five overlapped fragment ions present in both the in-source-CID-MS/MS of m/z 301.7 and m/z 306.7. They are $[Fe^{II}TPPS+H-2SO_3-C_6H_4]^{2-}$, $[Fe^{II}TPPS+H-2SO_3-SO_2]^{2-}$, $[Fe^{II}TPPS+H-SO_3-2SO_2]^{2-}$, $[Fe^{II}TPPS+H-SO_3-C_6H_4O]^{2-}$, and $[Fe^{II}TPPS+H-SO_3-SO_2]^{2-}$. All of the other fragment ions, with exception of m/z 452.5, are only present in the breakdown of either m/z 301.7 or m/z 306.7. See Figure A4.9 for the dissociation pathways of $[Fe^{II}TPPS+H]^{3-}$.

Fragment ion with m/z 452.5 is an independent channel: $[SO_3]^-$ loss from $Fe^{II}TPPS+H]^{3-}$ directly. However, this channel is ignored because it has a pretty low relative abundance (maximum 3.28%) compared with the other two channels, and it only appear at a high collision energy. Ignoring this channel will not influence the activation energy calculations of the other two channels.

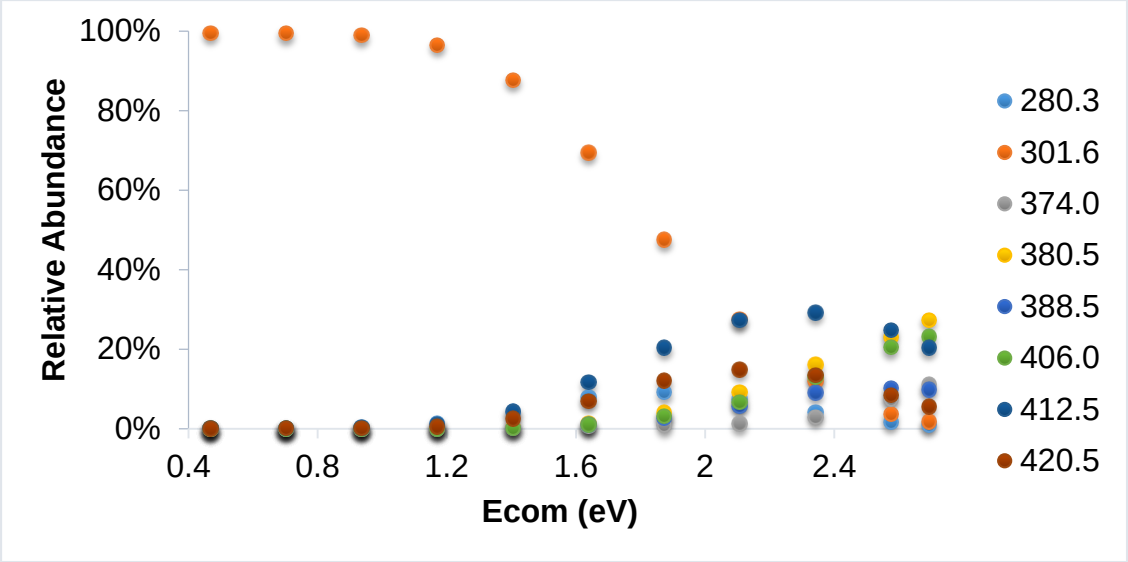

Figure A4.7 In-source-CID-MS/MS of $[Fe^{II}TPPS+H-SO_3]^{3-}$

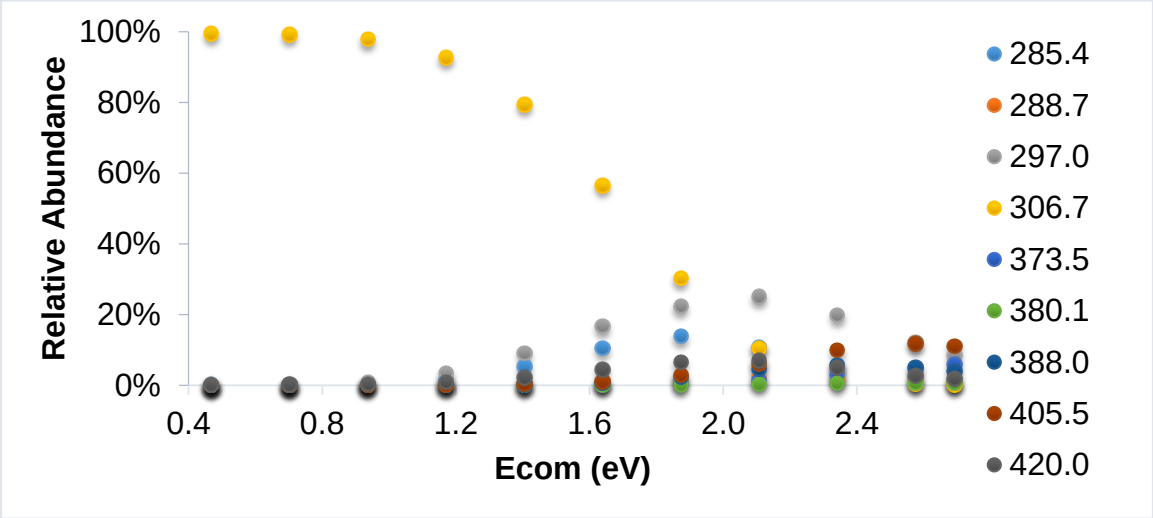

Figure A4.8 In-source-CID-MS/MS of $[Fe^{II}TPPS+H-SO_2]^{3-}$. Fragment ions with m/z 306.7 are $[Fe^{II}TPPS-SO_2]^{3-}$ instead of $[Fe^{II}TPPS+H-SO_2]^{3-}$.

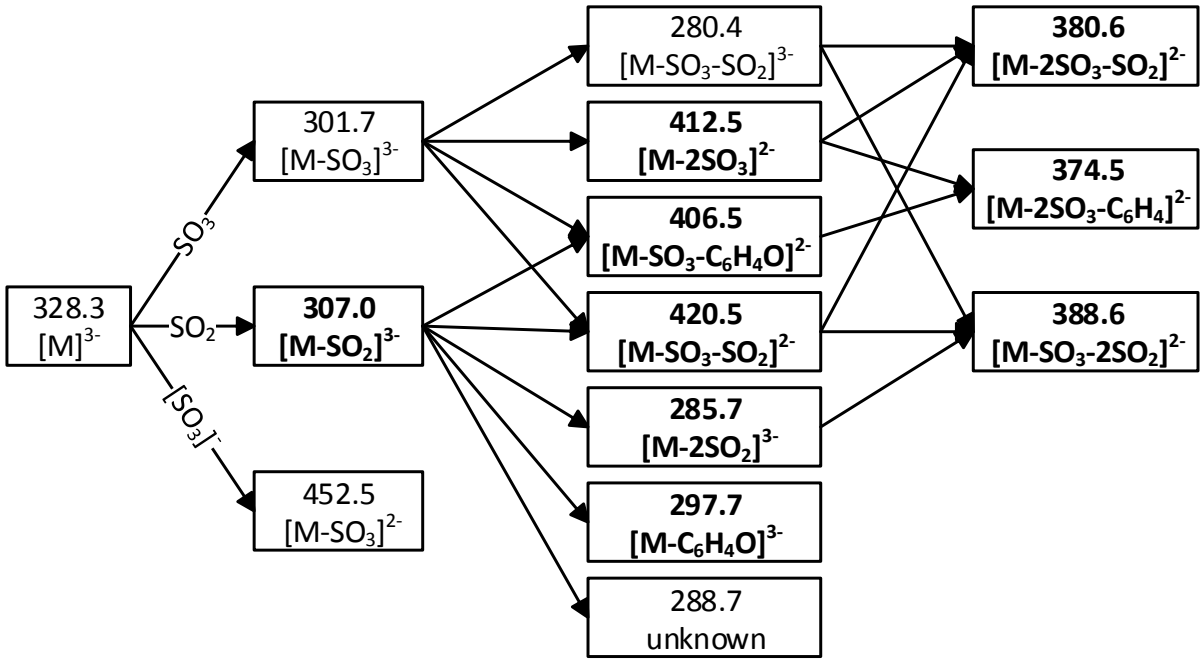

Figure A4.9 Possible dissociation pathways of $[M]^{3-}$ (where M = Fe^{II}TPPS+H). H loss from ions labeled in bold are pretty common, and this leads to the difference between the theoretical m/z in this figure and experimental m/z.

A4.5 Breakdown Diagram

The dissociation pathways of $[Fe^{II}TPPS+H]^{3-}$ have been evaluated in section A4.4. All the fragment ions, except for $[Fe^{II}TPPS+H-SO_3]^{2-}$, are created by these two channels: the breakdown of $[Fe^{II}TPPS+H-SO_3]^{3-}$ and $[Fe^{II}TPPS+H-SO_2]^{3-}$. However, the division of those five fragment ions still remains unclear. The total relative abundance percent of all the overlapped fragment ions increase from 0 to 51.2% when increasing the collision energy (Figure A4.10), which is too significant to ignore. The % contribution of $[Fe^{II}TPPS+H-SO_3]^{3-}$ to those five overlapped fragment ions are calculated by Equation 4.1. Figure A4.11 shows the % contribution of $[Fe^{II}TPPS+H-SO_3]^{3-}$ to those five overlapped fragment ions. Except for m/z 374.0, the % contribution of [Fe^{II}TPPS+H-

$SO_3]^{3-}$ seems to be consistent when increasing the collision voltage. However, the maximum relative abundance of m/z 374.0 is 3.4% (Figure A4.12), so its influence on the breakdown can be ignored.

As a result, the average percentage value of each overlapped fragment ion was used to divide the overlapped fragment ions to the channels $[Fe^{II}TPPS+H\text{-}SO_3]^{3-}$ and $[Fe^{II}TPPS+H\text{-}SO_2]^{3-}$ for the breakdown diagram of the parent ion $[Fe^{II}TPPS+H]^{3-}$.

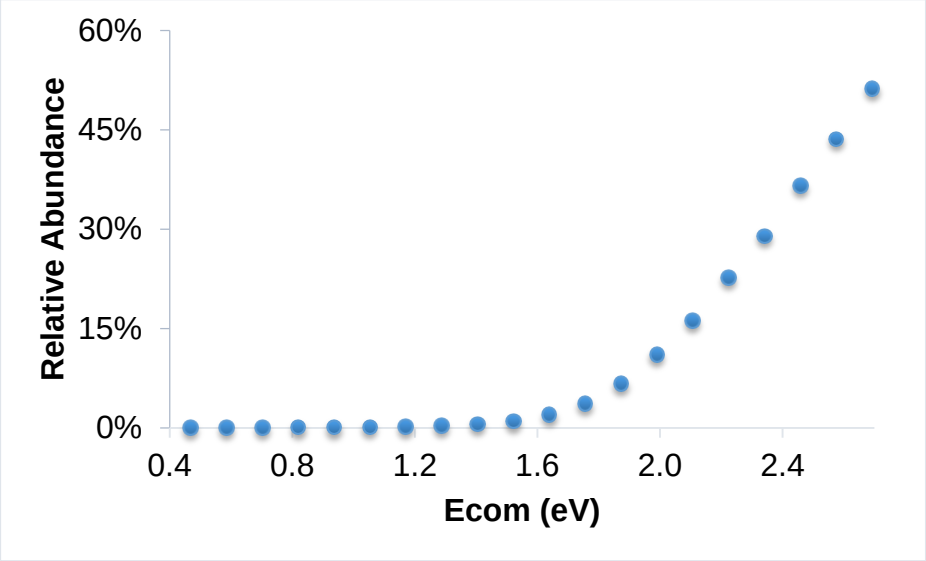

Figure A4.10 Total Relative abundance of the overlapped fragment ions from both $[Fe^{II}TPPS+H\text{-}SO_3]^{3-}$ and $[Fe^{II}TPPS+H\text{-}SO_2]^{3-}$

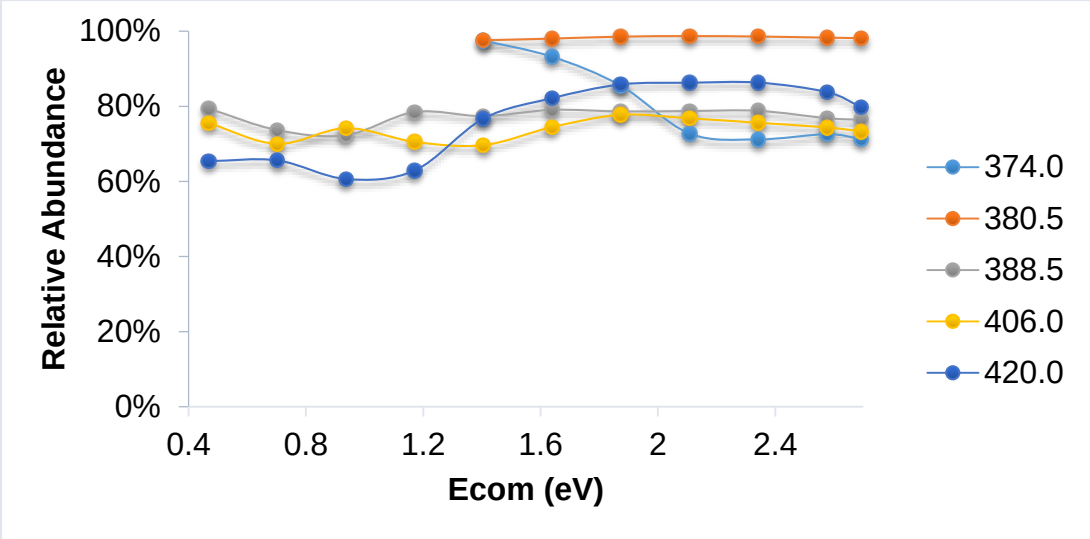

Figure A4.11 Relative abundance % contribution from $[Fe^{II}TPPS+H-SO_3]^{3-}$ to the overlapped fragment ions

Thus, equation 4.1 was used to assign the appropriate percentage of the five overlapping channels to the two main fragment ions to produce the breakdown diagram in Figure A4.12.

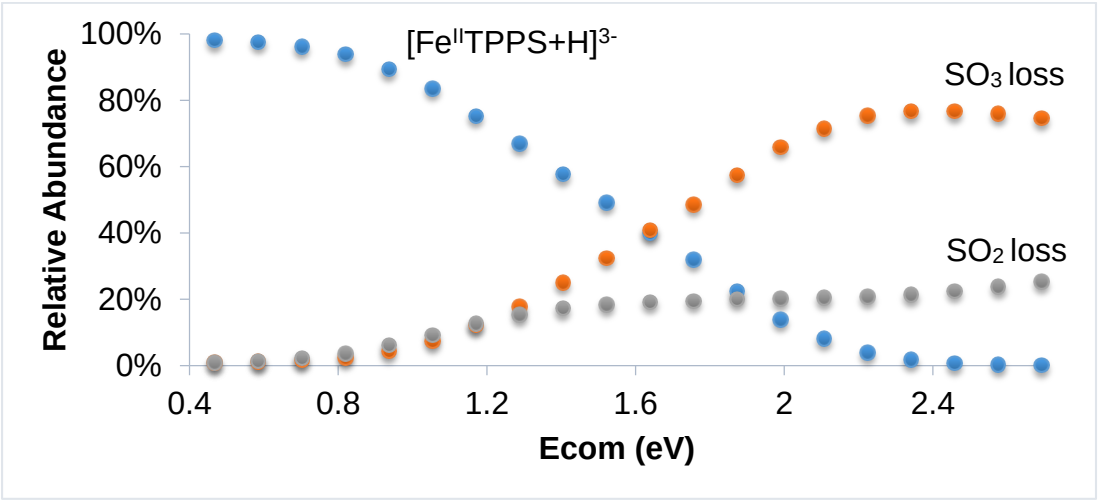

Figure A4.12 Final breakdown diagram for the dissociation of $[Fe^{II}TPPS+H]^{3-}$

A4.6 RRKM modeling

To understand CID mass spectra, the breakdown diagram was modeled by RRKM theory by using the harmonic vibrational frequencies of $[Fe^{II}TPPS+H]^{3-}$ (see Figure A6.1). Figure A4.13 shows the theoretical RRKM modeling and experimental breakdown diagram. They do not match each other pretty well when Ecom becomes bigger than 2.2 eV. This should be caused by the following reasons:

a) The relative abundance of each fragment ion is not accurate. As shown in Figure A4.9, H loss are common among almost all the fragment ions, what makes any m/z peak of a fragment ion obtained from the MS/MS cannot totally represent its real abundance. As a result, the relative abundance of each fragment ion is inaccurate.

b) H loss might happened before SO_2 loss from the parent ion. Figure A6.3 (see Chapter 6) shows that the peak for $[Fe^{II}TPPS-SO_2]^{3-}$ is much more significant than $[Fe^{II}TPPS+H-SO_2]^{3-}$. If this assumption is correct, the SO_2 loss channel should be changed to H loss channel, and the H loss before SO_3 loss should also be considered.

c) The division of fragment ions to channels of SO_2 and SO_3 loss might not be accurate. Because ESI-MS/MS and in-source-CID-MS/MS were not in totally the same experimental condition.

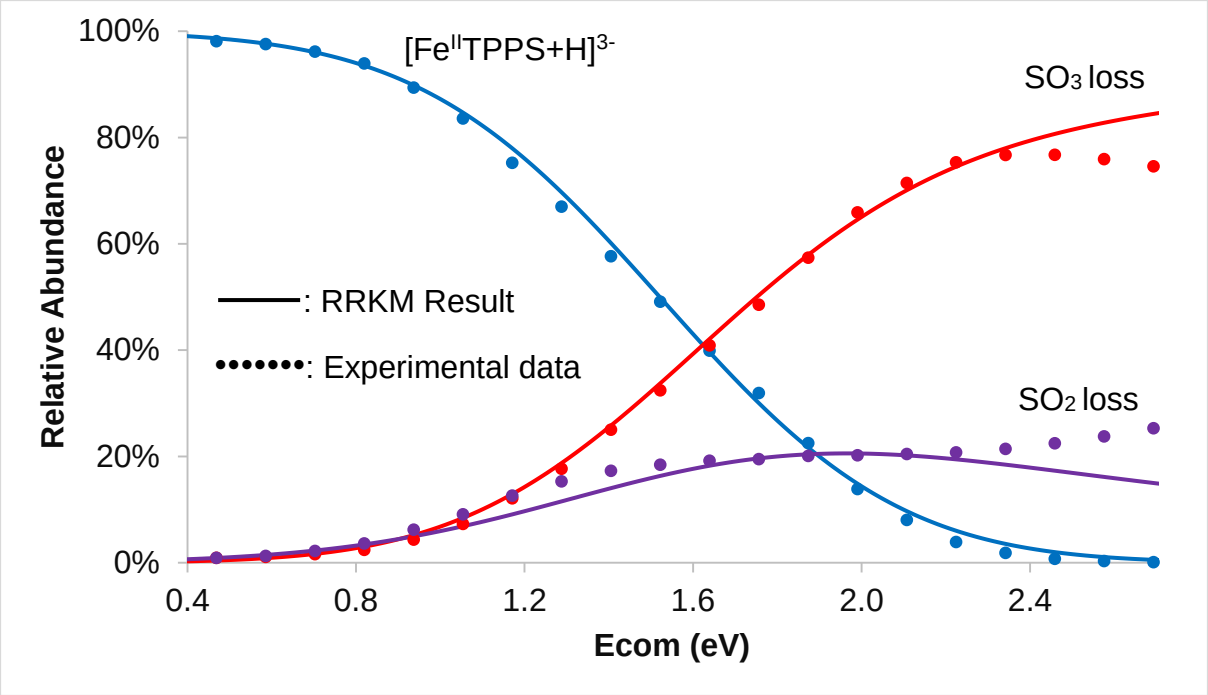

Figure A4.13 RRKM modeling results for the dissociation of [Fe^{II}TPPS+H]$^{3-}$

Table A4.1 contains all the parameters and results of the RRKM modeling. As mentioned in Chapter 2 section 2.3, E_0 and $\Delta^{\ddagger}S$ represent the activation energy and entropy of activation, respectively. T_{ini} is the pre-collision internal temperature of the ions. α represents the influence of the center-of-mass collision energy E_{com} on the post-collision effective temperature T_{eff}.

Table A4.1 RKKM modeling results for the dissociation of [Fe^{II}TPPS+H]$^{3-}$

Parent Ion	**IMS**	**RRKM Parameters**		**Channel**	**E_0** (eV)	**Entropy** (J.mol^{-1}·K^{-1})
		T_{ini} (K)	α (K·eV^{-1})			
[Fe^{II}TPPS+H]$^{3-}$	Off	400	150	SO$_3$ loss	0.80 ± 0.10	-81 ± 15
				SO$_2$ loss	0.55 ± 0.10	-132 ± 15

Appendix 5. RRKM modeling for the dissociation of $[Fe^{II}TPPS+2H]^{2-}$

A5.1 ESI-MS of $Fe^{II}TPPS$

As discussed in section A4.1 of Appendix 4, the mass spectrum of $Fe^{II}TPPS$ shows that there are different charge states of $Fe^{II}TPPS$ in a methanol solution, including $[Fe^{II}TPPS]^{4-}$, $[Fe^{II}TPPS+2H]^{2-}$, and a minimal amount of $[Fe^{II}TPPS+2H]^{2-}$. In this chapter, the primary focus is to study $[Fe^{II}TPPS+2H]^{2-}$. Mass spectrum (MS) (Figure A5.1) shows that the peak m/z 493.0 is a mix of monomer $[Fe^{II}TPPS+2H]^{2-}$ and dimer $[(Fe^{II}TPPS)_2+4H]^{4-}$. When selecting $Fe^{II}TPPS$ at m/z 493.0 by quadrupole and then separating it by ion mobility separation (IMS), IMS shows that m/z 493.0 contains a large abundance of both monomer and dimer in high concentration (2.5×10^{-4} mol/L), but for the vast majority it is composed of monomer at low concentration (0.5×10^{-5} mol/L) (Figure A5.1).

In order to achieve good concentration of monomer $[Fe^{II}TPPS+2H]^{2-}$ all while protecting the instrument, a low concentrated $Fe^{II}TPPS$ solution was used for the following ESI-MS/MS experiment. Figure A5.2 describes the mass spectrum of monomer after they were separated by IMS. In general, this figure coincides with its isotope model pretty well with the exception of the small peak at 492.6 (corresponding $[Fe^{II}TPPS+H]^{2-}$).

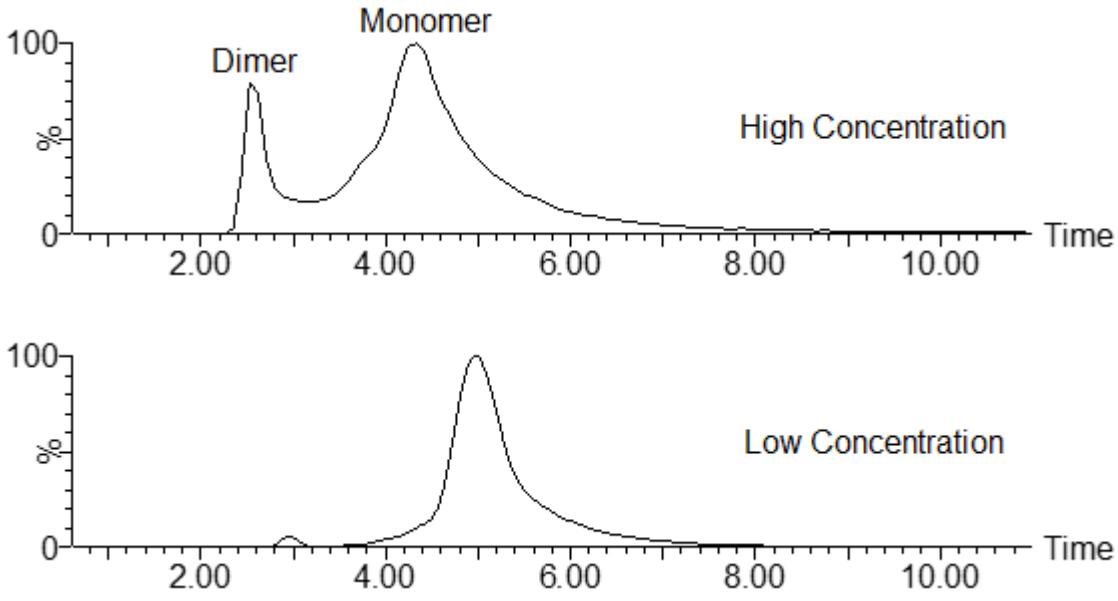

Figure A5.1 Ion mobility spectrometry of $Fe^{II}TPPS$ at high (2.5×10^{-4} mol/L) and low (0.5×10^{-5} mol/L) concentration

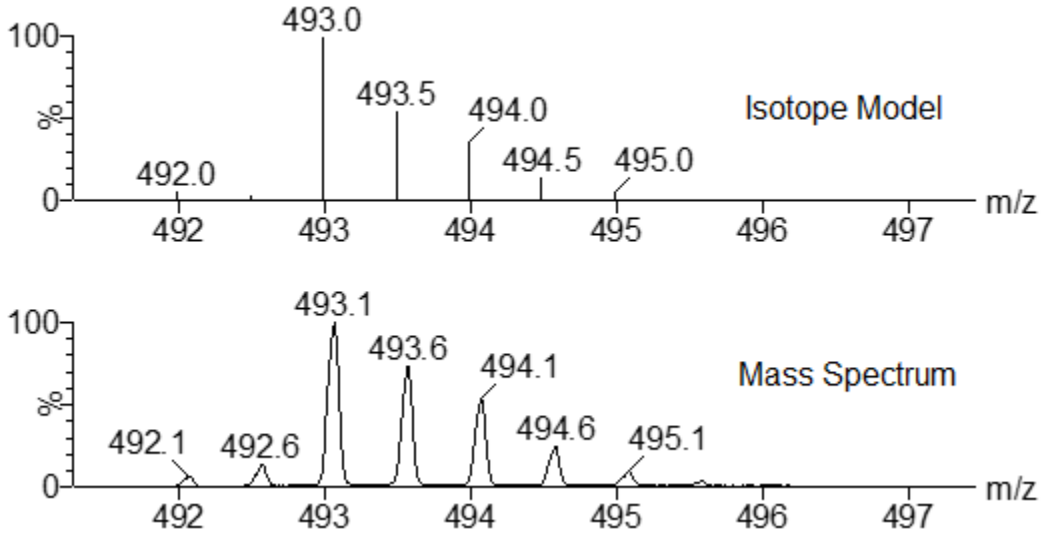

Figure A5.2 Mass spectrum of monomer $[Fe^{II}TPPS+2H]^{2-}$ and its isotope model

A5.2 ESI-MS/MS of $[Fe^{II}TPPS+2H]^{2-}$

The CID of $[Fe^{II}TPPS+2H]^{2-}$ was selected at m/z 493.0 with the collision voltage ranging from 4 V to 62 V. Increases of the collision voltage have the effect of breaking up the parent ion $[Fe^{II}TPPS+2H]^{2-}$ to the point at which it disappears entirely and only fragment ions are observed (Figure A5.4). At low collision energy, fragment ions are only m/z 453.1 and 461.2, but at higher collision energies, more fragment ions are formed. The lower half of Figure A5.3 contains all the main fragment ions resulting from the dissociation of $[Fe^{II}TPPS+2H]^{2-}$. The m/z of those fragment ions are 381.2, 389.2, 406.7, 413.2, 421.2, 429.1, 446.1, 453.1, 461.2, 669.3, 682.4, 698.4, 714.4, 733.3, 746.3, 762.3, 778.3, 813.3, 826.3, 842.3, and 905.3.

Figure A5.4 represents the breakdown diagram of $[Fe^{II}TPPS+2H]^{2-}$ with all the main fragment ions. They are plotted as a function of center-of-mass collision energy (E_{com}), which is a fraction of the laboratory kinetic energy (E_{lab}) (Equation 2.6). E_{lab} equals the collision voltage V_{lab} multiplied by the charge state of $[Fe^{II}TPPS+2H]^{2-}$ (Equation 2.5).

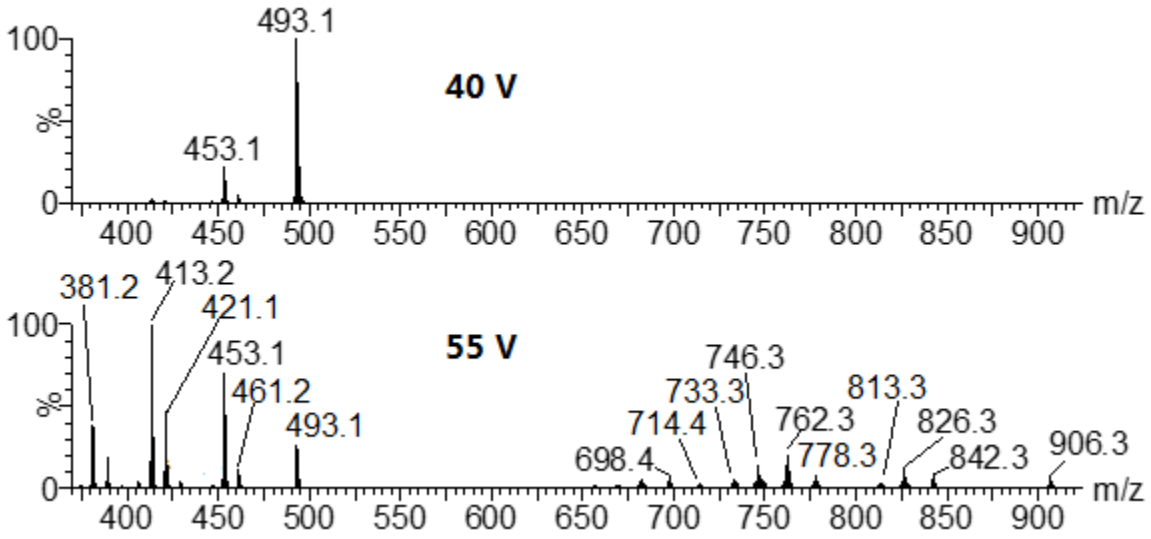

Figure A5.3 CID mass spectra of $[Fe^{II}TPPS+2H]^{2-}$ at different collision voltages. (There is no space in the MS to display the intensities of the following peaks with m/z: 389.2, 406.7, 429.1, 446.1, 669.3, and 682.4)

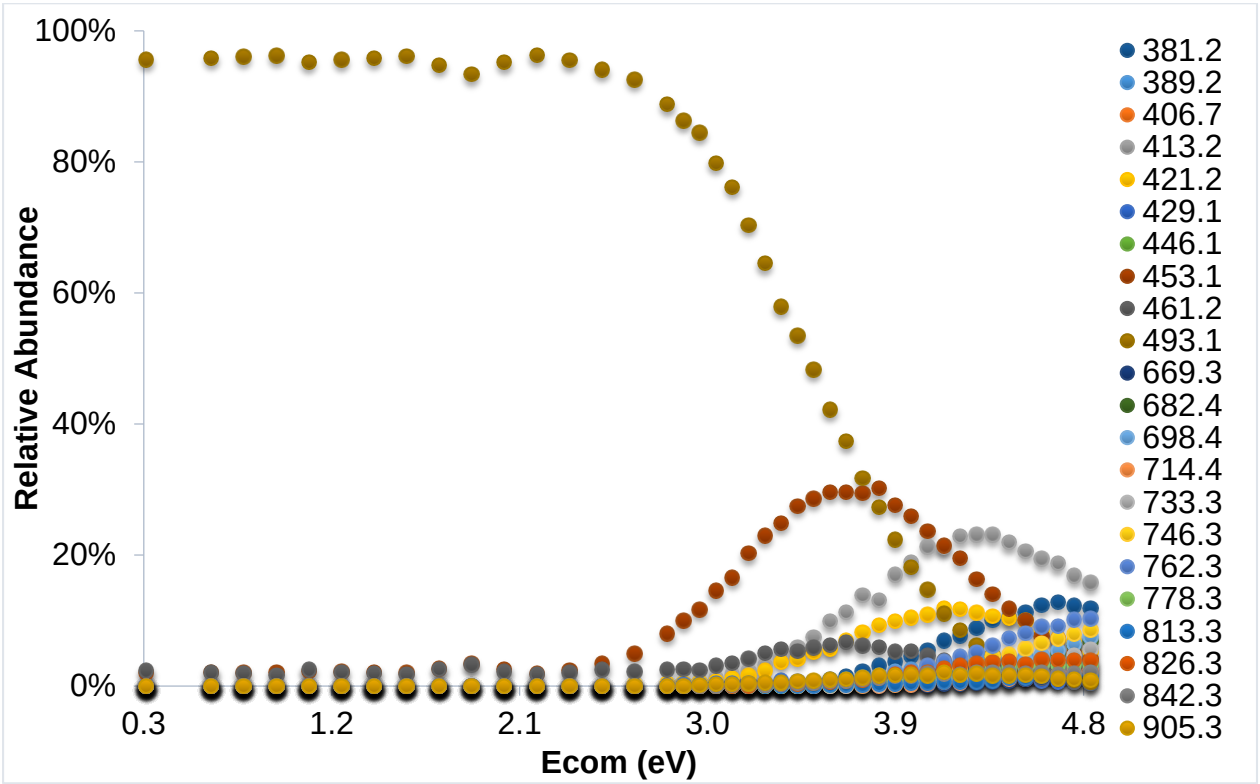

Figure A5.4 Breakdown diagram of $[Fe^{II}TPPS+2H]^{2-}$ with all the fragment ions

A5.3 Structure of parent and fragment ions

There are two possible structures of the parent ion $[Fe^{II}TPPS+2H]^{2-}$ (Figure A5.5). To know which structure is preferred, molecular simulations were performed to investigate the minimum energy state by using a B3-LYP/6-31G(d, p)+LANL2DZ//PM7 basis set, which was a combination of the 6-31G(d, p) basis set and the LANL2DZ effective core basis set. Molecular simulations show that the structure with two $–SO_3H$ functional groups at opposite positions is 0.16 eV lower in energy, compared with the structure with two $–SO_3H$ functional groups at adjacent positions. Therefore, the parent ion $[Fe^{II}TPPS+2H]^{2-}$ should have a structure with $–SO_3H$ functional groups in opposite positions.

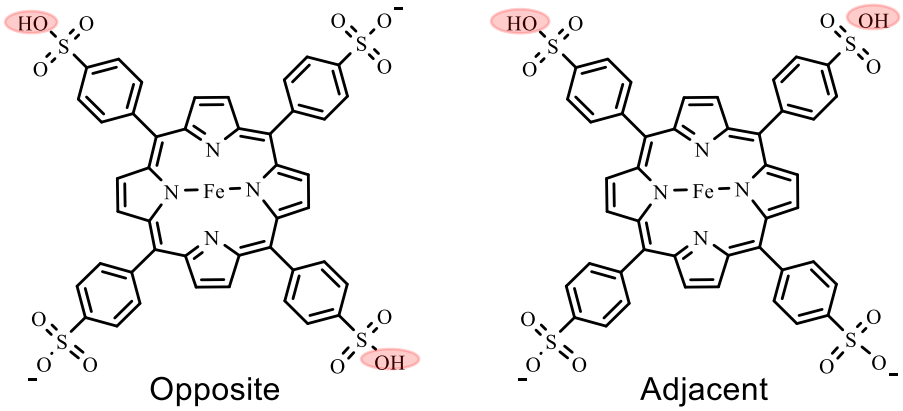

Figure A5.5 Possible structures of $[Fe^{II}TPPS+2H]^{2-}$: a) structure with two $–SO_3H$ functional groups in opposite positions, b) structure with two $–SO_3H$ functional groups in adjacent positions.

The structure of fragment ions mentioned in the section A5.2 can be calculated mathematically. For example, the mass spectrum shows that the fragment ion with m/z 453.1 has a -2 charge (Δm/z of adjacent peaks at m/z 453.1 is 0.5), so the mass

difference of this fragment ion and the parent ion is 2 × (493.1 – 453.1) = 80.0. Considering that the big porphyrin ring has four benzenesulfonate functional groups that might lose SO_3, the difference of m/z 80.0 should be a neutral SO_3, and the fragment ion m/z 453.1 should be $[Fe^{II}TPPS+2H-SO_3]^{2-}$. This result agrees with the mass spectrum isotope model of $[Fe^{II}TPPS+2H-SO_3]^{2-}$ from MassLynx (Figure A5.6). In the same manner, structures of all the fragment ions from $[Fe^{II}TPPS+2H]^{2-}$ dissociation were estimated. Figure A5.7 lists all of them.

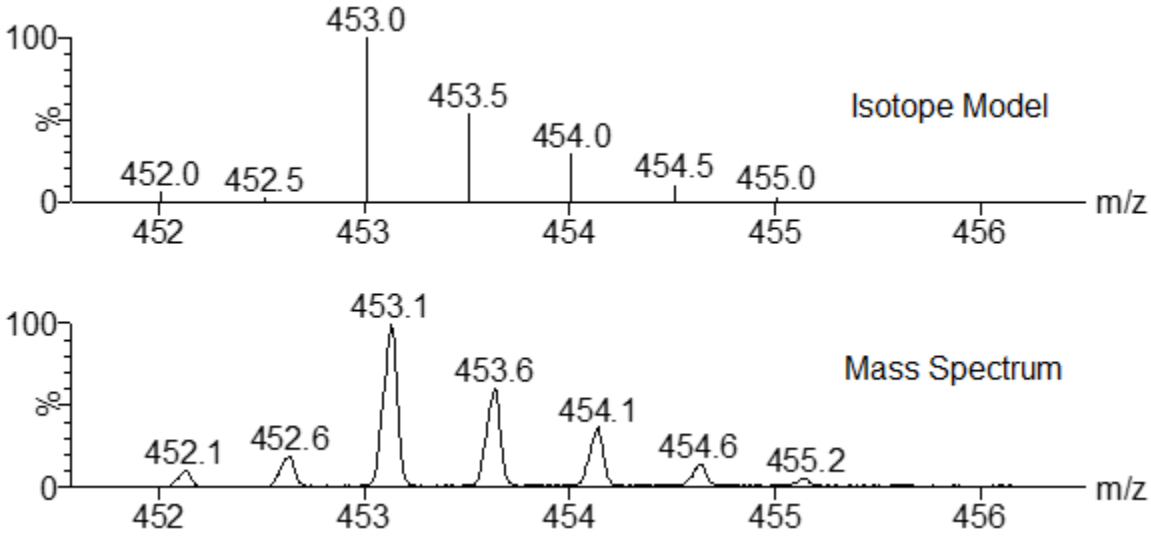

Figure A5.6 Mass spectrum of $[Fe^{II}TPPS+2H-SO_3]^{2-}$ and its isotope model

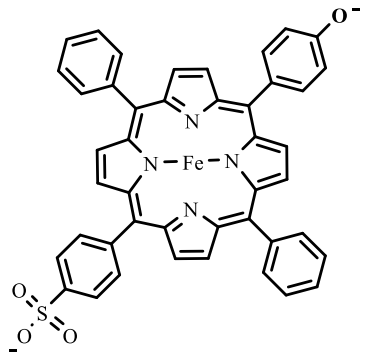

381.1: $[Fe^{II}TPPS+2H-2SO_3-SO_2]^{2-}$

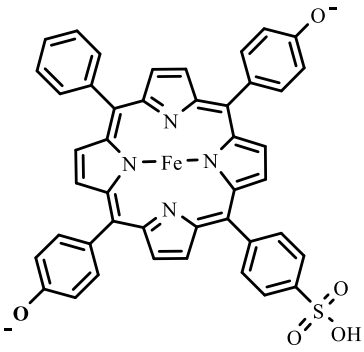

389.1: $[Fe^{II}TPPS+2H-SO_3-2SO_2]^{2-}$

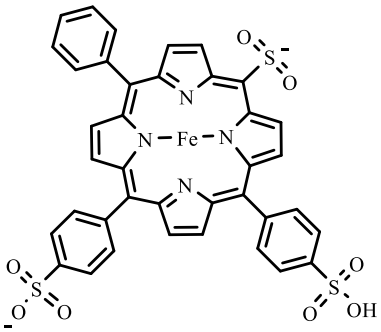

407.0: $[Fe^{II}TPPS+2H-C_6H_4O-SO_3]^{2-}$

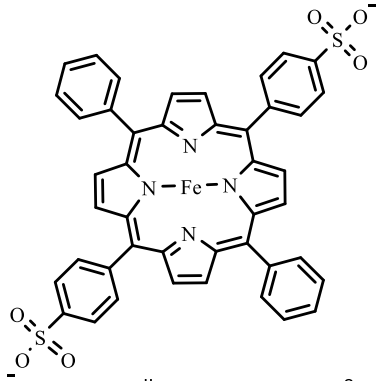

413.0: $[Fe^{II}TPPS+2H-2SO_3]^{2-}$

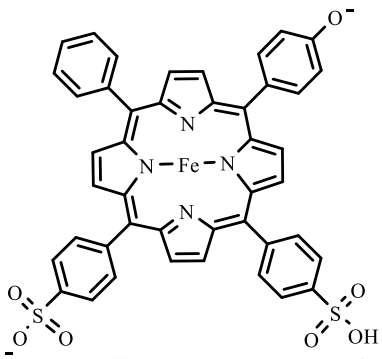

421.0: $[Fe^{II}TPPS+2H-SO_3-SO_2]^{2-}$

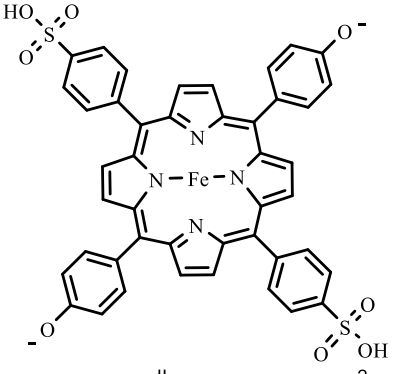

429.0: $[Fe^{II}TPPS+2H-2SO_2]^{2-}$

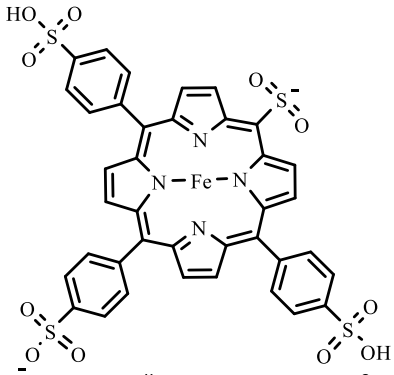

447.0: $[Fe^{II}TPPS+2H-C_6H_4O]^{2-}$

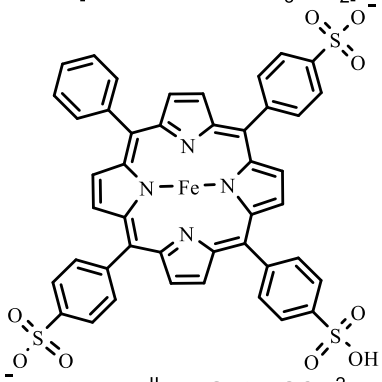

453.0: $[Fe^{II}TPPS+2H-SO_3]^{2-}$

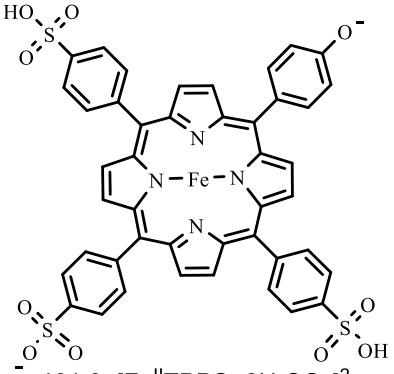

461.0: $[Fe^{II}TPPS+2H-SO_2]^{2-}$

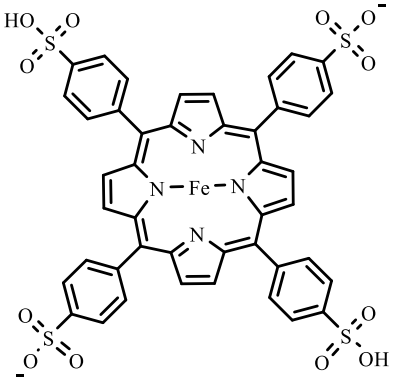

493.0: $[Fe^{II}TPPS+2H]^{2-}$

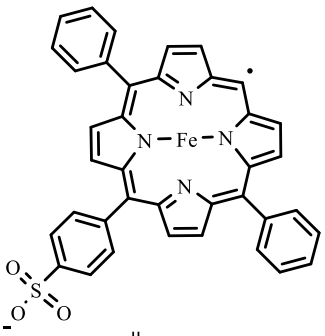

670.1: $[Fe^{II}TPPS+2H-3SO_3-C_6H_4]^{-}$

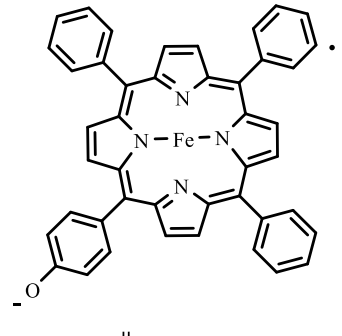

682.2: $[Fe^{II}TPPS+2H-3SO_3-SO_2]^{-}$

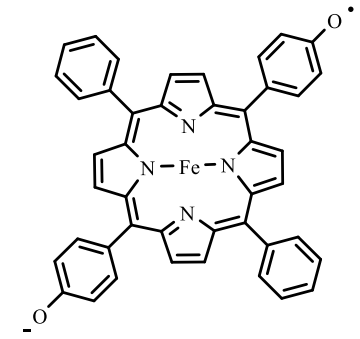

698.1: $[Fe^{II}TPPS+2H-2SO_3-2SO_2]^-$

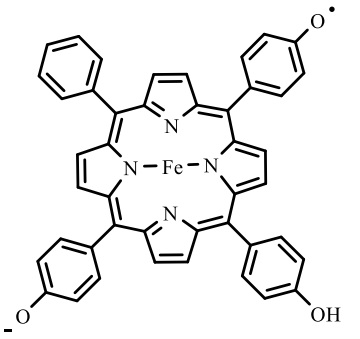

714.1: $[Fe^{II}TPPS+2H-SO_3-3SO_2]^-$

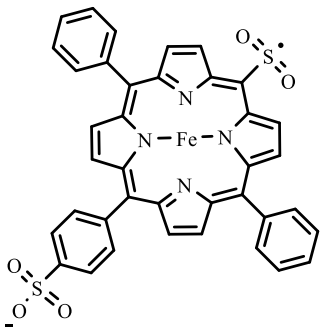

734.0: $[Fe^{II}TPPS+2H-C_6H_4O-2SO_3]^-$

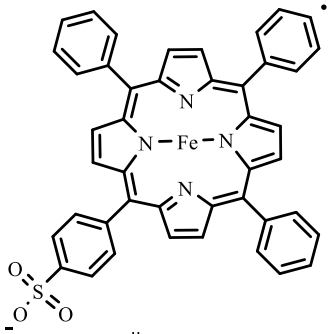

746.1: $[Fe^{II}TPPS+2H-3SO_3]^-$

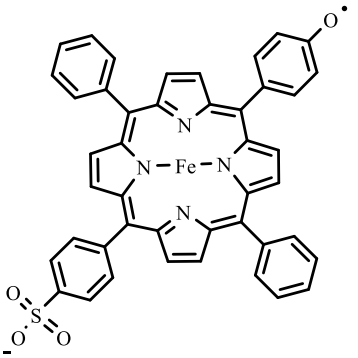

762.1: $[Fe^{II}TPPS+2H-2SO_3-SO_2]^-$

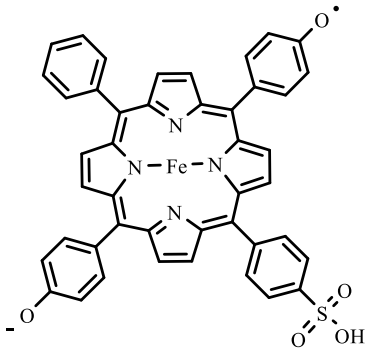

778.1: $[Fe^{II}TPPS+2H-SO_3-2SO_2]^-$

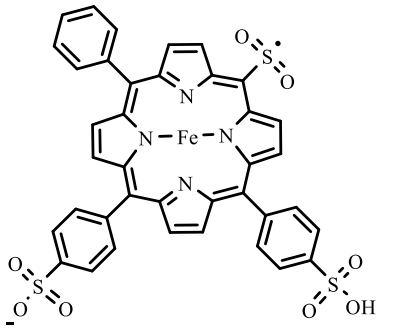

814.0: $[Fe^{II}TPPS+2H-C_6H_4O-SO_3]^-$

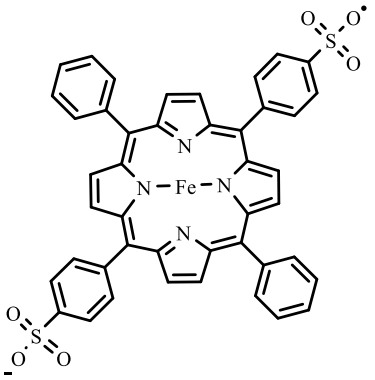

826.1: $[Fe^{II}TPPS+2H-2SO_3]^-$

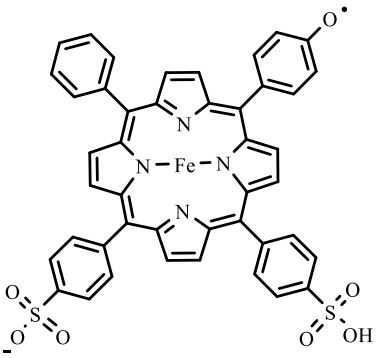

842.1: $[Fe^{II}TPPS+2H-SO_3-SO_2]^-$

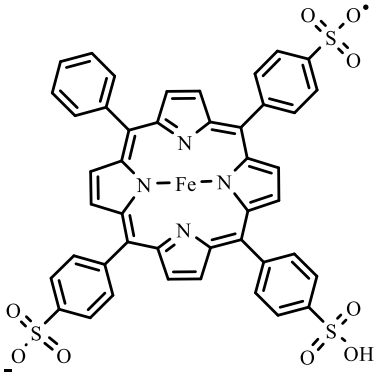

906.0: $[Fe^{II}TPPS+2H-SO_3]^-$

Figure A5.7 Possible structures of fragment ions from the $[Fe^{II}TPPS+2H]^{2-}$ dissociation.

A5.4 In-source-CID-MS/MS and the map of the fragmentation pathways

There are 21 main fragment ions from the dissociation of $[Fe^{II}TPPS+2H]^{2-}$ as mentioned in section A5.3. However, the pathways that these fragment ions take are still not clear. Structures of these fragment ions shows that all the fragment ions result from the loss of one or several neutral/negative SO_2, SO_3, and C_6H_4O. When the collision voltage is low, only fragment ions with m/z 453.1 and 493.1 appear. They are $[Fe^{II}TPPS+2H-SO_3]^{2-}$ $[Fe^{II}TPPS+2H-SO_2]^{2-}$, respectively. This is reasonable considering that $[Fe^{II}TPPS+2H]^{2-}$ has four benzenesulfonate groups, where it can lose SO_2/SO_3 with enough energy. Also, it seems that the other fragment ions, which appear at a higher collision voltage, may all come from the breakup of the two main fragment ions $[Fe^{II}TPPS+2H-SO_3]^{2-}$ and $[Fe^{II}TPPS+2H-SO_2]^{2-}$.

To verify this assumption, the in-source-CID-MS/MS of $[Fe^{II}TPPS+2H-SO_3]^{2-}$ and $[Fe^{II}TPPS+2H-SO_2]^{2-}$ was carried out. It must be noted that the selected ions should be m/z 453 and 461, instead of 452.5 and 460.5, for $[Fe^{II}TPPS+2H]^{2-}$ (Figure A5.8). The m/z for $[Fe^{II}TPPS+2H]^{2-}$ and $[Fe^{II}TPPS+H]^{3-}$ are both correct, so the instrument error can be ruled out. It should be caused by one hydrogen loss from $[Fe^{II}TPPS+2H]^{2-}$ during the in-source-CID. 65 eV cone voltage in the source might be enough to make H loss happen.

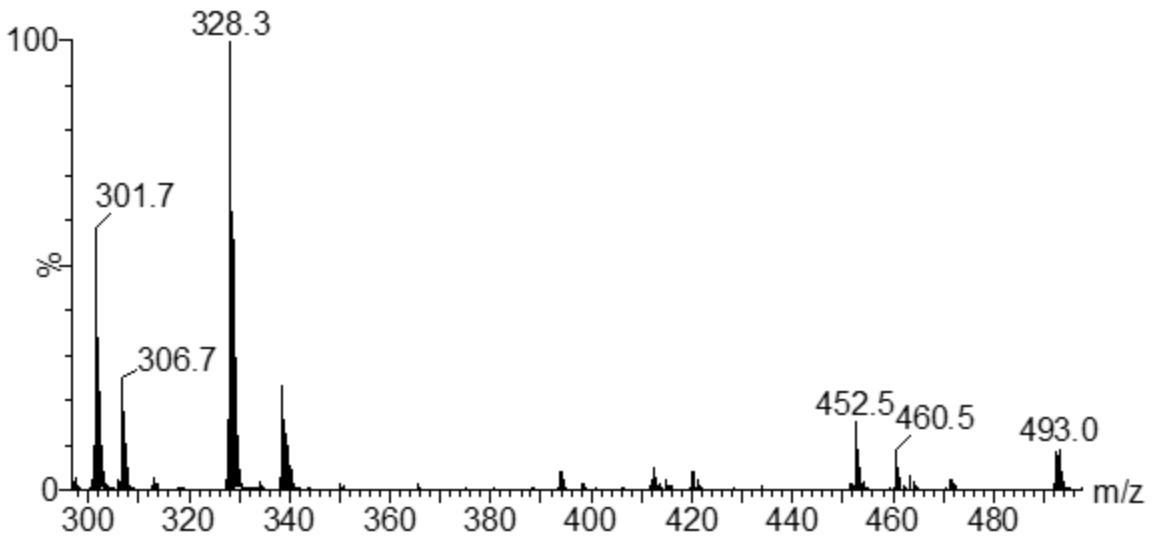

Figure A5.8 In-source-CID-MS of FeTPPS

The in-source-CID used a high sampling cone energy of 65 V to break up the parent ion in the source. Then all the negatively charged fragment ions continued to the quadrupole, where m/z 452.5 or 460.5 were selected and their CID mass spectra obtained.

Figure A5.9 and A5.10 represents the breakdown diagrams of m/z 452.5 and m/z 460.5 from collision voltage 12 V to 32 V, in which the center-of-mass $\mathrm{E_{com}}$ is established on the x axis (see Equation 2.5 and 2.6). There are ten overlapped fragment ions present in both the in-source-CID-MS/MS of m/z 452.5 and m/z 460.5. They are $[Fe^{II}TPPS+2H-SO_3-2SO_2]^{2-}$, $[Fe^{II}TPPS+2H-SO_3-C_6H_4O]^{2-}$, $[Fe^{II}TPPS+2H-SO_3-SO_2]^{2-}$, $[Fe^{II}TPPS+2H-2SO_3-2SO_2]^{-}$, $[Fe^{II}TPPS+2H-SO_3-3SO_2]^{-}$, $[Fe^{II}TPPS+2H-2SO_3-C_6H_4O]^{2-}$, $[Fe^{II}TPPS+2H-2SO_3-SO_2]^{-}$, $[Fe^{II}TPPS+2H-SO_3-2SO_2]^{-}$, $[Fe^{II}TPPS+2H-C_6H_4O-SO_3]^{-}$, and $[Fe^{II}TPPS+2H-SO_3-SO_2]^{-}$. All of the other fragment ions, with the exception of

m/z 906.3, are only present in the breakdown of either m/z 452.5 or m/z 460.5. See Figure A5.11 for the dissociation pathways of $[Fe^{II}TPPS+2H]^{2-}$.

The fragment ion with m/z 906.3 is an independent channel: $[SO_3]^-$ loss from $Fe^{II}TPPS+2H]^{2-}$ directly. However, this channel is ignored because it has a pretty low relative abundance (maximum 0.93%) compared to the other two channels, and it only appears at a high collision energy. Ignoring this channel will not influence the activation energy calculations of the other two channels.

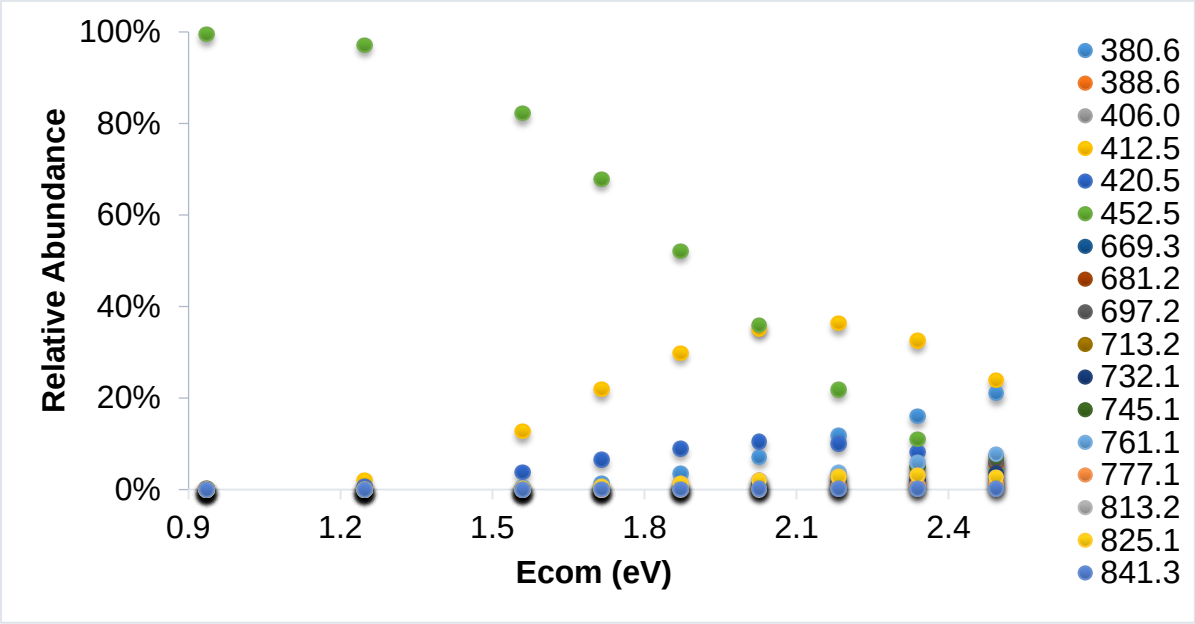

Figure A5.9 In-source-CID-MS/MS of $[Fe^{II}TPPS+2H-SO_3]^{2-}$

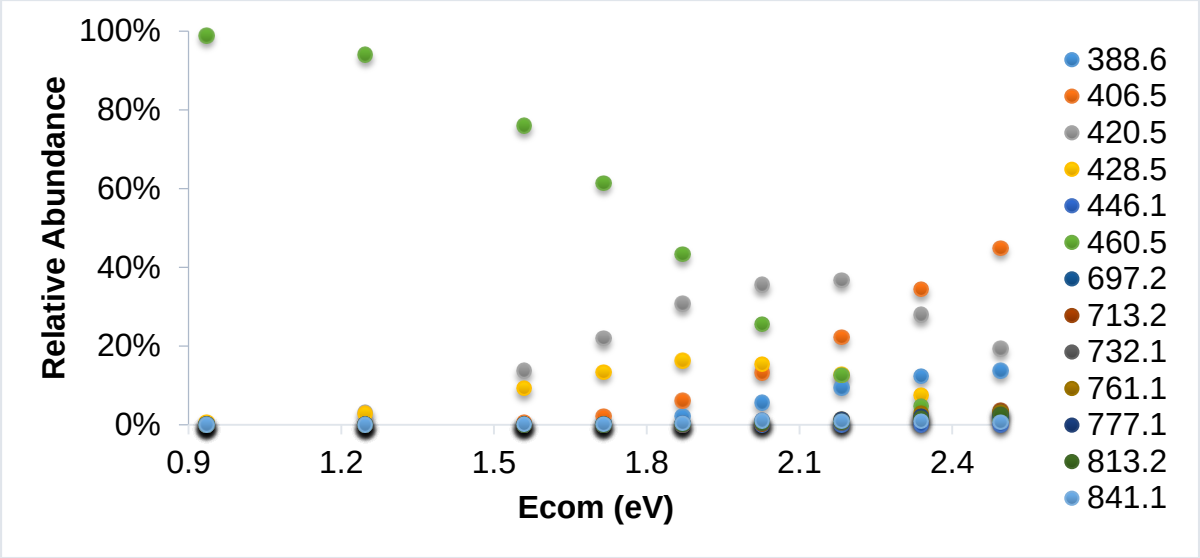

Figure A5.10 In-source-CID-MS/MS of $[Fe^{II}TPPS+2H-SO_2]^{2-}$

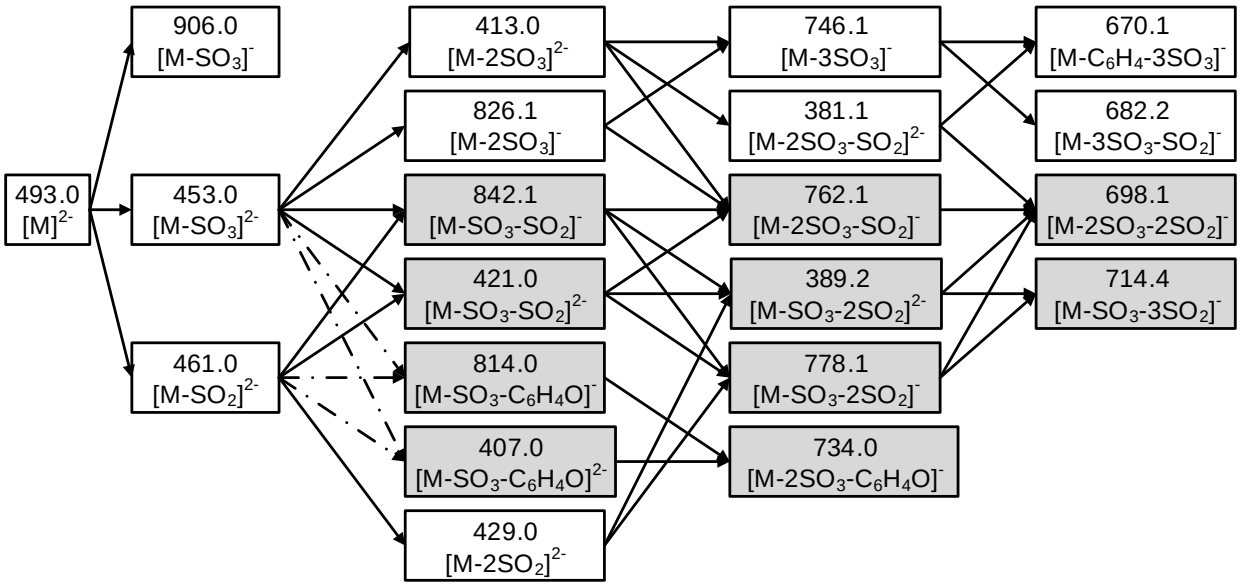

Figure A5.11 Possible dissociation pathways of $[M]^{2-}$ (where M = Fe^{II}TPPS+2H). All the m/z of ions are using theoretical values from Figure A5.7, so some of them are a little different from the experimental m/z. The boxes with light dark background represent overlapped fragment ions. Arrow with dash line means that it is a several steps reaction (There is no space for fragment with m/z 447.0, which should be between m/z 461.0 and 407.0/814.0).

A5.5 Breakdown Diagram

The dissociation pathways of $[Fe^{II}TPPS+2H]^{2-}$ have been evaluated in section A5.4. All the fragment ions, except for $[Fe^{II}TPPS+2H-SO_3]^{2-}$, are created by these two channels: the breakdown of $[Fe^{II}TPPS+2H-SO_3]^{2-}$ and $[Fe^{II}TPPS+2H-SO_2]^{2-}$. However, the division of those ten overlapped fragment ions into these two channels still remains unclear. The total relative abundance percentage of all the overlapped fragment ions increases from 0 to 43.8% when increasing the collision energy (Figure A5.12), which is too significant to ignore. The contribution of $[Fe^{II}TPPS+2H-SO_3]^{2-}$ to these four overlapped fragment ions are calculated by Equation 4.1.

Figure A5.13 shows the % contributions of $[Fe^{II}TPPS+2H-SO_3]^{2-}$ to those ten overlapped fragment ions. In general, the % contributions are consistent when increasing the collision voltage. As a result, the average percentage value of each overlapped fragment ion was used to divide the overlapped fragment ions to the channels $[Fe^{II}TPPS+2H-SO_3]^{2-}$ and $[Fe^{II}TPPS+2H-SO_2]^{2-}$ for the breakdown diagram of the parent ion $[Fe^{II}TPPS+2H]^{2-}$.

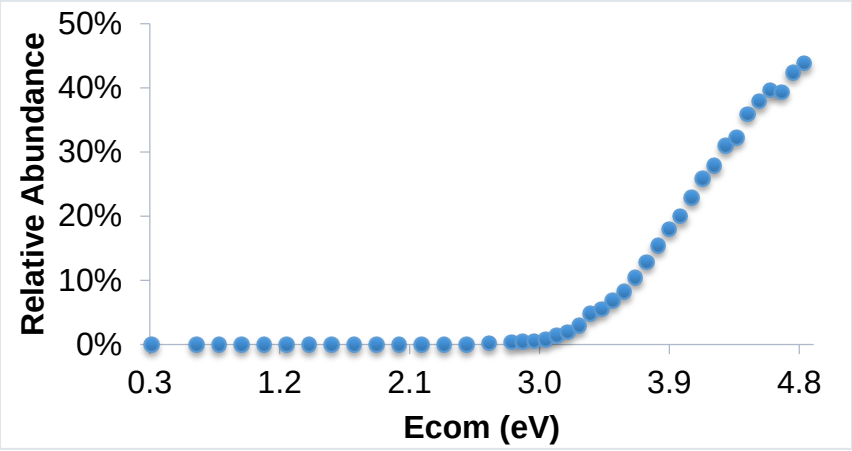

Figure A5.12 Total relative abundance of the overlapped fragment ions from both $[Fe^{II}TPPS+2H-SO_3]^{2-}$ and $[Fe^{II}TPPS+2H-SO_2]^{2-}$

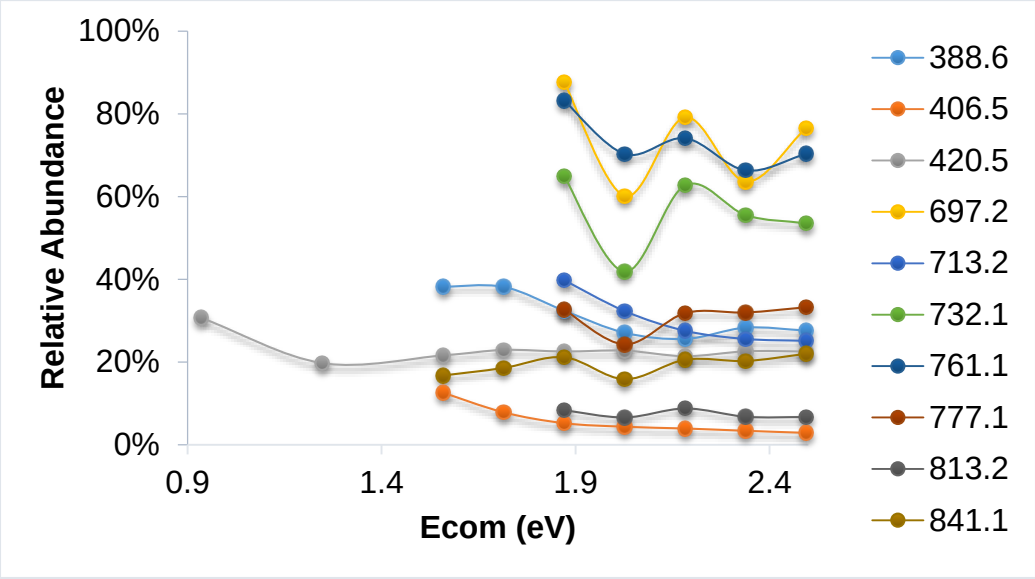

Figure A5.13 Relative abundance % contribution from $[Fe^{II}TPPS+2H-SO_3]^{2-}$ to the overlapped fragment ions

Thus, equation 4.1 was used to assign the appropriate percentage of the ten overlapping channels to the two main fragment ions to produce the breakdown diagram in Figure A5.14.

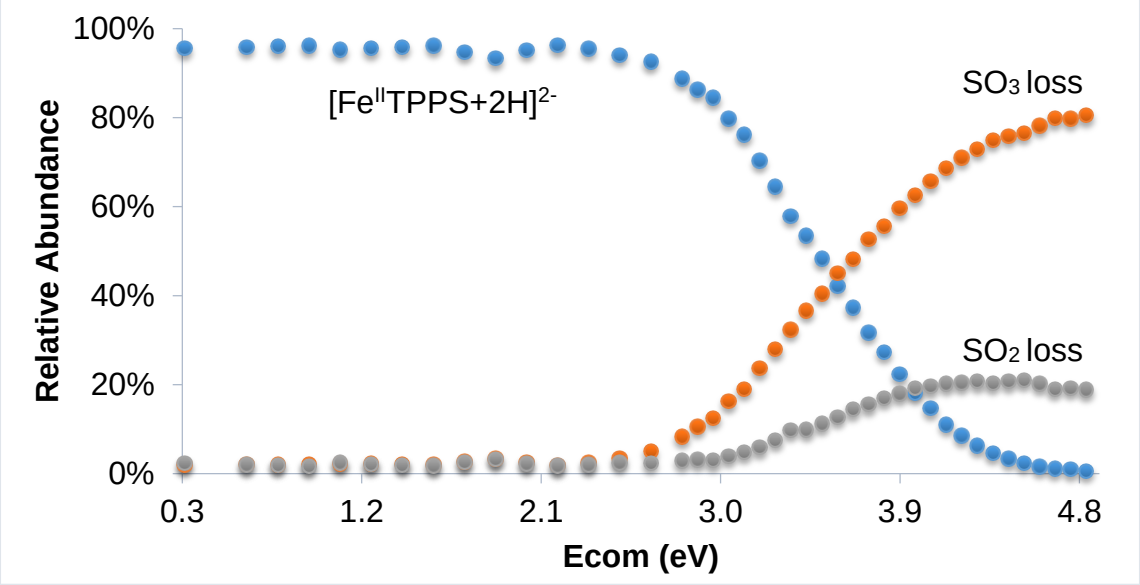

Figure A5.14 Final breakdown diagram for the dissociation of $[Fe^{II}TPPS+2H]^{2-}$

A5.6 RRKM modeling

RRKM theory was applied to model the dissociation of $[Fe^{II}TPPS+2H]^{2-}$ in order to obtain meaningful relative energies by using the harmonic vibrational frequencies of $[Fe^{II}TPPS+2H]^{2-}$ (see Table A6.1 in Appendix 6). Figure A5.15 shows that the theoretical RRKM modeling and experimental breakdown diagram. They match each other pretty well, but RRKM cannot model the end of those two channels. This can be ignored for the following two reasons:

a) Many news fragment ions, that only appeared at a low abundance when $\mathrm{E_{com}}$ became high, were not accounted.

b) The division of fragment ions to those two channels might not be accurate because ESI-MS/MS and in-source-CID-MS/MS were in different experimental condition, and the real contribution of those channels to the overlapped fragment ions are changing slightly with the increase of $\mathrm{E_{com}}$.

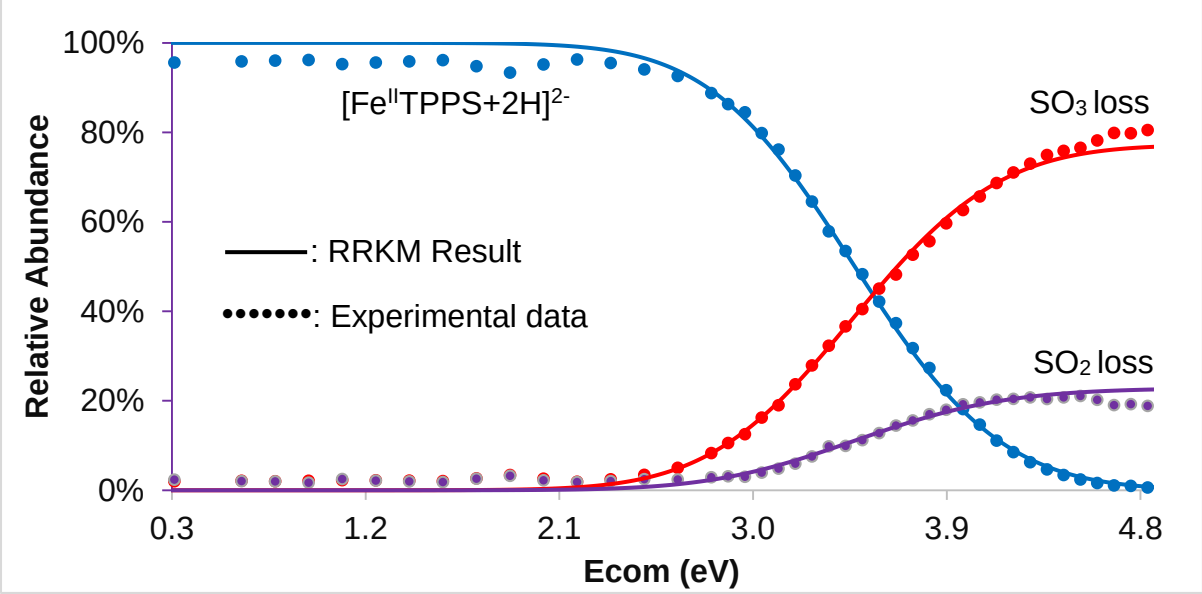

Figure A5.15 RRKM modeling results for the dissociation of $[Fe^{II}TPPS+2H]^{2-}$

Table A5.1 contains all the parameters and results of the RRKM modeling. As mentioned in section 2.3, E_0 and $\Delta^{\ddagger}S$ represent the activation energy and entropy of activation, respectively. T_{ini} is the pre-collision internal temperature of the ions. α represents the influence of the center-of-mass collision energy E_{com} on the post-collision effective temperature T_{eff}. See Chapter 6 for the discussion of the meaning of these parameters.

Table A5.1 RKKM modeling results for the dissociation of $[Fe^{II}TPPS+2H]^{2-}$

Parent Ion	**IMS**	**RRKM Parameters**		**Channel**	**E_0** (eV)	**$\Delta^{\ddagger}S$** ($J.mol^{-1}\cdot K^{-1}$)
		T_{ini} (K)	α ($K\cdot eV^{-1}$)			
$[Fe^{II}TPPS+2H]^{2-}$	On	400	150	SO_3 loss	1.47 ± 0.01	-48 ± 5
				SO_2 loss	1.49 ± 0.01	-57 ± 5

Appendix 6. Tables

Table A6.1 Harmonic vibrational frequencies of $[Ni^{II}TPPS+H]^{3-}$, $[Co^{III}TPPS]^{3-}$, $[Mn^{III}TPPS]^{3-}$, $[Mn^{III}TPPS+H]^{2-}$, $[Fe^{II}TPPS+H]^{3-}$, and $[Fe^{II}TPPS+2H]^{2-}$ for modeling their breakdown diagrams

	Harmonic vibrational frequencies (cm^{-1})
$[Ni^{II}TPPS+H]^{3-}$	6.67, 8.27, 8.48, 8.83, 12.43, 13.17, 15.93, 16.87, 17.77, 21.82, 25.49, 28.38, 31.29, 32.65, 34.02, 44.77, 60.23, 75.93, 78.24, 85.70, 89.04, 95.20, 105.01, 107.82, 109.35, 126.26, 129.19, 134.52, 137.50, 143.57, 147.78, 150.62, 158.36, 168.42, 188.55, 194.86, 200.46, 208.57, 214.93, 225.23, 235.50, 248.34, 257.07, 267.79, 272.60, 274.85, 280.55, 289.82, 294.34, 300.01, 313.80, 317.78, 321.77, 323.01, 326.63, 330.17, 333.23, 337.16, 341.34, 347.70, 347.99, 348.85, 355.48, 359.97, 364.19, 380.42, 397.42, 422.64, 428.23, 431.78, 433.79, 439.87, 443.28, 462.20, 463.46, 467.42, 468.47, 469.68, 474.05, 474.91, 483.24, 486.38, 514.35, 533.99, 544.73, 553.32, 553.85, 567.47, 571.46, 572.60, 576.50, 582.11, 582.79, 590.05, 599.77, 602.45, 604.37, 607.29, 608.75, 610.89, 612.80, 625.35, 667.72, 675.55, 679.57, 680.64, 711.14, 718.36, 720.67, 725.95, 729.56, 731.77, 744.22, 747.05, 749.87, 761.95, 796.72, 799.05, 823.24, 846.51, 864.17, 864.78, 866.72,, 870.11, 872.22, 872.88, 877.76, 878.45, 878.83, 879.74, 880.49, 891.37, 898.70, 908.64, 912.30, 927.97, 929.74, 936.16, 936.86, 939.32, 941.76, 943.93, 956.36, 970.40, 971.17, 971.27, 972.97, 975.30, 975.73, 975.89, 982.08, 986.34, 995.70, 1001.55, 1017.02, 1017.63, 1055.33, 1063.10, 1063.61, 1063.94, 1064.21, 1064.91, 1065.45, 1067.50, 1087.69, 1088.97, 1089.34, 1089.41, 1090.84, 1097.06, 1109.82, 1115.51, 1124.20, 1127.96, 1130.65,1132.45, 1146.86, 1154.36, 1163.96, 1176.92, 1182.35, 1189.57, 1207.91, 1210.75, 1211.25, 1214.18, 1214.69, 1214.94, 1215.43, 1215.70, 1226.70, 1253.14, 1257.22, 1261.21, 1281.77, 1282.03, 1282.43, 1284.89, 1288.09, 1292.51, 1315.29, 1340.15, 1344.61, 1357.51, 1359.22, 1365.11, 1372.33, 1376.97, 1410.30, 1422.44, 1431.46, 1453.04, 1454.22, 1454.55, 1464.83, 1496.80, 1509.31, 1518.79, 1521.78, 1524.47, 1539.39, 1550.68, 1564.73, 1578.90, 1581.26, 1587.33, 1611.29, 1619.32, 1621.64, 1623.08, 1632.92, 1647.37, 1647.72, 1649.30, 1649.91, 1658.97, 1678.02, 1745.89, 1749.99, 2487.52, 2725.89, 2726.65, 2729.70, 2730.16, 2730.39, 2731.59, 2732.44, 2732.83, 2754.21, 2757.13, 2759.18, 2759.61, 2760.17, 2762.12, 2762.62, 2762.82, 2765.49, 2765.96, 2770.87, 2772.56, 2782.49, 2783.72, 2783.80, 2785.60
$[Co^{III}TPPS]^{3-}$	5.82, 5.96, 6.52, 6.57, 7.06, 14.68, 16.47, 17.82, 17.83, 25.52, 28.64, 28.69, 34.88, 39.79, 42.40, 42.46, 64.42, 68.45, 71.39, 87.66, 87.73, 89.50, 99.67, 99.72, 108.61, 113.83, 116.54, 127.31, 139.22, 141.14, 141.15, 155.80, 155.90, 185.64, 194.27, 194.27, 205.01, 217.71, 224.23, 224.30, 224.33, 241.22, 249.57, 258.07, 258.09, 266.92, 292.04, 298.48, 300.64, 300.65, 313.27, 313.28, 324.51, 326.27, 329.78, 329.85, 332.72, 332.82, 343.84, 343.86, 346.75, 347.25, 347.81, 347.85, 355.41, 397.42, 409.36, 409.36, 418.81, 426.78, 430.96, 430.99, 431.73, 462.11, 464.54, 464.60 , 464.94, 466.88, 469.96, 476.15, 476.19, 505.59, 525.60, 525.62, 539.04, 560.28, 560.40, 562.67, 572.14, 576.17, 578.66, 578.74, 583.36, 604.27, 604.27, 605.27, 605.36, 607.81, 609.32, 609.32, 613.12, 668.83, 671.87, 671.88,

	676.74, 703.06, 713.89, 713.90, 721.80, 727.38, 737.08, 737.08, 744.62, 747.08, 763.58, 763.58, 775.33, 857.35, 867.21, 867.22, 869.03, 871.47, 873.71, 874.44, 874.49, 876.22, 877.64, 877.69, 888.16, 889.69, 889.74, 890.03, 890.97,934.66, 935.02, 935.03, 938.35, 943.22, 943.78, 943.81, 944.30, 970.53, 971.63, 971.65, 971.71, 971.74, 975.23, 975.25, 976.14, 976.62, 977.35, 977.36, 982.33, 1055.88, 1058.05, 1058.07, 1059.49, 1070.42, 1070.89, 1070.97, 1071.75, 1074.66, 1075.38, 1075.57, 1076.28, 1081.36, 1092.37, 1092.38, 1099.99, 1104.53, 1104.59, 1104.63, 1104.97, 1115.44, 1117.19, 1117.19, 1119.32, 1172.68, 1174.34, 1174.35, 1174.83, 1208.73, 1214.19, 1214.22, 1214.23, 1214.52, 1218.14, 1218.15, 1219.56, 1220.79, 1222.87, 1223.10, 1223.20, 1249.28, 1249.45, 1249.59, 1257.83, 1280.63, 1280.66, 1280.67, 1280.74, 1321.16, 1327.19, 1327.19, 1327.27, 1352.60, 1372.77, 1372.78, 1380.31, 1452.36, 1452.49, 1452.49, 1452.61, 1500.75, 1500.76, 1500.87, 1500.92, 1540.28, 1540.30, 1541.69, 1544.16, 1589.36, 1592.39, 1592.40, 1594.21, 1643.29, 1643.51, 1643.53, 1643.72, 1651.97, 1654.30, 1654.45, 1654.50, 1704.27, 1734.25, 1734.29, 1756.32, 2722.01, 2722.09, 2722.13, 2722.77, 2726.33, 2726.67, 2726.82, 2727.12, 2739.58, 2740.20, 2740.25, 2740.85, 2752.19, 2752.58, 2753.11, 2753.70, 2756.56, 2756.95, 2756.95, 2757.57, 2760.83, 2760.96, 2760.98, 2761.01
$[Mn^{III}TPPS]^{3-}$	4.94, 4.96, 6.48, 6.87, 9.44, 13.35, 14.74, 14.90, 16.37, 16.49, 21.56, 22.53, 23.93, 29.50, 33.23, 33.29, 35.16, 76.45, 77.14, 81.78, 85.59, 87.10, 93.09, 93.96, 108.63, 112.19, 125.21, 136.51, 138.16, 138.57, 149.92, 152.04, 153.54, 180.83, 194.35, 195.78, 199.69, 212.83, 229.84, 232.84, 234.36, 246.43, 251.61, 270.75, 271.14, 282.99, 289.08, 298.80, 311.75, 311.96, 322.20, 322.22, 323.68, 329.29, 330.71, 334.21, 335.92, 339.24, 346.76, 347.04, 347.40, 347.58, 354.48, 355.94, 363.88, 425.83, 428.40, 430.84, 434.42, 435.19, 451.18, 459.46, 460.29, 463.09, 468.70, 468.99, 471.00, 473.97, 476.83, 496.78, 497.12, 548.11, 554.09, 554.49, 559.72, 562.44, 567.18, 569.09, 573.15, 576.71, 578.35, 581.07, 584.64, 585.97, 590.26, 597.17, 605.27, 607.26, 607.76, 609.80, 615.08, 673.15, 677.07, 678.01, 680.20, 699.85, 704.88, 705.77, 709.86, 710.31, 718.78, 719.49, 726.40, 756.73, 790.00, 804.80, 816.82, 856.26, 857.71, 860.81, 866.83, 868.80, 869.53, 874.49, 876.53, 877.20, 878.51, 879.82, 882.09, 884.66, 897.83, 904.89, 905.23, 926.37, 926.68, 935.99, 936.14, 936.98, 940.18, 945.36, 946.67, 971.30, 971.54, 971.54, 971.62, 976.11, 976.16, 976.17, 976.21, 991.21, 997.41, 1003.56, 1021.04, 1064.02, 1064.33, 1064.99, 1065.17, 1068.19, 1068.73, 1069.32, 1069.90, 1080.47, 1090.49, 1091.80, 1091.89, 1092.04, 1092.67, 1100.33, 1104.03, 1106.10, 1108.12, 1111.48, 1114.22, 1137.52, 1141.21, 1156.32, 1165.12, 1177.39, 1178.75, 1181.23, 1186.82, 1211.54, 1211.54, 1211.61, 1211.70, 1213.76, 1213.85, 1214.15, 1214.26, 1219.31, 1228.88, 1239.12, 1244.59, 1252.74, 1257.18, 1281.40, 1281.60, 1281.60, 1281.93, 1282.60, 1283.63, 1297.92, 1309.97, 1335.03, 1341.03, 1361.47, 1363.66, 1393.46, 1394.39, 1412.61, 1428.41, 1455.21, 1455.28, 1455.31, 1455.42, 1520.96, 1521.37, 1522.04, 1522.38, 1575.22, 1583.25, 1608.49, 1609.79, 1618.37, 1618.39, 1618.52, 1618.80, 1652.57, 1652.64, 1652.67, 1652.67, 1690.41, 1691.66, 1732.54, 1739.48, 1767.57, 1770.97, 2728.61, 2728.64, 2728.87, 2728.92, 2730.42, 2730.48, 2730.55, 2730.93, 2748.81, 2750.72, 2760.17, 2762.16, 2764.76, 2764.92, 2765.10, 2765.41, 2766.38, 2766.52, 2768.83, 2769.20, 2769.37, 2769.37, 2774.12, 2775.82
$[Mn^{III}TPPS+H]^{2-}$	4.99, 7.93, 8.68, 9.63, 11.43, 13.02, 14.50, 15.24, 15.99, 18.21, 25.56, 26.75, 30.12, 30.96, 33.56, 36.04, 39.45, 73.09, 76.43, 80.33, 82.99, 87.27, 92.81, 95.25, 103.93, 106.49, 114.62, 126.18, 137.23, 137.78, 140.04, 150.62, 151.52, 155.34,

	181.42, 186.69, 196.52, 199.68, 210.33, 229.57, 233.22, 233.79, 245.15, 252.30, 270.02, 270.92, 282.83, 286.31, 297.40, 305.24, 309.24, 316.67, 320.29, 321.97, 324.98, 331.30, 332.78, 335.11, 340.41, 346.17, 346.50, 347.16, 349.36, 353.27, 355.67, 365.39, 416.83, 418.66, 425.82, 429.08, 432.34, 436.01, 450.53, 458.06, 460.26, 461.26, 467.40, 468.35, 471.61, 472.33, 492.96, 496.68, 540.13, 546.79, 554.40, 556.20, 559.99, 560.35, 566.56, 570.98, 575.41, 577.21, 579.32, 581.38, 582.99, 590.64, 598.56, 605.16, 606.39, 607.59, 609.53, 616.16, 671.49, 675.87, 676.31, 680.64, 698.90, 705.43, 706.61, 709.12, 710.82, 716.38, 720.79, 734.32, 756.32, 761.34, 791.20, 805.05, 817.68, 850.91, 859.15, 862.30, 866.95, 868.33, 872.28, 873.97, 875.65, 876.87, 878.15, 882.26, 884.90, 885.90, 898.98, 904.16, 908.58, 923.23, 932.05, 935.17, 935.70, 938.05, 946.91, 948.33, 971.14, 971.35, 971.48, 976.33, 976.55, 976.95, 978.62, 981.62, 989.39, 991.83, 997.13, 1004.07, 1020.42, 1060.94, 1066.93, 1069.51, 1071.03, 1071.56, 1072.13, 1074.74, 1081.29, 1091.29, 1097.48, 1097.71, 1099.43, 1099.53, 1101.43, 1104.68, 1105.48, 1107.32, 1110.73, 1113.70, 1136.21, 1141.65, 1156.80, 1166.24, 1171.00, 1175.54, 1178.23, 1182.53, 1194.41, 1212.17, 1212.38, 1212.79, 1213.76, 1214.57, 1214.81, 1219.72, 1222.82, 1228.31, 1234.69, 1238.64, 1244.32, 1250.13, 1262.19, 1279.88, 1280.43, 1280.76, 1282.95, 1286.39, 1289.86, 1294.15, 1315.07, 1334.87, 1344.22, 1360.67, 1367.13, 1393.07, 1397.07, 1412.64, 1429.47, 1455.40, 1455.82, 1455.96, 1459.22, 1515.94, 1517.54, 1518.14, 1522.11, 1574.48, 1582.92, 1604.08, 1607.16, 1609.59, 1609.90, 1613.15, 1629.83, 1638.20, 1652.76, 1653.83, 1654.28, 1678.79, 1689.41, 1729.31, 1738.15, 1758.27, 1768.98, 2473.06, 2716.65, 2718.35, 2723.14, 2725.24, 2726.34, 2727.09, 2728.25, 2731.29, 2738.41, 2744.32, 2749.99, 2755.87, 2756.02, 2758.76, 2761.19, 2763.00, 2765.06, 2765.27, 2767.06, 2767.88, 2769.12, 2770.26, 2774.25, 2787.68
$[Fe^{II}TPPS+H]^{3-}$	3.00, 4.79, 8.90, 9.35, 12.49, 13.82, 14.99, 16.75, 16.85, 20.36, 23.33, 27.79, 31.86, 32.86, 35.18, 37.23, 45.26, 71.22, 78.38, 83.87, 85.61, 92.32, 96.15, 100.48, 112.72, 114.87, 125.50, 135.11, 137.41, 138.12, 148.89, 152.36, 154.41, 169.05, 189.80, 191.90, 199.75, 201.17, 211.06, 227.27, 232.74, 236.26, 247.35, 252.75, 272.26, 273.18, 276.40, 290.59, 295.02,303.44, 310.38, 317.77, 318.49, 324.45, 327.15, 328.42, 331.75, 332.96, 343.23, 345.94, 347.81, 348.25, 349.02, 349.88, 352.26, 368.67, 412.88, 415.85, 421.68, 426.65, 429.77, 433.50, 441.62, 444.72, 455.46, 458.04, 461.30, 466.59, 469.13, 470.11, 470.24, 482.93, 536.36, 546.38, 551.85, 553.47, 561.26, 563.11, 566.08, 576.81, 577.56, 580.78, 583.38, 590.31, 598.91, 606.62,607.32, 607.84, 619.49, 629.22, 649.01, 664.82, 675.41, 679.21, 680.64, 685.53, 712.52, 719.29, 721.71, 725.04, 730.81, 734.29, 736.87, 741.42, 753.86, 761.73, 777.00, 789.05, 792.81, 850.14, 858.85, 861.25, 864.03, 872.69, 873.81, 874.41, 878.67, 879.27, 880.67, 880.75, 883.03, 884.17, 889.20, 893.30, 900.46, 913.81, 921.16, 935.78, 937.00, 937.23, 937.79, 940.05, 970.89, 971.41, 971.58, 975.33, 975.34, 975.83, 977.55, 980.81, 984.18, 987.48, 992.27, 995.48, 1007.17, 1056.34, 1058.77, 1059.92, 1060.23, 1062.35, 1062.72, 1064.32, 1065.24, 1067.69, 1080.16, 1085.26, 1085.79, 1086.46, 1089.24, 1105.30, 1107.93, 1109.80, 1111.41, 1113.16, 1119.18, 1120.99, 1129.08, 1136.70, 1170.11, 1180.89, 1182.46, 1186.49, 1193.78, 1202.52, 1210.05, 1210.34, 1210.54, 1214.71, 1215.22, 1215.24, 1215.60, 1223.43, 1243.25, 1248.03, 1251.89, 1263.91l, 1268.03, 1273.67, 1281.81, 1282.95, 1283.09, 1283.81, 1291.51, 1296.80, 1307.03, 1316.35, 1325.29, 1353.14, 1356.47, 1369.50, 1371.23, 1454.32, 1454.54, 1454.55, 1459.07, 1499.33, 1501.71, 1504.23, 1506.89, 1517.11, 1519.68, 1527.72, 1528.73, 1570.67, 1577.91, 1623.32, 1625.79, 1626.60, 1627.25, 1628.60, 1642.33, 1649.31, 1649.96, 1649.99, 1675.08, 1679.54, 1682.01, 1712.42, 1723.43, 2480.03, 2722.42, 2723.89,

	2731.57, 2731.99, 2732.05, 2732.99, 2733.98, 2734.45, 2744.01, 2750.30, 2755.49, 2760.41, 2760.83, 2762.21, 2762.54, 2764.03, 2765.78, 2766.30, 2772.04, 2780.79, 2782.98, 2788.80, 2789.94, 2802.52
$[Fe^{II}TPPS+2H]^{2-}$ with two $-C_6H_4SO_3H$ at opposite positions	2.66, 6.75, 8.52, 9.42, 12.38, 13.03, 14.21, 15.10, 16.30, 22.30, 26.93, 28.65, 31.67, 32.57, 33.85, 35.61, 43.35, 72.35, 76.71, 81.93, 84.39, 87.69, 95.79, 99.33, 108.45, 115.34, 126.38, 130.01, 134.50, 137.95, 140.77, 146.82, 149.02, 156.05, 160.01, 186.66, 190.69, 194.75, 198.67, 213.49, 224.20, 227.01, 234.92, 248.89, 252.20, 271.93, 272.76, 275.39, 288.81, 297.28, 302.30, 303.57, 312.11, 317.82, 319.26, 320.23, 326.63, 330.32, 331.57, 342.71, 345.34, 347.03, 347.40, 348.33, 350.46, 351.33, 368.70, 412.49, 415.26, 416.33, 421.94, 424.35, 427.38, 430.22, 438.00, 444.02, 453.46, 454.62, 460.62, 461.60, 468.06, 468.69, 482.69, 538.05, 545.39, 547.33, 550.29, 554.01, 557.99, 560.88, 574.62, 575.48, 577.86, 579.15, 589.72, 597.97, 606.09, 606.65, 607.34, 618.61, 627.69, 651.10, 665.20, 672.21, 678.41, 678.88, 684.49, 713.76 ,718.80, 722.26, 723.51, 732.47, 733.84, 738.17, 741.87, 755.79, 760.40, 761.36, 775.55, 789.01, 793.46, 854.57, 855.23, 859.20, 863.79, 871.75, 872.34, 878.78, 878.82, 879.30, 879.70, 881.70, 882.36, 885.57, 891.39, 893.98, 901.64, 919.19, 919.45, 936.11, 937.66, 937.86, 938.29, 971.15, 971.30, 975.79, 975.94, 977.49, 977.63, 980.35, 980.77, 984.39, 987.74, 990.48, 992.79, 995.90, 1007.10, 1057.80, 1058.61, 1061.88, 1063.72, 1065.14, 1067.28, 1068.25, 1070.06, 1084.16, 1087.95, 1091.25, 1091.65, 1100.84, 1101.62, 1108.99, 1110.39, 1112.14, 1114.03, 1119.21, 1119.84, 1129.14, 1136.63, 1169.19, 1171.40, 1180.88, 1181.98, 1193.47, 1194.60, 1207.43, 1211.23, 1212.19, 1212.77, 1214.44, 1214.82, 1222.61, 1222.86, 1236.36, 1236.88, 1251.92, 1257.60, 1262.02, 1267.85, 1279.35, 1281.40, 1281.86, 1289.21, 1289.87, 1291.21, 1292.09, 1302.00, 1312.25, 1323.86, 1355.61, 1356.95, 1372.00, 1372.59, 1454.99, 1455.07, 1458.82, 1458.87, 1501.18, 1503.27, 1504.29, 1505.86, 1515.43, 1517.03, 1527.28, 1529.07, 1576.71, 1576.95, 1619.22. 1619.32, 1627.18, 1627.80, 1633.57, 1634.21, 1648.25, 1651.29, 1651.52, 1655.87, 1682.50, 1686.86, 1718.22, 1724.37, 2476.34, 2476.61, 2720.15, 2720.25, 2721.43, 2721.69, 2729.42, 2729.56, 2730.98, 2731.75, 2745.14, 2746.48, 2750.82, 2751.03, 2752.14, 2753.23, 2761.23, 2761.64, 2765.22, 2765.45, 2777.44, 2777.91, 2784.32, 2784.75, 2798.42, 2799.36

Table A6.2 Detail settings for ESI-MS/MS experiments of $[Ni^{II}P+H]^{3-}$, $[Co^{III}P]^{3-}$, $[Mn^{III}P]^{3-}$, $[Mn^{III}P+H]^{2-}$, $[Fe^{II}P+H]^{3-}$, and $[Fe^{II}P+2H]^{2-}$ (where P represents TPPS)

	$[Ni^{II}P+H]^{3-}$	**$[Co^{III}P]^{3-}$**		**$[Mn^{III}P]^{3-}$**	**$[Mn^{III}P+H]^{2-}$**	**$[Fe^{II}P+H]^{3-}$**	**$[Fe^{II}P+2H]^{2-}$**
Collision V	4-42	4-20	4-30	4-50	4-23	4-62	4-23
IMS Manual Control	ON	OFF	ON	ON	OFF	ON	OFF
Set Mass	327.6	329	329	492	328.3	493	329
Capillary (kV)	2	2.5	2.5	2.3	2.5	2.6	2.5
Sampling Cone	50	35	29	60	35	90	35
Extraction Cone	0	4	4	0	4	4	4
Source Temperature (°C)	100	100	100	100	100	80	100
Desolvation Temperature (°C)	200	200	200	200	200	150	200
Cone Gas Flow (L/Hr)	30	40	40	127	40	43	40
Desolvation Gas Flow (L/Hr)	200	176	250	200	176	500	176
LM Resolution	15	10	15	15	10	12	10
HM Resolution	12	10	15	12	10	8	10
Trap Collision Energy	4	6	6	6	6	4	6
Trap Gas Flow (mL/min)	10	1.5	2	5.5	2.5	1.9	2.5
Source Gas Flow(mL/min)	50	18	8.6	18.5	18	11.7	18
IMS Gas Flow (mL/min)	40	24	24	40	28.7	35	28.7
Detector	1900	1950	1950	1900	1950	1900	1950
Trap Wave Height (V)	0.2	0.5	0.2	0.2	0.5	0.2	0.5
IMS Wave Velocity (m/s)	550	300	736	550	300	550	300
IMS Wave Height (V)	8.5	0.5	6	13	0.5	12	0.5
Transfer Wave Height (V)	3	0.2	3	3	0.2	3	0.2
Trap Extract Height (V)	10	10	10	10	10	5	10
Transfer Trap Height (V)	12	4	12	12	4	12	4
Transfer Extract Height (V)	8	15	8	8	15	8	15